A STUDY OF WARP-KNITTED SPACER FABRICS AS CUSHIONING MATERIALS FOR HUMAN BODY PROTECTION

LIU YANPING

Ph.D

The Hong Kong Polytechnic University

2013

THE HONG KONG POLYTECHNIC UNIVERSITY

INSTITUTE OF TEXTILES AND CLOTHING

A STUDY OF WARP-KNITTED SPACER FABRICS AS CUSHIONING MATERIALS FOR HUMAN BODY PROTECTION

Liu Yanping

A thesis submitted in partial fulfilment of the requirements for the degree of Doctor of Philosophy

November 2012

CERTIFICATE OF ORIGINALITY

I hereby declare that this thesis is my own work and that, to the best of my knowledge and belief, it reproduces no material previously published or written, nor material that has been accepted for the award of any other degree or diploma, except where due acknowledgement has been made in the text.

____________________________ (Signed)

Liu Yanping (Name of student)

To My Family

For their Love, Patience and Support

Abstract

Sports related injuries from impact accidents have been identified as a major public health problem. To protect people from injuries, protective equipment has been developed by including cushioning materials, which are normally polymeric foams, to absorb the impact energy under compression actions at a relatively constant stress over a large range of strain, to keep the maximum load below some limit that tissue or bones can bear. Lower air permeability and moisture transmission capability of polymeric foams cannot well meet the comfort requirement of protective equipment. As a result, although a variety of impact protectors are available on the market, the use of them is often rejected by wearers.

Warp-knitted spacer fabrics have a three-dimensional construction consisting of two separate outer fabric layers joined together but kept apart by spacer yarns. They have been recently proposed to be cushioning materials for replacing polymeric foams in developing impact protectors for human body protection to reduce the risk of sports injuries due to their good compressibility, high moisture conductivity, and excellent thermoregulation capability. It is crucial to develop impact protectors by using warp-knitted spacer fabrics with required properties. This requires a deep understanding of the deformation mechanism and quantitative structure–property relationships of warp-knitted spacer fabrics under compression. Some effort has already been made to investigate the static compression behaviour of warp-knitted spacer fabrics. It has been shown that spacer fabrics can be produced to have the key feature of behaving as cushioning materials, providing three distinct stages under compression, described

as linear elasticity, plateau and densification. However, all the warp-knitted spacer fabrics used in previous studies were designed empirically. There is a lack of systematic experimental investigations on the compression properties of warp-knitted spacer fabrics in terms of their structural parameters. In addition, no well accepted interpretation and theoretical model have been given to provide a reasonable understanding of the compression deformation mechanism. Clearly quantitative structure–property relationships have also not been well established. In order to establish a clear picture for engineering the cushioning properties of warp-knitted spacer fabrics for human body protection, the purpose of this study was to identify the compression mechanism, to establish the quantitative structure–property relationships under static compression, and to examine the dynamic and curved shape effects on the protective properties.

The study started with a preliminary experimental analysis on the compression properties of a warp-knitted spacer fabric with a typical structure under various test conditions. A potential deformation mechanism of the typical fabric was interpreted based on the analyses of the compression load–displacement curve obtained under a selected proper test condition and the cross-sectional pictures taken at different compression stages. Based on the compression behaviour of the typical spacer fabric and its structure analysis, an analytical model, without considering spacer monofilament radius, outer fabric layer thickness, contacts among spacer monofilaments and yarn material's nonlinearity, was developed to predict the compression properties of the spacer fabric. With this analytical model, the structural parameters affecting the compression behaviour of warp-knitted spacer fabrics were identified. To fully take into account the structural details and the interactions among elements of the fabric, a precise geometric model from Micro X-ray CT scanning was used to build eight finite element (FE) models with different constraints on spacer monofilaments, outer layer thicknesses and compression test boundary conditions. With the FE models, the precise deformation mechanism was identified for the typical spacer fabric. The effects of spacer yarn inclination angle and fineness as well as fabric thickness on compression properties of warp-knitted spacer fabrics were also parametrically studied with six extra FE models that were built by extending one of the eight FE models whose result fits well the experimental result. The identified structural parameters were used to develop twelve warp-knitted spacer fabrics for human body protection. Their static compression and cushioning properties were characterised with the selected compression test method, while their impact compression properties were evaluated with a drop-weight impact tester and analysed in terms of impact contact force–displacement curve, energy absorbed–contact force curve, and transmitted force–time curve. Finally, the twelve warp-knitted spacer fabrics with different laminated layers in hemispherical shape were tested by using the drop-weight impact tester according to the Europe Standard BS EN 1621-1:1998 to assess their protective properties.

The experimental investigations, analytical modelling and finite element modelling clearly revealed the compression mechanism of the typical warp-knitted spacer fabric with typical cushioning properties. Furthermore, the developed FE models successfully bridged the fabric structural parameters, i.e., spacer yarn inclination angle, spacer yarn fineness and fabric thickness, with the compression load–displacement relationships, providing an effective approach to predict the compression behaviour of a spacer fabric with a specified structure quantitatively.

The theoretical and experimental results suggested that spacer fabrics with larger spacer yarn inclination angles, higher fabric thicknesses, finer spacer yarns and larger size mesh of the outer layers have lower resistance under static flatwise compression. Under impact flatwise compression, spacer fabrics with coarser spacer yarns, small-size mesh or close structure outer fabric layers have lower peak contact forces and peak transmitted forces. In addition, an optimized fabric thickness and spacer yarn inclination exist for getting better protective performance. The impact tests in hemispherical shape showed that spacer fabrics with coarser spacer yarns, higher thicknesses, and more stable outer layer structures will have a better force attenuation capacity. Increasing the inclination of spacer monofilaments to around 35º will enhance their shear resistance and therefore increases the force attenuation of the spacer fabric under impact in hemispherical shape. Three layers of the spacer fabric knitted with chain plus inlay structure for both outer layers with a thickness about 2.5 cm in total can comply with the European Standard BS EN 1621-1:1998. The systematic study laid down a principle for engineering the cushioning properties of warp-knitted spacer fabrics for human body protection.

List of Publications Arising from the Thesis

Refereed Journal Papers

1. Yanping Liu, Hong Hu, et al. Compression Behavior of Warp-knitted Spacer Fabrics for Cushioning Applications, Textile Research Journal, 2012, 82(1): 11–20.

2. Yanping Liu, Hong Hu, et al. Impact Compressive Behavior of Warp-knitted Spacer Fabrics for Protective Applications, Textile Research Journal, 2012, 82(8): 773–788.

3. Yanping Liu, Wai Man Au and Hong Hu. Protective Properties of Warp-knitted Spacer Fabrics under Impact in Hemispherical Form. Part I: Impact Behavior Analysis of a Typical Spacer Fabric, Textile Research Journal, in press.

4. Yanping Liu, Hong Hu and Wai Man Au. Protective Properties of Warp-knitted Spacer Fabrics under Impact in Hemispherical Form. Part II: Effects of Structural Parameters and Lamination, Textile Research Journal, in press.

5. Yanping Liu, Hong Hu. An Experimental Study of Compression Behavior of Warp-knitted Spacer Fabric, Journal of Engineered Fibers and Fabrics, in press.

6. Yanping Liu, Hong Hu. Finite Element Modelling of the Compression Behavior of Warp Knitted Spacer Fabric, to be submitted.

Refereed Conference Papers

1. Yanping Liu, Hong Hu. Identifying and modelling the deformation mechanism of warp knitted spacer fabric in compression, Proceedings of the 3rd World Conference on 3D Fabrics and Their Applications, Wuhan, P. R. China, 20–21 April 2011, pp.34–39.

2. Yanping Liu, Hong Hu. Nonlinear Compression Behavior of Warp-knitted Spacer Fabric, Fiber Society 2012 Spring Conferences, EMPA, St. Gallen, Switzerland, May 23–25.

Paper Competition Award

1. Yanping Liu, Hong Hu. Nonlinear Compression Behavior of Warp-knitted Spacer Fabric, The First Place of the poster competition of The Fiber Society Spring 2012 Conference, EMPA, St.Gallen, Switzerland, May 23–25, 2012

Acknowledgements

First of all, I am deeply indebted to my chief supervisor Dr. Hu Hong to whom goes my deepest gratitude for his kindly guidance, constructive and creative comments, and great patience.

I would like to acknowledge with gratitude the financial support of Vincent & Lily Woo Trust for offering me a postgraduate scholarship to study for a PhD.

I have to express my sincere gratitude to my external examiner, Professor Frank K. Ko at The University of British Columbia, who provided me with numerous suggestions to improve the thesis. I would like to give my great thanks to technical staffs Mr Zhou Jinyun, Mr Ng Yuifat, Mr Hui Kevin, Ms Sun M. N. and Ms Liu Su for their assistance in running the experiments included in this thesis. I would also like to thank my friends and colleagues for their kindness and keeping me entertained during my time at PolyU: Ge Zhaoyang, Hu Huawen, Li Gang, Li Qiao, Wang Zhengyue, Xu Kun, Xu Ziwei, Zhang Yifan and countless others.

I am especially grateful to my wife Zheng Yuanyuan, my parents and sisters who give me braveness and confidence in my life. Their love makes this thesis possible.

Finally, I would like to express my special acknowledgment to Hong Kong Innovation and Technology Commission and Hong Kong Research Institute of Textile and Apparel for providing funding support to my PhD study through the project GHP/063/09TP.

Table of Contents

List of Figures

List of Tables

Nomenclatures

A	A constant	[-]
A_c	Area of a cushioning material	[m^2]
a	Acceleration	[m/s^2]
a^*	A constant	[-]
a_i	Acceleration experienced by an ideal absorber	[m/s^2]
a_m	Maximum acceleration	[m/s^2]
B	A constant	[-]
b^*	A constant	[-]
C	A constant	[-]
C_0	A constant of integration	[-]
CC_{xx}	Compression stress–strain characteristic	[kPa]
c^*	A constant	[-]
D	A constant	[-]
d	Displacement of the striker	[mm]
d^*	A constant	[-]
d_m	Knockover comb bar distance	[mm]
E	Young's modulus	[MPa]
E_c	Efficiency of cushioning materials	[-]
EI	Bending rigidity	[$cN \cdot cm^2$]
$E(k,\phi)$	Incomplete elliptic integral of second kind with amplitude ϕ and modulus k	[-]
F	Force	[N]
F_c	Peak contact force	[kN]
F_t	Peak transmitted force	[kN]
$F(k,\phi)$	Incomplete elliptic integral of first kind with amplitude ϕ and modulus k	[-]
G_m	g-level	[-]
g	Gravity acceleration (9.8 m/s^2)	[m/s^2]
g_m	Machine gauge	[-]
H	The vertical height of the elastic rod	[mm]

H_p	The vertical height of planar pillar spacer yarn	[mm]
H_t	The vertical height of planar tricot spacer yarn	[mm]
H_c	Drop height of a mass	[mm]
H_s	Drop height of the striker	[mm]
h	The normalized vertical height of the elastic rod	[-]
h_0	Initial thickness	[mm]
h_c	Thickness of a cushioning material	[mm]
h_f	Thickness of spacer fabric	[mm]
h_l	The height of a needle loop in the outer fabric layer	[mm]
h_{lm}	The height of a needle loop in the outer fabric layer on machine	[mm]
h_w	The width of a needle loop in the outer fabric layer	[mm]
I	The moment of inertia of cross-sectional area	[mm^4]
I_c	Ideality of cushioning materials	[-]
J	Janssen factor	[-]
K	Energy absorbing efficiency	[-]
k	The modulus of the elliptic integrals	[-]
L	The total length of the elastic rod	[mm]
L_p	The total length of a pillar spacer yarn	[mm]
L_t	The total length of a tricot spacer yarn	[mm]
l	The normalized total length of the elastic rod	[-]
M	Bending moment	[N·mm]
M_1	Bending moment at the origin of elastic rod	[N·mm]
M_2	Bending moment at the endpoint of elastic rod	[N·mm]
m	Mass of a body	[kg]
m^*	Normalized bending moment	[-]
m_c	Constant of a cushioning material in defining shape factor	[-]
n_c	Constant of a cushioning material in defining shape factor	[-]
n_{cm}	A number represents connect model of spacer yarns	[-]
n_u	The number of needles underlapped	[-]
P	The vertical force on the elastic rod	[N]
P_Z	The component force along Z-axis of the vertical force on the elastic rod	[N]

P_Y	The component force along Y-axis of the vertical force on the elastic rod	[N]
p	The normalized vertical force on the elastic rod	[-]
Q	The horizontal force on the elastic rod	[N]
q	The normalized horizontal force on the elastic rod	[-]
R	Radius of the anvil	[mm]
r	Radius of the spacer monofilament	[mm]
r^*	Radius of the contact area between striker and spacer fabric	[mm]
r_c	Constant of a cushioning material in defining shape factor	[-]
S	Arc length	[mm]
s	Normalized arc length	[-]
s_c	Constant of a cushioning material in defining shape factor	[-]
s_s	Displacement	[mm]
T	Normalized energy per unit volume	[-]
t	Time	[s]
U_{damage}	Energy dissipated by damage to filaments	[J]
U_{elastic}	Energy stored by the elastic deformation of a spacer fabric	[J]
$U_{\text{elastoplastic}}$	Energy absorbed by the elastoplastic deformation of a spacer fabric	[J]
U_{kinetic}	Kinetic energy of the striker	[J]
U_{machine}	Energy stored by the elastic deformation of testing system	[J]
$U_{\text{mechanical}}$	Energy absorbed by the elastic and elastoplastic deformations of a spacer fabric	[J]
U_{residual}	Residual kinetic energy of the striker after being absorbed by the elastic and elastoplastic deformations of a spacer fabric	[J]
v	Velocity	[m/s]
W	The horizontal width of the elastic rod (mm)	[mm]
W_i	Energy absorbed by an ideal cushioning material	[J]
W_c	Energy absorbed per unit volume	[kJ/m^3]
W_p	The horizontal width of planar pillar spacer yarn	[mm]
W_t	The horizontal width of planar tricot spacer yarn	[mm]

w	The normalized horizontal width of the elastic rod	[mm]
α	A constant angle	[º]
β	The inclination angle of a spacer yarn	[º]
γ	Shear displacement between two outer layers	[mm]
ε	Strain	[-]
ε_m	Maximum strain	[-]
θ	The angle of any point in elastic rod with the vertical	[º]
θ_1	The angle at the origin of elastic rod with the vertical	[º]
θ_2	The angle at the endpoint of elastic rod with the vertical	[º]
μ	Friction coefficient	[-]
σ	Stress	[kPa]
σ_m	Maximum stress	[kPa]
ϕ	The amplitude of the elliptic integrals	[-]
ϕ_1	The amplitude of the elliptic integrals for the origin point of the rod	[-]
ϕ_2	The amplitude of the elliptic integrals for the endpoint of the rod	[-]
$\psi(\epsilon)$	Empirical shape factor	[-]

CHAPTER 1 INTRODUCTION

1.1 Motivation of the research

Sports related injuries from impact accidents have been identified as a major public health problem [1, 2]. To protect people from injuries under impact, a wide range of protective equipment has been developed by including cushioning materials to absorb the impact energy. A cushioning material dissipates the kinetic energy of an impacting mass while keeping the maximum load (or acceleration) below some limit [3]. It generally absorbs the kinetic energy under compression at a relatively constant stress over a large range of strain. In this way, the protected object would not have to endure a concentrated high-energy or high-load impact that would occur if a mass directly impacts on it.

This kind of energy-absorbing material is always integrated or inserted into clothing or protective equipment specially designed for protecting the human body from impact stroke, blows or falls [4-6]. The areas of the body for protection are those which are at greatest risk of impact in case of accidents, including head, shoulder, elbow and forearm, hip, knee, leg, upper and middle tibia. Different kinds of impact protectors have been widely used in traumatic sports such as motorcycling, cycling, horse riding, skiing, skating, skateboarding, and snowboarding; contact sports such as rugby, hockey, basketball, football, handball, and wrestling; as well as other cases such as martial arts, medical devices, and construction work [7, 8]. The wide applications have led to an increasing market need of this kind of product.

Conventionally used impact protectors are normally made by including polyurethane (PU) foams [9]. However, these foams suffer from some insurmountable disadvantages as cushioning materials used for impact protectors. Lower air permeability and moisture transmission capability of polymeric foams cannot well meet the comfort requirement of most protective clothing used in sports and other extreme activities where sweat is easily to be generated and should be transmitted from skin surface to outer layer of the clothing. It has been found that although a variety of impact protectors are available, and most wearers are aware of their effectiveness in preventing injuries, the use of personal protective equipment (PPE) is often rejected by wearers [10].

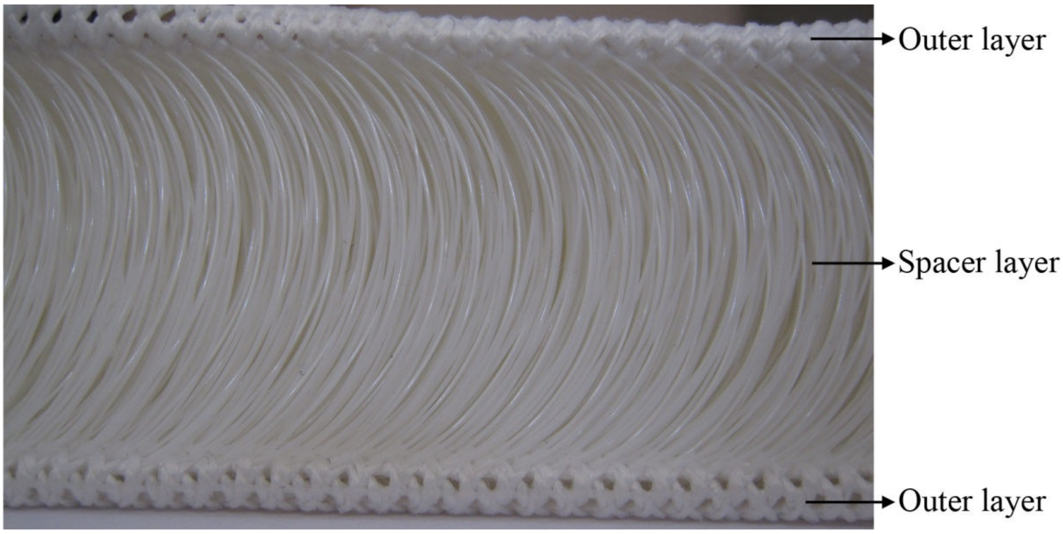

Figure 1.1 A typical warp-knitted spacer fabric.

Recently, warp-knitted spacer fabrics, a kind of three-dimensional (3D) textile, have been proposed for cushioning applications [11, 12]. Such fabrics consist of two separate outer fabric layers joined together but kept apart by spacer yarns, as shown in Figure 1.1 [13]. Unlike other 3D textiles [14-16], the space formed between two independent layers is the most important structural feature. A combination of good compressibility, high moisture conductivity, and excellent thermoregulation capability makes this kind of knitted structure very suitable for human body protective applications.

Some effort has already been made to experimentally and theoretically investigate the static compression behaviour of warp-knitted spacer fabrics. It has been shown that warp-knitted spacer fabrics can be capable of cushioning properties; i.e., their overall compression load–displacement relationships can be designed to have three main stages, i.e., linear elasticity, plateau, and densification [12, 17-19], as required by cushioning materials [3]. However, all the warp-knitted spacer fabrics in earlier studies were designed empirically. There is a lack of systematic experimental investigations on the compression properties of warp-knitted spacer fabrics in terms of their structural parameters. No well accepted interpretation and theoretical model have been given to provide a reasonable understanding of the compression deformation mechanism. Clearly quantitative structure–property relationships have also not been well established for warp-knitted spacer fabrics under compression.

Besides, although the static compression load–displacement relationship obtained and the absorbed energy calculated at a low strain rate can be used as a reference to optimize the cushioning performance of a warp-knitted spacer fabric, the fabric will not have exactly the same behaviour at higher strain rates under impact [20]. In fact, the impacting mass undergoes a period of deceleration, which is determined by the predefined impact energy and the strain rate dependency compression behaviour of the fabric [21, 22]. During an impact process, the maximum deceleration is related to the peak contact force and the peak transmitted force [23]. For human body protection, the force transmitted to the particular part of the body from the impact contact force should not exceed the tolerance that could induce tissue or bone injuries. In other words, the contact force and the transmitted force are not identical during impact. This is quite different from a constant and low speed static compression test that only a static contact force can be measured. In this regard, the dynamic contact force–displacement relationship and the peak transmitted force of a warp-knitted spacer fabric during an impact process of specified energy and velocity are the two key factors which need to be considered when a spacer fabric is designed for protecting a particular part of the human body. Therefore, to understand the exact behaviour of warp-knitted spacer fabrics under impact and to assess the energy absorption capability, real-life impact tests are required. Unfortunately, there is no study concerned with the impact behaviour and energy absorption capacity of warp-knitted spacer fabrics.

Furthermore, in order to offer an adequate level of protection and comfort in wearing, a protective material should well fit with the curvature of the body part to be protected. There is no doubt that the impact properties of a protective material in a curved shape are different from those in a planar shape due to the change of boundary conditions in loading. In this regard, a full investigation on the energy absorption mechanism and force attenuation properties of warp-knitted spacer fabrics of curved shape is very necessary.

Lack of knowledge about fundamental relationships among the materials, structures and properties results in the difficulty of optimized design of warp-knitted spacer fabrics, and this limits their further applications as cushioning materials for human body protection. Therefore, there is a need to identify the precise deformation mechanism and the quantitative structure–property relationships of warp-knitted spacer fabrics under static compression. There is also a need to study the compression behaviour of warp-knitted spacer fabrics with different curvatures under dynamic impact conditions.

1.2 Objectives

In view of the above, this study was aimed at establishing a clear picture for engineering the cushioning properties of warp-knitted spacer fabrics for human body protection with the following specific objectives:

(1) To identify the compression deformation mechanism of warp-knitted spacer fabrics;

(2) To identify the structural parameters that influence the compression and cushioning performance of warp-knitted spacer fabrics;

(3) To establish the quantitative structure–property relationships of warp-knitted spacer fabrics;

(4) To systematically and experimentally investigate the static compression and cushioning properties of warp-knitted spacer fabrics for understanding their structure–property relationships;

(5) To systematically and experimentally investigate the impact compression properties of warp-knitted spacer fabrics for understanding their structure–property relationships;

(6) To experimentally investigate the impact protective performance of warp-knitted spacer fabrics in the curved shape of the human body.

With the successful completion of this study, the principle for engineering the cushioning properties of warp-knitted spacer fabrics can be established, and the optimization approaches can be developed. It is helpful to design and optimize warp-knitted spacer fabrics to be better applied as cushioning materials for human body protection.

1.3 Methodology

The purpose of this study was to identify the compression mechanism, to establish the quantitative structure–property relationships, and to examine the dynamic and curved shape effects on the protective properties of warp-knitted spacer fabrics. In accordance with the specific objectives, both theoretical and experimental approaches were adopted. A flowchart in Figure 1.2 summarises the methodology.

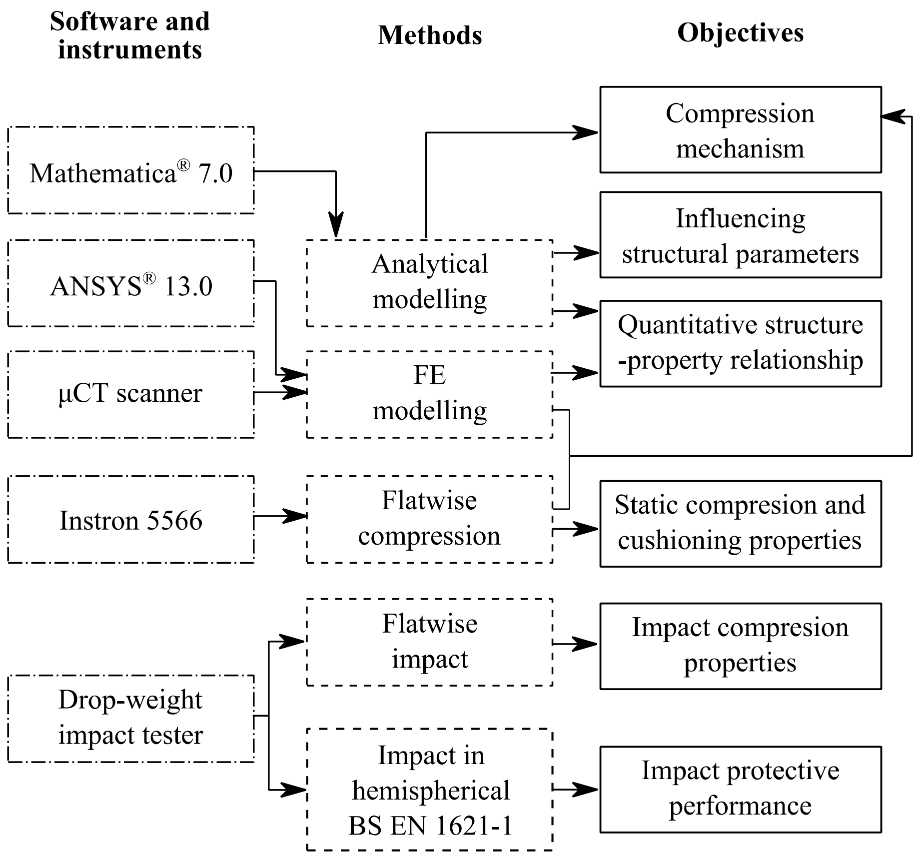

Figure 1.2 Flow chart of overall methodology.

To identify the deformation mechanism of warp-knitted spacer fabrics under compression, flatwise compression tests, analytical modelling and finite element modelling were employed to study a fabric with a typical structure. The fabric was tested under a proper test condition on an Instron 5566 Universal Testing Machine equipped with two circular compression platens of 15 cm in diameter. The potential deformation mechanism was first speculated based on the analyses of both the compression load–displacement curve and cross-sectional pictures of the fabric taken at different compression stages. Then an analytical model based on planar elastica theory was built to theoretically interpret the compression mechanism. In addition, a series of finite element models were established with a precise geometric model from Micro X-ray computed tomography (μCT) scanning to obtain the accurate deformation mechanism.

To identify the structural parameters that influence the compression behaviour of warp-knitted spacer fabrics, the analytical model was used in conjunction with a fabric structural analysis. The identification was achieved by linking the parameters in the governing equations of the analytical model with fabric structural parameters.

To establish the quantitative structure–property relationships of warp-knitted spacer fabrics under compression, both the analytical model and the FE models were used. A parametric study using the analytical model with nondimensional parameters was conducted to investigate the quantitative relationships between the identified structural parameters and the compression properties of warp-knitted spacer fabrics. Experimental validation was performed using a real warp-knitted spacer fabric for the analytical model. The FE models were also used to bridge the structural parameters with the compression load–displacement relationships with high accuracy. In addition, a parametric study was carried out by extending a validated FE model to examine the structure–property relationships of warp-knitted spacer fabrics under compression.

To systematically and experimentally investigate the static compression and cushioning properties of warp-knitted spacer fabrics, twelve warp-knitted spacer fabrics were produced on a double-needle bar Raschel machine for human body protection by varying the identified structural parameters. The fabrics were tested on the Instron 5566 Universal Testing Machine. Both stress–strain relationship and energy–absorption diagram were used to elucidate the compression and cushioning properties of the fabrics.

To systematically and experimentally investigate the impact compression properties of warp-knitted spacer fabrics, the developed fabrics were tested using a drop-weight impact tester equipped with two circular compression platens of 15 cm in diameter. The impact compression behaviour of the spacer fabrics was analysed using impact contact force–displacement curve, energy absorbed–contact force curve, and transmitted force–time curve. The relationship between the peak contact forces and peak transmitted forces of the spacer fabrics with different structures were also discussed.

To experimentally investigate the impact protective performance of warp-knitted spacer fabrics in the curved shape of the human body, the spacer fabrics with different laminated layers were tested at different energy levels using the drop-weight impact tester according to the Europe Standard BS EN 1621-1:1998.

1.4 Thesis outline

Chapter 2 reviews the achievements and presents limitations and gaps of earlier work in the relevant disciplinary areas so as to present the general understanding of background. This determines knowledge gaps and identifies research objectives and significances.

Chapter 3 presents a preliminary experimental study on the effects of test conditions on the compression behaviour of a warp-knitted spacer fabric with a typical structure. The potential compression deformation mechanism is interpreted based on the analyses of both the compression load–displacement curve obtained under a selected proper test condition and the cross-sectional pictures of the fabric taken at different compression stages.

Chapter 4 describes an analytical model established with planar elastica theory for predicting the compression properties of warp-knitted spacer fabrics. The structural parameters affecting the compression properties of spacer fabrics are identified using the model, and a parametric study to examine the effects of the identified parameters on the reaction force in nondimensional is given. An experimental validation of the analytical model with a real spacer fabric is also presented.

Chapter 5 focuses on finite element modelling of a warp-knitted spacer fabric with a typical structure under compression. FE models are established using a precise geometric model from micro-CT scanning. With the models, the precise compression mechanism of the fabric is identified, and the effects of structural parameters on compression behaviour are parametrically studied.

Chapter 6 contains an experimental study on the effects of different structural parameters, including spacer yarn inclination angle and fineness, fabric thickness, and outer layer structure, on the compression and cushioning properties of warp-knitted spacer fabrics.

Chapter 7 presents an experimental study on the effects of different structural parameters on the impact compression behaviour of warp-knitted spacer fabrics in terms of energy absorption, contact force, and transmitted force.

Chapter 8 describes an experimental investigation into the protective properties of warp-knitted spacer fabrics against impact in a hemispherical form with different levels of impact energy and laminated layers.

Chapter 9 presents general conclusions, contributions, limitations, and suggestions for future work.

CHAPTER 2 LITERATURE REVIEW

2.1 Introduction

This chapter reviews the literature relevant to the objectives of this study. It first draws upon the literature dealing with human body protection, including human body response to shock, existing personal protective equipment (PPE) and its relevant measurement techniques. Next the principle, characteristics and evaluation methods of cushioning materials, which constitute the PPE, are covered. Typical cushioning materials are also surveyed. Then past work on warp-knitted spacer fabrics is reviewed. Finally, the existing literature and the highlighted research gaps relevant to the primary objectives of this study are summarised.

2.2 Human body protection

2.2.1 Human body response to shock

People are frequently suffering unexpected mechanical shock impulses in working, sports and daily life. Mechanical shocks include several types of force actions on human body with similar harmful effects. Explosions, explosive compression or decompression, and impacts and blows from rapid changes in body velocity or from moving objects produce shock forces [24]. Damage is usually to lungs, intestines, heart, head, neck, or brain with tissue destruction, or to bone with fracture. Differences in injury patterns arise from differences in rates of loading, peak force, duration, and localization of forces [24].

The greatest focus of impact injury related research has been in understanding and preventing motor vehicle related injuries due to the large number of deaths in motor vehicle crashes [25, 26]. Recently, there has been a parallel interest in sports related impact injuries because they have also been identified as a major public health problem [27, 28]. The difference of sports in comparison to motor vehicle related injuries is that, in many cases the impact energies are related to gravity and velocities reached under human power [27]. According to the findings reported by Conn et al. [1], as reproduced in Tables 2.1 and 2.2, around seven million Americans received medical attention for sports and recreation (SR) related injuries, annually. The most frequently activity related to injury episode was basketball, with a rate of about four injury events per 1000 population. Fracture accounted for 22% of injury episodes. The most common mechanisms of injury were struck by/against (34%), fall (28%), and overexertion (13%). Schneider, et al. also reported the sports injuries results from national health survey for Germany [2]. The results for relative incidences classified by accident type and site are reproduced in Figure 2.1. It shows that six out of ten sports injuries are dislocations, distortions, and/or torn ligaments. The second most common type of injury (18%) was fracture. The most common fracture sites involved the lower extremities. Both the results from US and Germany show that fracture, apparently related to impact stroke, is one of the key injuries. Prevention effort aimed at reducing sports injuries through the use of PPE to mitigate the impact energies has already been made and will be surveyed in the next section.

Table 2.1 Estimated annual number and percentage of sports and recreational related injury episodes, rate per 1000 population, and 95% confidence interval (CI) by type of activity for persons aged 5 years and older: US, 1997–99 (Reproduced from [Injury Prevention, J M Conn, et al., 9, 117–123, 2003] with permission from BMJ Publishing Group Ltd.)

Activity	No in 1000s (%)*	Rate (95% CI)
Basketball	977 (14.4)	3.9 (3.3 to 4.5)
Pedal cycling	649 (9.6)	2.6 (2.1 to 3.1)
Recreational sport‡	647 (9.5)	2.6 (2.2 to 3.0)
Exercising	614 (9.1)	2.5 (2.1 to 2.9)
Football	572 (8.4)	2.3 (1.9 to 2.7)
Baseball/softball	492 (7.3)	2.0 (1.6 to 2.4)
Soccer	352 (5.2)	1.4 (1.1 to 1.7)
Ice/roller skating/skateboarding	342 (5.0)	1.4 (1.1 to 1.7)
Gymnastics/cheerleading	302 (4.5)	1.2 (0.9 to 1.5)
Snow sports	284 (4.2)	1.1 (0.7 to 1.5)
Playground equipment	238 (3.5)	1.0 (0.7 to 1.3)
Water sports	226 (3.3)	0.9 (0.7 to 1.1)
Combative sports	180 (2.7)	0.7 (0.5 to 0.9)
Other individual sports‡	493 (7.3)	2.0 (1.6 to 2.4)
Other team sports	414 (6.1)	1.7 (1.3 to 2.1)
Total	6781 (100.0)	27.2 (25.6 to 28.8)

*Numbers and percentages may not sum to total due to rounding. †Estimates may be unstable because they are based on <20 cases or the coefficient of variation >30%. ‡Recreational sports includes tennis, racquetball, badminton and other racquet sports, as well as golf, bowling, fishing, hunting, hiking, mountain climbing and other leisure sports; other individual sports includes all other sport recreation categories; for example, horseback riding, all-terrain vehicle, frisbee, and catch; and other team sports includes volleyball, rugby, hockey, lacrosse, cricket, and others.

Table 2.2 Estimated annual number of episode related injury diagnoses* for persons aged 5 years and older: US, 1997–99 (Reproduced from [Injury Prevention, J M Conn, et al., 9, 117–123, 2003] with permission from BMJ Publishing Group Ltd.)

	Diagnoses (in 1000s)†	Overall (%)†	Body part (%)†
Head/neck	1109	14.8	100.0
Open wound	622	8.3	56.1
Internal organs	191	2.5	17.2
Superficial/contusions	165	2.2	14.9
Fracture	67‡	0.9	6.0
Unspecified	64‡	0.9	5.8
Torso	577	7.7	100.0
Sprains/strains	164	2.2	28.4
Superficial/contusions	141	1.9	24.4
Fracture	120	1.6	20.8
Internal organs	14‡	0.2	2.4
Open wounds	7‡	0.1	1.2
Crushing	6‡	0.1	1.0
Unspecified	125	1.7	21.7
Upper extremities	2342	31.2	100.0
Fracture	998	13.3	42.6
Sprains/strains	627	8.4	26.8
Superficial/contusions	219	2.9	9.4
Dislocations	135	1.8	5.8
Open wounds	131	1.7	5.6
Crushing	17‡	0.2	0.7
Amputations	8‡	0.1	0.3
Burns	7‡	0.1	0.3
Nerves	6‡	0.1	0.3
Unspecified	193	2.6	8.2
Lower extremities	2922	38.9	100.0
Sprains/strains	1566	20.9	53.6
Fracture	464	6.2	15.9
Superficial/contusions	285	3.8	9.8
Open wounds	196	2.6	6.7
Dislocations	109	1.5	3.7
Amputations	11‡	0.1	0.4
Blood vessels	4‡	0.1	0.1
Unspecified	286	3.8	9.8
Other body parts§	553	7.4	100.0
Total	7503	100.0	

*Includes 8.6% of injury episodes that involved more than one diagnosis. †Numbers and percentages may not sum to total due to rounding. ‡Estimates may be unstable because they are based on <20 cases or the coefficient of variation >30%. §Includes injuries to the spine and back, other multiple/unspecified body parts, and late effects.

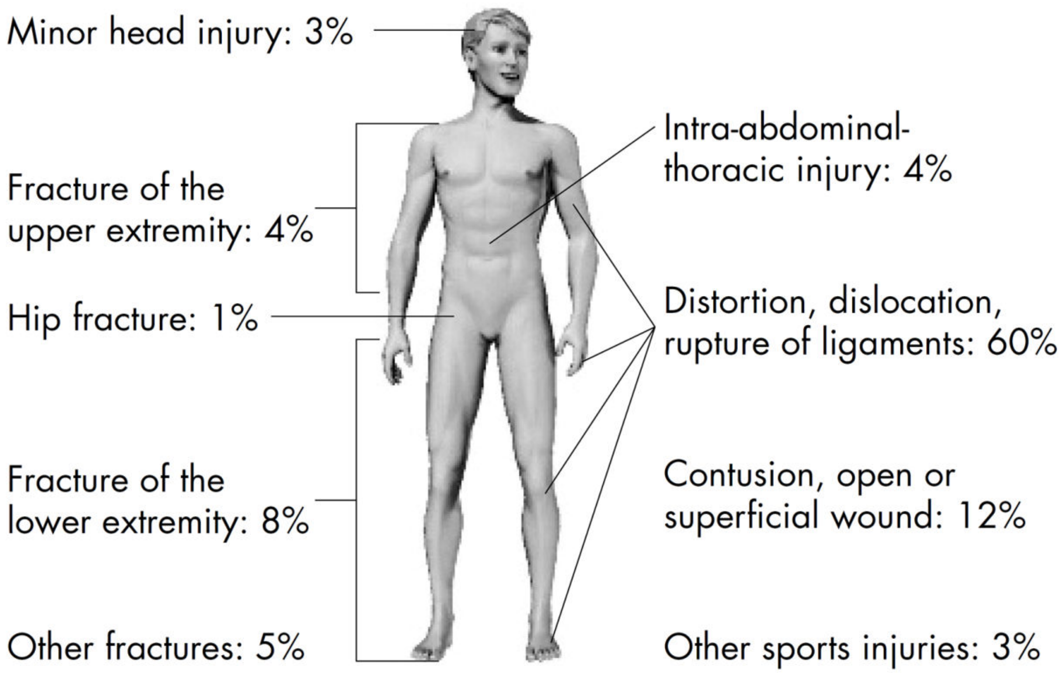

Figure 2.1 Relative distribution of sports injuries by type and location (both sexes). German national health survey.

(Reproduced from [Br J Sports Med, S Schneider, et al., 40, 334–339, 2006] with permission from BMJ Publishing Group Ltd.)

2.2.2 Personal protective equipment

To protect human body from injuries under various exposure conditions, a wide range of PPE has been developed [29-34]. Most commercial PPE, also called impact protector, is designed for sports uses to reduce the risk of injury to players. There are numerous impact protectors for different parts of body under various kinds of sports. Major PPE for some popular sports is summarised as listed in Table 2.3.

Impact protectors are designed to protect people from injury, but their shock-absorbing ability often stands in contradiction to their wearing comfort and freedom of movement. It has been found that although a variety of impact protectors are available, and most wearers are aware of their effectiveness in preventing injuries, the use of PPE is often rejected by wearers [35].

Table 2.3 Typical PPE for popular sports

Sports	PPE
Equestrianism	Helmet, body protector, shoulder protectors
Snowboarding	Helmet, wrist guards, knee pads, elbow pads, hip pads, upper body protector
In-line skating	Helmet, wrist guards, elbow and knee pads
Football	Shin guards, gloves
Ice Hockey	Helmet, shoulder protectors, elbow pads, padded gloves, padded pant, shin guards
Rugby	Helmet, vest, shoulder pads, elbow and forearm guard, bicep guards
Motorcycling	Helmet, shoulder protectors, elbow and forearm guard, hip protector, knee and tibia pads, leg protectors, body protector

2.2.3 Measurement techniques for PPE

A series of standard tests has been developed for evaluating the protective performance of commercial impact protectors. Some typical standards are listed in Table 2.4. Impact protection is generally measured by the force transmitted during impact; a striker of specified shape, size, and weight drops freely onto the protector placed on a hemispherical anvil with the required velocity and impact energy. The shape, size, and weight of the strikers used for different protectors are determined according to the application situations. The strikers should be circular flat surface plate, narrow or wide rectangular flat surface bar, rectangular bar with curved surface, and ball shape, etc. Two weights 2500 g and 5000 g are generally used for the strikers. The hemispherical anvils have different curvatures to simulate the areas of the body to be protected. The radius of the anvils ranges from 12.5 to 150 mm

(Table 2.5), and the impact energy levels for the various types of protectors lie between 1 and 60 J.

Table 2.4 Test standards for PPE

Standard	Protectors	Situations
BS EN 1621-1:1998	Shoulder, elbow and forearm, hip, knee and tibia, leg	Motorcycling
BS EN 1621-2:2003	Back protectors	Motorcycling
BS EN 13277-2:2000	Instep protectors, shin protectors and forearm protectors	Taekwondo, Karate, Kick-boxing
BS EN 13277-3:2000	Trunk protectors	
BS EN 13277-4:2001	Head protectors	
BS EN 13277-5:2002	Genital protectors and abdominal protectors	
BS EN 13277-6:2003	Breast protectors	
BS EN 13277-7:2009	Hand and foot protectors	Boxing
BS EN 13546:2002	Hand, arm, chest, abdomen, leg, foot and genital protectors	Hockey
BS EN 13158:2009	Protective jackets, body and shoulder protectors	Equestrian
BS 7930-1:1998	Eye-protectors	Squash
BS 7928-2:2009	Face protectors	Cricket
BS 7928:1998	Head protectors	Cricket
BS 6183-2:2000	Genital protectors	Cricket
BS 6183-3:2000	Leg protectors	Cricket
BS 6183-4:2001	Gloves	Cricket
BS EN 13567:2002	Hand, arm, chest, abdomen, leg, genital and face protectors	Fence
BS EN 14120:2003	Wrist, palm, knee and elbow protectors	Roller sports
BS EN 13061:2009	Shin guards	football

Table 2.5 Hemispherical anvils for impact tests of PPE

Types	Radius	Protectors
A	12.5 mm	Lower leg, forearm, upper arm, fingers and palms, digit ends, shin protectors
B	25 mm	Malleolar region of shin and elbow protectors
C	50 mm	Knee and shoulder protectors
D	100 mm	Kickers, gloves, genital protectors
E	150 mm	Abdominal, chest, breast, thigh and hip protectors

Since PPE is used to attenuate the impact force to protect people from injury, its key components are cushioning materials for absorbing impact energy. In the next section, the principle, characteristics and evaluation methods of cushioning materials as well as typical cushioning materials will be surveyed.

2.3 Cushioning materials

2.3.1 Principle of cushioning materials

Cushioning materials are used to absorb impact energy to defend an object under the level of its allowable stress [36]. Impact protectors are normally manufactured to include energy-absorbing materials in the form of pads. They are integrated or inserted into protective clothing or equipment specially designed for protecting the human body from impact, blows or falls [37]. The principle of a cushioning material is to reduce the force created when one surface comes abruptly into contact with another, by compressing or deforming so as to produce a gradual, rather than instantaneous, change in velocity. This reduces potentially high decelerations to more moderate values and thereby minimizes damaging impact forces. To meet the requirement of the function, cushioning materials generally absorb kinetic energy under compression actions at a relatively constant stress over a large range of displacement.

2.3.2 Characteristics of cushioning materials

In view of the function of cushioning materials that is to absorb as much as possible of the energy generated during impact and to transmit a force lower than the allowable value, an ideal cushioning material may be defined as one that transmits a constant force to the object when compressed throughout its thickness [20, 38]. The stress–strain curve of such a material is shown schematically in Figure 2.2(a). The energy absorbed W_i by such a material is

$$W_i = \sigma A_c h_c, \tag{2.1}$$

where σ is the compression stress, A_c is the contact area, and h_c is the thickness of the cushioning material. The constant force transmitted by it is σA_c. However, it is difficult to produce such an ideal cushioning material, and the real one generally has the stress–strain curve as shown in Figure 2.2(b). Its overall compression stress–strain relationship can be split into three main stages, i.e., linear elasticity, plateau, and densification. In the plateau stage, the material can absorb a large amount of energy but keep a relatively constant stress. The energy absorbed by the material is low in the densification stage, but the stress increases steeply. For a specific application, the cushioning material preferably absorbs all the energy before reaching the densification stage in order to prevent the unpredictably increased reaction stress in this insecure stage.

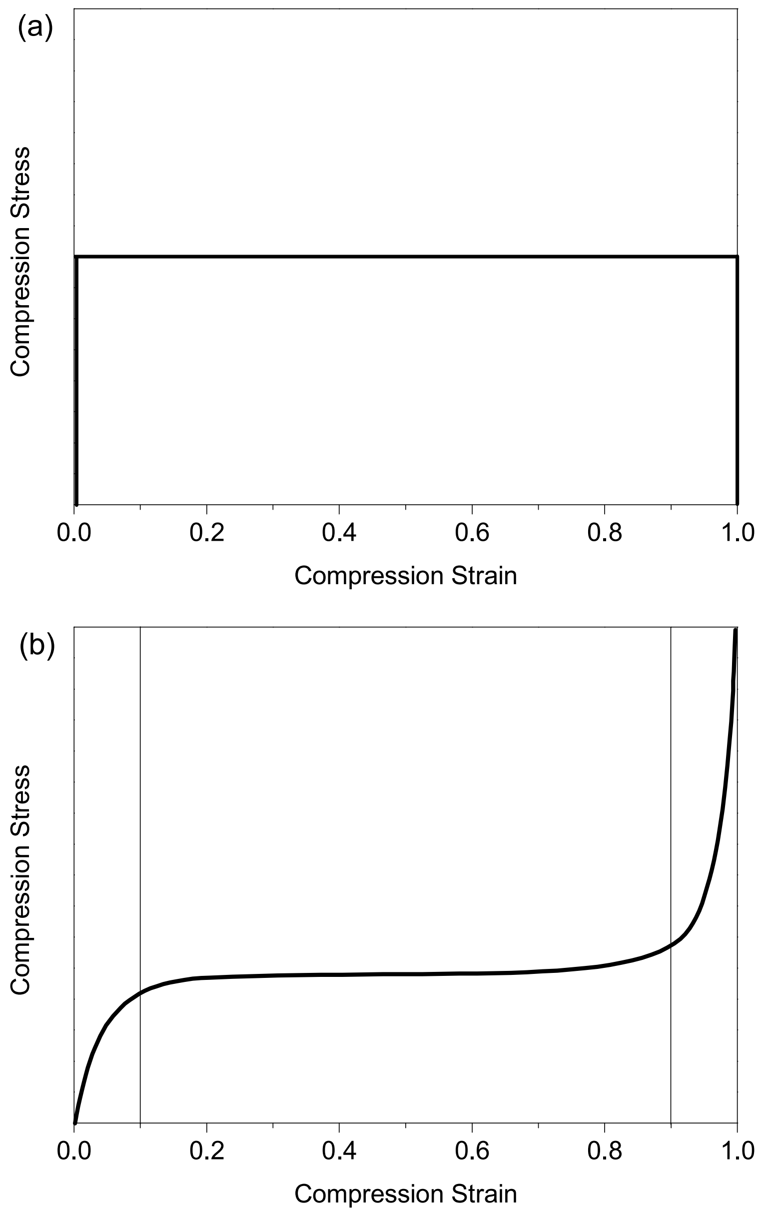

Figure 2.2 Schematic stress–strain curves for: (a) an ideal cushioning material and (b) a real cushioning material [38].

(Reproduced with permission of John Wiley & Sons, Inc.)

2.3.3 Evaluation methods for cushioning materials

It is of great importance to quantitatively assess the cushioning properties for selecting or producing an appropriate cushioning material for a particular application [39]. The commonly used methods include compression stress–strain curves, cushioning curves [40, 41], efficiency curves [20, 21, 38], ideality curves [20, 21, 38], energy absorption diagrams [3], Janssen factor [42, 43], and Rusch curves [44].

For cushioning curves, assume that a body of mass m is dropped onto a cushioning material of an area A_c and a thickness h_c from a height H_c. The cushioning material restrains the body while undergoing compression to a maximum strain ε_m under a maximum stress σ_m. Regarding the energy absorbed due to the compression of the material, we have

$$mgH_c = A_c h_c \int_0^{\varepsilon_m} \sigma \, d\varepsilon. \tag{2.2}$$

The static stress generated in the cushioning material being mg/A_c, given by

$$\frac{mg}{A_c} = \frac{h_c}{H_c} \int_0^{\varepsilon_m} \sigma \, d\varepsilon. \tag{2.3}$$

The dimensionless maximum deceleration (g-level) G_m can be expressed as

$$G_m = \frac{\sigma_m A_c}{mg} = \frac{\sigma_m A_c}{(A_c h_c / H_c) \int_0^{\varepsilon_m} \sigma \, d\epsilon} = \frac{H_c}{h_c} \frac{\sigma_m}{\int_0^{\varepsilon_m} \sigma \, d\varepsilon}. \tag{2.4}$$

For a cushioning material with a given stress–strain curve, the value of ε_m for any static stress, thickness, and drop height can be obtained, G_m can be calculated by Equation (2.4), and thus the cushioning curve can be obtained by plotting G_m against the static stress mg/A_c.

The efficiency E_c is defined as the ratio between the energy absorbed by a real cushioning material compressed to a maximum strain ε_m and the energy absorbed by an ideal cushioning material that transmits the same maximum but constant stress σ_m to the protected object when fully compressed. It can be rewritten as

$$E_c = \frac{A_c h_c \int_0^{\varepsilon_m} \sigma \, d\varepsilon}{A_c h_c \sigma_m} = \frac{\int_0^{\varepsilon_m} \sigma \, d\varepsilon}{\sigma_m}. \tag{2.5}$$

The efficiency curves then can be obtained by plotting the efficiency E_c against the stress σ.

The ideality I_c is defined as the ratio between the energy absorbed by a real cushioning material and that by an ideal one compressed to the same strain,

$$I_c = \frac{A_c h_c \int_0^{\varepsilon_m} \sigma \, d\varepsilon}{A_c h_c \sigma_m \varepsilon_m} = \frac{\int_0^{\epsilon_m} \sigma \, d\varepsilon}{\sigma_m \varepsilon_m}. \tag{2.6}$$

The ideality curves then can be obtained by plotting the ideality I_c against the stress σ.

An energy–absorption diagram is obtained by plotting the absorbed energy per unit volume W_c against the stress σ. The energy absorbed per unit volume up to a strain ε is given by

$$W_c = \int_0^{\varepsilon} \sigma(\varepsilon) \, d\varepsilon. \tag{2.7}$$

Janssen factor has been widely used to compare the energy absorbing capacity of different cushioning materials. The efficiency of a cushioning material in absorbing an energy J can be defined as the ratio of the maximum acceleration experienced by the material a_m to the acceleration which would be experienced by an ideal absorber a_i, namely,

$$J = \frac{a_m}{a_i}. \tag{2.8}$$

The ideal absorber can absorb energy at a constant force F, and it can deform completely. Thus, the acceleration is

$$a_i = \frac{F}{m}. \tag{2.9}$$

The kinetic energy equals the work done by the constant force in the cushioning material through a displacement equal to its thickness

$$\frac{1}{2}mv^2 = ma_i h_c, \tag{2.10}$$

where v and m are the initial velocity and the mass of the cushioned object, respectively, and h_c is the height of the cushioning material. Then the acceleration is

$$a_i = \frac{v^2}{2h_c}. \tag{2.11}$$

The Janssen factor J is often plotted against the impact energy W_c per unit volume of the cushioning material.

Rusch [44] first noted that the shape of the stress–strain curve of a cushioning material can be defined by an empirical shape factor $\psi(\varepsilon)$, defined by

$$\sigma = E\psi(\varepsilon)\varepsilon, \tag{2.12}$$

where σ is the compression stress, E is the Young's modulus of the cushioning material, and ε is the strain. The shape factor is found empirically to have the form:

$$\psi(\varepsilon) = m_c\varepsilon^{-n_c} + r_c\varepsilon^{s_c}, \tag{2.13}$$

where m_c, n_c, r_c, and s_c are constants of the particular cushioning material. Rusch defined the energy-absorbing efficiency K as the maximum deceleration produced by an ideal material a_i divided by that of the material under investigation a_m. It can be written as

$$K = \frac{v^2}{2h_c a_m} = \frac{1}{J}, \tag{2.14}$$

and T is the impact energy per unit volume of the cushioning material normalized by the Young's modulus

$$T = \frac{W_c}{E}. \tag{2.15}$$

The ratio T/K gives the peak stress normalized by the modulus

$$\frac{T}{K} = \frac{mv^2}{2A_c h_c E} \cdot \frac{2h_c a_m}{v^2} = \frac{ma_m}{A_c E} = \frac{\sigma_m}{E}. \tag{2.16}$$

The optimum cushioning material for absorbing a given amount of energy with a maximum allowable peak stress can be determined by plotting *T/K*, the peak stress normalized by the modulus, against *T*, the energy per unit volume of the impact normalized by the modulus.

To generate stress–strain curves for evaluating cushioning properties using abovementioned methods, there are two recognized standards which are usually employed. Static compression tests can be conducted according to ASTM D575 Standard Test Methods for Rubber Properties in Compression. The acceleration-time data of cushioning materials can be achieved from dropping a falling guided platen assembly onto a motionless sample according to ASTM 1596 Standard Test Method for Dynamic Shock Cushioning Characteristics of Packaging Material.

2.3.4 Typical cushioning materials

Typical cushioning materials include polymeric foams, polymeric solid elastomers, rubberized fibre cushion [45], air cushion [46], and corrugated fibreboard [39, 47-50].

Polymeric foams are the most commonly used cushioning materials for human body impact protection. Several kinds of polymers have been applied for producing foams, such as polyurethane (PU) [3, 51, 52], polystyrene (PS) [53-55], polyethylene (PE) [56, 57], polypropylene (PP) [58-60], Acrylonitrile-Butadiene-Styrene (ABS) [55], phenolic [61], and olefinic [62].

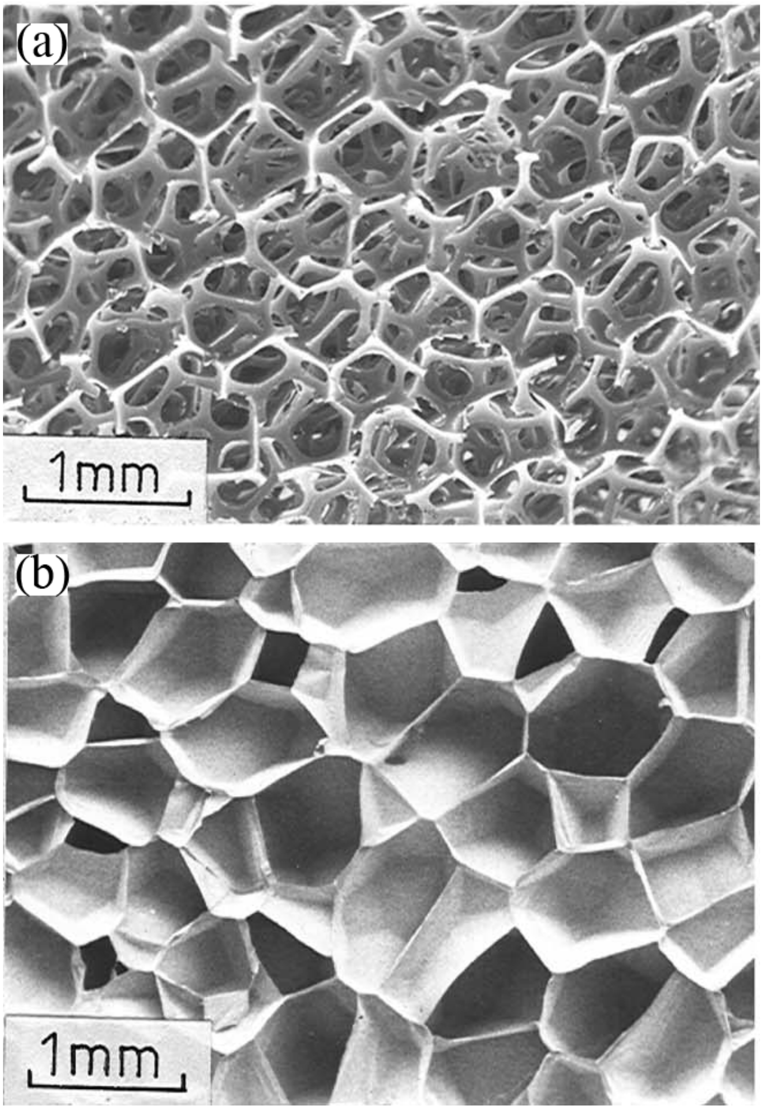

Figure 2.3 Polyurethane foam: (a) open-cell; (b) closed-cell [63].

(Reproduced with permission of Cambridge University Press)

Polymeric foams can be classified into two categories, i.e., open cell [64-66] and close cell [67, 68], according to their cells' microstructures [63] (Figure 2.3). They are called open cells when cells are connected by beam-type edges only. On the other hand, it is called closed-cell when a cell is fully enclosed with cell walls [69]. Typical compression stress–strain curves are shown in Figure 2.4 for closed-cell rigid polyurethane foams of various densities [51]. Each curve has three stages: linearly elastic response, yielding with a plateau stress, and densification when the stress increases rapidly with strain. As explained by Gibson [70], the linearly elastic regime is corresponding to cell edge bending or face stretching; the stress plateau is corresponding to progressive cell collapse by elastic buckling, plastic yielding or brittle crushing, depending on the nature of the solid from which the material is made; and the densification is corresponding to collapse of the cells throughout the material and subsequent loading of the cell edges and faces against one another. Cellular materials normally have low relative densities (10–20%) so that they can be deformed up to large strains (70–80%) before densification occurs [70].

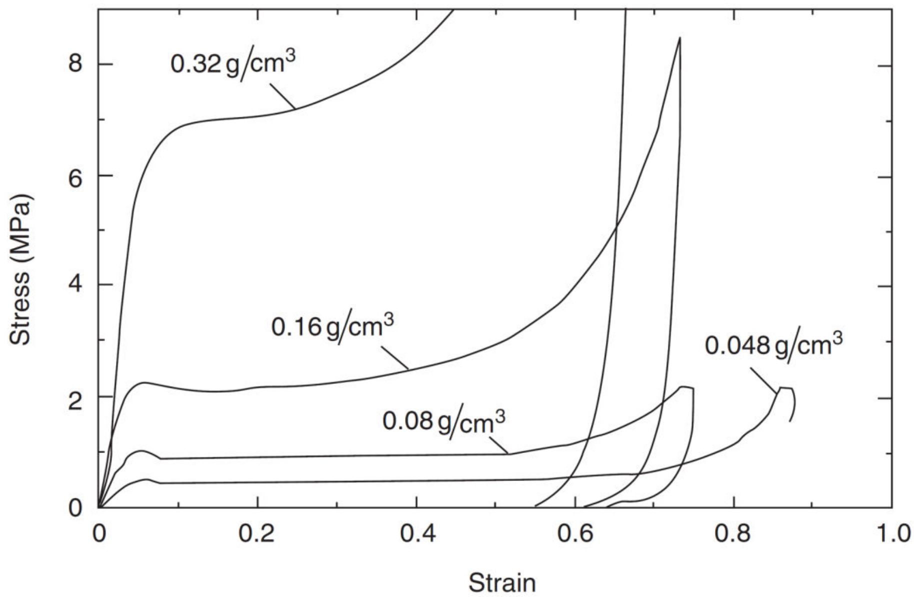

Figure 2.4 Stress–strain curves for closed cell rigid polyurethane foams of various densities [51].

(Reproduced with permission of American Society of Civil Engineers)

Commercial impact protectors are generally made of polymeric foams. Although their cushioning properties are pleasing, lower air permeability and moisture transmission capability of foams cannot well meet comfort requirement of most protective clothing used in sports and other extreme activities. A combination of excellent compressibility, high moisture conductivity, and good thermoregulation capability makes warp-knitted spacer fabrics very suitable as alternative cushioning materials for human body protection. In the next section, the structure and production principle of warp-knitted spacer fabrics are presented, and their properties, applications, and theoretical studies which were studied and developed in previous years are reviewed.

2.4 Warp-knitted spacer fabrics

2.4.1 Structure and production principle

Spacer fabrics are of a 3D structure consisting of two separate outer fabric layers joined together but kept apart by spacer yarns. This kind of fabric can be manufactured by warp knitting [12, 17, 71], weft knitting [72-76], weaving [77-86], and nonwoven [87, 88] technologies (Figure 2.5).

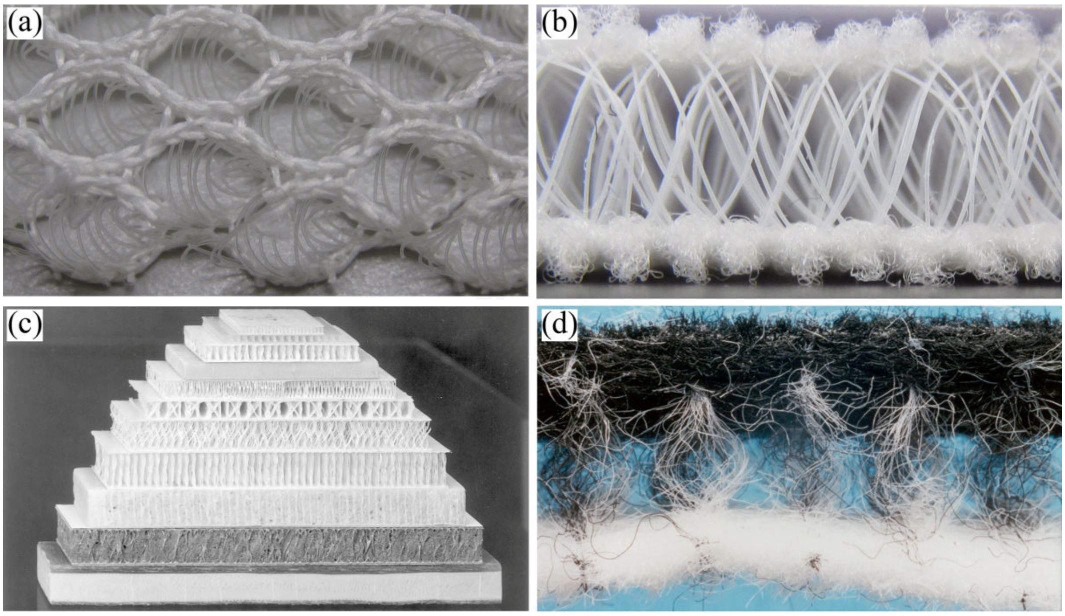

Figure 2.5 Different types of spacer fabrics: (a) warp-knitted; (b) weft-knitted; (c) woven [79][1]; (d) nonwoven [88].

[1] Reprinted from Composite Science and Technology, 60, A. W. van Vuure, et al., Modelling the core properties of composite panels based on woven sandwich-fabric preforms, 1263–1276, 2000, with permission from Elsevier

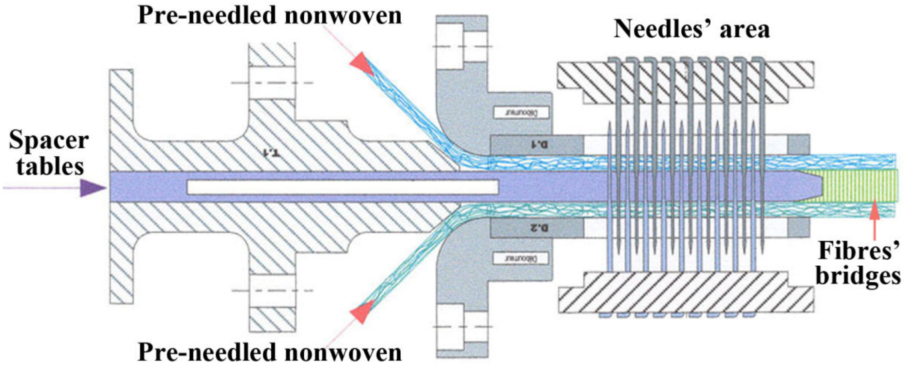

Figure 2.6 Schematic illustration of the Napco® technology [88, 89].

(Reproduced with kind permission from Springer Science and Business Media)

Nonwoven spacer fabrics are manufactured by needle-punching two pre-needled nonwoven fabric layers with a defined space [87, 90]. Figure 2.6 shows a patented technology NAPCO® for producing nonwoven spacer fabrics using the needle-punching process [91]. This technology enables the manufacture of nonwoven spacer fabrics of thickness ranging from 3 to 60 mm [89]. The fabrics are mainly used for composite applications because their spacer layers are easily crushed when vertically compressed [90].

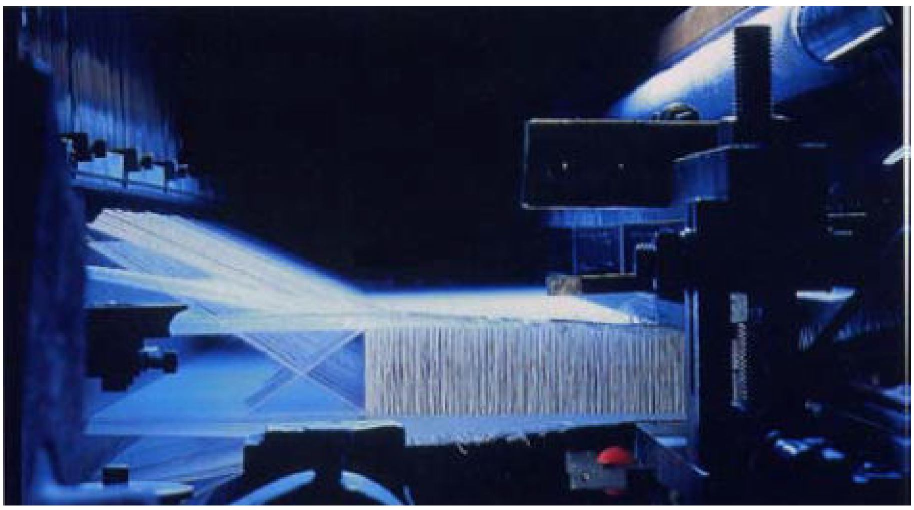

Figure 2.7 Girmes double-wall fabric on a weaving machine [85].

Woven spacer fabrics are produced by using a velvet weaving technique [86]. A velvet loom weaves warp and weft yarns into two separate ground fabrics with a certain space simultaneously, while pile warp yarns interlace alternately with the two separate ground fabrics (Figure 2.7). The pile yarns are cut by means of a knife during the weaving process to form two velvet fabrics [85]. If the knife is deactivated, a woven spacer fabric is obtained through this process. Figure 2.7 shows the weaving process of a woven spacer fabric from Girmes GmbH called double-wall fabrics or drop-stitched fabrics. They are available with a wide range of thicknesses of up to 1000 mm. The fabrics with polyester spacer yarns and coated surfaces have been widely used for building inflatable boats. Upon inflation, the fabrics can form flat or curved panels of variable thickness controlled by the spacer yarn lengths. Glass fibres have also been processed with this technique, and their products are called 3D fibreglass, which have been widely used in composites [78, 80, 82, 86].

Weft-knitted spacer fabrics are manufactured with either circular or flat weft knitting machines with two sets of needles (Figure 2.8). Producing spacer fabrics on circular weft knitting machines is using dial needles and cylinder needles to create two distinctive layers of fabric separately and then connect the two fabric layers with tucks on both the dial and cylinder needles (Figure 2.8(b)). The distance between the two individual fabric layers can be adjusted by varying the dial height relative to the machine cylinder. Spacer fabric thicknesses preset in this way can vary between 1.5 and 5.5 mm [92]. On the market, typical circular knitting machines for producing spacer fabrics include the Technit D3 by Mayer & Cie. GmbH & Co. KG, Albstadt, Germany, and the UCC548 and the UCC572 by Terrot GmbH, Chemnitz, Germany.

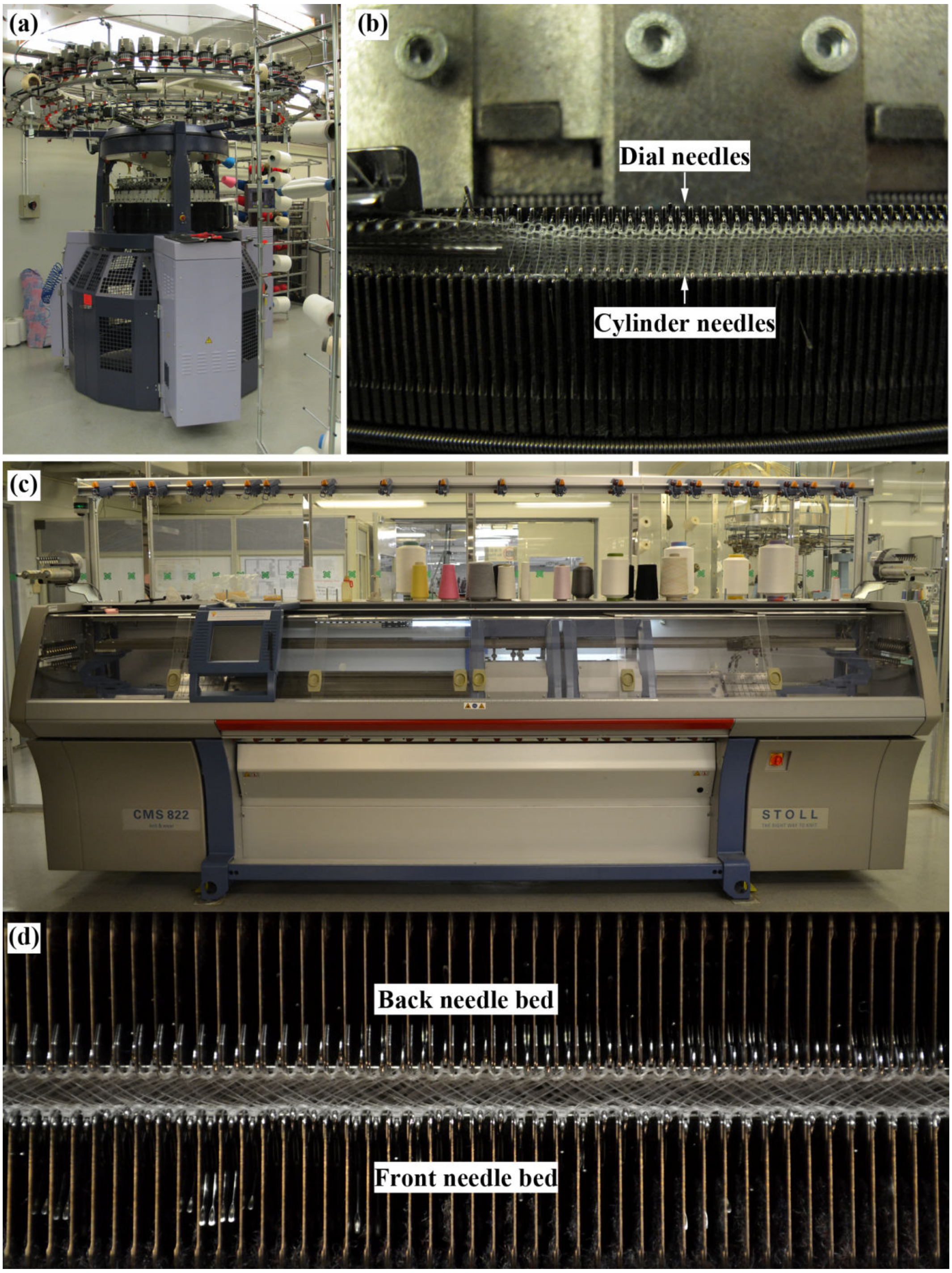

Figure 2.8 Producing spacer fabrics on weft knitting machines: (a) a Terrot double-jersey circular machine; (b) knitting a spacer fabric on the circular machine; (c) a Stoll computerized flat knitting machine; (d) knitting a spacer fabric on the flat machine.

Similar to the production of spacer fabrics on circular machines, producing spacer fabrics on flat machines is creating two independent fabric layers on the front- and back-needle beds separately and then connecting them by tucks on both the needle beds (Figure 2.8(d)). The distance between the two needle beds determines the spacer fabric thickness. Unlike circular weft knitting machines, the distance between the two needle beds of a flat weft knitting machine is normally fixed around 4 mm. By using computerized flat knitting machine with elastomeric yarns, spacer fabric thicknesses can vary in a wide range (Figure 2.9) [13]; however, the productivity is very low for knitting thicker spacer fabrics. The mechanism of tucking on two sets of needles leads to ineffective constraints on spacer yarns provided by outer fabric layer stitches. As shown in Figure 2.10, the spacer yarns are not knitted into the outer fabric layers through tuck stitches, causing the spacer yarns easy to shear when subjected to compression loading, thereby exhibiting lower compression resistance.

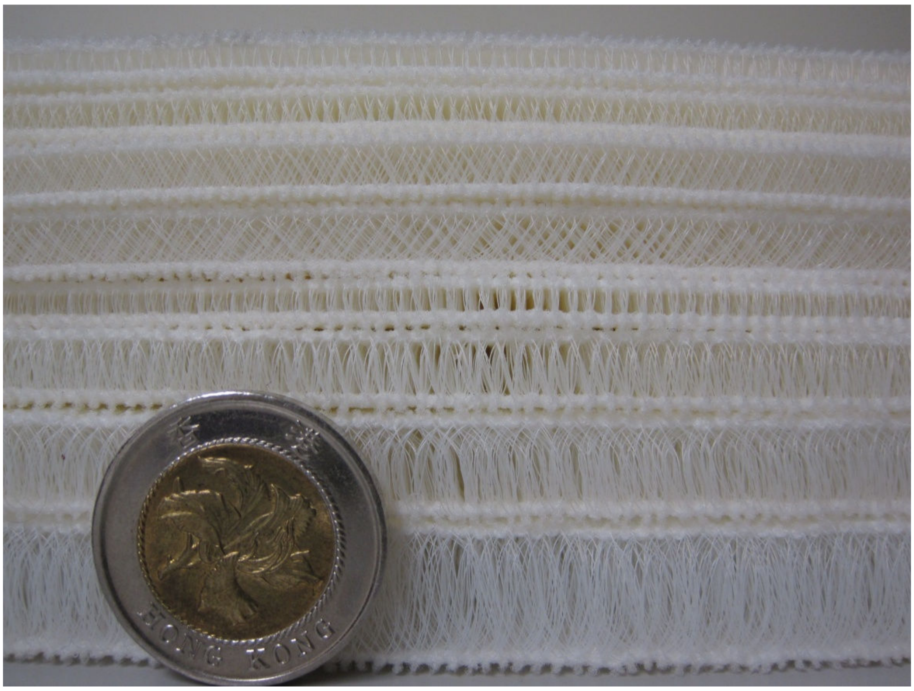

Figure 2.9 Spacer fabrics produced with a computerized flat knitting machine Stoll CMS 822, E14 (the coin of a diameter 2.4 cm).

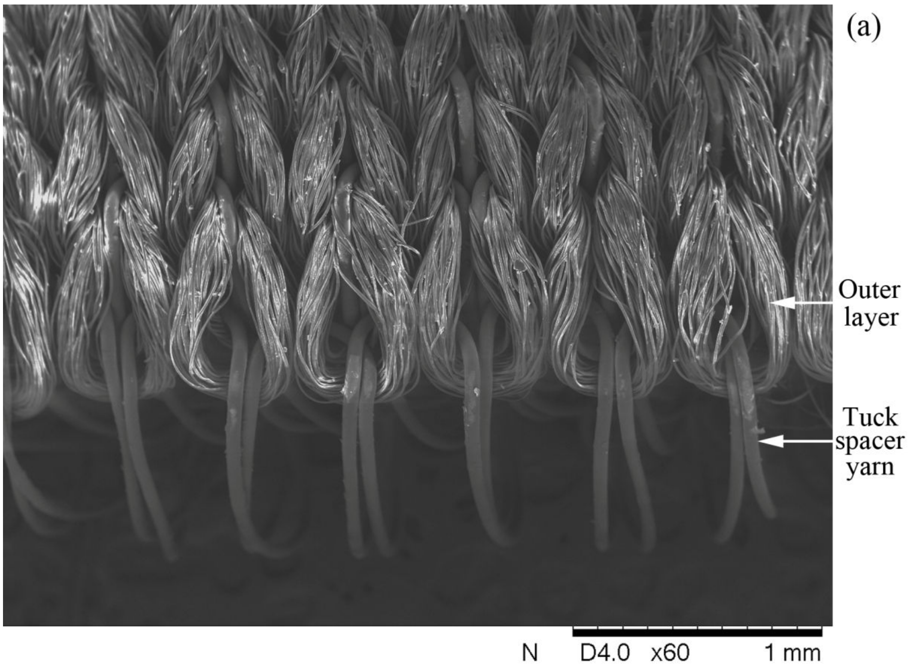

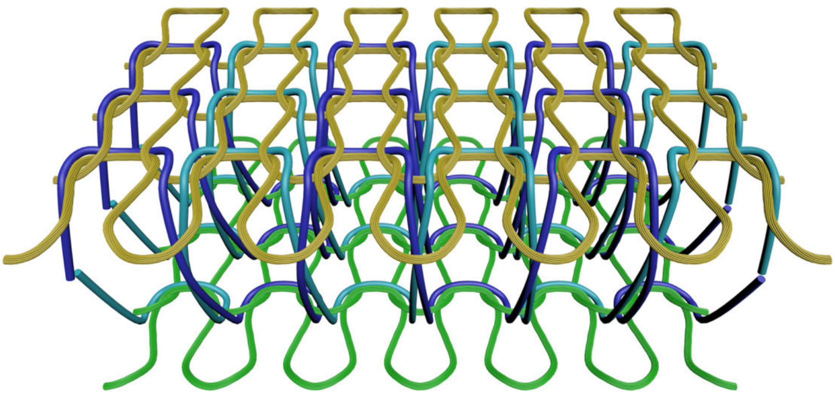

Figure 2.10 Structure of a typical weft-knitted spacer fabric produced with circular weft knitting machine: (a) real fabric; (b) scheme.

Warp knitting technology is the most commonly used technology for producing spacer fabrics, and its products called warp-knitted spacer fabrics have attracted great attention due to their low cost, high productivity, and wide structure variations compared to the other kinds of spacer fabrics. The critical characteristic distinguishing warp-knitted spacer fabrics from other kinds of spacer fabrics is that their three basic structural elements, i.e., top layer, bottom layer, and spacer layer, are knitted together in the same knitting cycle.

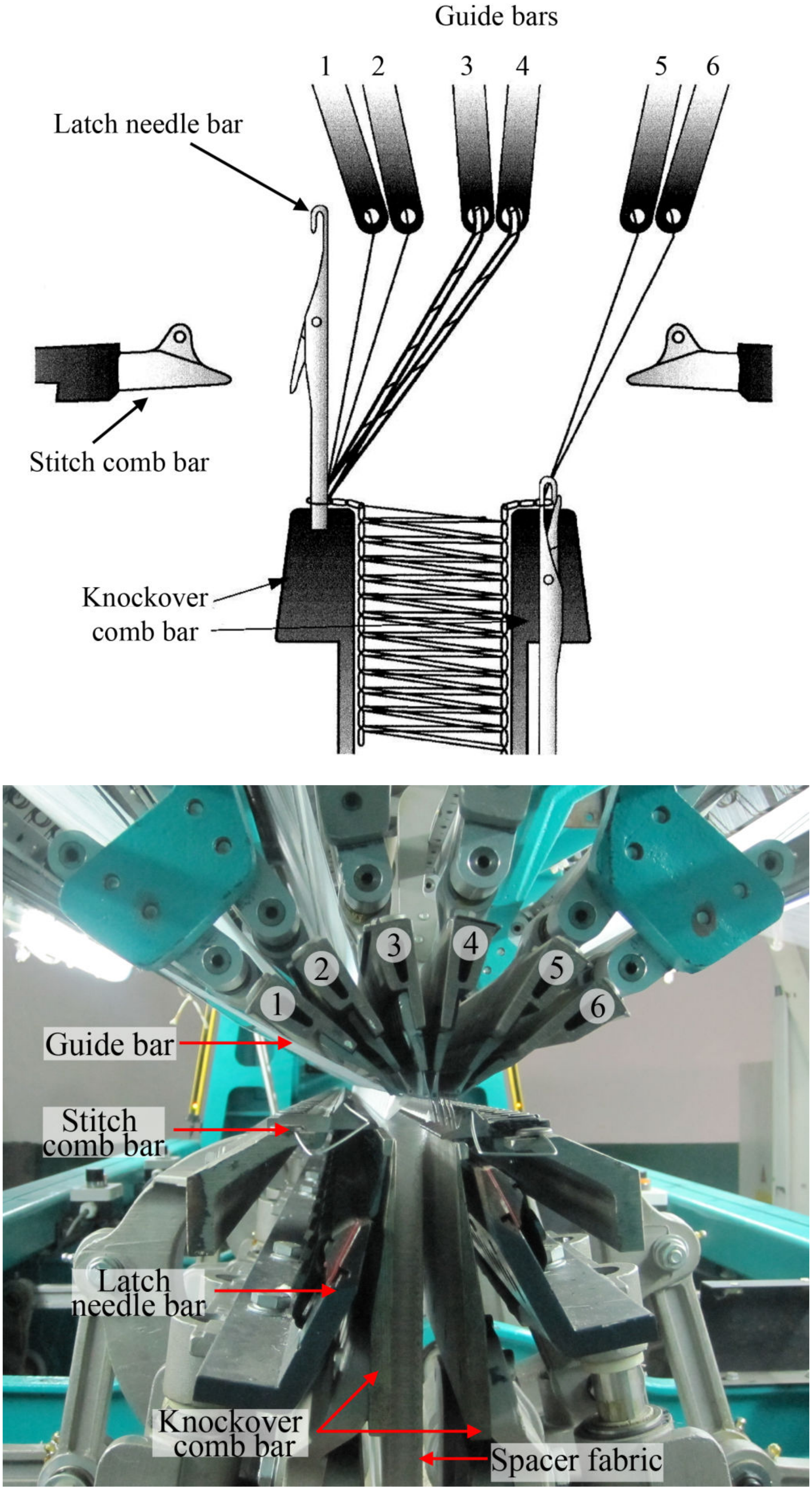

Figure 2.11 Principle of producing spacer fabrics on a double-needle bar Raschel machine: (a) scheme [93]; (b) RD 6 by Karl Mayer.

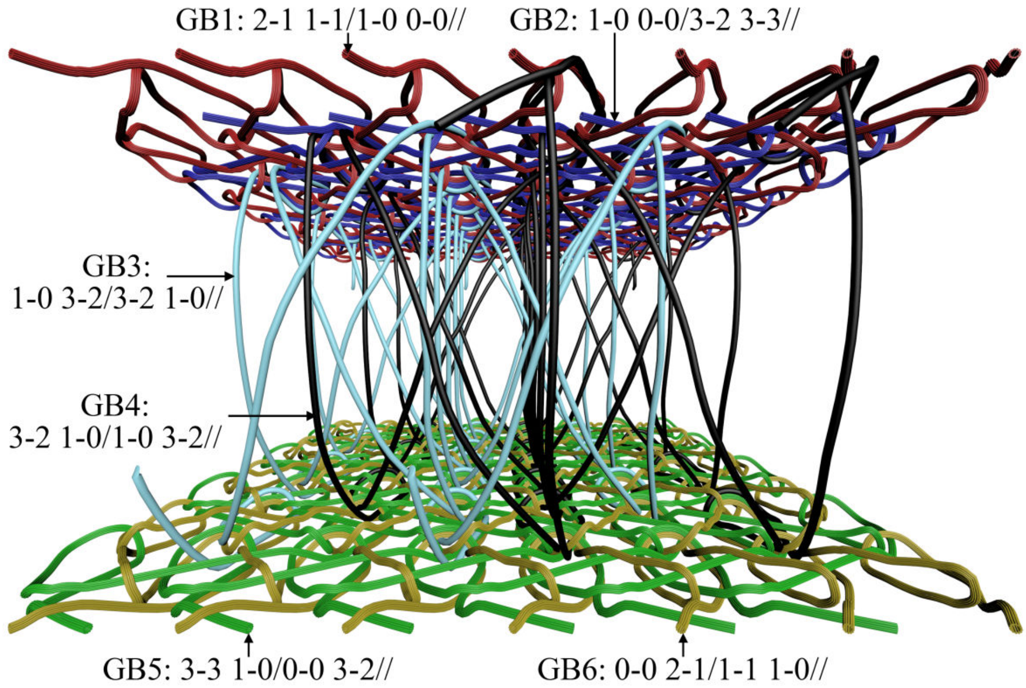

Figure 2.12 A schematic spacer fabric structure knitted with six guide bars.

Warp-knitted spacer fabrics are produced on double-needle bar Raschel machines; the principle is schematically shown in Figure 2.11(a). While the guide bars 1 and 2 lap the front-needle bar, and the guide bars 5 and 6 lap the back-needle bar, to knit the top outer layer and the bottom outer layer, respectively, the guide bars 3 and 4 lap the spacer yarns around both the needle bars in succession. A spacer fabric being produced on a double-bar Raschel machine RD 6 by Karl Mayer is shown in Figure 2.11(b). Figure 2.12 shows a schematic spacer fabric structure knitted with six guide bars using the abovementioned principle. The yarns of the same colour are lapped by one guide bar simultaneously during the same knitting cycle. Raschel machines produce both outer layers simultaneously on two needle bars with their own sets of needles. Thus, it is possible for front- and back-needle bars to knit different yarns and form different structures. By using different threading on and different lapping movements of each guide bar, different outer layer structures, i.e., mesh or close structures with different patterns, can be obtained. That is, two outer layers can either be the same or different; either both faces or only one can be of mesh structure, even with different mesh sizes on each side according to the end use of warp-knitted spacer fabrics.

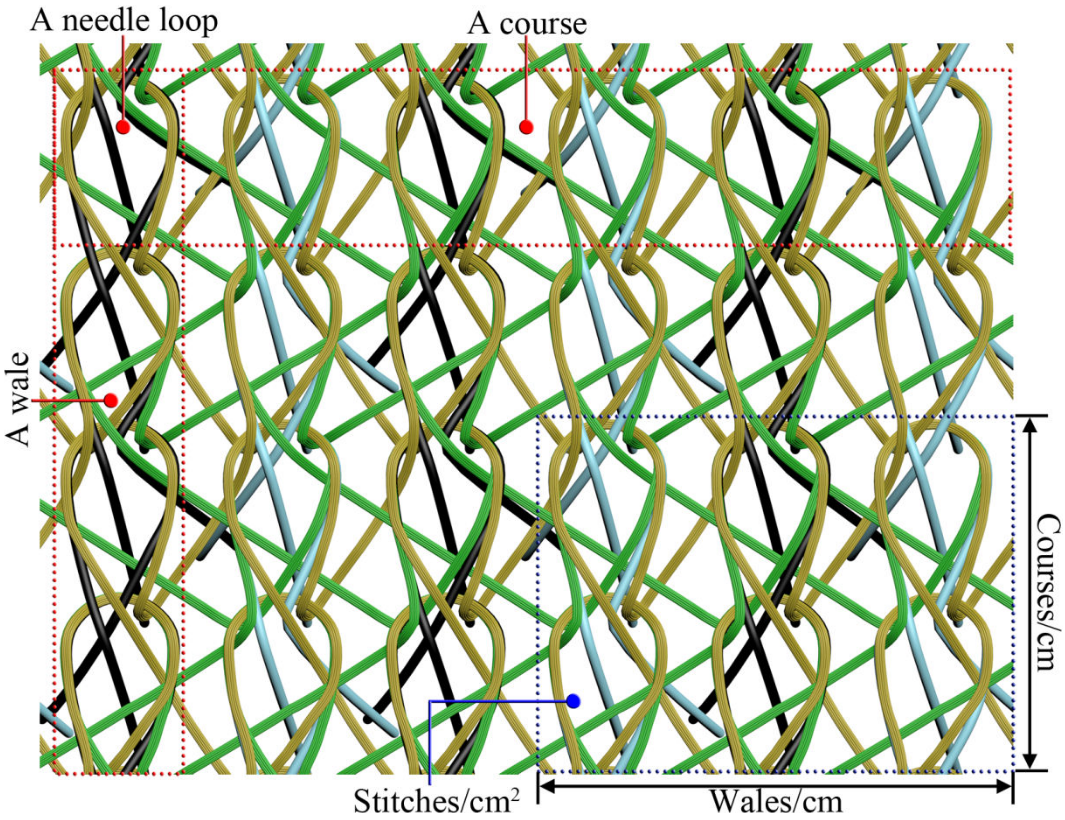

Figure 2.13 A schematic spacer fabric outer layer.

Figure 2.13 shows a schematic warp-knitted spacer fabric outer layer cut from the schematic structure presented in Figure 2.12. An outer layer structure is produced by a combination of the intermeshed needle loops and yarns passing from needle loop to needle loop. Needle loops are arranged in rows; a course is a horizontal row of needle loops produced by adjacent needles during the same knitting cycle, while a wale is a vertical column of intermeshed needle loops produced by the same needle knitting at successive knitting cycles. Course density is defined as the number of courses in a unit length in the walewise direction (courses/cm), and wale density is defined as the number of wales in a unit length in the coursewise direction (wales/cm). Stitch density is a measure of the total number of loops in a measured area (stitches/cm^2). A needle loop consists of one head and two side limbs (Figure 2.14). Needle loops may be open or closed, connected together by underlaps. Geometric configurations of spacer yarns can be tailored by adjusting underlapping movements, threading, and knockover comb bar distance. Three configurations of spacer yarns, i.e., vertical, diagonal, and vertical plus diagonal, are available depending on their inclination angle β as illustrated in Figure 2.15. Obviously, different spacer yarn configurations will bring about different mechanical behaviour of the resultant spacer fabrics. After the knitting process, a spacer fabric is needed to be subjected to a heat setting treatment to achieve and fix a required form.

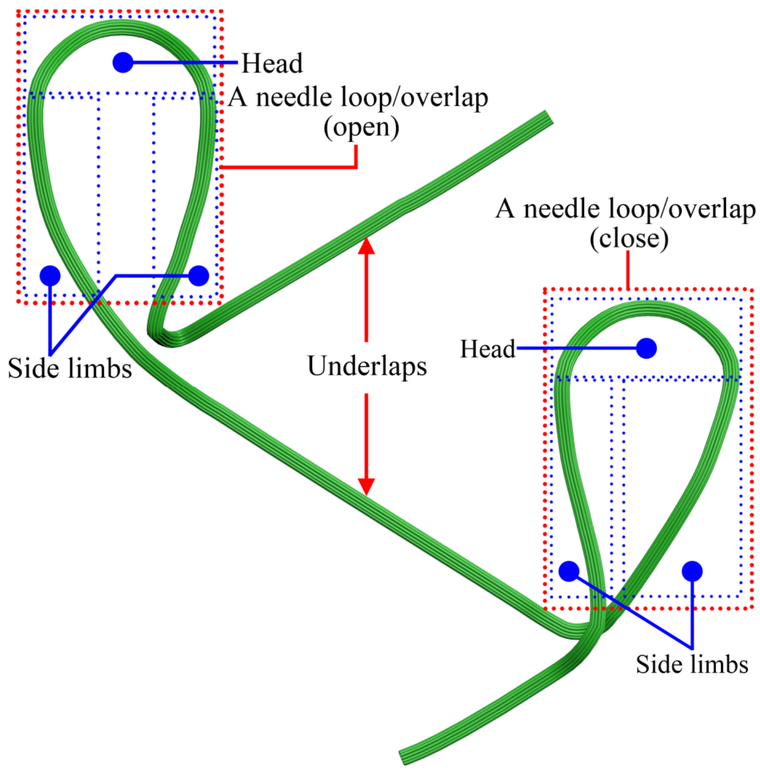

Figure 2.14 The elements of a warp-knitted loop structure.

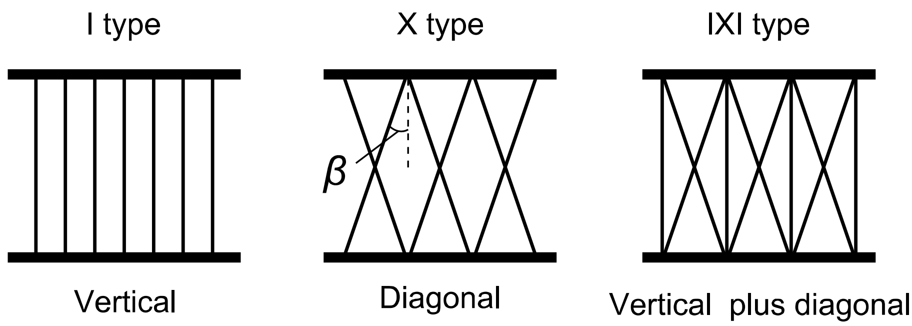

Figure 2.15 Spacer yarn configurations.

Raschel machines have the greatest production capabilities, in terms of greater range in yarn fineness, higher production speeds, and the ability to adjust knockover comb bar distance giving greater opportunity for spacer thickness. While spacer yarns are chosen mainly from monofilament yarns, multifilament yarns are always used to knit outer layers. The properties of spacer yarns affect the properties of final products. Therefore, the spacer yarns to be used should be selected relevant to the properties expected from the final products. Over the past few decades, there have been many double-needle bar Raschel machines available on the market for the production of warp-knitted spacer fabrics, such as DG 506 from LIBA, MDK80 from Jakob Müller AG, and a series of machines including RD 6 (DPLM), RD 7 (DPLM), and HighDistance® from Karl Mayer. HighDistance® equipped with six electronically controlled guide bars achieves swing distances of up to 65 mm which can produce a great variety of spacer fabrics with thicknesses of 20 mm up to 65 mm.

A comparison of the five kinds of spacer fabrics in terms of thickness variation, productivity, surface pattern variation, spacer structure variation, and compression resistance is given in Table 2.6. It is clear that warp-knitted spacer fabrics possess the best performance in all the aspects. The unique feature of warp-knitted spacer fabrics makes them a better candidate for cushioning applications than the other types of spacer fabrics. By manipulating the fibre materials and structures used in each fabric layer, the properties of a warp-knitted spacer fabric are designable to meet specific end-uses. Since the creation of warp-knitted spacer fabrics, a great deal of research has been done to explore their applications.

Table 2.6 Comparison of different types of spacer fabrics

Spacer fabrics	Thickness variation	Productivity	Surface pattern variation	Spacer Structure variation	Compression resistance
Warp knitted	1–65 mm	~1000 rpm	Large	Large	Designable
Flat knitted	3–12 mm	~1.2 m/sec for carriage	Small	Medium	Designable
Circular knitted	1.5–5.5 mm	~30 rpm	Large	Small	low
Woven	Up to 1000 mm	~400 rpm	Small	Small	low
Nonwoven	3–60 mm	3–10 m/min	No	Large	Very low

2.4.2 Properties and applications

Warp-knitted spacer fabrics have special properties compared to conventional textiles due to their unique 3D structures, and their special properties lead to a great variety of application fields. Some effort has already been made to experimentally study the properties of this kind of fabric for exploring new applications. Current applications of warp-knitted spacer fabrics are generally based on their compression resistance; therefore, most past work has been focused on the compression properties.

Miao and Ge [12] investigated the compression behaviour of a warp-knitted spacer fabric with spacer monofilaments in order to evaluate its performance as a cushioning material for pressure relief. They reported a compression stress–strain curve of the fabric but did not give its structural parameters and component materials. The compression test method was also missed in their paper. They claimed that there had been three stages in the compression deformation including linear elasticity, collapse plateau, and densification. The detailed deformations of the fabric corresponding to the three stages were not explained in their paper.

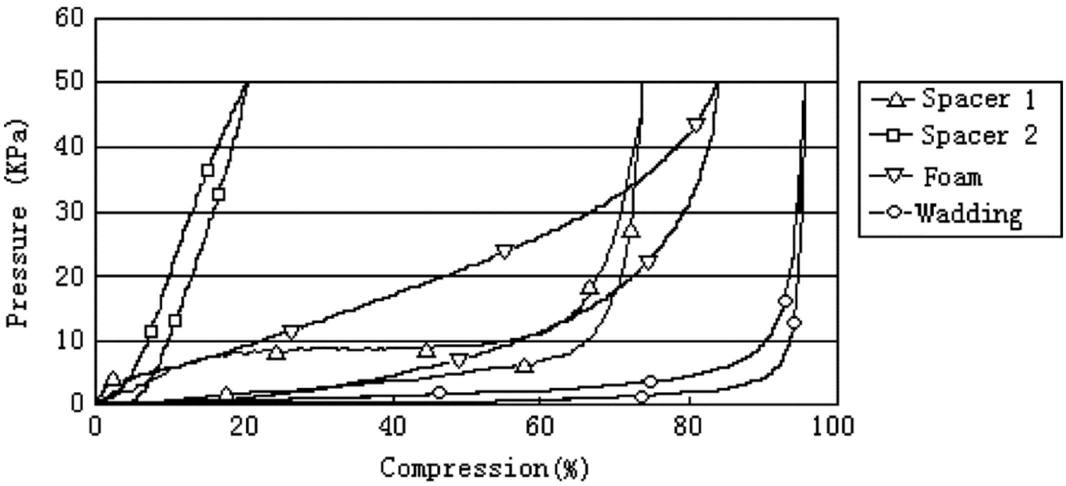

Figure 2.16 Comparison among the stress–strain curves of spacer fabrics, foam, and wadding [17].

(Reproduced with permission of Taylor & Francis)

Ye et al. [17, 94] also studied warp-knitted spacer fabrics as cushioning materials for the application in car seat. Six fabrics knitted with polyester monofilaments of different finenesses and multifilaments as spacer and knitting yarns, respectively, were tested using a presser foot with a contact area of 10 cm^2 at a speed of 10 mm/min without giving the sample size in their study. Two fabrics were compared their compression stress–strain characteristics with those of a polyurethane foam and a nonwoven PP wadding (Figure 2.16). It was shown that the spacer fabric 1 has the abovementioned three stages; however, only the linearly elastic stage was given for the spacer fabric 2. The spacer fabric 2 has high compression resistance in the elastic stage equivalent to that of the spacer fabric 1 in the densification stage. They interpreted the deformations in the three stages as follows. In the elastic stage, the spacer yarn was compressed axially, and it buckled within the elastic limit. In the plateau stage, the spacer yarn began to bend beyond the elastic limit. In the densification stage, the compression of the yarn structures took place. They contended that the compression characteristics depend on the bending rigidity and structure of the spacer yarn as well as the fabric thickness. This implies that warp-knitted spacer fabrics can be produced to have the key feature of behaving as cushioning materials, providing three distinct stages in compression, by using suitable structural parameters. Unfortunately, they neither simultaneously observed nor theoretically proved the deformations of the spacer yarn to support their explanations. The effects of the structural parameters on the compression stress–strain relationships of the fabrics were not experimentally investigated in their study.

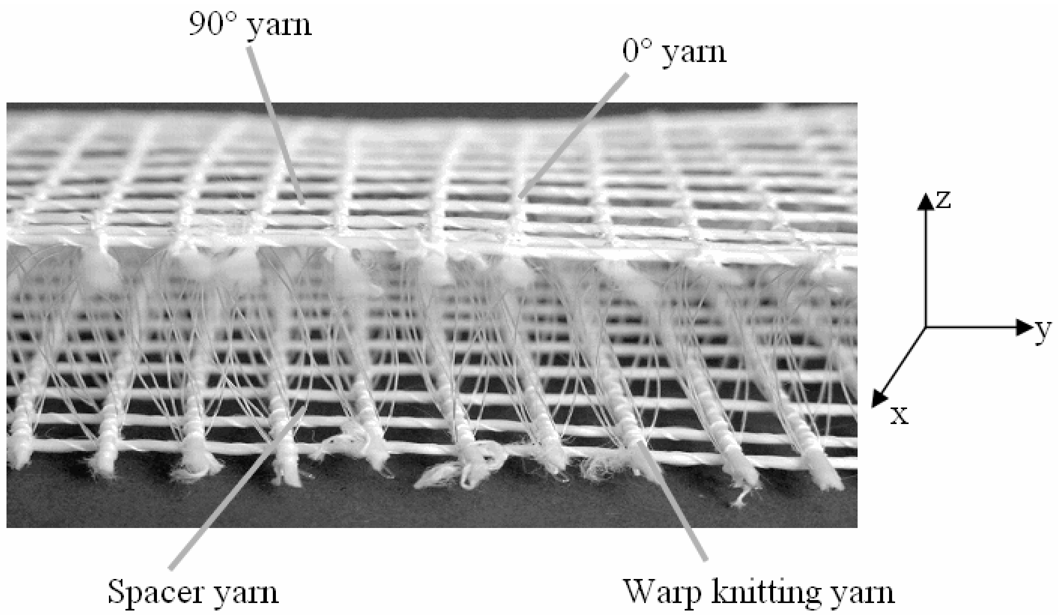

Figure 2.17 The structure of grid-net-like warp-knitted spacer fabric [19].

(Reproduced with permission of Sage Publications)

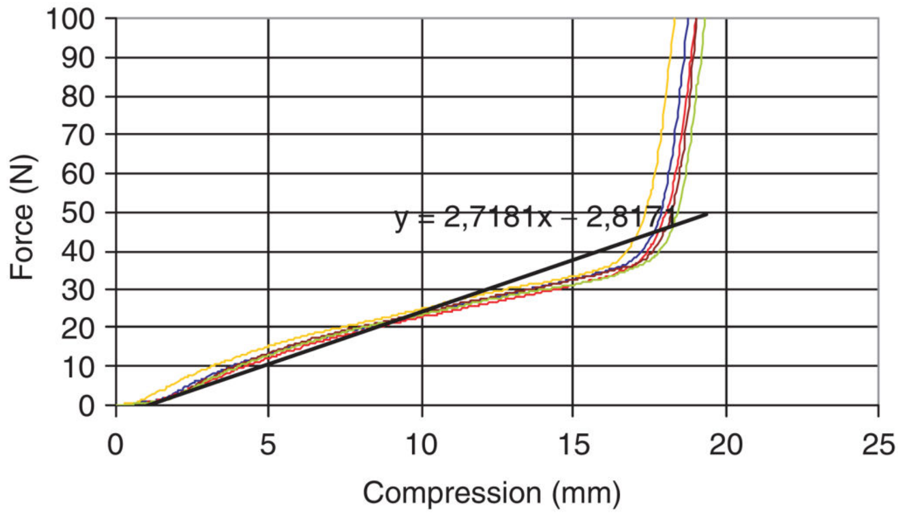

Figure 2.18 Test result of compressing a grid-net-like warp-knitted spacer fabric with 50 mm^2 stamp at 100 mm/min test speed [95].

(Reproduced with permission of Sage Publications)

A novel grid-net-like warp-knitted spacer fabric (Figure 2.17) was developed by researchers at RWTH Aachen University in Germany on a modified double-needle bar Raschel machine (HDR 6-7 DPLM) for concrete reinforcement applications [18, 19, 95]. They applied different yarns to knit different fabric elements. The spacer yarns, the warp-knitting yarns and the surface yarns were of PES monofilament, PP multifilament and AR-glass roving, respectively. This spacer fabric has the load–displacement relationship as shown in Figure 2.18, in which each curve can be divided into two distinct deformation stages. This further proves that fabric structures determine the stress–strain characteristics. They also investigated the effects of the structural parameters, including spacer yarn material, pattern, and threading, on the compression behaviour of a series of warp-knitted spacer fabrics for concrete applications [18]. Their results showed that the location angle and distribution density of the spacer yarns affected the compression behaviour of the fabrics. Besides, they also made effort to study the effects of test methods on the compression behaviour of such spacer fabrics [19]. By using three different contact areas (10, 20 and 25 cm^2) and three different sample sizes (100, 300 and 450 cm^2) in circular and square with and without stabilization form at test speeds of 10 mm/min and 100 mm/min, they concluded that the test speed, sample size, and contact area did not have significant influences on the compression test results.

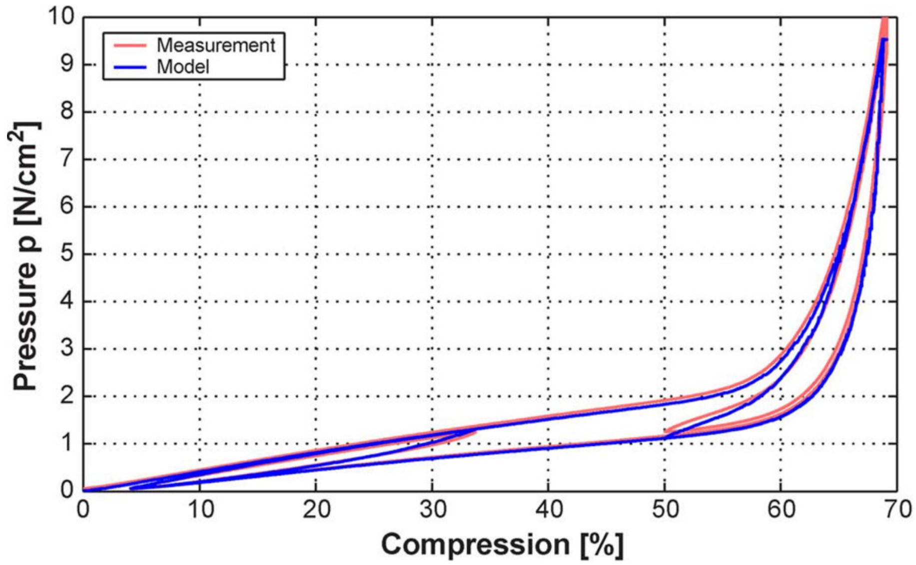

Figure 2.19 Compression stress–strain of a warp-knitted spacer fabric made of polyester yarns (Müller Textile, Germany) with 6 mm thickness © 2010 IEEE[96].

The designable compression behaviour also makes warp-knitted spacer fabrics very suitable for producing textile compression pressure sensors. Meyer et al. [96-98] developed a capacitive textile pressure sensor made of a warp-knitted spacer fabric for measuring pressure distribution on the human body. Their results showed that the textile sensor performed similarly to a commercial non-textile pressure sensing mat for this application. The compression stress–strain curve of the employed spacer fabric is shown in Figure 2.19. It shows that there are two stages of deformation during compression similar to the compression behaviour of the fabrics for concrete applications.

Spacer fabrics can have good air and moisture permeability because the outer layers can be of mesh structures, and there is space in the spacer layer. The space gap can be designed to provide climate comfort with natural thermal and humidity regulation. These properties are especially essential for human body related applications. Besides the compression characteristics, a number of studies concerned with the comfort performance have also been carried out in terms of air permeability, moisture transmissibility, and thermoregulation capability.

The properties of a warp-knitted spacer fabric for knee braces were investigated by Pereira et al. and Lee et al. [99, 100], and they suggested that the warp-knitted spacer fabrics with appropriate elastic and recovery properties have desirable physical, mechanical, and thermophysiological characteristics for knee braces. Warp-knitted spacer fabrics have also been applied for the prevention of chronic wounds due to their designable qualities for pressure relief as well as regulation of heat and moisture [101-103].

Yip and Ng [104] experimentally investigated the low-stress mechanical properties, air permeability, and thermal conductivity of an elastic warp-knitted spacer fabric of spacer monofilaments for intimate apparel, and they asserted that the compression properties depend on the spacer yarn type and the spacer yarn arrangement. Later on, they [105] further studied the moulding properties of the fabric for bra cup applications and concluded that the fabric of polyester spacer yarns can be moulded to have a required cup depth and maintain good performance, and the moulding properties are closely related to the material used for the spacer yarns and the fabric density. Bartels [106] investigated the thermal comfort of warp-knitted spacer fabrics for aeroplane seats and found that the fabrics exhibit better cushion with a high sweat moisture transport property in comparison to a moulded foam pad. Mao and Russell [71] proposed warp-knitted spacer fabrics with a mechanically integrated wool fibre surface for thermal insulation in view of their superior cyclic compression-recovery properties. They reported that, in contrast to conventional homogeneous fabrics, the wool fibre web-spacer fabric had markedly reduced thermal conductivity, while there was little change in the overall fabric density. Borhani et al. also studied the moisture transmissibility of warp-knitted spacer fabrics and found that water vapour produced by sweating can be easily and quickly transferred from the skin to the outer surfaces of the fabrics to keep the skin dry [107].

Apart from the applications based on the compression and comfort properties, some applications in other fields have also been explored. Dias et al. [108, 109] studied the sound absorption behaviour of spacer fabrics with different spacer layer structures and materials to reduce automotive interior noise. Liu and Hu [110] considered a warp-knitted spacer fabric with small size meshes in the outer layers as a microperforated panel sound absorber and studied its sound absorption behaviour. Warp-knitted spacer fabrics have also been proposed to construct flat-sheet membranes as filtration panels [111], to be used as the substrate for textile patch antennas [112-115], and to be used as solar thermal collectors [116]. In view of the special properties of warp-knitted spacer fabrics, a wide range of applications have been found in different fields. The main applications can be categorized into five areas as listed in Table 2.7.

Table 2.7 Applications of warp-knitted spacer fabrics

Areas	Examples
Automotive	Car seat cover, door panelling, car roof lining, car window shelf, car head liner, car rear seat pockets, car seat heating, dash board cover, car boot liners, truck rain water mist protector
Medical	Bandage, knee braces, decubitus mats, absorbent fleece, neck supports, wheelchair cushions, sensor fabrics for patient monitoring, operating table mats, thermal mats
Industrial	Water purification, concrete, sound absorption, textile antenna, composite reinforcement, electronic cases, solar thermal collectors
Sports and Leisure	Sports protectors, sportswear, sports shoe, mattress, pillows
Safety and protection	Hip protector, cycle helmets, body armour

Despite numerous investigations on the exploration of applications for warp-knitted spacer fabrics, systematic studies of their cushioning properties have still been lacking. Only a little work has been reported on their static compression properties as abovementioned. However, the compression mechanism and the structure–property relationships of warp-knitted spacer fabrics in compression are still unclear. Such a situation limits the applications of warp-knitted spacer fabrics for human body protection.

2.4.3 Theoretical studies

In order to reduce cost and carry out exact design of spacer fabrics to meet specific requirements, theoretical modelling is required. Some studies have been conducted to model the geometric features and compression behaviour of spacer fabrics.

To predict the mechanical properties of spacer fabrics, it is useful to have knowledge about the yarn geometry and the yarn interactions within the fabrics. Renkens and Kyosev [117] developed a model that calculates the yarn axes in warp-knitted structures by transforming the needle loops from the flat state to their proper places in 3D space. Two warp-knitted spacer fabrics were simulated as shown in Figure 2.20, which presents the topology of the structures, without considering the mechanical interactions among and inside the yarns.

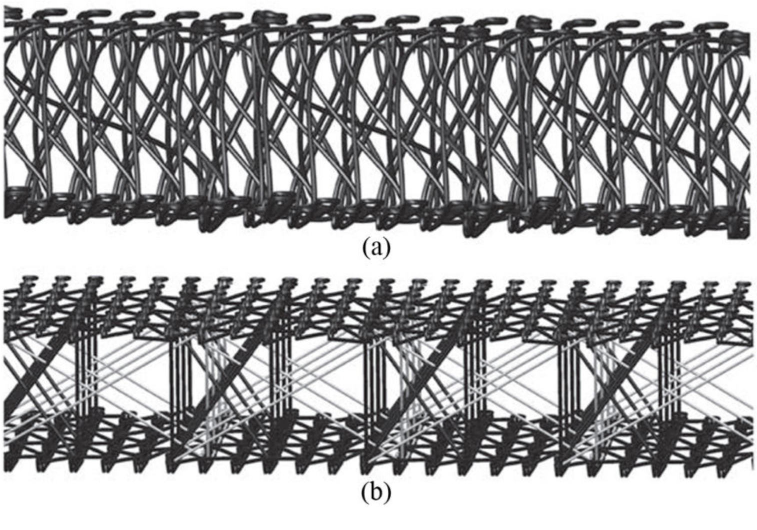

Figure 2.20 Models of spacer fabrics: (a) produce of three spacer yarn systems; (b) fabric with two spacer yarn systems for better shear stability [117].

(Reproduced with permission of Sage Publications)

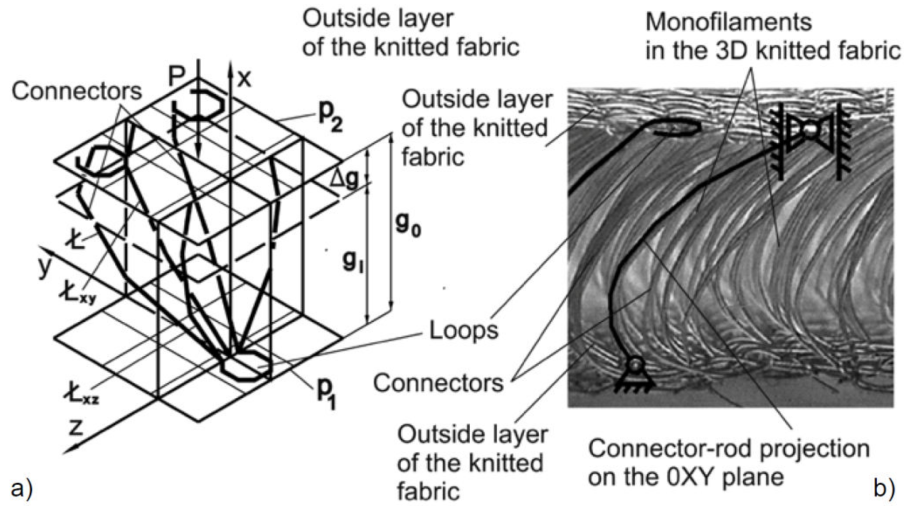

Figure 2.21 3D knitted spacer fabric: (a) design of the fabric; (b) photograph of the cross-section of the fabric [118].

(Reproduced with permission of FIBRES & TEXTILES in Eastern Europe)

The deformations of spacer yarns are the key issue in modelling the compression behaviour of warp-knitted spacer fabrics. Konopasek [119] established a set of analytical models for describing the tensile, torsion and bending deformations of the fibre or yarn. These models can be used in modelling the deformations of spacer yarns. With this approach, Bogdan and Zbigniew [118, 120] built a model for a warp-knitted spacer fabric by using articulated joints with different boundary conditions as shown in Figure 2.21. They considered the spacer yarn as a slender rod with an assumed shape and calculated the buckling behaviour with Euler-Bernoulli beam theory. However, the small deflection theory was used in the model, which is not consistent with the nature of the spacer yarn undergoing a large deflection under compression. Later on, they revised the model by using the large deflection theory and considered the spacer yarn as an elastica [121]. Their revised model is theoretically correct, but the boundary conditions adopted are not applicable to spacer fabrics, and they only took the initially straight vertical rod into account.

Mokhtari et al. [122] proposed an analytical model by assuming a constant curvature along spacer yarn length during compression. This assumption is not consistent with the fact that the spacer yarns undertook postbuckling rather than pure bending. Hence, this model cannot be used to represent the deformation mechanism of spacer fabrics.

Sheikhzadeh et al. [123] applied Van Wyk's law for modelling compressed fibres [124] to model the lateral compression behaviour of warp-knitted spacer fabrics. This model cannot simulate the real buckling behaviour of spacer yarns; therefore, it is not helpful in understanding the compression behaviour of warp-knitted spacer fabrics.

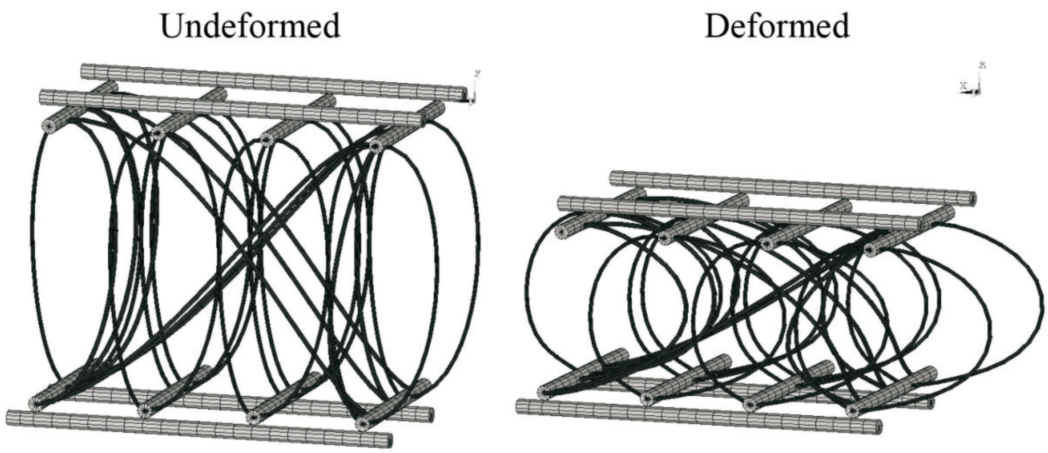

Figure 2.22 Finite element model of the unit cell of the spacer fabric for concrete application [125].

(Reproduced with permission of FIBRES & TEXTILES in Eastern Europe)

In addition to analytical modelling, numerical simulation is another important method to study the compression behaviour of warp-knitted spacer fabrics. Vassiliadis et al. [125] proposed a numerical model for studying the compression behaviour of warp-knitted spacer fabrics for concrete applications using the finite element (FE) method. By utilizing the proposed numerical model, they investigated the effects of structural and physical parameters on the compression properties of the developed spacer fabrics, achieving moderate agreement between the simulated and experimental results. However, their model only focused on the grid-net-like warp-knitted spacer fabric for concrete applications, which is not representative of warp-knitted spacer fabrics. The simulated outer fabric layers were presented as grid nets, and no contact between the spacer yarns and outer layers was included as shown in Figure 2.22. They acquired the initial spacer yarn shapes by selecting spline curves to connect the binding points, which not considering the physical reality is inaccurate. Lee et al. [100] also reported a FE model for a warp-knitted spacer fabric with two mesh outer layers. They claimed that the FE model was helpful in predicting the physical properties of spacer fabrics. Unfortunately, the details and evaluation of their model were not given in their paper.

2.5 Conclusions

This chapter has reviewed the literature related to this study, including human body protection, cushioning materials and warp-knitted spacer fabrics. It has been shown that the diversity of demands in sports requires a wide range of protective products for providing sufficient body protection with sufficient comfort performance. The previous empirical studies on warp-knitted spacer fabrics have shown that such fabrics are possible to be capable of cushioning properties and good comfort properties. The use of warp-knitted spacer fabrics in developing impact protectors is a potential way to gain wider acceptance of wearing impact protectors in sports or extreme activities. In doing so, a clear picture for engineering the cushioning properties of warp-knitted spacer fabrics is required. This needs an in-depth understanding of the deformation mechanism and structure–property relationships of warp-knitted spacer fabrics under static and impact compression with different boundary conditions. However, the current warp-knitted spacer fabric structures are all designed empirically; design, fabrication and testing processes require many iterations before an optimized design is chosen, leading to high costs. This is because their compression deformation mechanism is unclear, and the clearly quantitative structure–property relationships have not been well established. Besides, there is no study concerned with the impact behaviour and energy absorption capacity of warp-knitted spacer fabrics. In this connection, to conduct exact design of warp-knitted spacer fabrics for specific cushioning applications, systematic experimental and theoretical studies to identify the precise deformation mechanism and to establish the quantitative structure–property relationships under various compression conditions should be conducted.

In the next chapter, a preliminary experimental investigation into the compression behaviour of a warp-knitted spacer fabric with a typical structure under various test conditions will be presented. The potential deformation mechanism of the fabric is interpreted based on the analyses of both the compression load–displacement curve obtained under a selected proper test condition and the cross-sectional pictures of the fabric taken at different compression stages.

CHAPTER 3 EXPERIMENTAL ANALYSIS ON THE COMPRESSION BEHAVIOUR OF WARP-KNITTED SPACER FABRIC

3.1 Introduction

As reviewed in Chapter 2, the compression behaviour is vital to the cushioning performance of warp-knitted spacer fabrics. In the literature [12, 17], it has been shown that the compression load–displacement relationships of warp-knitted spacer fabrics can have three main stages, i.e., linear elasticity, plateau and densification. This is the typical behaviour required by a cushioning material in compression. However, the main limitations in those experimental investigations are that the effects of test conditions on the results were not considered, and a suitable method for simultaneously observing the deformation of spacer yarns within the fabric during the compression process is still lacking. As a consequence, no well accepted interpretation has been given to provide a reasonable understanding of the deformation mechanism and the structure–property relationships of warp-knitted spacer fabrics in compression. However, such knowledge is of great importance to the development of warp-knitted spacer fabrics as cushioning materials for human body protection. Since the lack of this knowledge, the warp-knitted spacer fabrics developed currently for various applications were designed empirically. In order to develop the products for specific applications, the detailed deformation mechanism and structure–property relationships of warp-knitted spacer fabrics should be well understood. For this purpose, as an initial trial, the typical features of the structural elements of a spacer fabric with a typical structure under compression are required to be experimentally investigated with a proper test method and analysed based on the resultant compression stress–strain curve.

There is no recognized test standard specially developed for testing the compression behaviour of warp-knitted spacer fabrics. The literature review has shown that different test methods were adopted by different researchers. For instance, Ye et al. conducted the compression tests of warp-knitted spacer fabrics for car seats by using a contact area of 10 cm^2 at a speed of 10 mm/min without indication of sample sizes [17]. Mecit and Roye tested the compression properties of warp-knitted spacer fabrics for concrete applications by using three different contact areas (10, 20 and 25 cm^2), and three different sample sizes in both circular and square shapes (100, 300 and 450 cm^2) with and without stabilization of samples at two different compression speeds (10 and 100 mm/min) [19]. Their study demonstrated that the compression speed, sample size and contact area did not have significant influences on the test results. However, this conclusion is only valid for the warp-knitted spacer fabrics designed for concrete applications. In such a kind of fabric, the outer layers are grid nets, and the contacts between spacer yarns and outer layers as well as the contacts among spacer yarns are not evident due to the low areal density of outer layers. In addition, this kind of spacer fabric also has a symmetric structure in both the through-thickness and in-plane directions. Therefore, evident effects of test boundary condition and sample size cannot be observed. However, the warp-knitted spacer fabrics designed for cushioning applications should be different from this kind of spacer fabric. In view of the function to absorb the impact energy which may cause injuries to human body, the spacer fabrics as cushioning materials should be designed to have relatively high areal density. Such a kind of spacer fabric will has more complicated compression behaviour because the interaction among spacer yarns and the interaction between the spacer yarns and the outer fabric layers are exceedingly complex. These complicated deformation modes can lead to unstable compression behaviour of the fabrics when the sample size is below some limit. In this regard, it is of importance to include effects of test boundary condition and sample size in the analysis of the compression behaviour of the spacer fabric.

The objective of this chapter is first to investigate how a warp-knitted spacer fabric with a typical structure behaves when tested with different compression boundary conditions and sample sizes. From here, the potential compression mechanism of the fabric is identified based on the analyses of both the compression load–displacement curve obtained under a selected proper test condition and the cross-sectional pictures of the fabric taken at different compression stages. It is expected that such a study could generate the knowledge for the understanding of the deformation mechanism and structure–property relationships of warp-knitted spacer fabrics in compression. This knowledge will be useful in establishing the theoretical models for predicting the compression behaviour and identifying the structural parameters that influence the compression properties of spacer fabrics.

3.2 Experimental

3.2.1 Spacer fabric

A warp-knitted spacer fabric S1 with a typical structure was tested. It was knitted on a GE296 high speed double-needle bar Raschel machine of six yarn guide bars built by Wuyang Warp Knitting Machine Limited in China. The machine gauge is E18. While 300D/96F polyester multifilament was used to create the binding structure in the knitting process through GB1, GB2 for the top outer layer and GB5, GB6 for the bottom outer layer, the polyester monofilament of 0.2 mm in diameter was used as spacer yarns to connect the two outer layers together through GB3 and GB4. The chain notation and materials used for each guide bar are listed in Table 3.1. After the knitting process, the fabric was removed from the machine and subjected to a heat setting treatment at a temperature of 180 ºC for 3 minutes. The fabric thickness measured with a digital thickness tester (SDL Atlas M034e) and other structural parameters are listed together in Table 3.2.

Table 3.1 Chain notation and yarns used for the spacer fabric S1

Layers	Guide bars	Chain notation	Threading	Yarn
Top layer	GB1	1-0 0-0 / 3-2 3-3 //	Full	300D/96F Polyester DTY
	GB2	2-1 1-1 / 1-0 0-0 //	Full	300D/96F Polyester DTY
Spacer layer	GB3	1-0 3-2 / 3-2 1-0 //	1 full 1 empty	0.2 mm in diameter Polyester monofilament
	GB4	3-2 1-0 / 1-0 3-2 //	1 full 1 empty	0.2 mm in diameter Polyester monofilament
Bottom layer	GB5	0-0 2-1 / 1-1 1-0 //	Full	300D/96F Polyester DTY
	GB6	3-3 1-0 / 0-0 3-2 //	Full	300D/96F Polyester DTY

Table 3.2 Structural parameters of the spacer fabric S1

Thickness (mm)	Areal density (g/m^2)	Bulk density (kg/m^3)	Stitches/ cm^2
7.52±0.06	1008.29±10.68	134.08±1.42	41.15

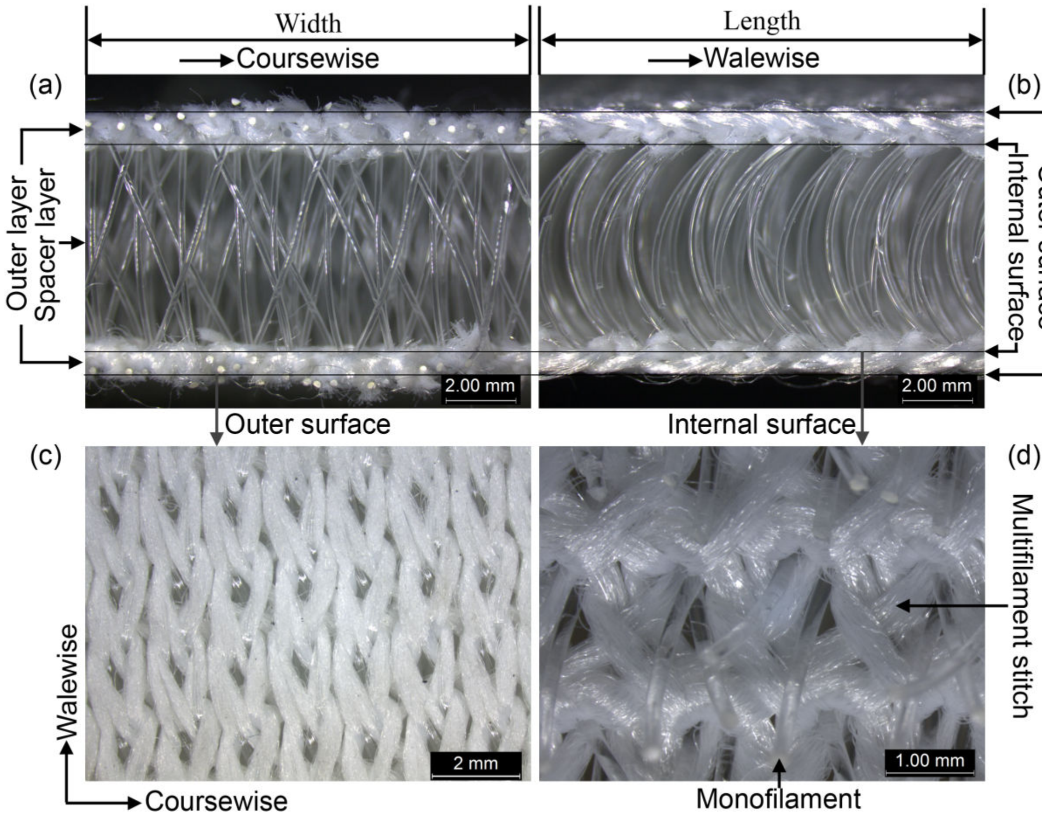

Figure 3.1 Pictures of the spacer fabric S1 viewed from: (a) walewise direction; (b) coursewise direction; (c) outer surface; (d) internal surface.

The pictures of the fabric taken from various directions are shown in Figure 3.1. From Figure 3.1(a) and (b), it can be seen that the spacer fabric consists of two separate outer fabric layers linking together by a layer of spacer monofilaments. Figure 3.1(a) also shows that there are two types of spacer monofilaments observed from the walewise direction, i.e., vertical and inclined spacer monofilaments. The spacer monofilaments were knitted into the outer layers to form the monofilament stitches simultaneously with multifilaments. The outer surface and internal surface are shown in Figure 3.1(c) and (d), respectively. It can be seen not only that the monofilament stitches are covered by the multifilament stitches (Figure 3.1(c)) but also that the spacer monofilaments are wrapped by the fluffy multifilament stitches, and voids are formed in the outer fabric structure (Figure 3.1(d)). The above morphological identification indicates that the spacer fabric has a highly heterogeneous and discontinuous structure.

3.2.2 Compression tests

As mentioned above, the boundary condition and sample size are two important factors affecting the compression test results of a warp-knitted spacer fabric due to the highly heterogeneous and discontinuous structure.

To analyse the effect of boundary condition, two cases, i.e., gluing or not gluing a fabric sample to the surfaces of two compression platens, were considered. In the first case, a spacer fabric sample was simply placed on the fixed compression platen without gluing it to the compression platens. In this case, shear may occur due to possible slippage between the fabric sample and the compression platens if the fabric structure is not sufficiently symmetrical. In the second case, two outer fabric layers were glued to the surfaces of the two compression platens. Since the in-plane movement of the two outer layers was constrained, only the vertical displacement was allowed.

To analyse the effect of fabric sample size, it should be noted that a spacer fabric is a highly anisotropic structure, and it has different mechanical behaviour in different directions. The different size ratios between the walewise and coursewise directions can cause different compression behaviour of the fabric. In addition, the spacer monofilaments in the fabric can contact one another during compression. Since these contacting points depend on the fabric size, different fabric sample sizes can also lead to different compression test results of the fabric. In view of these facts, different spacer fabric samples in rectangular shapes with different lengths and widths were selected. As shown in Figure 3.1, the length and width of a sample are defined as the length of the fabric in the walewise direction and the width of the fabric in the coursewise direction, respectively. Two cases were considered: (i) keeping the width constant and changing the length, and (ii) keeping the length constant and changing the width. Five values, i.e., 2, 4, 6, 8 and 10 cm, were selected for each direction. Therefore, 25 samples in total with different lengths and widths were used for compression tests.

The compression tests were conducted on an Instron 5566 Universal Testing Machine set up with two compression circular platens of 15 cm in diameter (Figure 3.2) according to the modified Standard Test Methods for Rubber Properties in Compression ASTM D 575. The tests were carried out at a speed of 12 mm/min up to a deformation of 80% to the initial thickness of the fabric in an environment of 20 °C and 65% relative humidity.

For comparing the boundary effect, only the samples in a size of 10 cm × 10 cm were used. The samples were tested under two test conditions, i.e., either the samples were glued or not glued to the surfaces of the two compression platens by using double-side adhesives. For comparing the sample size effect, the samples were not glued to the compression platens. Five tests were carried out for each size of a fabric sample with the same boundary condition.

Figure 3.2 Compression testing set-up for warp-knitted spacer fabric tests.

3.3 Compression behaviour

3.3.1 The effect of test boundary condition

Figure 3.3(a) and (b) respectively show the compression stress–strain curves of the spacer fabric tested with two test boundary conditions, under which two outer layers of the fabric were glued or not glued to the surfaces of the compression platens. It can be seen that the overall trends of the stress–strain curves under the two conditions are similar. The only difference in the stress–strain curves between the two boundary conditions is that the curves of the samples not glued to the platens have some slight fluctuations in the plateau stage, especially at the end of the plateau stage. The reason is that different boundary conditions can result in different actions of the outer fabric layers on the spacer monofilaments. When a fabric sample was simply placed on the smooth platens without gluing it to them, the highly buckled spacer monofilaments in the plateau stage can more easily cause the deformation and slippage of the multifilament stitches in the outer layers, leading to the change of the constraints provided by the outer layers to the spacer monofilaments. As a result, the fluctuations of the stress–strain curves were produced in the plateau stage due to the loss of structural stability. By contrast, in the case where the fabric samples were glued to the surfaces of the two compression platens, the multifilament stitches within the outer layers were not easy to deform and slip during the compression tests. As the constraints on the spacer monofilaments provided by the multifilament stitches cannot suddenly change, the stress–strain curves became smoother and more consistent. These results indicate that the different boundary conditions can affect the compression behaviour of a warp-knitted spacer fabric to some extent.

According to the requirement for a cushioning material, the amount of the energy absorbed before reaching the densification stage and the stress level in the plateau stage, are two key parameters needed to be optimized for a warp-knitted spacer fabric to meet such a requirement. Although the slight stress fluctuations can be produced in the stress–strain curves when the samples are not fixed with the compression platens, these fluctuations cannot significantly affect the cushioning performance of the fabric. It should be noted that spacer fabrics for impact protection are normally integrated or inserted into protective clothing or equipment for protecting human body against impact. Considering the outer layers of the spacer fabric enclosed in an impact protector cannot be securely constrained, the test condition under which a fabric is simply placed on the compression platens is closer to a real boundary condition of a spacer fabric in use. Since this boundary condition also makes compression tests easier to be carried out, it was adopted to test fabric samples with different sizes in this study.

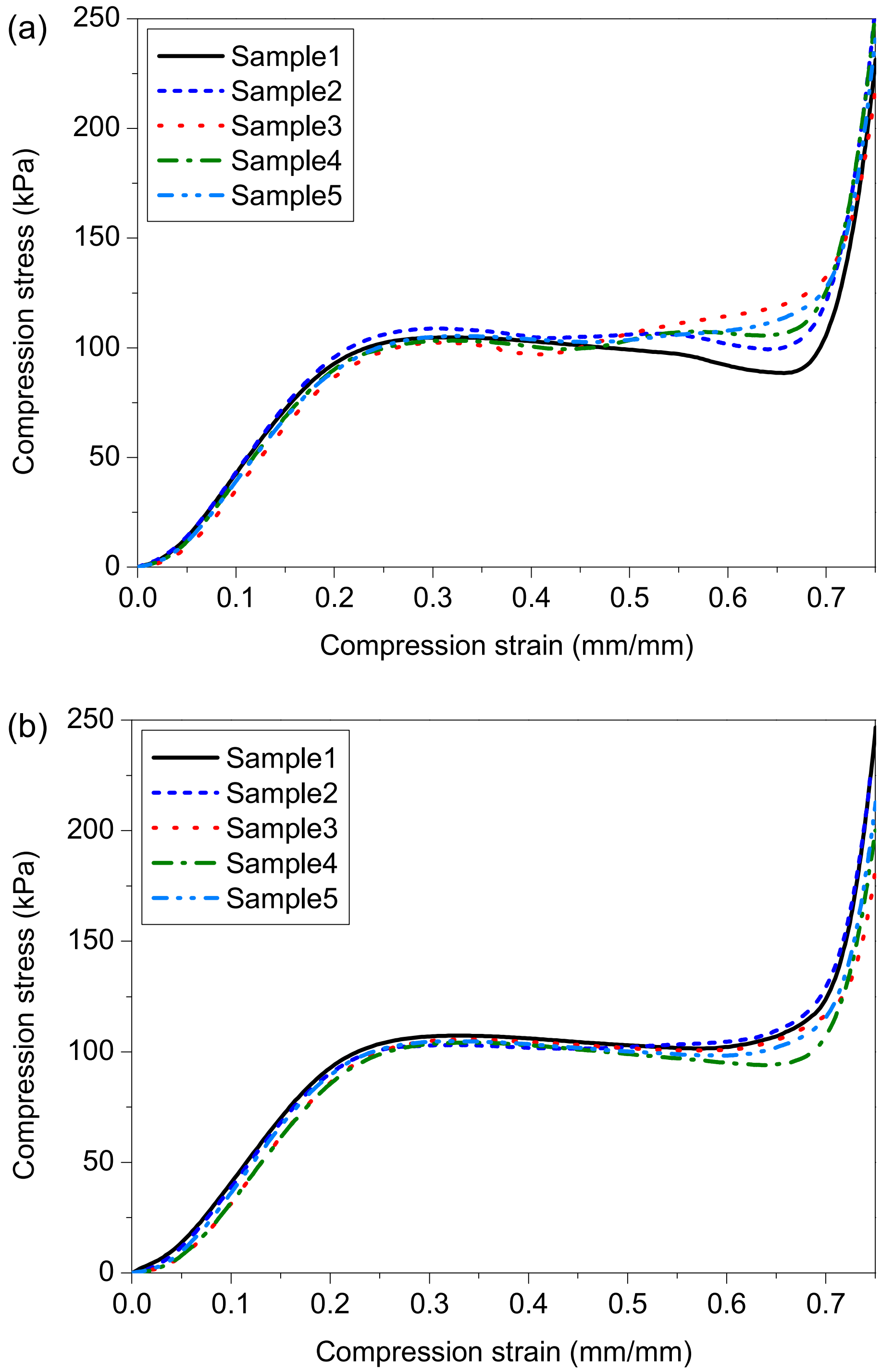

Figure 3.3 Stress–strain curves of the spacer fabric S1 under different test conditions: (a) not glued and (b) glued to platens surfaces.

3.3.2 The effect of sample size

To investigate the sample size effect, 25 samples of different lengths and widths were tested under the test condition not gluing them to the compression platens. According to the European Standard EN ISO 3386 "Flexible cellular polymeric materials – Determination of stress–strain characteristics in compression", the compression stress–strain characteristic (CC) expressed in kilopascals, at a specified strain, can be given by Equation (3.1)

$$\mathrm{CC}_{xx} = 1000\frac{F}{A_c} \tag{3.1}$$

where CC_{xx} is the compression stress–strain characteristic at a strain xx; F is the force, in newtons, at the specified strain; A_c is the area, in square millimetres, of the test piece. Stresses are usually quoted at compressions of (25 ± 1) %, (40 ± 1) %, (50 ± 1) % and (65 ± 1) %, being designated CC_{25}, CC_{40}, CC_{50} and CC_{65} respectively. Herein, CC_{25} is appropriate to represent the plateau stress of the spacer fabric and thus was used to be an indicator to evaluate the effect of sample size on the compression stress–strain characteristic of the spacer fabric.

The test results for the effects of the sample length and the sample width are presented in Figure 3.4 and Figure 3.5, respectively. Figure 3.4 indicates that, for a given sample width, the plateau stress of the fabric increases as the sample length increases. This means that the sample length has a significant effect on the test results of the fabric. From Figure 3.5, it can be observed that, for a given sample length, the plateau stress of the fabric first increases and then decreases as the sample width increases. However, the effect of the sample width is no longer obviously observed when the fabric length reaches 10 cm. These findings indicate that the effect of the sample length along the walewise direction on the test results is more significant than that of the sample width along the coursewise direction.

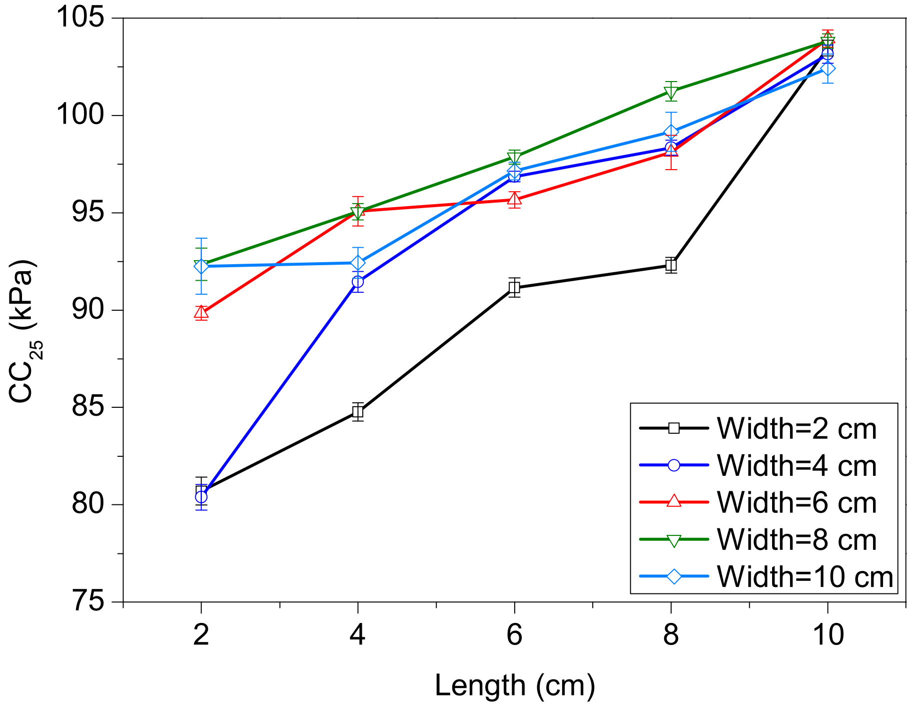

Figure 3.4 Effect of the sample length on compression stress–strain characteristic.

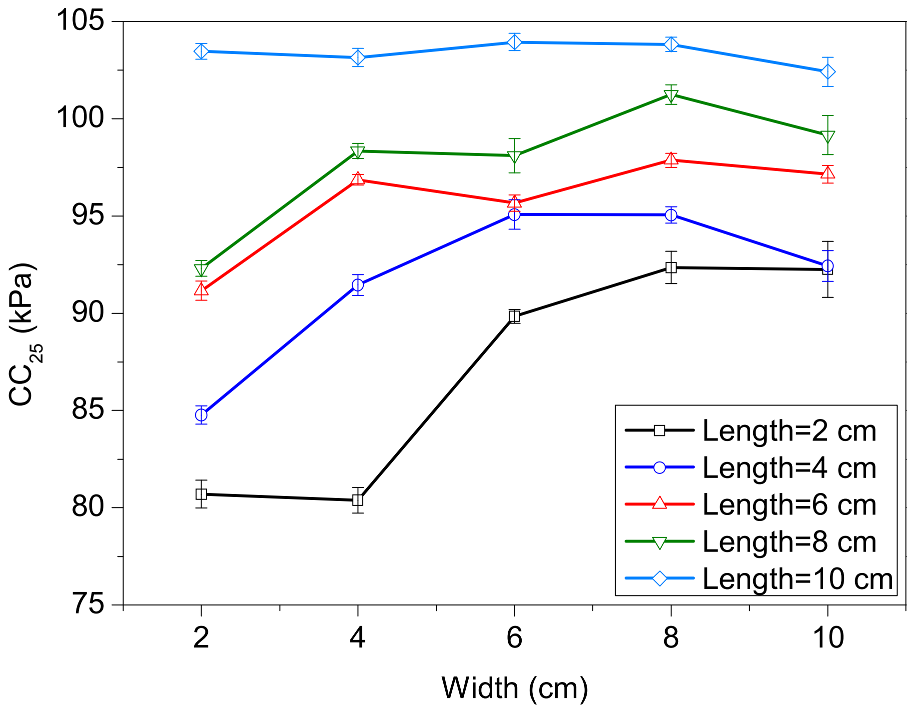

Figure 3.5 Effect of the sample width on compression stress–strain characteristic.

This phenomenon can be explained by analysing the different arrangements of spacer monofilaments in the fabric structure. As shown in Figure 3.1(b), all the spacer monofilaments have curved forms along the length direction (walewise). Due to the asymmetric geometric arrangement of the spacer monofilaments, shear between the two outer layers along the walewise direction can be easier to occur when the sample length is small. As the increase of the sample length can decrease the shear occurrence during compression, the compression stress in the plateau stage is increased as the sample length increases. Differently, as shown in Figure 3.1(a), the geometric arrangement of spacer monofilaments in the width direction (coursewise) is more symmetrical than that in the length direction (walewise) because the spacer monofilaments are in vertical and symmetrically arranged in two inclined directions. This arrangement makes the spacer fabric more stable, and shear between the two outer fabric layers along the width direction cannot easily occur. The above analysis indicates that the compression results of the fabric when tested with a relatively smaller sample length are not stable and cannot be used to properly represent the compression behaviour of the fabric. The curves in Figure 3.5 show that the samples with a length of 10 cm can bring more stable results regardless of their widths. Therefore, the compression load–displacement curve of the fabric sample in a size of 10 cm × 10 cm is selected to further analyse the compression deformation mechanism of the fabric, together with an analysis of the pictures of the fabric structure taken at different compression stages.

3.4 Compression deformation mechanism

The compression deformation mechanism is important to the design of warp-knitted spacer fabrics as cushioning materials for human body protection. The experimental results presented above reveal that whereas the sample size affects the compression behaviour significantly under not glued test condition, the test boundary condition only slightly influences the plateau stage of the compression deformation when the fabric is of 10 cm × 10 cm in size. This means that employing an appropriate sample size in test is of crucial importance to obtain the accurate deformation mechanism. To better interpret the potential deformation mechanism of the fabric, both the compression load–displacement curve and the pictures of the fabric structure taken at different compression stages are used for the discussion. The results under the condition (sample size: 10 cm × 10 cm; boundary condition: gluing to the compression platens) are used because it is easier to capture the pictures of the spacer fabric under the glued condition.

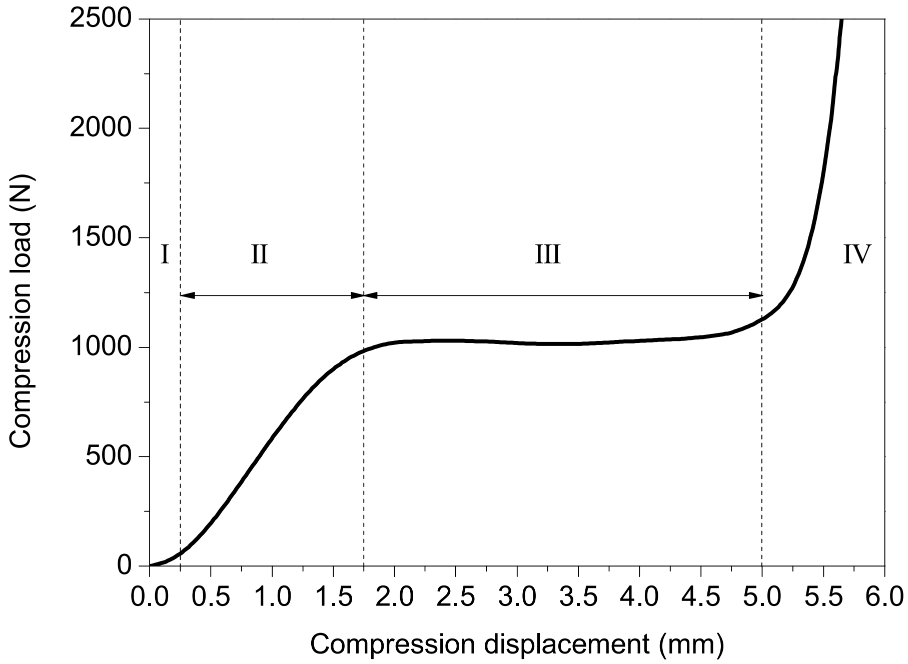

Figure 3.6 Compression load–displacement curve of the spacer fabric S1 under glued test condition.

For the sake of convenience, the stress–strain curve of Sample 2 presented in Figure 3.3(b) is reproduced in the form of load–displacement curve in Figure 3.6. To facilitate the analysis of the compression behaviour of the fabric, the compression process is divided into four different stages, i.e., initial stage (stage I), linearly elastic stage (stage II), plateau stage (stage III) and densification stage (stage IV), according to the changes in the slope of the curve. The cross-sectional microscopic pictures of the spacer fabric with different displacements were captured with a light microscope (LEICA M165 C) and are respectively shown in Figure 3.7 for the initial and linearly elastic stages, Figure 3.8 for the plateau stage and Figure 3.9 for the densification stage.

Unlike the typical stress–strain curves of PU foams presented in Figure 2.4 that each curve starts with a linearly elastic stage, the spacer fabric has a short initial stage before reaching the linearly elastic stage. In this initial stage (stage I), a lower slope is observed and might be due to the compression of the loose outer layers and their ineffective constraints on the spacer monofilaments (Figure 3.1). As each loose multifilament stitch around a spacer monofilament cannot tightly constrain the spacer monofilament in this stage, the slight slipping of the monofilament stitches embed in the outer layers can occur. Besides, the spacer monofilaments undertake postbuckling freely due to the existing of voids in the outer fabric layers. When the fabric is further compressed into the linearly elastic stage (stage II), the spacer monofilaments start to contact the stitches of the outer layers. In this case, additional constraints are created at the contacting points between the spacer monofilaments and outer layers. This makes the spacer monofilaments not freely post-buckled. The postbuckling of spacer monofilaments at a larger scale as shown in Figure 3.7 with the additional constraints at the contacting points leads to a rapid increase of the compression force, i.e., a stiffer mechanical behaviour of the fabric.

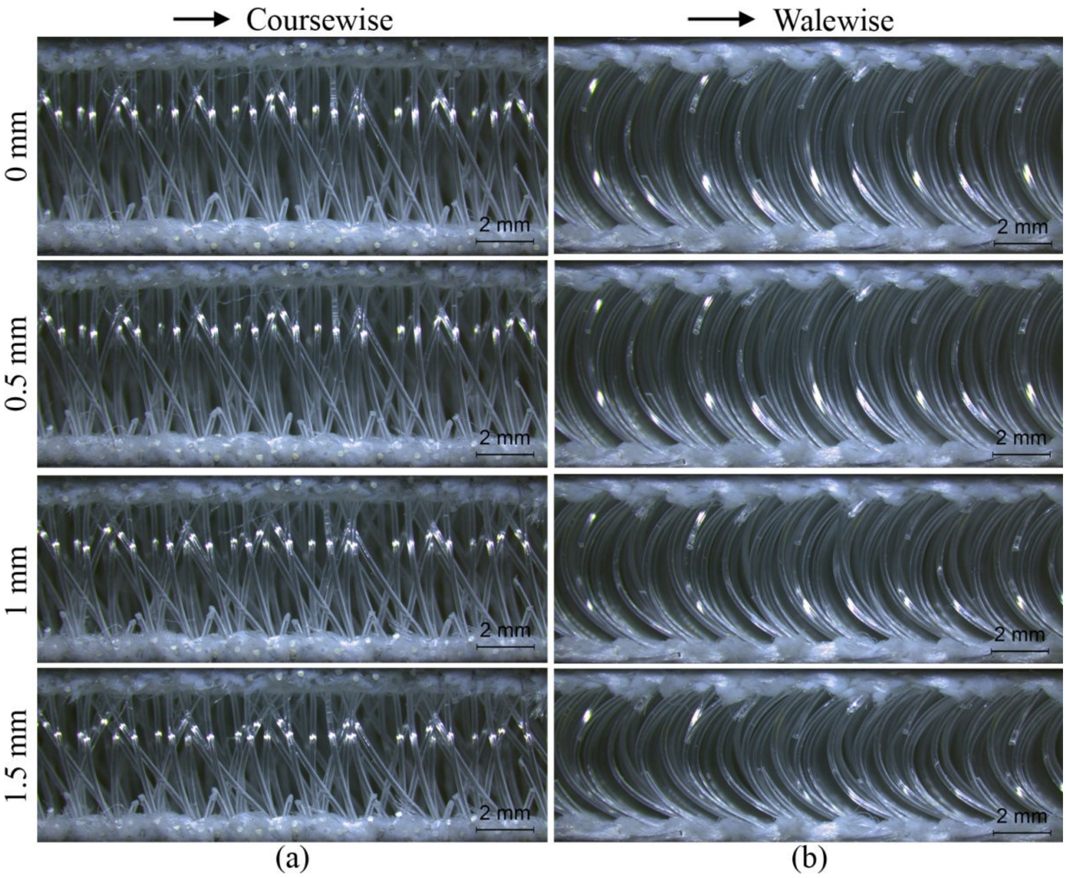

Figure 3.7 Cross-sectional pictures of the spacer fabric S1 taken in the initial and linearly elastic stages (displacements: 0–1.5mm): (a) from walewise direction; (b) from coursewise direction.

A nearly constant force is obtained in the plateau stage (stage III). The deformation mechanism of the fabric in this stage is complicated, which could be affected by the postbuckling, torsion, shear, rotation and contacts of the spacer monofilaments among themselves and with the outer layers. By observing the pictures of the fabric taken from the walewise direction as shown in Figure 3.8(a), it can be clearly seen that torsion, shear and rotation of the initially vertical spacer monofilaments occur, which lead to the formation of three different states of the spacer monofilaments, i.e., left-oblique, right-oblique and vertical. These deformations imply that all the initially vertical spacer monofilaments do not behave identically when compressed in the plateau stage. This phenomenon might be attributed to the different constraints applied by the multifilament stitches to the endpoints of the spacer monofilaments and different initially spatial shapes of the vertical spacer monofilaments. Another possible reason is the contacts among the spacer monofilaments which could affect their postbuckling behaviour. From the pictures of the fabric taken from the coursewise direction (Figure 3.8(b)), which clearly demonstrate the detailed postbuckling process of the spacer monofilaments within the plateau stage, it can be seen that line-to-surface contacts are formed between the spacer monofilaments and the wavy internal surface of the outer fabric layers. By splitting a spacer monofilament into three sections, i.e., two end sections and a middle section, it can be found that with the increase of displacement in the plateau stage, the lengths of the two end sections contacted with the outer fabric layers are increased and the length of the middle section without contact is shortened. Therefore, the effective lengths of the spacer monofilaments in postbuckling decrease. As a result, the total reaction force of the spacer monofilaments increases according to the Euler-Bernoulli beam theory. On the other hand, the torsion and shear deformations of the spacer monofilaments as shown in Figure 3.8(a) can cause a decrease of the total reaction force. Therefore, a balance of both the effects maintains a nearly constant overall reaction force of the fabric at this stage of deformation.

The compression in the densification stage (stage IV) shows a rapid increase of the force due to the swift densification of the entire fabric. As shown in Figure 3.9, in this stage, the spacer monofilaments within the fabric collapse and contact one another, and therefore really high stiffness is obtained.

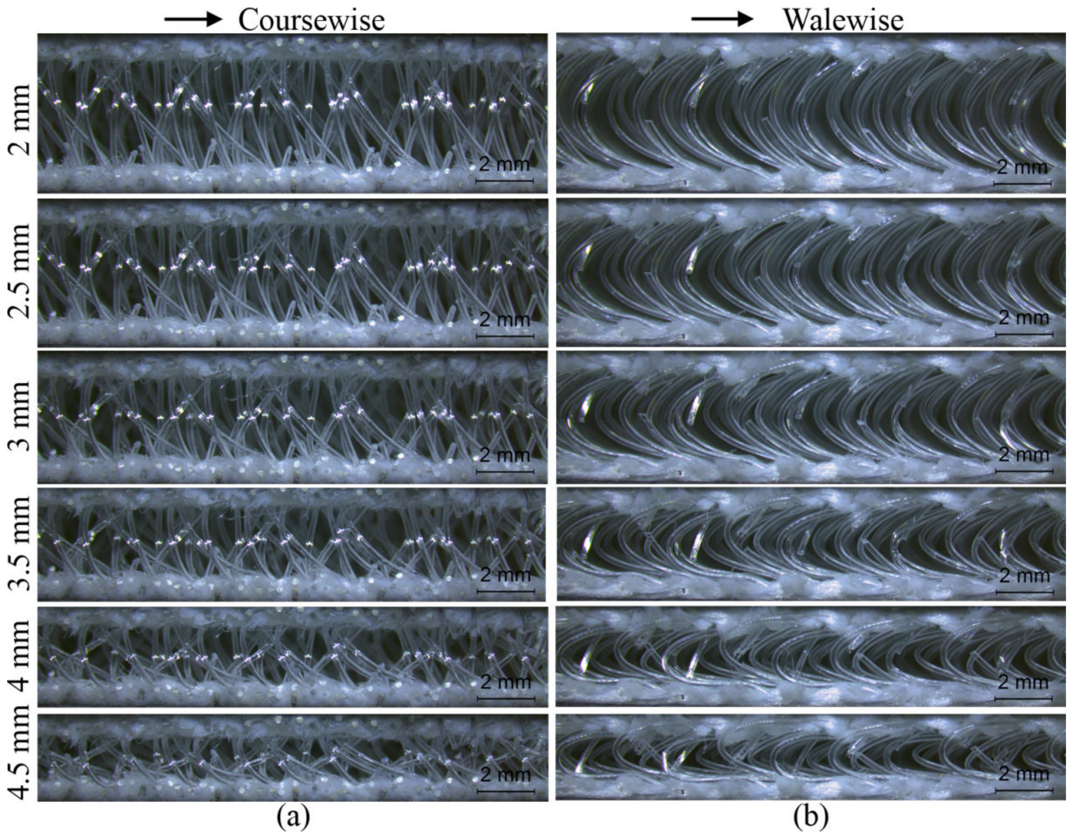

Figure 3.8 Cross-sectional pictures of the spacer fabric S1 taken in the plateau stage (displacements: 2–4.5mm): (a) from walewise direction; (b) from coursewise direction.

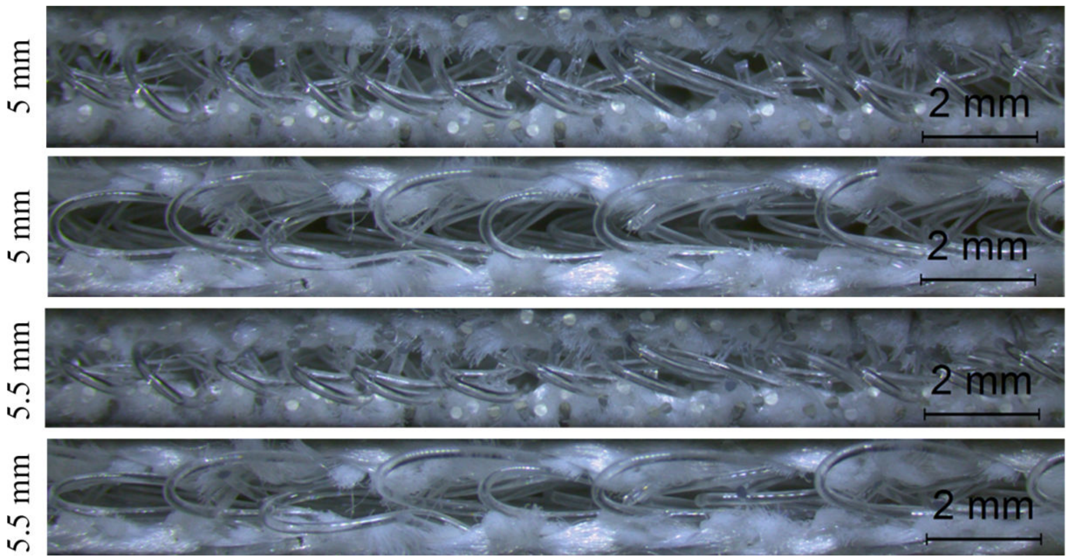

Figure 3.9 Cross-sectional pictures of the spacer fabric S1 taken in the densification stage (displacements: 5–5.5mm).

3.5 Conclusions

In this chapter, the effects of test boundary condition and sample size on the compression stress–strain characteristics of a typical spacer fabric developed as a cushioning material for human body protection were investigated. The deformation mechanism of the fabric was identified based on the analyses of the load–displacement curve obtained under a given test condition and the pictures of the fabric structure taken at different compression stages. According to the study, the following conclusions can be obtained.

- The compression test boundary condition only affects the deformation behaviour of the fabric in the plateau stage. Some slight fluctuations exist in the compression stress–strain curves when the fabric samples are not glued to the compression platens due to occurrence of shear and slippage of the outer layers of the fabric.
- The sample size has an obvious effect on the compression behaviour of the fabric, especially in the walewise direction. However, the effect of the fabric size in the coursewise direction is no longer observed when the sample size in the walewise direction is over 10 cm. The samples in a size of 10 cm × 10 cm can have stable compression test results.
- The compression mechanism of the spacer fabric was affected by its loose structure, postbuckling, torsion, shear, rotation and contacts of spacer monofilaments as well as by the constraints on the endpoints of spacer monofilaments and the contacts between spacer monofilaments and outer fabric layers.
- The compression behaviour of the spacer fabric can be split into four different stages of the deformation. A slower increase of total compression

force in the initial stage is due to the loose structure of the fabric, and a linear increase of total compression force in the elastic stage is due to additional constraints by the outer layers on the endpoints of spacer monofilaments. The long plateau stage is attributed to a combined effect of the shortened effective lengths of spacer monofilaments with their torsion, shear and rotation deformations in postbuckling. A rapidly increasing of total compression force in the final stage comes from the collapse and contacts of spacer monofilaments.

The compression deformation mechanism is important to design warp-knitted spacer fabrics as cushioning materials for human body protective applications. In this chapter, the potential deformation mechanism has been experimentally identified, and the possible reasons for the nonlinear load–displacement relationship qualitatively have also been given. To give a deeper understanding of the effects of the fabric structural parameters on its compression properties, theoretical modelling is needed to simulate the compression process and identify the influencing structural parameters quantitatively. A well developed theoretical model is also helpful in identifying the more accurate compression mechanism. For this purpose, in the following two chapters, both the analytical method and finite element method will be utilized to address this problem. In the next chapter, an analytical model based on planar elastica theory is presented; with the model, an attempt is made to explain the mechanism identified in this chapter theoretically.

CHAPTER 4 ANALYTICAL MODELLING OF WARP-KNITTED SPACER FABRIC

4.1 Introduction

This chapter aims to develop an analytical model for better understanding the compression deformation mechanism of warp-knitted spacer fabrics and also to study their structure–property relationships under compression quantitatively.

As analysed in Chapter 3, the changes in the slope of the load–displacement curve of a spacer fabric are dependent on the postbuckling, torsion, shear, rotation and contacts of spacer monofilaments as well as the contacts between spacer monofilaments and outer fabric layers. This implies that spacer monofilaments are the main load-carrier of a spacer fabric. Hence, a theoretical model for describing the compression behaviour of spacer monofilaments can be used to predict that of an entire spacer fabric approximately. Some effort has already been made to theoretically predict the compression behaviour of warp-knitted spacer fabrics as reviewed in Chapter 2. Spacer monofilaments have been considered as elastic rods and modelled by using Euler-Bernoulli beam theory with a small or large deflection method. The large deflection method, i.e., elastica theory, is more suitable for this problem because the spacer monofilaments are undertaking large deformation when compressing a spacer fabric. The existing analytical models based on elastica theory only took initially straight vertical rods into account, which is not applicable to spacer fabrics because spacer monofilaments in spacer fabrics are usually inclined rather than vertical. There is a need to develop a generalized model; with that, initially straight vertical spacer monofilaments can be considered as a special case, and spacer monofilaments with different inclination angles can be modelled.

This chapter is organized as follows. The structural features of warp-knitted spacer fabrics are first analysed in Section 4.2. Then the formulations for the generalized model based on planar elastica theory, considering a spacer monofilament as an initially straight, and elastic rod, is presented in Section 4.3. Next, with the developed generalized model coupled with a fabric structural analysis, the structural parameters affecting the compression properties of spacer fabrics are identified in Section 4.4. In Section 4.5, the identified structural parameters are employed for a parametric study. Finally, the analytical model is validated using a real warp-knitted spacer fabric with a typical structure in Section 4.6.

4.2 Structural analysis

Warp-knitted spacer fabrics are consisting of two separate outer fabric layers joined together but kept apart by spacer yarns. Spacer yarns are overlapped on both the needle bars of a double-needle bar Raschel machine in succession as illustrated in Figure 4.1. There are two types of lapping movements to connect the two separate outer layers, i.e., pillar (i.e., lapping the opposite needle on the other needle bar and the laying angle being 90º) and tricot (i.e., underlapping no less than one-needle space, and the laying angle being greater than 0º and less than 90º), as shown in Figure 4.1(a). The pillar spacer yarns are initially vertical observed from walewise, whereas the tricot spacer yarns are inclined, and their inclination angles are determined by the number of needles space underlapped, machine gauge and knockover comb bar distance. Both tricot and pillar spacer yarns can be used to connect an opposite or subsequent course of the other outer layer (Figure 4.1(b)). In this way, there are a large number of combinations for spacer yarns to constitute the spacer layer of a warp-knitted spacer fabric; i.e., it can be manipulated by incorporating different types of spacer yarns to achieve specific mechanical performance.

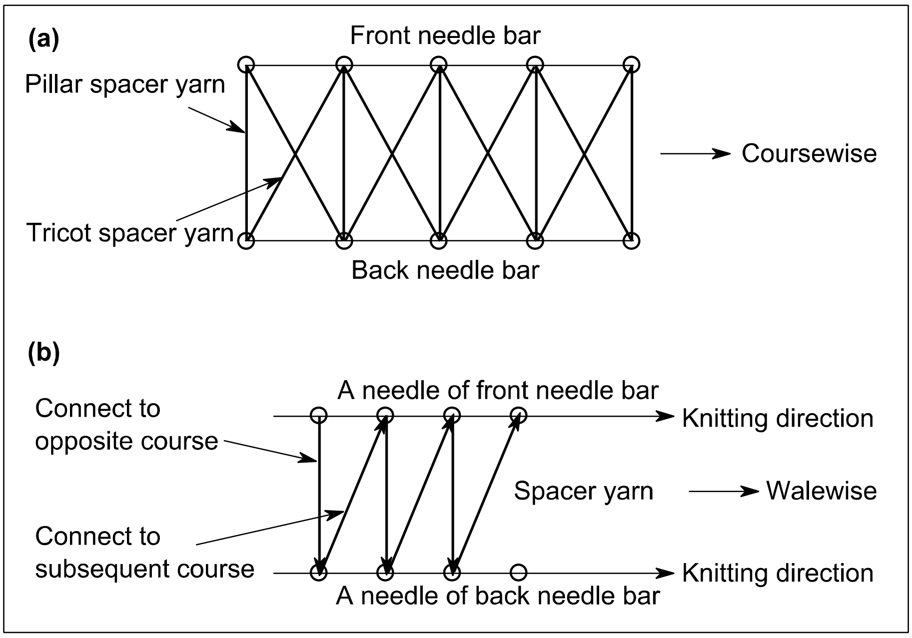

Figure 4.1 Spacer yarn knitting process for warp-knitted spacer fabrics: (a) observed from the walewise direction; (b) observed from the coursewise direction.

The spacer yarns of a warp-knitted spacer fabric are straight on the machine; however, they will change to be of curved shape after removed from the machine and subjected to a heat setting process. An example with a typical combination of spacer yarns is given in Figure 4.2 to illustrate the two states. A schematic fabric formed with this combination of spacer yarns is shown in Figure 4.3.

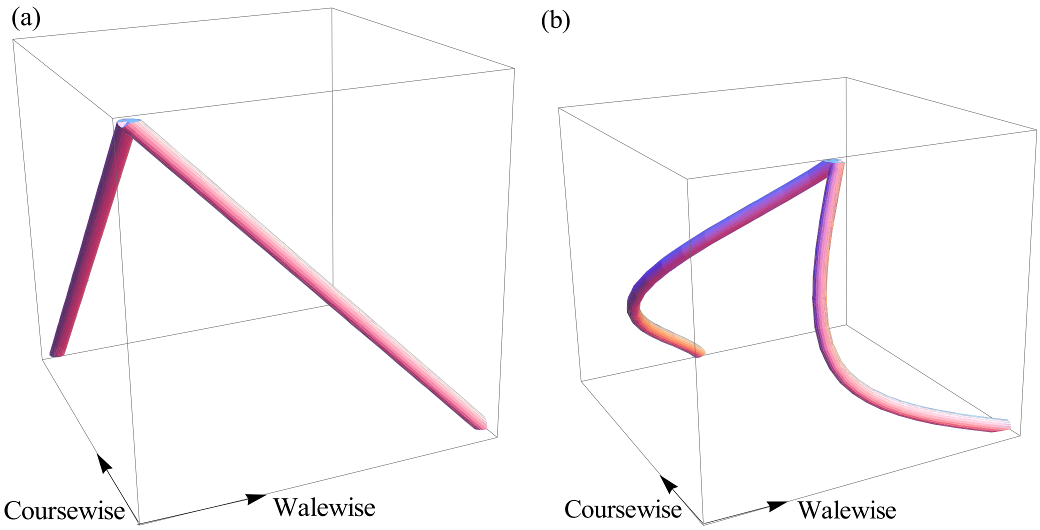

Figure 4.2 Schematic configuration of the spacer layer by chain notation 1-0 3-2/3-2 1-0//: (a) on the machine; (b) in finished fabric.

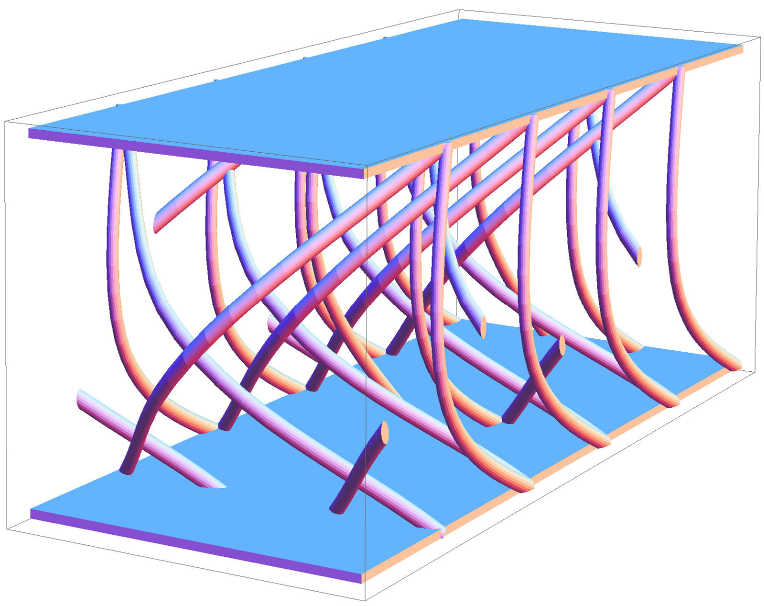

Figure 4.3 Schematic finished structure of the warp-knitted spacer fabric formed with the spacer layer by chain notation 1-0 3-2/3-2 1-0//.

Spacer yarns are the structural elements in spacer fabrics withstanding applied compression loads; therefore, the total resistance force of a spacer fabric in compression is the summation of the reaction forces of its spacer yarns. To understand the compression behaviour of a spacer fabric, the study on the mechanical behaviour of a single spacer yarn is required.

4.3 The mathematical formulations for the generalized model

Straight spacer monofilaments buckled to have curved shapes after removed from the machine, leading to a reduction in the distance between the two outer layers of a spacer fabric. The spacer monofilaments will continue to buckle at a large scale as the fabric thickness decreases under compression. Two steps should be adopted to model the compression behaviour of a spacer fabric. The first step is to calculate the initial shapes of the spacer monofilaments based on the manufacturing parameters. In the second step, displacement increments are applied to the obtained spacer monofilaments of initial curved shapes to calculate the corresponding reaction forces.

A spacer monofilament can be treated as an initially straight, flexible, and slender elastic rod. Such a rod first buckles to have an initially curved shape and then undertakes postbuckling in response to an applied displacement. Assume that the two phases of deformation are elastic, and then they can be modelled with elastica theory. In doing so, the following assumptions are made:

- the monofilament is homogenous and linearly elastic;
- the monofilament diameter and weight are neglected;
- the torsion of the monofilament is neglected;
- the outer fabric layer thickness is neglected;
- the contacts between the outer layers and the monofilament are assumed to be hard, and the friction between them is neglected.

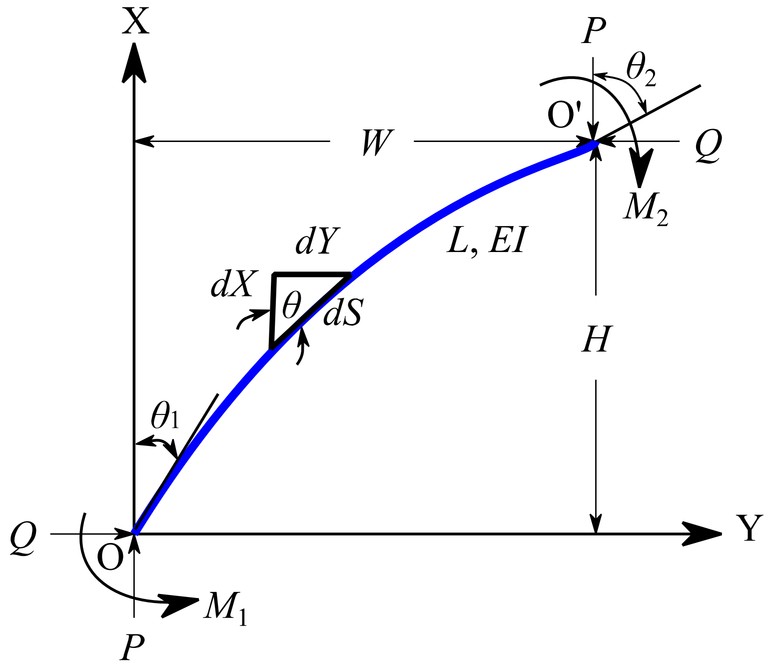

Figure 4.4 A generalized flexible slender elastic rod under applied end loads and moments.

Consider a general, flexible, slender, inextensible, and elastic rod which is initially straight and buckled by a vertical end force P, a horizontal end force Q, and two end moments M_1 and M_2 as shown in Figure 4.4. The global coordinate system is used as XOY. The inclination angle with the X-axis at an arbitrary point along the curve is denoted by θ, and the corresponding arc length measured from the origin point O is denoted by S.

The moment equilibrium equation of this elastic rod is

$$M_1 = M_2 + PW - QH. \tag{4.1}$$

The moment required for equilibrium at any general point (X, Y) with an arc length S can be expressed as

$$M = M_1 - PY + QX. \tag{4.2}$$

By referring to Euler-Bernoulli Law and the geometric relationships of elastica, the following relationships exist

$$\begin{aligned} M &= EI\frac{d\theta}{dS}, \\ \frac{dX}{dS} &= \cos\theta, \\ \frac{dY}{dS} &= \sin\theta. \end{aligned} \tag{4.3}$$

Differentiating each side of Equation (4.2) with respect to S and then substituting Equations (4.3) give

$$EI\frac{d^2\theta}{dS^2} = -P\sin\theta + Q\cos\theta\,. \tag{4.4}$$

This is a typical two-point boundary value problem. Using proper boundary conditions at the two endpoints of the rod, implicit differential Equation (4.4) can be solved with numerical methods, such as shooting and finite difference methods. There is a large amount of literature in solving this equation with different boundary conditions [126-129]; however, such methods always require too much effort in iterations. Another way to deal with the problem is by transforming the differential equation into an algebraic equation with elliptical integration because it is easier to solve an algebraic equation than to solve a differential equation. A classic problem was formulated in the book by Timoshenko and Gere [130], in which a slender rod fixed at the base and free at the upper end was considered, and the detailed transformation of the differential equation to an algebraic equation by using elliptical integration was presented. However, their formulated problem was specified with the specific boundary condition, namely, fixed-free for the two endpoints in the transformation. Shoup [131] proposed a way to solve Equation (4.4) without specifying the boundary conditions in the transformation from differential to algebraic. The following solving process follows Shoup's approach to obtain a generalized solution to Equation (4.4).

Multiply Equation (4.4) by $d\theta$ and integrate to obtain

$$\frac{EI}{2}\left(\frac{d\theta}{dS}\right)^2 = P\cos\theta + Q\sin\theta + C_0, \tag{4.5}$$

where C_0 is a constant derived from the integration. Rearranging this expression gives an expression for the curvature of the elastic rod at any point:

$$dS = \pm\frac{d\theta}{\sqrt{2(P\cos\theta + Q\sin\theta + C_0)/EI}}. \tag{4.6}$$

Substituting this curvature expression into the moment-curvature relationship gives the expression for the moment at any angle along the elastica, which is

$$M(\theta) = \pm EI\sqrt{2(P\cos\theta + Q\sin\theta + C_0)/EI}. \tag{4.7}$$

From the geometric relationships, integrate over the length of the elastic rod, i.e., the entire range of θ where $\theta_1 \le \theta \le \theta_2$, and then the parameters L, W and H can be expressed as

$$L = \int dS\,, H = \int \cos\theta\, dS, W = \int \sin\theta\, dS. \tag{4.8}$$

According to the literature [132], by using change of variables and integral transforms, the above equations can be transformed to nonlinear algebraic equations containing elliptic integrals of first and second kind. The integrals $F(k,\phi)$ and $E(k,\phi)$ are incomplete elliptic integrals of first and second kind, respectively. These two kinds of integrals are expressed as

$$\begin{aligned} F(k,\phi) &= \int_0^\phi \frac{d\phi}{\sqrt{1-k^2\sin^2\phi}}, \\ E(k,\phi) &= \int_0^\phi \sqrt{1-k^2\sin^2\phi}\, d\phi. \end{aligned} \tag{4.9}$$

To apply the elliptic integrals, Shoup [131] made the changing of variables

$$\frac{2P}{EI} = A = D\cos\alpha\,, \frac{2Q}{EI} = B = D\sin\alpha\,, \frac{2C_0}{EI} = C \tag{4.10}$$

and used the following expressions for transforming above integrals into elliptic integrals

$$\cos(\theta - \alpha) = A/D\,\text{Cos}\theta + B/D\,\text{Sin}\theta = 1 - 2k^2\sin^2\phi \tag{4.11}$$

where k is defined as

$$2k^2 - 1 = \frac{C}{D}. \tag{4.12}$$

By using the above variables and integral transforms, according to Shoup [131], the complete governing nonlinear equations for the initially straight elastic rod in the null form become

$$\begin{aligned}
&-\frac{L(P^2+Q^2)^{\frac{1}{4}}}{\sqrt{EI}} \pm \big(F(k,\phi_2) - F(k,\phi_1)\big) = 0,\\
&-\frac{H(P^2+Q^2)^{\frac{3}{4}}}{\sqrt{EI}} \pm P\big(2E(k,\phi_2) - F(k,\phi_2) + F(k,\phi_1) - 2E(k,\phi_1)\big)\\
&\qquad \pm 2kQ(\cos\phi_2 - \cos\phi_1) = 0,\\
&-\frac{W(P^2+Q^2)^{\frac{3}{4}}}{\sqrt{EI}} \pm Q\big(2E(k,\phi_2) - F(k,\phi_2) + F(k,\phi_1) - 2E(k,\phi_1)\big)\\
&\qquad \pm 2kP(\cos\phi_1 - \cos\phi_2) = 0,\\
&\qquad M_1 = \pm EIk\sqrt{2D}\cos\phi_1,\\
&\qquad M_2 = \pm EIk\sqrt{2D}\cos\phi_2,\\
&(2k^2\sin^2\phi_1 - 1)\sqrt{P^2+Q^2} + P\cos\theta_1 + Q\sin\theta_1 = 0,\\
&(2k^2\sin^2\phi_2 - 1)\sqrt{P^2+Q^2} + P\cos\theta_2 + Q\sin\theta_2 = 0.
\end{aligned} \tag{4.13}$$

The coordinates (X, Y) of an arbitrary point in the elastica curve corresponding to ϕ_i where $\phi_1 \le \phi_i \le \phi_2$ can be calculated by using the formulas given by Shoup [131] as follows

$$X = \pm\left(\frac{A}{D}\right)\sqrt{\frac{2}{D}}\big(2E(k,\phi_i) - 2E(k,\phi_1) - F(k,\phi_i) + F(k,\phi_1)\big)$$
$$\pm\left(\frac{2Bk}{D}\right)\sqrt{\frac{2}{D}}(\cos\phi_i - \cos\phi_1),$$
$$Y = \pm\left(\frac{B}{D}\right)\sqrt{\frac{2}{D}}\big(2E(k,\phi_i) - 2E(k,\phi_1) - F(k,\phi_i) + F(k,\phi_1)\big)$$
$$\pm\left(\frac{2Ak}{D}\right)\sqrt{\frac{2}{D}}(\cos\phi_1 - \cos\phi_i). \tag{4.14}$$

The buckled rod shape can be drawn using the coordinates of the points in the range of $\phi_1 \leq \phi_i \leq \phi_2$.

The process of changing from the initially straight form into a curved form of a spacer yarn might include outer layer shrinking, spacer yarn buckling and slipping. This dynamic process is complex and therefore not easy to address; however, the buckled yarn in a steady state obeys the above model.

4.4 Identification of influencing structural parameters

Governing Equations (4.13) are typical nonlinear algebraic equations, containing elliptic integrals of first and second kind. The parameters in Equations (4.13), i.e., *EI*, *W*, *H*, *L*, ϕ_1 and ϕ_2, are the factors determining the mechanical behaviour of an elastic rod. While *W*, *H* and *L* are the geometric parameters, *EI* is the bending rigidity of an elastic rod, and the boundary conditions of its two endpoints are determined by ϕ_1 and ϕ_2. As stated previously, there are two configurations of spacer yarns. The force analysis and the coordinate system chosen for the two kinds of spacer yarns are shown in Figure 4.5 for identifying the structural parameters that influence the fabric compression behaviour.

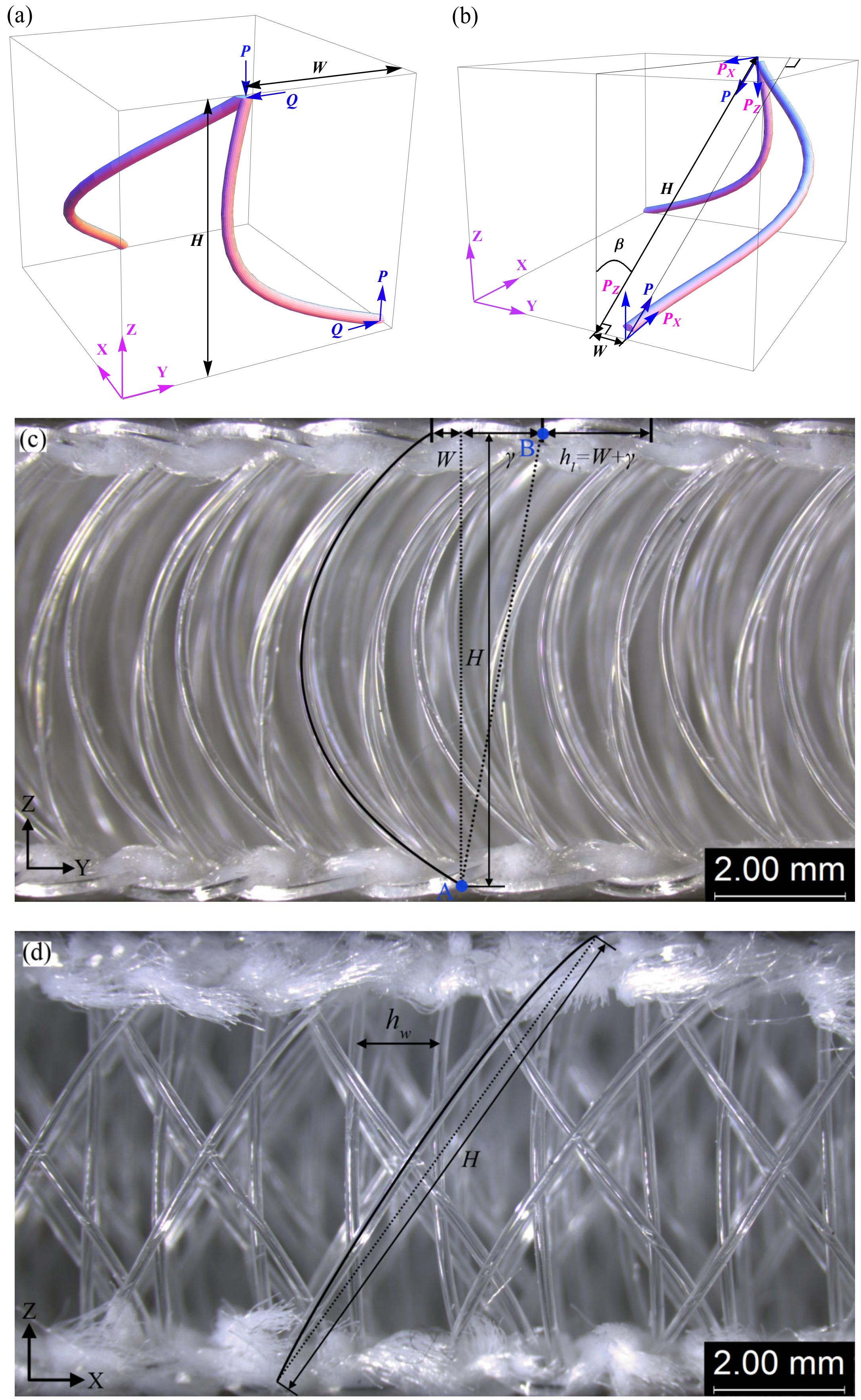

Figure 4.5 Force analysis for spacer yarns: (a) and (c), pillar; (b) and (d), tricot.

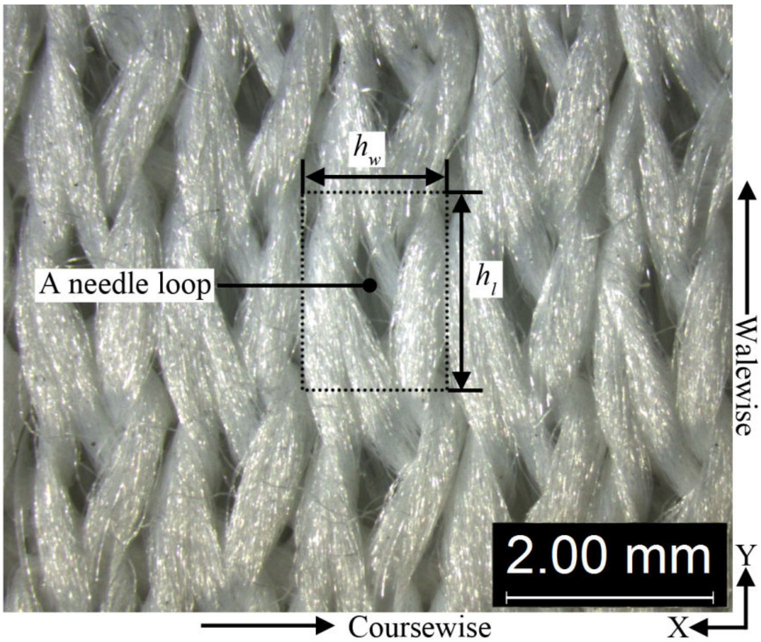

Figure 4.6 An outer layer of a warp-knitted spacer fabric.

The geometric parameters W, H and L are related to the structural parameters of a specified spacer fabric. Two subscripts p and t are used to denote pillar and tricot, respectively. Figure 4.5 shows that W_p and W_t are determined by the loop height h_l of the outer layer (Figure 4.6) and the shear displacement γ between the two outer layers. When the fabric was on the machine, the points A and B should be exactly opposite; however, after removed from the machine and heat setting, shear took place between the two outer layers. Hence, W_p and W_t are given by

$$W_p = n_{cm}h_l - \gamma \text{ , } W_t = n_{cm}h_l + \gamma, \tag{4.15}$$

where n_{cm} depends on the connect mode, equal to 0 when connecting to an opposite course and equal to 1 when connecting to a subsequent course. The parameter H_p equals the fabric thickness h_f, whereas H_t depends on the loop width h_w and fabric thickness h_f. The relationships can be expressed as

$$H_p = h_f, H_t = \sqrt{{h_f}^2 + (n_u h_w)^2}, \tag{4.16}$$

where n_u is the number of needles space underlapped. While the pillar spacer yarn is vertical, the inclination of the tricot spacer yarn termed β is illustrated in Figure 4.5(b). The spacer yarn length L is determined by the number of needles space underlapped, machine gauge g_m (distance between two neighbouring needles in the same needle bar), knockover comb bar distance d_m, and course density setting (the height of a loop in the outer layers on the machine h_{lm}). For the pillar spacer yarn L_p and the tricot spacer yarn L_t, the relationships are given by

$$L_p = \sqrt{{d_m}^2 + (n_{cm}h_{lm})^2},$$
$$L_t = \sqrt{(n_u g_m)^2 + {d_m}^2 + (n_{cm}h_{lm})^2}. \tag{4.17}$$

Therefore, for the pillar spacer yarn, the load P in Z-axis completely contributes to the fabric compression resistance; in contrast, for the tricot spacer yarn, only the component force P_z contributes to the fabric compression resistance, which is

$$P_z = \frac{h_f}{\sqrt{{h_f}^2 + (n_u h_w)^2}} \cdot P. \tag{4.18}$$

Spacer yarn bending rigidity EI depends on Young's modulus E and moment of inertia of the cross-sectional area I. For a circular-shaped monofilament, I is given by

$$I = \frac{\pi}{4} r^4, \tag{4.19}$$

where r is the radius. The boundary condition parameters ϕ_1 and ϕ_2 are related to the outer layer structure. Whereas a compact outer layer leads to high moments at the spacer yarn endpoints, a loose outer layer results in low moments.

In summary, the structural parameters affecting the compression behaviour of warp-knitted spacer fabrics include spacer yarn inclination angle and diameter, fabric thickness, and outer layer structure and density, as summarised in Table 4.1.

Table 4.1 Influencing structural parameters on compression behaviour

Parameters in Equations	Pillar spacer yarn	Tricot spacer yarn
W	Wale density	-
H	Fabric thickness	Fabric thickness, course density, wale density, number of needles space underlapped
L	Knockover comb bar distance, course density	Knockover comb bar distance, machine gauge, number of needles space underlapped
EI	Spacer yarn modulus and diameter	
ϕ_1 and ϕ_2	Outer layer structure tightness	

4.5 Parametric study of the structural parameters

To examine the quantitative effects of the identified structural parameters on the compression resistance of spacer fabrics, a parametric study is carried out in this section. For simplicity, the following nondimensional parameters are employed:

$$\begin{gathered} s = S/L\ , x = X/L, y = Y/L, h = H/L, w = W/L, \\ p = (PL^2)/EI, q = (QL^2)/EI, m^* = ML/EI, c^* = \frac{C_0L^2}{EI}, \\ a^* = 2p, b^* = 2q, d^* = \sqrt{a^{*2} + b^{*2}}. \end{gathered} \tag{4.20}$$

The nondimensional null form of Equations (4.13) [133] can be rewritten as

$$\begin{gathered} -(p^2 + q^2)^{1/4} \pm \big(F(k, \phi_2) - F(k, \phi_1)\big) = 0, \\ -h(p^2 + q^2)^{\frac{3}{4}} \pm p\big(2E(k, \phi_2) - 2E(k, \phi_1) - F(k, \phi_2) + F(k, \phi_1)\big) \\ \pm 2qk(\cos\phi_2 - \cos\phi_1) = 0, \\ -w(p^2 + q^2)^{\frac{3}{4}} \pm q\big(2E(k, \phi_2) - 2E(k, \phi_1) - F(k, \phi_2) + F(k, \phi_1)\big) \\ \pm 2pk(\cos\phi_1 - \cos\phi_2) = 0, \\ m^*{}_1 = \pm 2(p^2 + q^2)^{1/4} k \cos\phi_1, \\ m^*{}_2 = \pm 2(p^2 + q^2)^{1/4} k \cos\phi_2, \\ (2k^2 \sin^2\phi_1 - 1)\sqrt{p^2 + q^2} + p\cos\theta_1 + q\sin\theta_1 = 0, \\ (2k^2 \sin^2\phi_2 - 1)\sqrt{p^2 + q^2} + p\cos\theta_2 + q\sin\theta_2 = 0. \end{gathered} \tag{4.21}$$

Accordingly, the nondimensional coordinates (x, y) of an arbitrary point in the elastica curve corresponding to ϕ_i where $\phi_1 \le \phi_i \le \phi_2$ can be expressed as

$$
\begin{aligned}
x = &\pm\left(\frac{a^*}{d^*}\right)\sqrt{\frac{2}{d^*}}\left(2E(k,\phi_i) - 2E(k,\phi_1) - F(k,\phi_i) + F(k,\phi_1)\right) \\
&\pm\left(\frac{2b^*k}{d^*}\right)\sqrt{\frac{2}{d^*}}(\cos\phi_i - \cos\phi_1), \\
y = &\pm\left(\frac{b^*}{d^*}\right)\sqrt{\frac{2}{d^*}}\left(2E(k,\phi_i) - 2E(k,\phi_1) - F(k,\phi_i) + F(k,\phi_1)\right) \\
&\pm\left(\frac{2a^*k}{d^*}\right)\sqrt{\frac{2}{d^*}}(\cos\phi_1 - \cos\phi_i).
\end{aligned}
\tag{4.22}
$$

The effects of spacer yarn inclination angle, spacer yarn fineness, course density and fabric thickness on the normalized compression resistance of spacer fabrics are studied. The studied spacer yarns are assumed to be initially straight (curved in reality), and the constraints at the two endpoints are defined as pinned. In this case, zero moments at the two endpoints of a spacer yarn are assumed. A single spacer yarn is considered for each parameter in the study, neglecting the contacts between the spacer yarn and outer layers. Therefore, the parametric study presented later on is only valid for small displacements, and it gives preliminary estimates for the relationships between the geometric features of spacer yarns and the compression properties of warp-knitted spacer fabrics.

4.5.1 Spacer yarn inclination angle

Spacer yarn inclination angle β is defined in Figure 4.5(b), depending on the number of needles space underlapped, machine gauge and knockover comb bar distance. It is also dependent on fabric thickness and wale density (the number of wales in a unit length) in a finished fabric. Five spacer yarn inclinations are selected to investigate their effects on the compression resistance. These spacer yarns are used to connect the opposite course. Their nondimensional lengths are identical and equal to 1; that is, the fabrics formed with these spacer yarns have different thicknesses. The schematic diagram for these spacer yarns is presented in Figure 4.7. The vertical spacer yarn with an inclination angle of 0º is pillar, and the other inclined ones are tricot.

Normalized displacements (h=H/L) are applied to the top endpoints, and the normalized reaction load for each yarn is plotted against the normalized strain in Figure 4.8. While h_0 is the initial thickness, h is the thickness during compression. The results show that higher compression resistance is obtained at a smaller inclination, and thus the vertical spacer yarn possesses the highest compression reaction load. This implies that the more the spacer yarns are vertical to the outer layers, the higher the compression resistance of the fabric is addressed. In addition, the spacer yarns with high inclinations such as 75º and 60º make negative contributions to the compression resistance with further displacement increments. Therefore, the fabric with a smaller number of needles space underlapped has higher compression resistance.

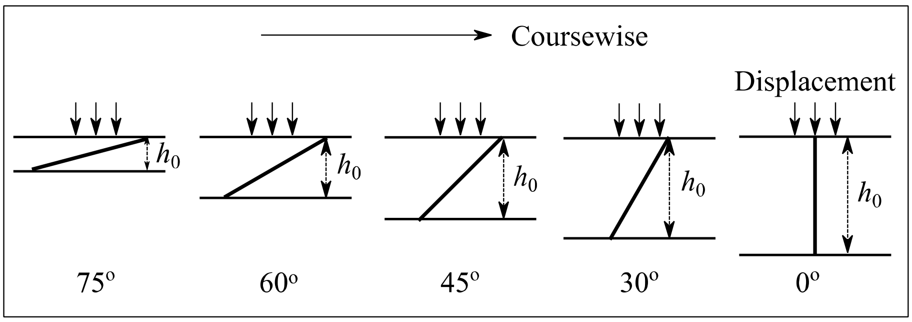

Figure 4.7 A schematic diagram for the spacer yarns with different inclinations observed from the walewise direction.

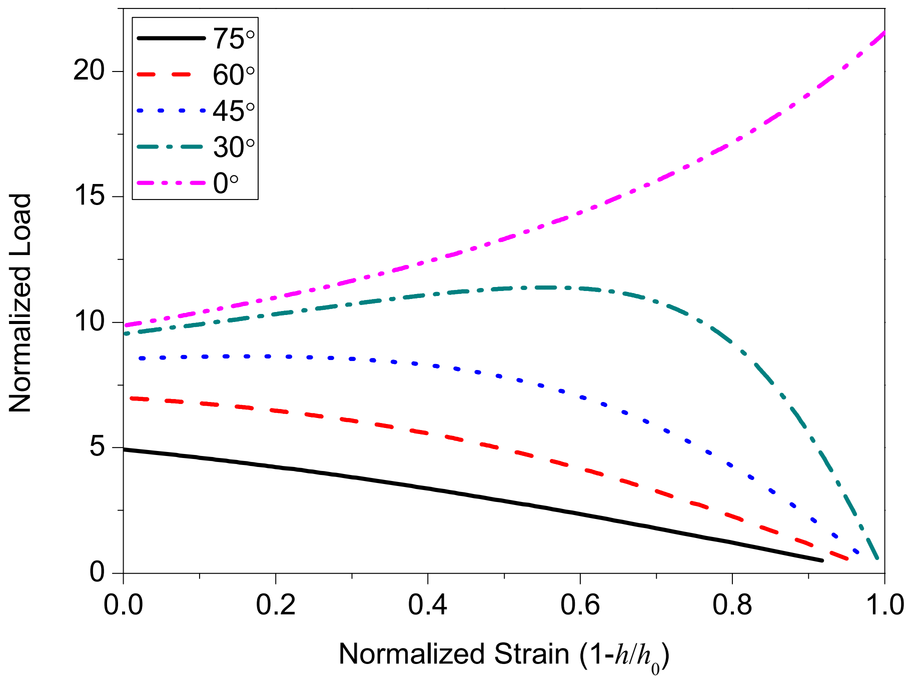

Figure 4.8 Effect of spacer yarn inclination on compression resistance.

4.5.2 Spacer yarn fineness

To investigate the effect of spacer yarn fineness on the normalized compression resistance, vertical pillar spacer yarns connecting to an opposite course are used. Except for the spacer yarn radius, other structural parameters are the same as the yarn with an inclination of 0º shown in Figure 4.7. The normalized loads of the yarns with different radii are plotted against the normalized strain in Figure 4.9, showing a significant effect on the compression resistance. The higher the radius of the spacer yarn, the higher the compression resistance of the spacer fabric. This is easy to understand by referring to Equation (4.19) that the bending rigidity of a circular spacer yarn is proportional to the fourth power of its radius.

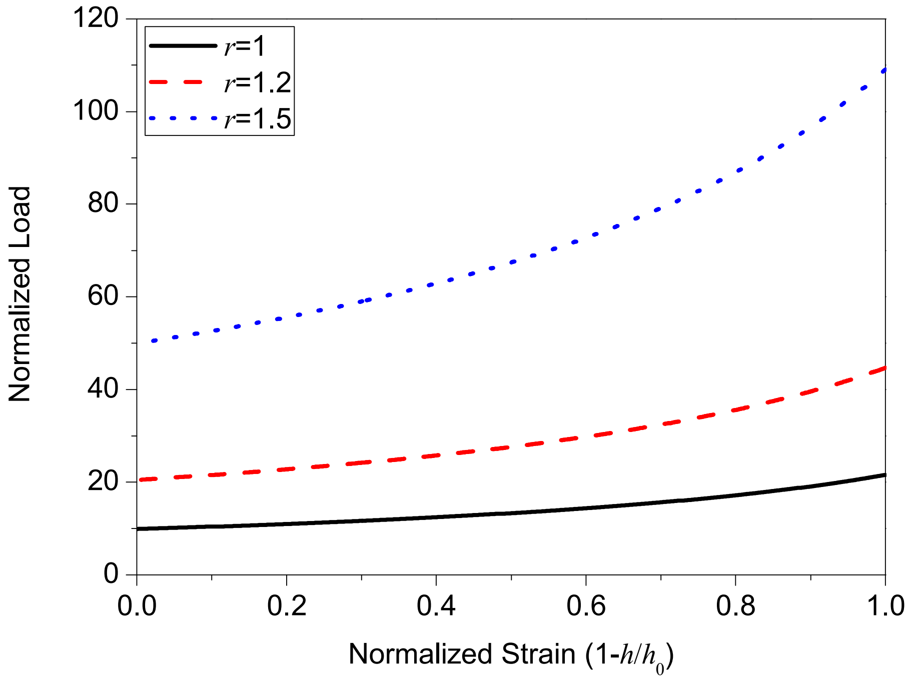

Figure 4.9 Effect of spacer yarn radius on compression resistance.

4.5.3 Course density

Course density is the number of courses in a unit length of outer fabric layers in the walewise direction. According to the definition in Figure 4.6, the loop height h_l can be used as the structural parameter to investigate the effect of course density on the normalized compression resistance of spacer yarns. Both pillar and tricot spacer yarns can be used to connect to subsequent courses; h_l affects the inclinations of such spacer yarns. To study the course density effect, initially straight pillar spacer yarns are selected with five values defined for the parameter h_l, and the schematic diagram is presented in Figure 4.10.

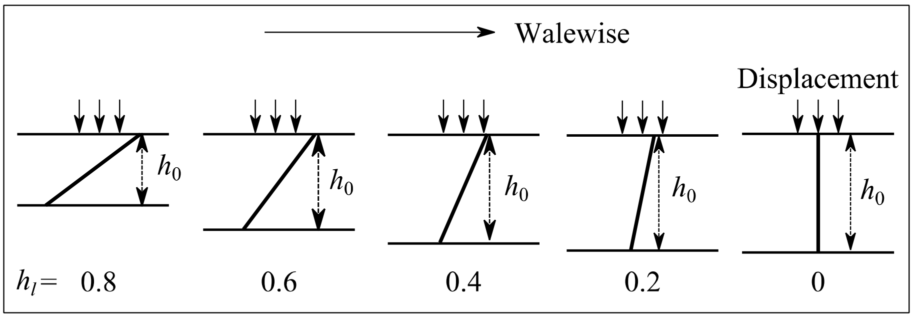

Figure 4.10 A schematic diagram for the spacer yarns with different course densities observed from the coursewise direction.

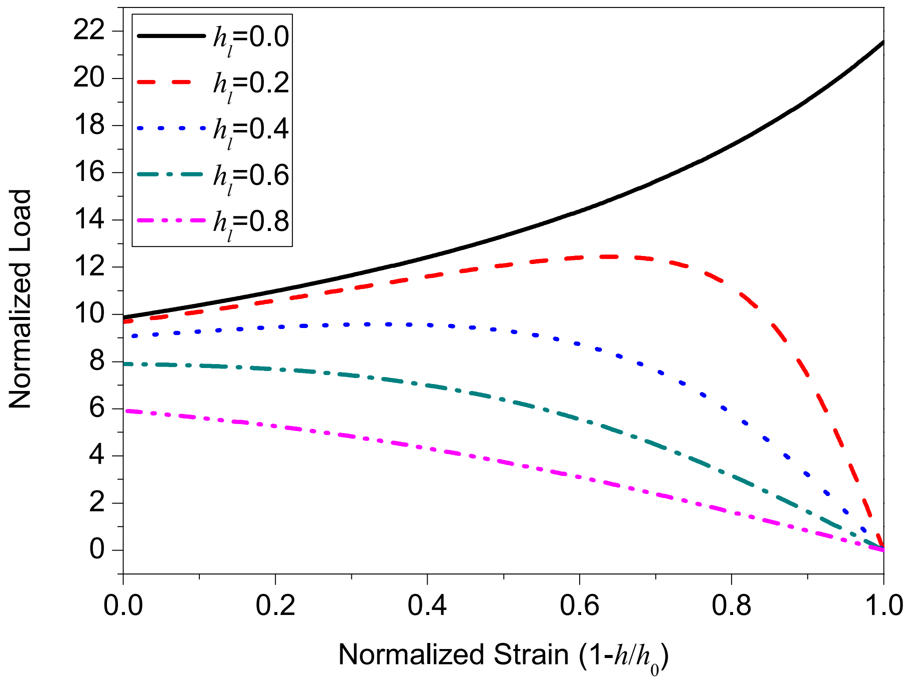

Figure 4.11 Effect of course density on compression resistance.

Figure 4.11 plots the normalized loads for the spacer yarns with different course densities against the normalized strain, showing a similar effect to that of the spacer yarn inclination. The spacer yarn with a lower loop height (higher course density) has higher compression resistance. The higher course density of the outer layers leads to the spacer yarns more vertical to the outer layers, and therefore the relevant spacer fabric possesses higher compression resistance.

4.5.4 Fabric thickness

To investigate the fabric thickness effect, vertical pillar spacer yarns connecting to opposite courses are selected. Except for their lengths, the selected spacer yarns have the same geometric feature as the yarn with an inclination of 0º shown in Figure 4.7 or the yarn with h_l=0 shown in Figure 4.10. In this case, the fabric thickness equals the spacer yarn length. Figure 4.12 shows the effect of the fabric thickness (i.e., the spacer yarn length) on the normalized compression resistance. The results show that the spacer fabric with a lower thickness has higher compression resistance.

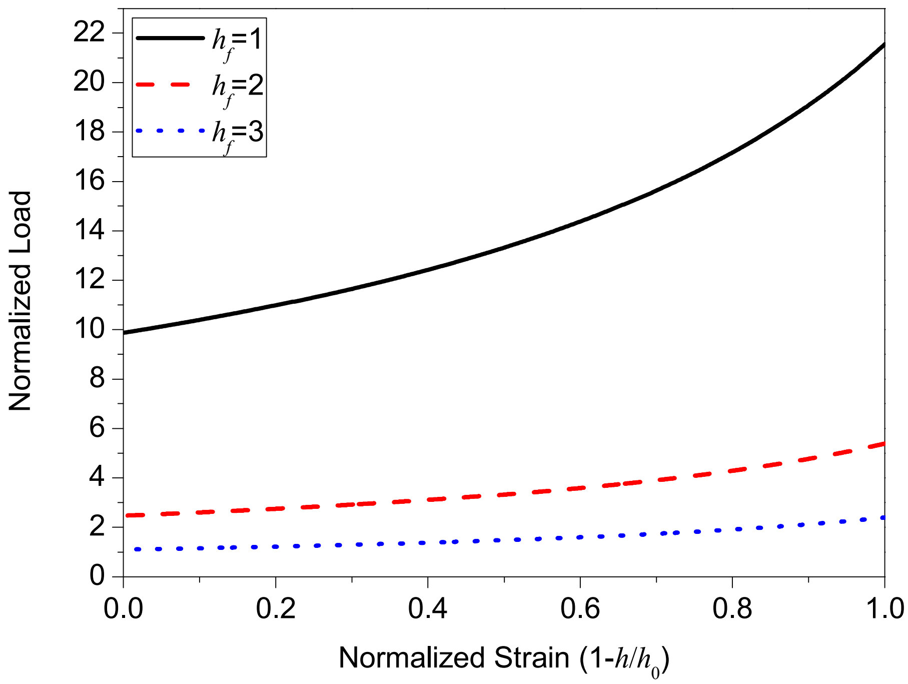

Figure 4.12 Effect of fabric thickness on compression resistance.

In summary, the spacer fabric with a lower spacer yarn inclination, coarser spacer yarn, higher course density of the outer layers and lower fabric thickness has higher compression resistance. However, it should be noted that the structural parameters are interdependence and have combined effect on the resultant compression resistance of spacer fabrics; for instance, course density affects spacer yarn inclination, and for a spacer yarn with a specified length the increase of the fabric thickness results in the reduction of the spacer yarn inclination. Furthermore, a spacer fabric can be composed of spacer yarns with different inclinations, which are not initially straight and could contact the outer fabric layers at large displacements during compression. Therefore, the conclusions from the parametric study might be only valid within small compression displacements. To extend the study of the effects of those structural parameters on the compression behaviour of spacer fabrics, a real spacer fabric is modelled with the analytical model in the next section.

4.6 Experimental validation

This section deals with the experimental validation of the analytical model. The spacer fabric S1, the experimental results of which were discussed in Chapter 3, is adopted. Initially, the parameters for the governing Equations (4.13) are acquired by analysing the fabric structure. Then the acquired parameters are substituted into the governing equations to obtain the initial shapes of the spacer yarns. After that, the correlations between the reaction loads and displacements of the spacer yarns will be calculated separately by considering the contacts between the spacer yarns and the outer layers. Finally, the predicted load–displacement curve of the entire fabric is achieved and compared with the experimental one.

4.6.1 Acquisition of governing equation parameters

The fabric includes two types of spacer yarns; pillar spacer yarns connecting to a subsequent course by the notation 1-0/1-0 and tricot spacer yarns connecting to an opposite course by the notation 3-2/1-0. A schematic diagram for the two types of spacer yarns on the machine state and in the finished fabric state within a 3D global coordinate system OXYZ is shown in Figure 4.13. For simplicity, shear displacement between the two outer fabric layers γ was not considered in the calculation. The compression resistance of the spacer fabric S1 is the summation of the resistance of the pillar and tricot spacer yarns. Hence, the compression load–displacement relationships of the two spacer yarns are needed to be calculated separately.

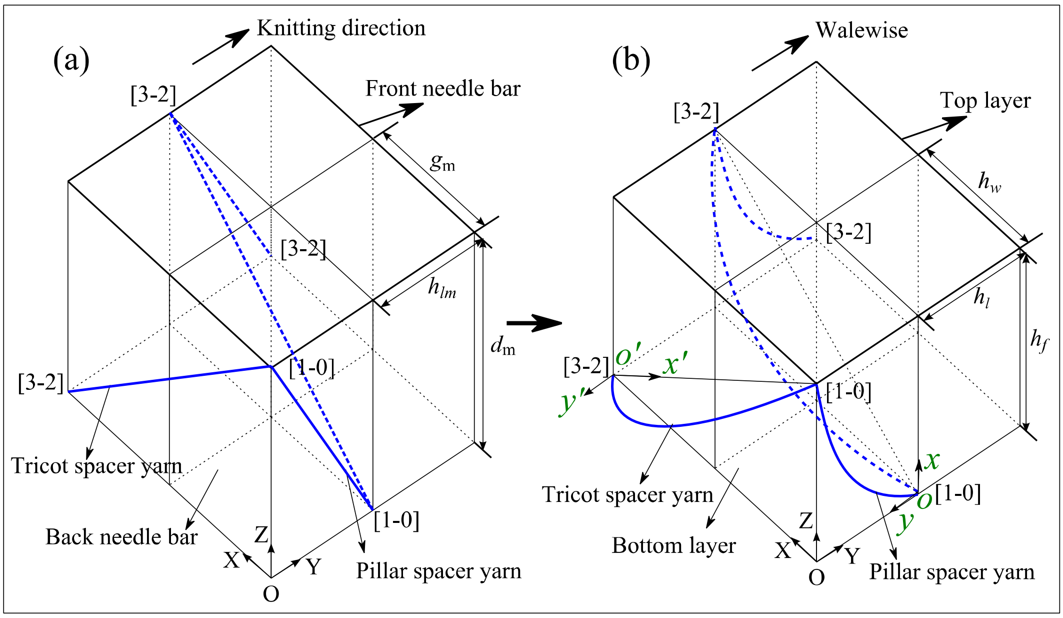

Figure 4.13 A schematic diagram of the configuration and arrangement of the spacer yarns: (a) fabric on the machine; (b) finished fabric.

In order to conduct the theoretical calculations for the two spacer yarns, their initial geometric shapes should be determined first. For this purpose, the parameters involved in Equations (4.13), i.e., EI, W, H, L, ϕ_1 and ϕ_2 for the two spacer yarns, were acquired. The parameter EI, the bending rigidity, can be experimentally measured. The geometric parameters W, H and L are different for the two types of spacer yarns and can be obtained by analysing the fabric structure. Besides, ϕ_1 and ϕ_2, which determine the boundary conditions for the spacer monofilaments, can also be defined according to the spacer fabric structure. By substituting these parameters into Equations (4.13), the unknowns P, Q, k, θ_1 and θ_2 can be solved for the two spacer yarns. Then by substituting these solved five parameters into Equations (4.10) and (4.14), the buckled shapes of the spacer yarns can be obtained. The acquisition of the parameters EI, W, H, L, ϕ_1 and ϕ_2 is presented in the following.

Firstly, the polyester monofilament bending rigidity EI was measured on a KES-FB2 pure bending tester. Twenty monofilaments attached in parallel to a paper sheet having a 1.1×2.5 cm rectangular hole were mounted for testing by placing the paper sheet in the chucks with 1 cm distance of the instrument as described in the literature [134]. Ten samples were tested, and the result is 0.6836 ± 0.0384 cN/cm^2. Secondly, W and H can be easily measured from the finished fabric; however, the spacer yarn length L cannot be directly measured. It is determined by the machine setting parameters as discussed in Section 4.4. Therefore, the parameters W and H for the two spacer yarns can be calculated by referring to Figure 4.13(b), while the lengths of them L can be calculated by referring to Figure 4.13(a). The parameters used in Figure 4.13 were defined in Section 4.4. For the sake of convenience, the descriptions for them are recalled here. Table 4.2 lists the descriptions and values of them. Using Equations (4.15–4.17), the geometric parameters W, H and L for the two types of spacer yarns were calculated, and the results are listed in Table 4.3. Thirdly, the parameters ϕ_1 and ϕ_2 are related to the boundary conditions for the spacer monofilament endpoints. The experimental study in Chapter 3 showed that the fluffy multifilament stitches in the loose outer layers do not provide effective constraints on the spacer monofilaments in the initial stage of compression. This implies that the two endpoints of each spacer yarn are pinned and can rotate in-plane freely. In this case, the moments at the endpoints M_1 and M_2 defined in Equations (4.13) can be assumed to be equal to zero. Thus, the two inflection points ϕ_1 and ϕ_2 of the first mode of the buckled shape are at $\pi/2$ and $3\pi/2$, respectively. These values for the two yarns are also listed in Table 4.3.

Table 4.2 Structural parameters of the machine setting and the finished fabric

Structural parameters	Descriptions	Values (mm)
h_{lm}	The loop height on the machine determined by course density	1.25
g_m	The distance between two adjacent needles determined by the machine gauge	1.41
d_m	The knockover comb bar distance	11.9
h_l	The loop height of the finished fabric outer layers	1.7687
h_w	The loop width of the finished fabric outer layers	1.374
h_f	The thickness of the finished fabric	7.52

Table 4.3 Governing equation parameters for the spacer yarns

Structural parameters	EI (cN·cm^2)	W (mm)	H (mm)	L (mm)	ϕ_1	ϕ_2
Pillar spacer yarn	0.6836	1.7687	7.52	11.965	$\pi/2$	$3\pi/2$
Tricot spacer yarn	0.6836	0	8.00637	12.2296	$\pi/2$	$3\pi/2$

4.6.2 Initial shapes of the spacer yarns

Governing Equations (4.13) are typical nonlinear algebraic equations. All the parameters required by Equations (4.13) are listed in Table 4.3. Five unknowns (P, Q, k, θ_1 and θ_2) and five equations (the two equations for the relationship between M and ϕ were not included) were solved with Newton's method by the subroutine

FindRoot in Wolfram Mathematica® 7.0 for students. By substituting the solutions to Equations (4.13) into Equations (4.14), the initial shapes of the two spacer yarns were obtained as shown in Figure 4.14(a). These curves were also rotated and moved in three-dimensional space to form the spacer layer of the warp-knitted spacer fabric as shown in Figure 4.14(b).

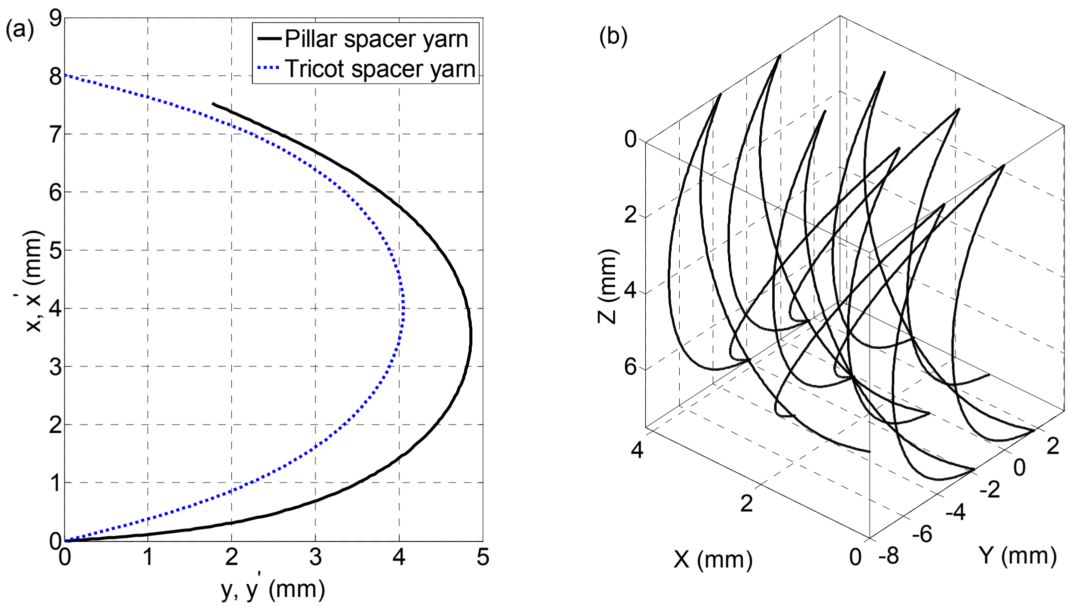

Figure 4.14 Geometric model of the spacer fabric S1: (a) planar spacer yarns; (b) spacer layer.

4.6.3 Compression process analysis

In this section, displacement increments are applied to the endpoints of the obtained spacer monofilaments of initial shapes to investigate their compression process and calculate the corresponding reaction forces.

The static force analysis for the two spacer yarns is illustrated in Figure 4.15. For the pillar spacer yarn, the load P in Z-axis completely contributes to the fabric compression resistance. In contrast, for the tricot spacer yarn, only the component force P_z defined by Equation (4.18) contributes to the fabric compression resistance. Besides, the spacer yarns will contact the outer layers when the applied displacement rises up to a certain value; their different initial shapes lead to different contact behaviours. In this connection, the compression process of the two spacer yarns should be studied separately.

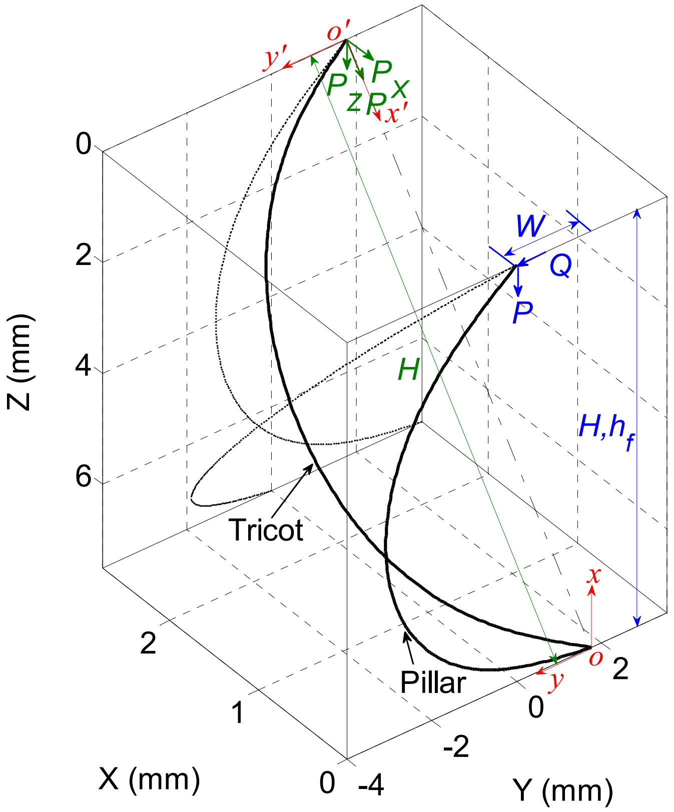

Figure 4.15 Force analysis of the spacer yarns.

4.6.3.1 Pillar spacer yarn

The pillar spacer yarn is considered first. A local coordinate system *xoy* is selected as illustrated in Figure 4.15. Because the load P is governed by Equations (4.13), by varying the parameter H, the corresponding reaction load can be calculated. For this particular spacer yarn, the parameter H equals the fabric thickness h_f. Reducing the value of H in Equations (4.13) is identical to decreasing the fabric thickness and thus used to simulate the compression deformation process of the pillar spacer yarn.

It should be noted that, for governing Equations (4.13), constraints are only imposed at the two endpoints of a spacer yarn. This pillar spacer yarn, however, will contact the outer layers when reaching a certain displacement, providing additional constraints on the spacer yarn, thereby affecting its mechanical behaviour. Such contacts were considered in the calculation. The pillar spacer yarn presented in Figure 4.15 can be divided into three sections: two end sections (top and bottom) and a middle section. Due to its asymmetrical initial shape, there are three phases of deformation: (i) free postbuckling, (ii) the bottom end section in contact with the bottom outer layer and (iii) the top end section in contact with the top outer layer. To conduct the calculation, the two dividing points among the three phases should be identified.

At the beginning (Phase i), the entire spacer yarn undertakes postbuckling freely. The inclination angles with the x-axis at the two endpoints (i.e., θ_1 for the bottom endpoint and θ_2 for the top endpoint as defined in Figure 4.4) increase with the displacement. The pillar spacer yarn does not contact the two outer layers, keeping a constant effective length in postbuckling in this phase.

Compressing the pillar spacer yarn to be of a specific displacement, at the beginning point of phase ii, the bottom end section starts to contact the bottom outer layer. At this moment, the inclination angle with the x-axis at the endpoint of the bottom end section θ_1 equals $\pi/2$ due to the pinned constraint. From then on, line to surface contact occurs. The contact length between the bottom end section of the yarn and the bottom outer layer increases as the displacement increases; meanwhile, the effective length of the yarn in postbuckling decreases. Since the line contact part of the bottom end section does not contribute to the compression resistance any more, it is excluded in the calculation. In this way, as the displacement increases, the endpoint of the bottom end section is moving to the point that is about to contact the bottom outer layer, and the angle θ_1 is keeping constant being $\pi/2$ in this phase.

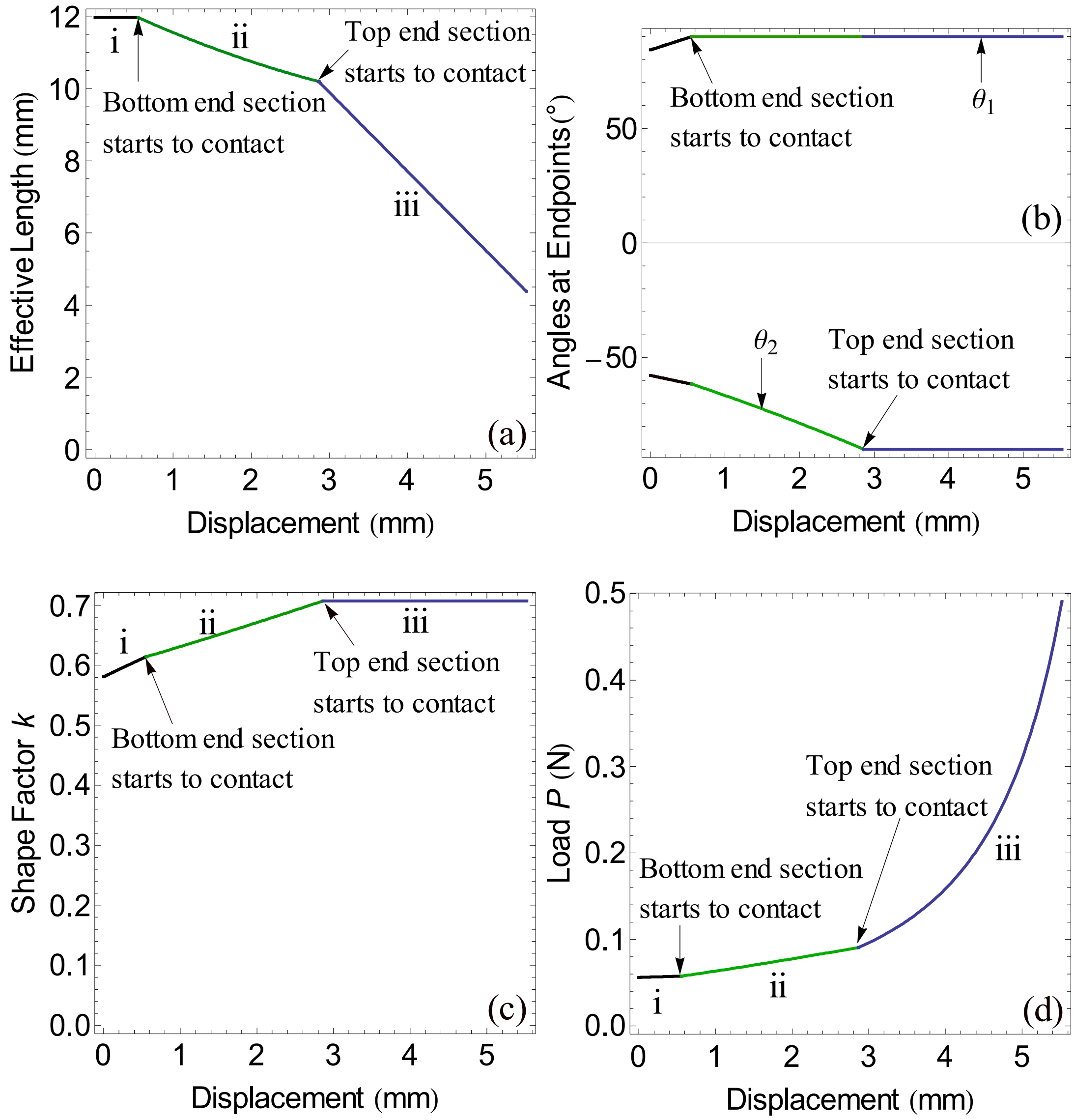

Figure 4.16 Numerical results of the pillar spacer yarn: (a) effective length; (b) angles at endpoints; (c) shape factor k; (d) reaction load P.

During the phase ii, the inclination angle with the x-axis at the endpoint of the top end section θ_2 also increases. The top end section of the pillar spacer yarn starts to contact the top outer layer when this angle rises to $-\pi/2$ with increasing the displacement. This is the beginning point of phase iii. After that, the shape of the non-contact part of the pillar spacer yarn keeps constant, but varies in scale. Its top and bottom end sections are exactly symmetrical in postbuckling and contacting with the outer layers.

The two beginning points of the phase ii and phase iii correspond to the changes of the boundary conditions of the two endpoints. In order to address the mechanical response and geometric deformation process of this spacer yarn under compression, the parameter H (or displacement) at these two critical points should be calculated first. For the first beginning point, the relevant parameter H is calculated by assuming θ_1 being $\pi/2$. For the second beginning point, it is calculated by assuming θ_2 being $-\pi/2$. Then the calculations can be carried out, and the results are presented in Figure 4.16.

In the phase i, the effective length of the pillar spacer yarn in postbuckling keeps constant being 11.965 mm (Figure 4.16(a)), whereas the angles at the two endpoints increases with the displacement (Figure 4.16(b)). The parameter k defined by Equations (4.11 and 4.12), the modulus of the elliptic integral, is a shape factor determining the elastica shape. It varies through this phase, implying the shape change of the spacer yarn (Figure 4.16(c)). Meanwhile, the reaction load P increases slightly (Figure 4.16(d)). In the phase ii, the effective length decreases due to the contact between the bottom end section of the pillar spacer yarn and the bottom outer layer (Figure 4.16(a)), while the angle at the bottom endpoint θ_1 keeps constant being $\pi/2$, but the angle at the top endpoint θ_2 increases (Figure 4.16(b)). The pillar spacer yarn shape changes through this phase, according to the shape factor k (Figure 4.16(c)). At the same time, the reaction load P increases gradually (Figure 4.16(d)). In the final phase, two end sections are both in contact with the outer layers. Its effective length decreases rapidly (Figure 4.16(a)), but the two angles at the two endpoints keep constant (Figure 4.16(b)). In addition, the spacer yarn shape in postbuckling remains and just changes in scale during this phase (Figure 4.16(c)), while the reaction load P rises dramatically (Figure 4.16(d)).

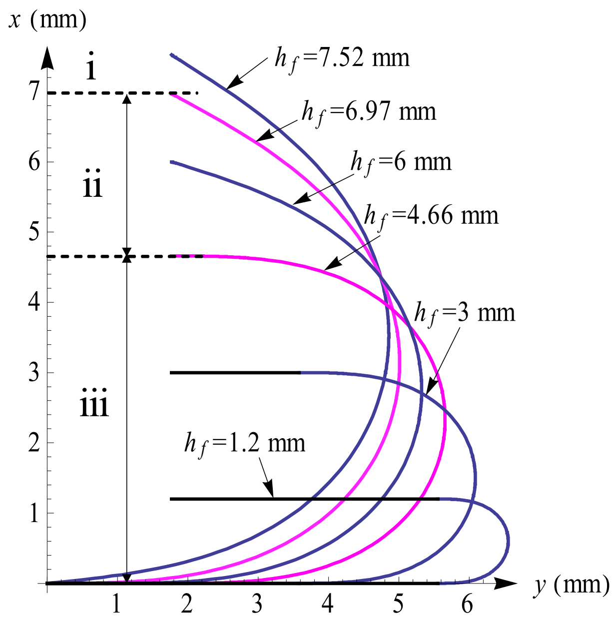

Figure 4.17 Pillar spacer yarn shape in the compression process.

The changes of the pillar spacer yarn shape in the compression process with the selected local coordinate system *xoy* (see Figure 4.15) are shown in Figure 4.17. It gives the side view observed from the coursewise direction, in which the three phases and the corresponding fabric thicknesses (h_f) are annotated, demonstrating the detailed deformation process.

4.6.3.2 Tricot spacer yarn

A local coordinate system *x'o'y'* is selected for the tricot spacer yarn as illustrated in Figure 4.15. Similar to the pillar spacer yarn, the reaction load P is calculated by solving Equations (4.13). The difference in solving the equations between the two types of yarns is that the parameter H for the tricot spacer yarn is not identical to the initial fabric thickness h_f. According to Equation (4.16), the parameter H for this particular yarn is given by

$$H = \sqrt{{h_f}^2 + (2h_w)^2}, \tag{4.23}$$

where the value for h_w is listed in Table 4.2. The same way as that for the pillar spacer yarn was used to obtain the deformation process for the tricot spacer yarn.

Unlike the pillar one, the tricot spacer yarn has a symmetrical initial shape. There are two phases of deformation: (i) free postbuckling, (ii) two end sections in contact with the outer layers. In the phase i, the entire spacer yarn undertakes postbuckling freely (Figure 4.18(a)), while the inclination angles with the *x'*-axis at the two endpoints (θ_1 and θ_2) increase with the displacement (Figure 4.18(b)). No contact is involved, and the shape changes through this phase (Figure 4.18(c)). The reaction load P increases slightly, while the component load P_z contributing to the fabric compression resistance has a lower slope (Figure 4.18(d)). When the spacer yarn is compressed by a further displacement of a specific value, the two end sections start to contact the outer layers simultaneously, being the beginning point of phase ii. The effective length decreases rapidly (Figure 4.18(a)), and the inclination angles at the two endpoints θ_1 and θ_2 are equal to $\pi/2$ and $-\pi/2$, respectively, due to the pinned constraints (Figure 4.18(b)) in this phase. In addition, the spacer yarn shape keeps constant but just changes in scale (Figure 4.18(c)). The reaction load P increases sharply, but the component load P_z contributing to the fabric compression resistance rises gradually (Figure 4.18(d)).

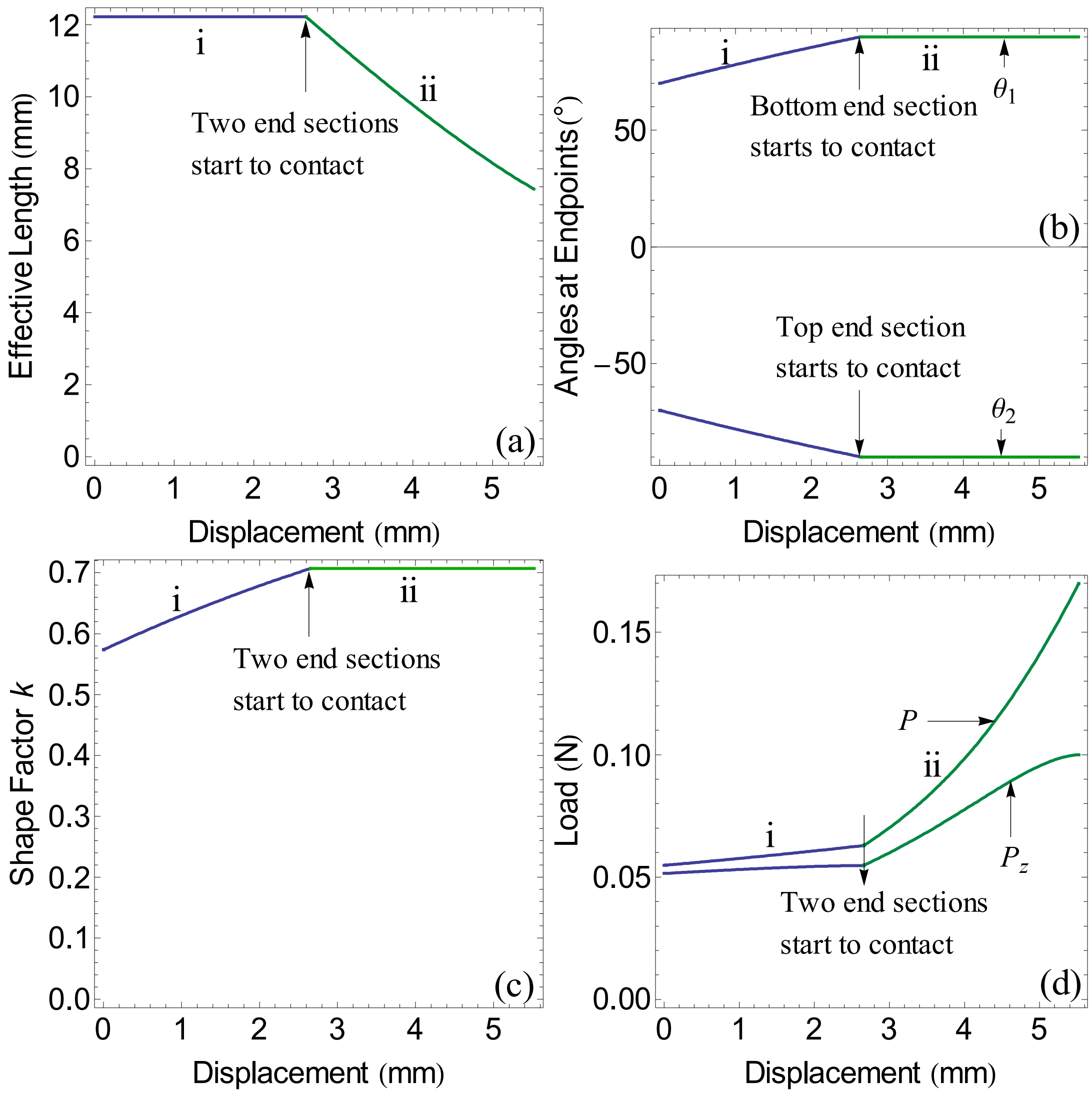

Figure 4.18 Numerical results of the tricot spacer yarn: (a) effective length; (b) angles at endpoints; (c) shape factor *k*; (d) reaction load.

The changes of the tricot spacer yarn shape in the compression process with the selected local coordinate system *x'o'y'* (see Figure 4.15) are shown in Figure 4.19. Note that the tricot spacer yarn shape in the spacer fabric is inclined. To obtain the real view, the local coordinate system *x'o'y'* should be rotated according to Figure 4.15. The two phases and the corresponding fabric thicknesses (h_f) are annotated, demonstrating the detailed deformation process.

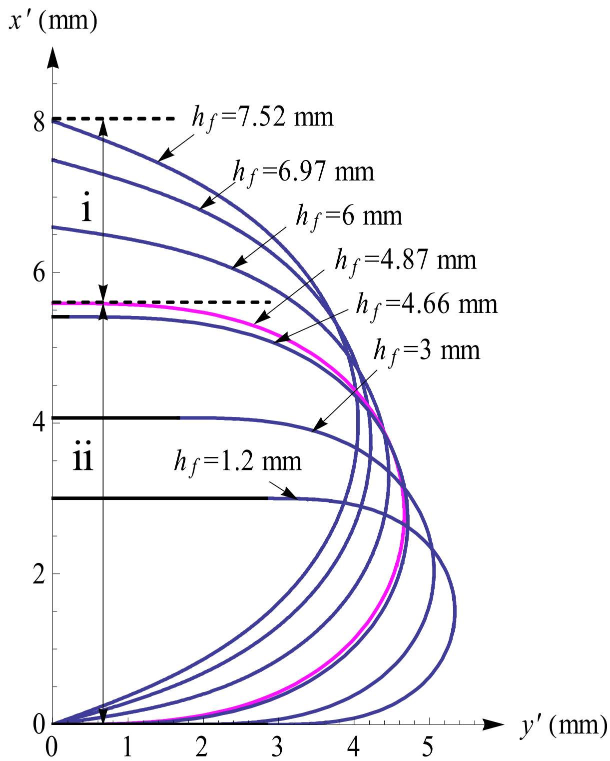

Figure 4.19 Tricot spacer yarn shape in the compression process.

In summary, the compression process predicted with the analytical model includes the spacer yarn postbuckling, and the contacts between the spacer yarns and outer layers. The two types of spacer yarns behave differently in contact with the outer layers. While the pillar spacer yarn first contacts the bottom outer layer and then the top outer layer, the tricot spacer yarn contacts the two outer layers simultaneously. The results show that the pillar spacer yarn contributes more to the fabric compression resistance than the tricot spacer yarn.

4.6.4 Comparison between experimental result and theoretical prediction

This section makes a comparison between the theoretical and experimental load–displacement curves. Each needle loop in the outer layer carries two spacer yarns, i.e., a pillar and a tricot. According to the fabric stitch density 41.15 stitches/cm^2 as listed in Table 3.2, the sample with the size of 100 cm×100 cm used in the experimental tests has 4115 needle loops. Therefore, the theoretical load of the fabric is 4115 times of the summation of the pillar spacer yarn reaction load and the tricot spacer yarn component load along Z-axis.

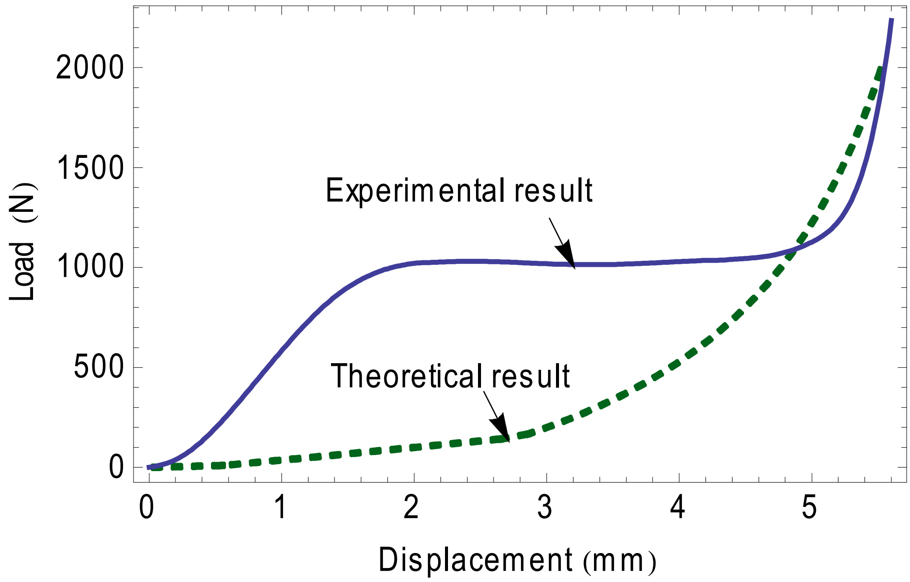

Figure 4.20 A comparison between the experimental and theoretical load–displacement curves.

Figure 4.20 gives a comparison between the theoretical and experimental load–displacement curves. The test result for the sample 2 under the glued test condition presented in Figure 3.3(b) is selected for the comparison. For the theoretical curve, the loads at the initial state of the two spacer yarns were subtracted to eliminate the initial curvature effect. A remarkable deviation between the theoretical and experimental results can be observed in the initial, linearly elastic and plateau stages. In the densification stage, moderate agreement is achieved.

The big differences in the initial, elastic and plateau stages between the theoretical and experimental results might be due to the assumptions made in the analytical model not considering the precise geometric structure of the spacer fabric and the physical properties of the knitted yarns. The differences between the real and theoretical fabrics and how these differences affect the theoretical result are summarised as follows:

- The spacer monofilament diameter, and the outer layer thickness and morphologies were neglected in the calculation, leading to an overestimate of the spacer yarn lengths. Obviously, a longer spacer yarn results in a lower reaction load. Besides, in reality, the two spacer yarn end sections contact the outer fabric layer internal surfaces. The outer layer thickness and morphologies will affect the contact behaviour. More specifically, the spacer yarns contact the internal surfaces at a smaller displacement in the real-life test than that in the predicted process. That is one reason why the theoretical loads are lower than the experimental loads.
- The initial spacer yarn shapes were calculated by assuming that the stitch loops in the top and bottom outer fabric layers are exactly opposite. In fact, the heat setting process and the fabric relaxation led to shear between the two outer layers both along the coursewise and walewise directions. Thus, the pillar spacer yarn is not exactly vertical observed from the walewise direction (i.e., W for this spacer yarn was overestimated). This means that, in the real fabric, the pillar spacer yarn's initial curvature is smaller than that of the calculated initial shape. The overestimate of W for the pillar spacer yarn decreased the prediction of the reaction load.
- The two spacer yarns have initial torsion imperfections. As a result, torsion and shear of them, which were not considered in the calculation, will occur in the compression of the fabric.
- The contacts and friction among spacer yarns were neglected. These contacts

could effectively affect the boundary conditions of the spacer yarns, and thus the experimental result differs greatly from the theoretical one.

- The intricate structure of the outer layers was not considered, possibly neglecting more complex constraints on the spacer yarns. This model only takes account of the simply support pinned constraint; out-of-plane deformation is not allowed for the spacer yarns. In reality, the constraints imposed on the spacer yarns by the outer layers can change during the compression. The assumption, which cannot describe the interactions between the outer layers and spacer yarns as in real-life specimens, can affect the theoretical result.

4.7 Conclusions

In this chapter, the analytical model has been established with planar elastica theory. The structural parameters affecting the compression properties of spacer fabrics have been identified with the developed model, and the parametric study has been conducted to examine the effects of the identified parameters on reaction load in nondimensional. Finally, the experimental result of the spacer fabric S1 presented in Chapter 3 has been used to validate the analytical model. According to the obtained results and analyses, the following conclusions can be drawn.

- The structural parameters affecting the compression properties of warp-knitted spacer fabrics include spacer yarn inclination, spacer yarn fineness, course density and fabric thickness. The spacer fabric with a smaller spacer yarn inclination, higher spacer yarn diameter, higher course density of the outer layers and lower thickness has higher compression resistance.
- The compression process includes the spacer yarn postbuckling, and the

contacts between the spacer yarns and outer layers. The two types of spacer yarns behave differently in contact with the outer layers. While the pillar spacer yarn first contacts the bottom outer layer and then the top outer layer, the tricot spacer yarn contacts the two outer layers simultaneously. The results show that the pillar spacer yarn contributes more to the fabric compression resistance than the tricot spacer yarn.

- The load–displacement relationship predicted by the analytical model is not in satisfactory agreement with the experiment. The main reasons for the failure to accurately predict the load–displacement relationship include the imprecise initial geometric model, the neglect of the interactions among spacer yarns and the neglect of the interactions between the spacer yarns and the outer layers.

Although the analytical model does not give an accurate prediction on the load–displacement relationship of the spacer fabric, it is still helpful in understanding the compression process and the deformation mechanism. To achieve better agreement between the theoretical and experimental load–displacement results and to fully reveal the deformation mechanism, the next chapter will use a precise geometric model and fully consider the interactions among spacer yarns as well as the interactions between the spacer yarns and the outer layers by finite element modelling.

CHAPTER 5 FINITE ELEMENT MODELLING OF WARP-KNITTED SPACER FABRICS

5.1 Introduction

In the previous chapter, the analytical model was developed to predict the compression behaviour of warp-knitted spacer fabrics. The analytical model provides insights into how certain structural parameters will affect the compression behaviour, such as spacer yarn inclination and fineness, course density and fabric thickness. However, the load–displacement relationship predicted with the analytical model is not in satisfactory agreement with the experiment. The reason for the failure to accurately predict the load–displacement relationship is thought to be the assumptions of linearly elastic, planar and no torsion for the spacer yarns made in the model affecting the results. The neglect of the spacer yarn diameter, the outer layer internal surface structures, and the contacts among spacer yarns also contributes to the inaccurate prediction. In fact, the compression deformations of the spacer yarns with initially stress-free imperfections within the spacer fabric are highly nonlinear with complicated contacts rather than simple postbuckling.

This chapter presents a further theoretical study using the finite element (FE) method. With the use of Micro X-ray computed tomography (μCT), a precise geometric model of the typical fabric S1 studied in Chapter 4 was obtained. Eight FE models were built, by fully considering the interactions among spacer yarns as well as the interactions between the spacer yarns and the outer layers. The developed FE models are used to reveal the precise compression mechanism of the spacer fabric and also to address a more accurate prediction on the compression load–displacement relationship.

The organization of this chapter is as follows. Section 5.2 describes in detail the proposed geometric unit cell for the spacer fabric S1. Then eight FE models built with the geometric unit cell, by selecting proper finite elements, applying loading and boundary conditions, and assigning the nonlinear properties of yarns, are presented in Section 5.3. In Section 5.4 modelling of the fabric in compression is discussed by focusing on the contributions of constraints on spacer monofilaments, geometric profile of outer fabric layers and test boundary conditions. Finally, one out of the eight FE models, the result of which fits well the experimental result, is extended to represent spacer fabrics with different structural features, and the significance of different parameters on fabric compression responses is discussed in Section 5.5.

5.2 Geometric modelling

The spacer fabric S1 is selected for the FE simulations because its typical structure makes the fabric very representative of warp-knitted spacer fabrics. To fully consider the structural features of the spacer fabric, a precise geometric model is needed.

5.2.1 μCT scanning of the spacer fabric

A μCT system was used to scan the fabric, and the obtained data were used to construct a 3D geometric model. The size of the specimen to be scanned was 20 mm × 20 mm, and the scanning was conducted along its thickness using a Scanco/VivaCT 40 micro-CT system (SCANCO Medical AG, Fabrikweg 2, CH-

8306 Brüttisellen, Switzerland) as shown in Figure 5.1, with the following scanning conditions: spot size 5 μm, 50–70 kVp and 160 μA. In addition, a specified jig was used to fix the fabric during the scan also shown in Figure 5.1.

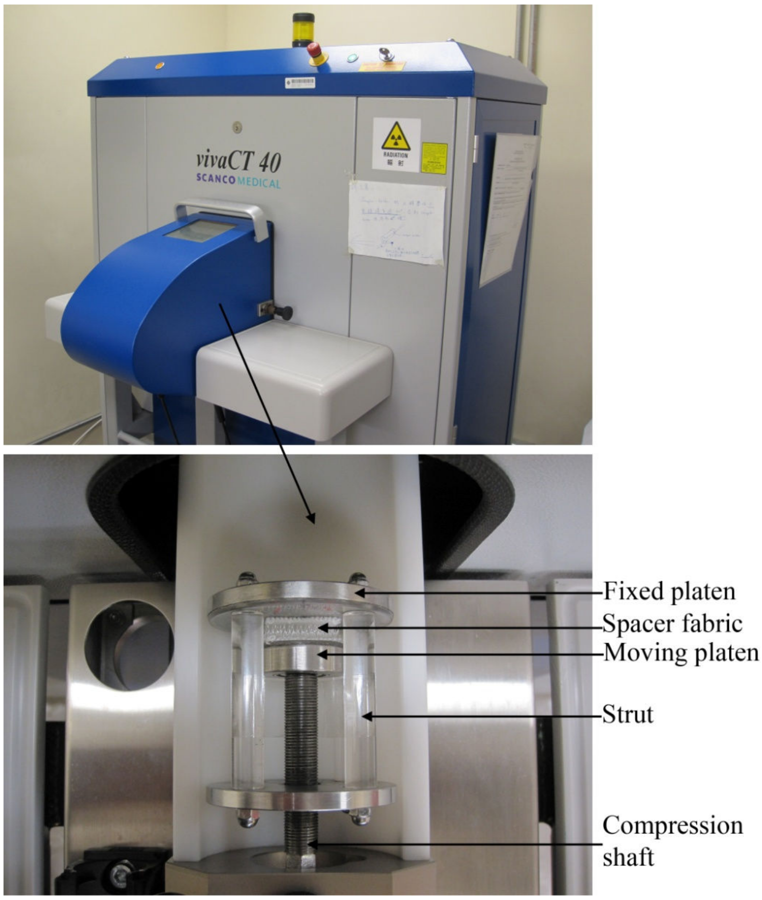

Figure 5.1 Scanco/VivaCT 40 micro-CT system and the specified jig.

Figure 5.2 presents a μCT reconstruction of the fabric at the initially stress-free state, showing the precisely reconstructed spacer monofilaments; however, the outer layers are not well reconstructed due to the resolution limitation of the μCT system. Obviously, the 3D reconstructed geometric model is hard to mesh and thus not suitable for a FE analysis directly. On the other hand, the spacer monofilaments are the main load-carrier of the spacer fabric under compression, whereas their outer layers do not deform significantly, playing the role of boundary layers. Therefore, the outer layers can be simplified as two isotropic flat plates to address a reasonable approximation. In this way, the geometric model can be divided into three parts, i.e., a spacer layer and two outer layers. Since the fabric structure is periodic as discussed in Chapter 4, a representative unit cell, i.e., the smallest element including all the geometric features of the entire fabric, is preferable to represent the fabric to reduce the computational cost. In the following sections, the unit cell's spacer layer is identified first, and the investigation of the unit cell's outer layer will be presented subsequently.

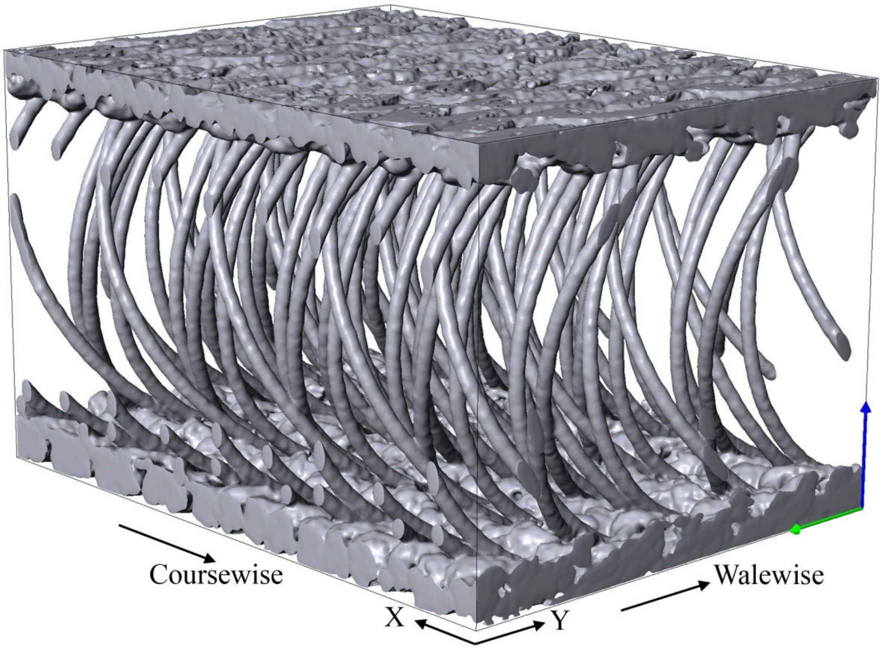

Figure 5.2 A μCT reconstruction of the spacer fabric S1 at the initially stress-free state.

5.2.2 Unit cell's spacer layer

This section aims to build the geometric model of the unit cell's spacer layer by means of image processing techniques using the μCT slices. To build the unit cell's spacer layer, there is a need to differentiate the spacer layer and the two outer layers because the spacer monofilaments are knitted into the outer layers (Figure 5.2). For this purpose, two split layers should be selected to divide the fabric into three parts through the thickness.

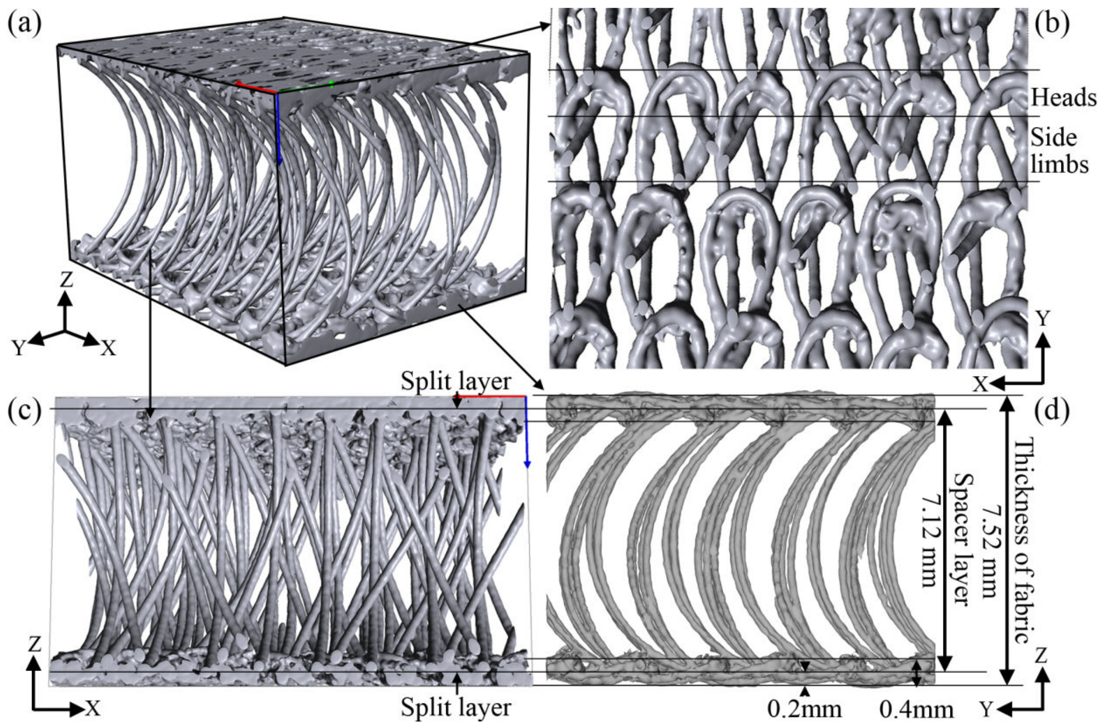

Figure 5.3 μCT reconstruction of the spacer fabric S1 from different viewpoints: (a) 3D profile; (b) outer layer; (c) side view from walewise; (d) side view from coursewise.

To include the geometric details of the spacer monofilaments as many as possible for obtaining more accurate simulations, the connection between the spacer monofilaments and the outer layers is analysed first. Figure 5.3(a) presents the 3D μCT reconstruction observed from another viewpoint with respect to that presented in Figure 5.2, while one of its outer layers is shown in Figure 5.3(b) by filtering out the multifilaments. Figure 5.3(b) shows that the spacer monofilaments are entangled by the monofilament stitches within the outer layer, having an uneven outer layer internal surface. Its thickness ranges from 0.2 mm for the part consisting of only one monofilament (side limbs of the monofilament needle loops) to 0.4 mm for the part consisting of two monofilaments (heads of the monofilament needle loops) as illustrated in Figure 5.3(b)–(d). The spacer layer for the FE simulations is defined as illustrated in Figure 5.3(d). Along the fabric thickness direction, two split layers are defined to exclude the two parts only consisting of one monofilament to build the spacer layer, selecting from 0.2 to 7.32 mm along the fabric thickness.

The selected spacer monofilaments can be digitalized by image processing. There are 358 slices for the whole scanning, and one slice represents 0.021 mm through the specimen thickness. Therefore, the total thickness from scanning is 7.518 mm close to 7.52 mm measured with a digital thickness tester (SDL Atlas M034e). According to the two split layers, the first 9 slices and the last 10 slices from the scanning were excluded in the image processing. Figure 5.4 presents one of the used slices, showing the cross sections of spacer monofilaments. The pixel size in the image is also 0.021 mm. The centroids of the spots provide the information on the dimensions, shapes, and relative positions of respective spacer monofilaments. Since the cross sections of spacer monofilaments from μCT scanning are not exactly circular, and there are too many slices to handle manually, an algorithm was developed with image processing techniques and implemented with the software Mathematica®. As an example, the slice shown in Figure 5.4(a) is used to demonstrate the image processing, and resultant images after main procedures are presented in Figure 5.4(b)–(c). Firstly, the original image was trimmed to eliminate edge effects. Then the trimmed image (Figure 5.4(a)) was converted into the binary image (Figure 5.4(b)) with a proper threshold. After that, white components within a given range of areas were selected (Figure 5.4(c)), and their centroids were calculated (Figure 5.4(d)).

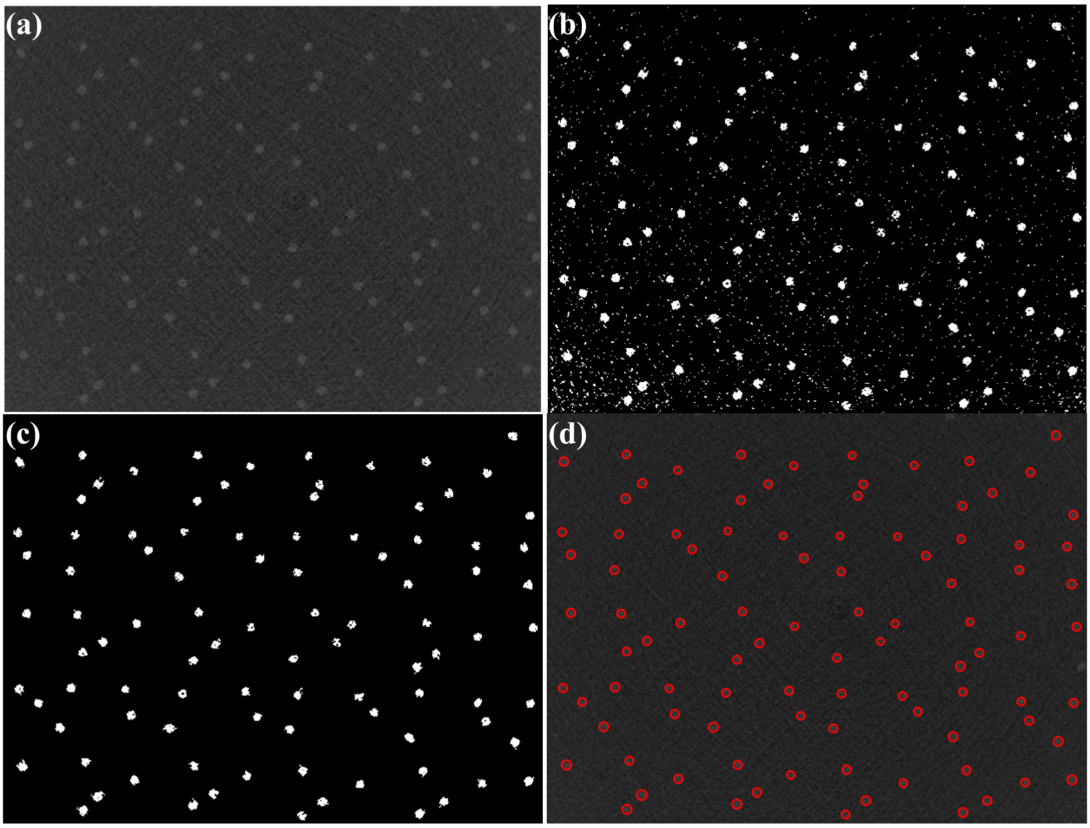

Figure 5.4 Image processing of a CT scanning slice.

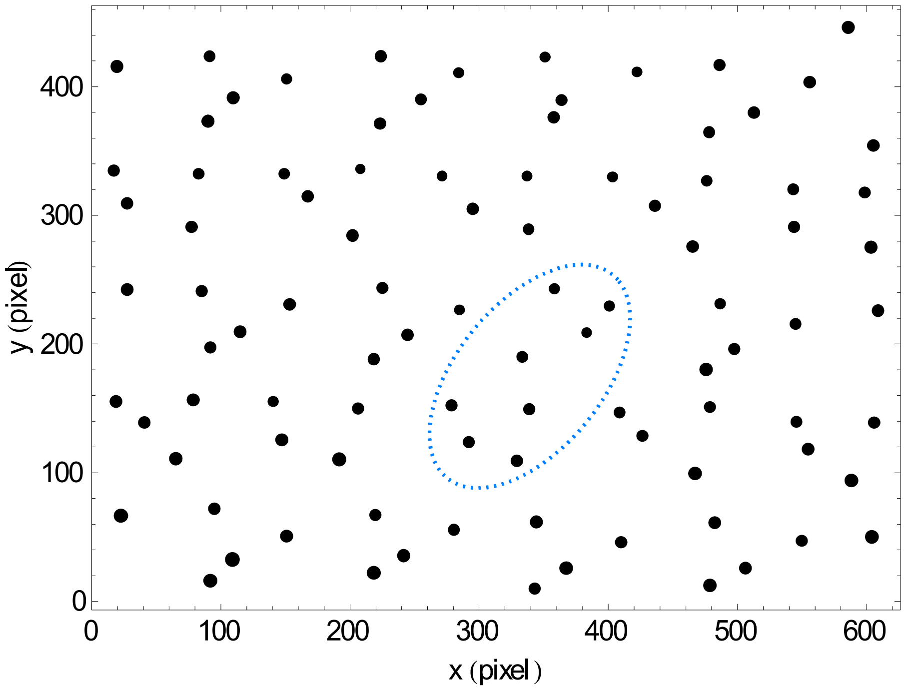

Figure 5.5 Reconstructed centroids of the cross sections of spacer monofilaments.

Figure 5.5 shows the reconstructed centroids of the cross sections of spacer monofilaments, in which a unit cell consisting of eight spacer monofilaments is circled. Since the pixel size of this image is known, the exact coordinates of the centroids of the circled spacer monofilaments can be calculated. The same method was applied to the other slices, and the 3D coordinates for the selected eight spacer monofilaments were addressed accordingly.

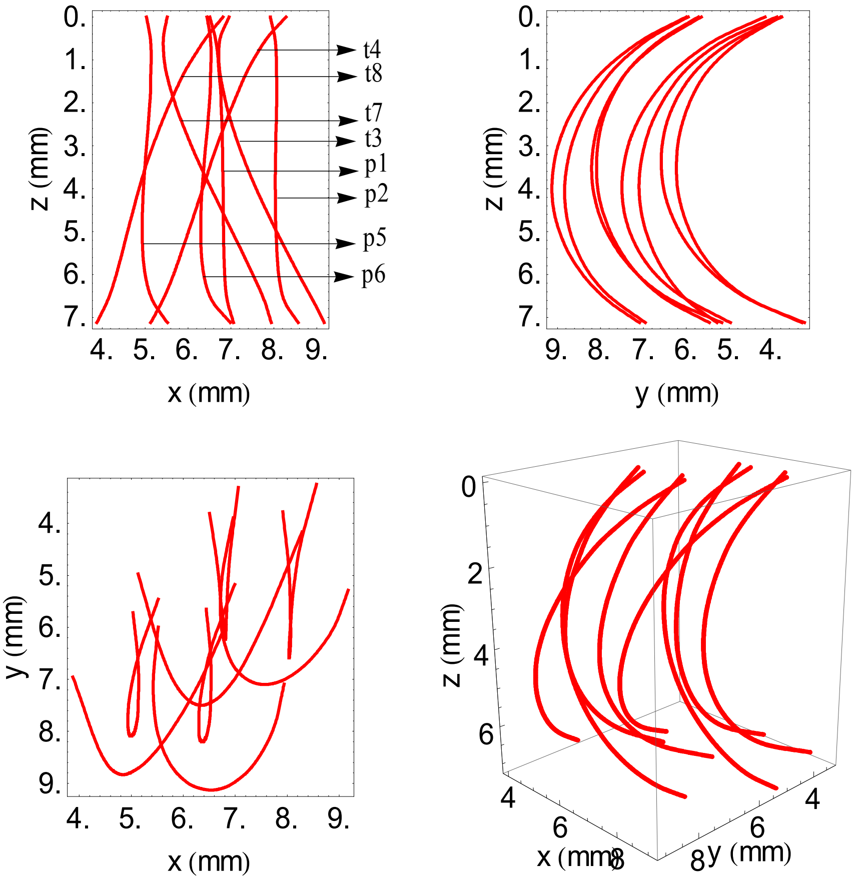

Figure 5.6 List point plots of the eight spacer monofilaments from different viewpoints.

Figure 5.6 shows the list point plots using the obtained coordinates for the eight spacer monofilaments from different viewpoints. As discussed in Chapter 3 and Chapter 4, there are two types of spacer monofilaments in the spacer fabric S1, i.e., tricot (inclined observed from walewise) and pillar (vertical observed from walewise). For the sake of convenience, the four pillar spacer monofilaments are denoted by p1, p2, p5 and p6, while the four tricot spacer monofilaments are denoted by t3, t4, t7 and t8. It can be seen that both the tricot and pillar spacer monofilaments are different from one another. Moreover, obvious torsion can be observed from the pillar spacer monofilaments. This is quite different from the calculated initial shapes with the analytical model presented in Chapter 4, implying a modified fabric structure after the process of removal from the machine and heat setting. Therefore, using the manufacturing structural parameters is unable to predict the fabric structure with high accuracy. This also explains that the analytical model did not accurately predict the compression behaviour of the spacer fabric.

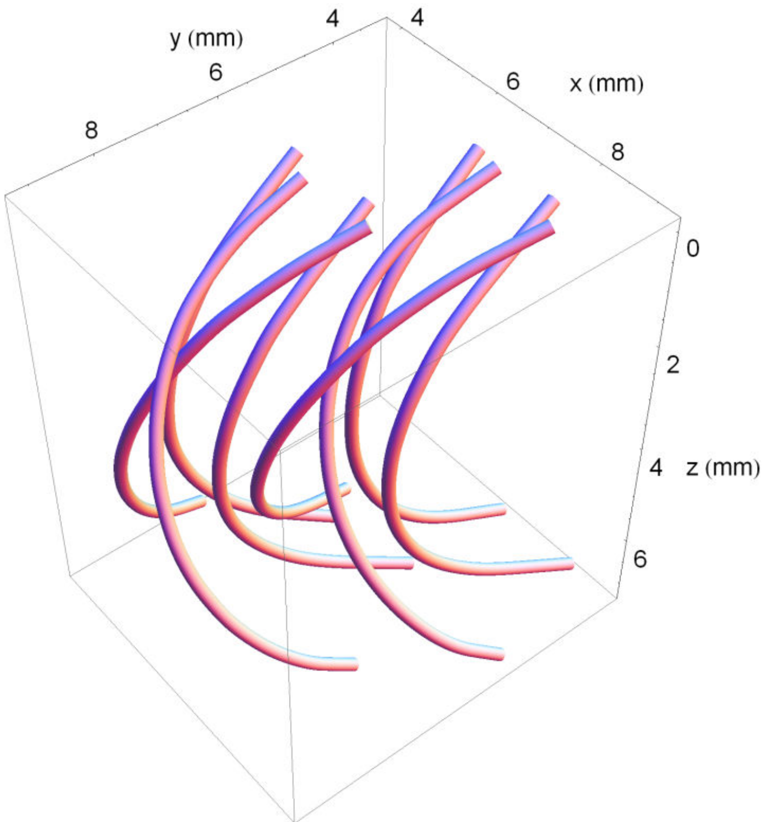

Figure 5.7 3D visualization of the unit cell’s spacer layer.

Finally, the precise unit cell's spacer layer is obtained, and its 3D visualization is shown in Figure 5.7, by adding the spacer monofilament diameter (0.2 mm). From this 3D visualization, the geometric feature of the spacer layer can be easily observed. The unit cell's spacer layer is connected to the two outer layers; their connections and interactions determine the constraints on the spacer monofilaments and affect the fabric compression properties. This will be discussed in the next section.

5.2.3 Unit cell's outer layer

It is of importance to know the detailed structures of the outer layers and how they connect to the spacer layer. With this information, the unit cell's outer layer can be built accordingly. This section analyses in detail the binding structures of the outer layers, determining the constraints on the spacer monofilaments, and the morphologies of the outer layer internal surfaces, affecting the contacts between the spacer monofilaments and the outer layers.

The binding structures of the outer layers are first analysed. Figure 5.8 shows the morphologies of the outer layers. To differentiate the two outer layers, the one connected to the ends of spacer monofilaments at z=0 (see Figure 5.7) is denoted as the top layer, while the other one is denoted as the bottom layer. The outer and internal surfaces of the top layer are shown in Figure 5.8(a) and (c), respectively, and those of the bottom layer are shown in Figure 5.8(b) and (d), respectively. The images were obtained with a HITACHI TM3000 Tabletop Scanning Electron Microscope (SEM). To capture the internal surfaces, the spacer monofilaments were cut transversely. It is found that the spacer monofilaments are knitted into the outer layers by forming needle loops simultaneously with multifilaments (Figure 5.8(a) and (b)). Ideally, the monofilament needle loops within the outer layers are invisible on the outer surfaces and partially visible on the inner surfaces, due to the overlap between multifilament and monofilament stitches. In reality, the monofilament needle loops are invisible on the internal surfaces; however, they are not completely covered by the multifilament stitches on the outer surfaces, especially in the top layer (Figure 5.8(a)). This is due to the slippage and uneven tension of yarns during the manufacturing process.

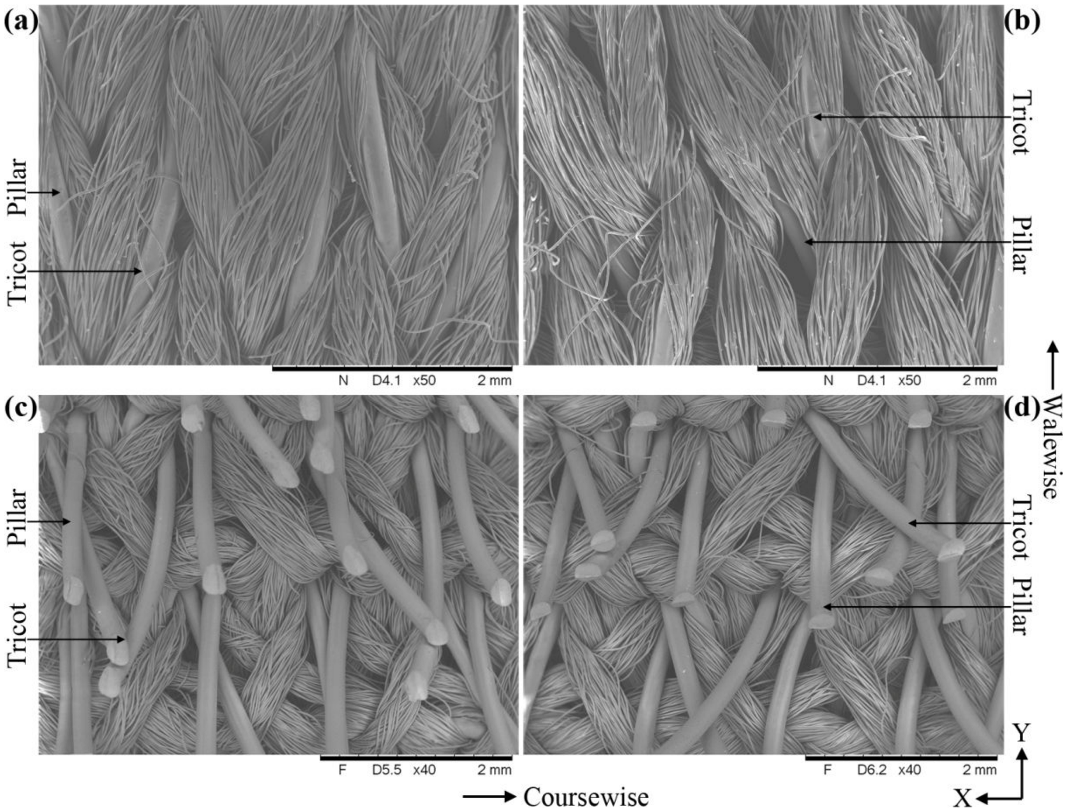

Figure 5.8 Structure of the spacer outer fabric layers: (a) outer surface of top layer; (b) outer surface of bottom layer; (c) internal surface of top layer; (d) internal surface of bottom layer.

The monofilament needle loops are partially visible from the outer surfaces and completely invisible from the internal surfaces, giving rise to the challenge in evaluating their exact geometric structures. Thanks to the μCT technique, Figure 5.9

shows the reconstruction of the monofilament stitches within the outer layers by filtering out the multifilament stitches. It is obvious that each wale is separate from neighbouring wales, while each needle loop within the same wale is secured by the loop of the previous course. The separate wales in the two outer layers are joined together through the spacer monofilaments, and they are also tied together within the same outer layer by the multifilament stitches. In such a way, the multifilament stitches, the monofilament stitches and the spacer monofilaments constitute the spacer fabric. Obviously, the outer layers, consisting of voids and two components, are complex, discontinuous and uneven.

To simulate the compression behaviour of the entire fabric, the unit cell's outer layer should be capable of demonstrating its own responses and the interactions with the spacer layer. The contacts, friction and slide among monofilaments and multifilaments occur when an external compression force is applied to the fabric. The postbuckling behaviour of the spacer monofilaments and the contacts between the spacer monofilaments and the outer layers are mainly determined by the constraints provided by the outer layers to the spacer monofilaments. There are two approaches to model the constraints. One approach is to include the real geometric structure consisting of all the multifilament and monofilament stitches as well as the spacer monofilaments in FE models, leading to a high computational cost and making the FE models too complex to converge. The other approach is much more focused on selecting suitable degrees of freedom (DOFs) for the spacer monofilament endpoints to achieve an equivalent effect of the constraints provided by the outer layers. The second approach is more practical, and thus it was adopted in this study.

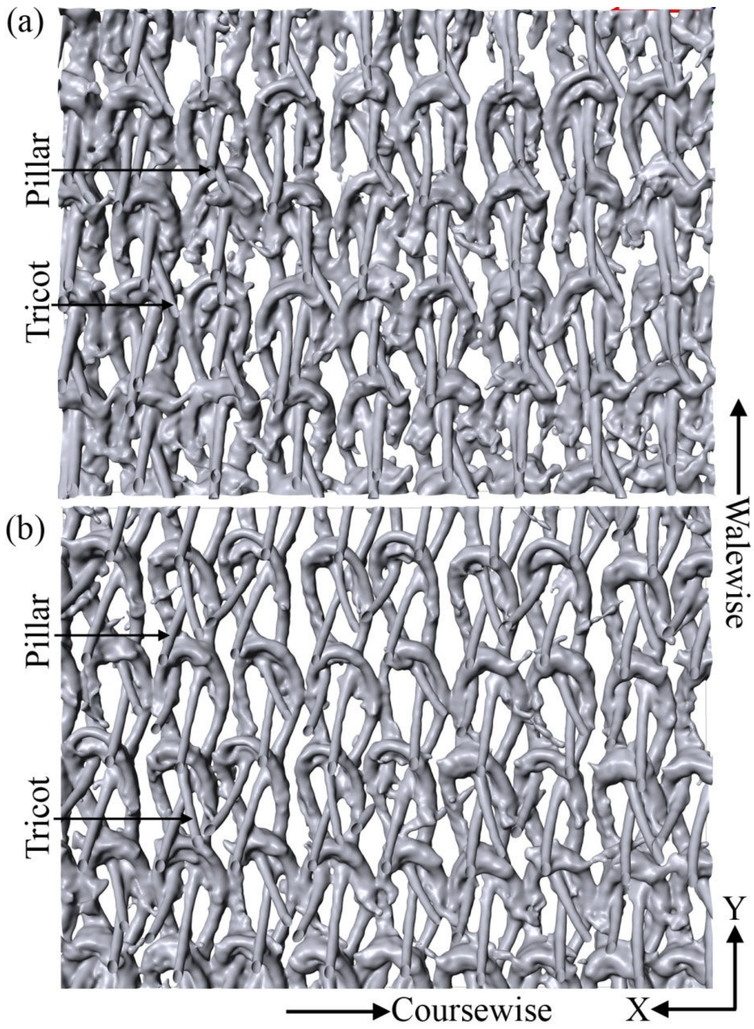

Figure 5.9 μCT reconstruction of monofilament stitches within outer layers: (a) top layer; (b) bottom layer.

Figure 5.8 and Figure 5.9 demonstrate that the constraints imposed on the spacer monofilaments are complicated, and therefore the DOFs at the spacer monofilament endpoints are difficult to determine. From a mechanics point of view, there are no translational DOFs along the X- and Y-axes (UX and UY) at the endpoints when the spacer monofilaments are under compression along the Z-axis (UZ); however, their rotational DOFs exist. The rotational DOF about the X-axis (ROTX) certainly exists due to the relatively low bending stiffness of the spacer monofilaments. Their rotational DOFs about the Y- and Z-axes (ROTY and ROTZ) are determined by the outer layer structures, which bind the spacer monofilaments.

To apply appropriate DOFs at the respective spacer monofilament endpoints, the details of how the multifilament stitches bind the spacer monofilaments should be analysed. Because there are too many underlaps of the multifilament stitches within the internal surfaces, using direct observation is not easy to find out the precise binding structures. For this reason, the multifilament stitches binding the spacer monofilaments in accordance with the chain notations (Table 3.1), the μCT reconstruction (Figure 5.9), and the SEM pictures (Figure 5.8) are schematically illustrated in Figure 5.10, to help in selecting suitable DOFs for the spacer monofilament endpoints. The binding structure of the top outer layer is shown in Figure 5.10(a), which is a schematic of Figure 5.8(c). It can be found that while the pillar spacer yarns are tightly bound by the underlaps, the tricot spacer yarns are located between the two neighbouring side limbs of the needle loops. Hence, the rotational constraints on the tricot spacer yarns are weaker than those of the pillar spacer yarns. Figure 5.10(b), a schematic of Figure 5.8(d), shows the binding structure of the bottom outer layer. It can be observed that while the pillar spacer yarns are tightly bound by the two side limbs of the needle loops, the constraints on the tricot yarns are similar to those in the top layer. Therefore, the constraints on the pillar spacer yarns in the bottom layer are also stronger than those of the tricot spacer yarns. It can be argued that the pillar spacer yarns have lower rotational DOFs about Y- and Z-axes than the tricot spacer yarns.

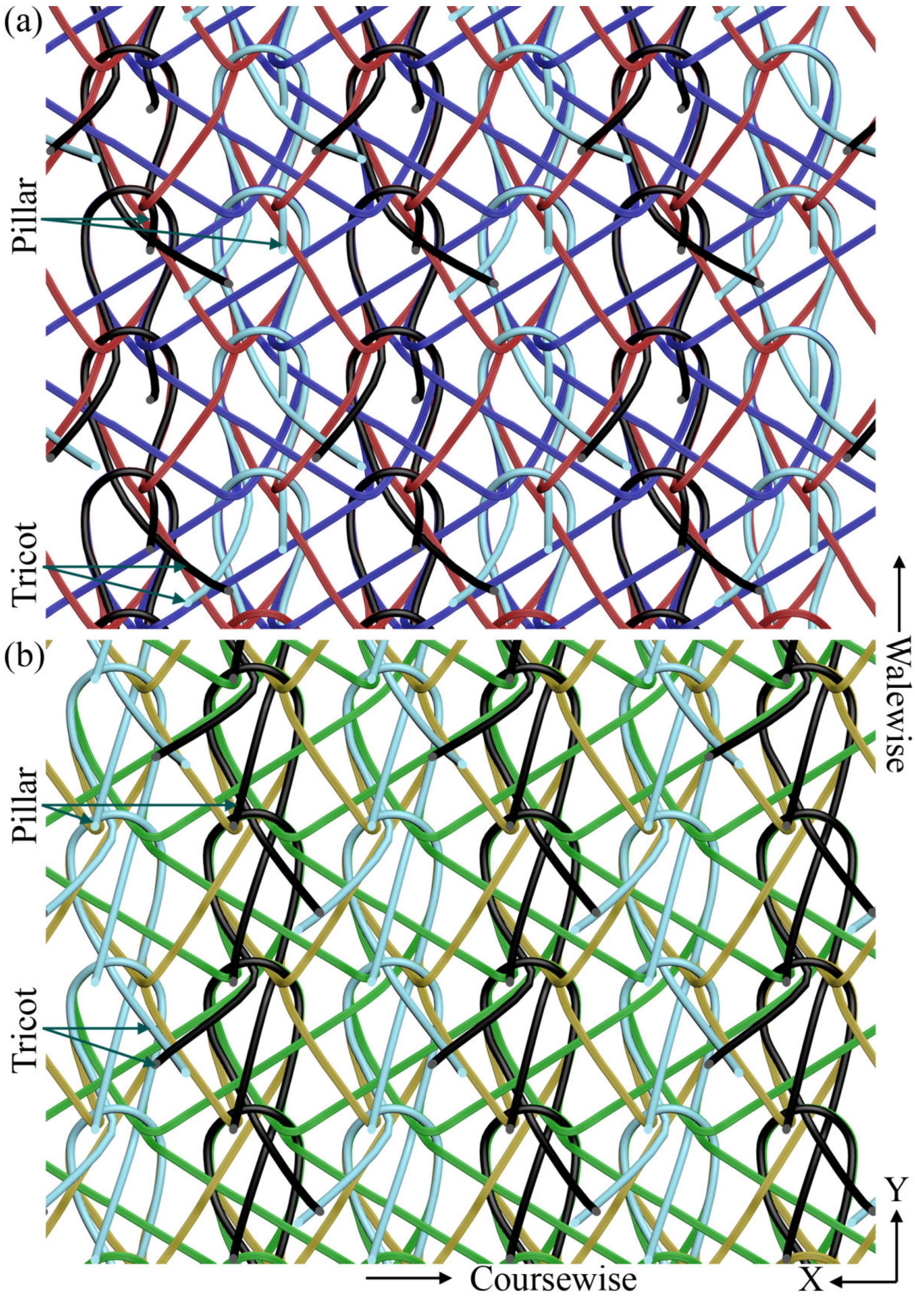

Figure 5.10 Schematic binding structures of the outer layers: (a) top internal surface; (b) bottom internal surface.

Although the above analysis on the binding structures of the outer layers provides some insights into the constraints on the spacer monofilaments, it is still difficult to define the precise DOFs at the endpoints of the eight spacer monofilaments. In this connection, different combinations of DOFs at the spacer monofilament endpoints are used in modelling, to investigate the effects of the DOFs on the compression properties of the spacer fabric.

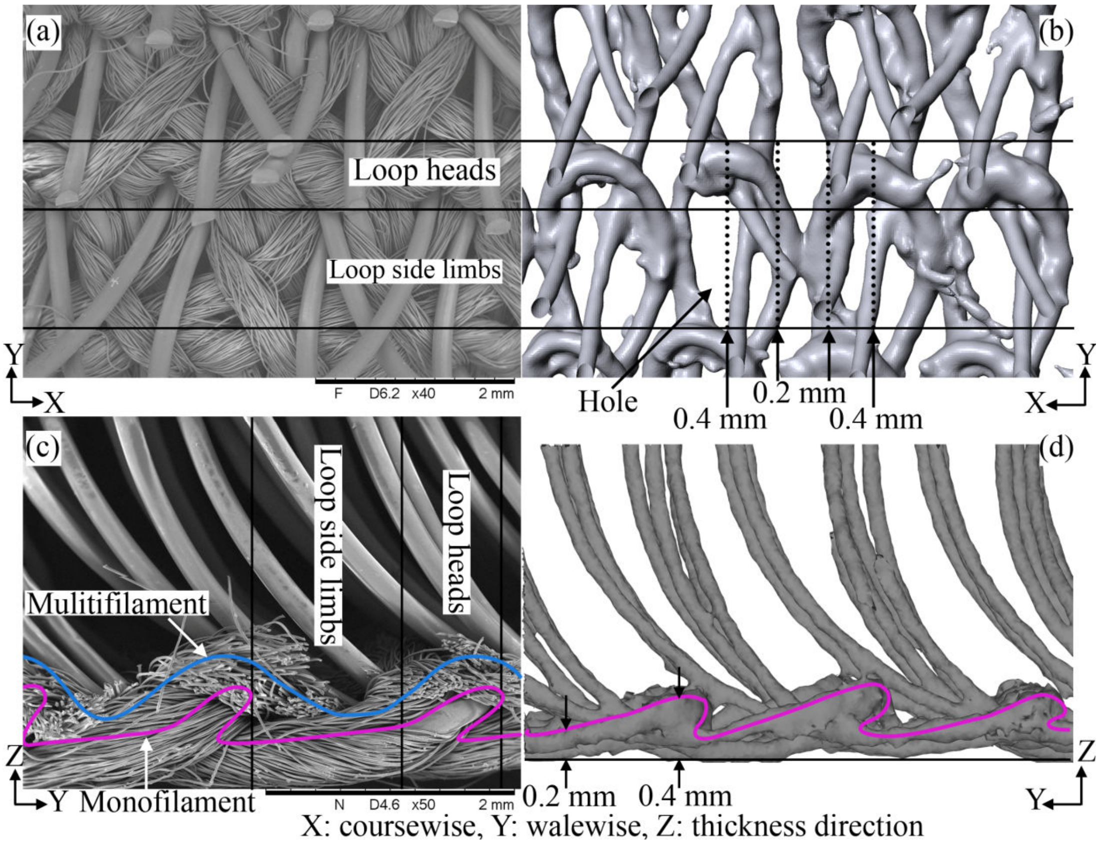

Figure 5.11 The morphologies of the outer layer internal surface.

In addition to the rotational DOFs, depending on the binding structures, which determine the deformation behaviour of the spacer monofilaments, the uneven outer layer internal surfaces can affect the contacts between the outer layers and the spacer monofilaments, thereby affecting the compression properties of the spacer fabric. For illustrative purpose, Figure 5.11 shows the bottom outer layer internal surface from different viewpoints. As shown in Figure 5.11(a) and (b), the monofilament needle loops are bound by the multifilament underlaps. Two zones are defined, including the zone of loop heads and the zone of loop side limbs. In the zone of the monofilament needle loop heads, through the fabric thickness direction, there are two monofilaments (a monofilament needle loop head on the top of two side limbs) and six multifilaments (two heads, two side limbs and two underlaps through the thickness). The profile formed by the multifilaments looks like a sinusoidal wave (Figure 5.11(c)) along the walewise direction, while the profile formed by the monofilaments is of a nonlinear wave shape (Figure 5.11(d)). Since the multifilaments can easily deform under compression, they are not considered in the FE simulations. Then the outer layer thickness varies from 0.2 mm (a side limb) to 0.4 mm (the peak of a loop head) along the walewise direction as illustrated in Figure 5.11(d). The profiles of the two zones along the coursewise direction are different. In the zone of loop heads, the thickness variation is similar to that along the walewise direction. It varies from 0.4 mm at the peak of a loop head to 0.2 mm for a side limb. In contrast, the thickness variation in the zone of side limbs is simple, varying from 0 mm (the hole of a loop) to 0.2 mm (a side limb). The complex outer layer internal surfaces result in complicated contact behaviour between the spacer monofilaments and the outer layers. To take into account the wavy internal surfaces in developing the unit cell's outer layer, how they affect the contact behaviour should be analysed.

To analyse the contact behaviour, a pillar spacer monofilament is selected as an example for illustrating. Figure 5.12(a) schematically illustrates its initial geometric feature, constructed in strict accordance with the μCT reconstruction. To facilitate the analysis, the spacer monofilament is divided into three parts: two end sections and a middle section. Based on the geometric feature and the experimental observation presented in Chapter 3, the compression process can be speculated as follows. At the beginning, the bottom end section will contact the bottom outer layer quickly, while the top end section will undertake postbuckling freely without in contact with the top outer layer (Figure 5.12(b)). When the fabric is compressed by a certain displacement increment, the top end section starts to contact the top outer layer (Figure 5.12(c)). With the increase in the external displacement, the contact between the spacer monofilament middle section and the loop head of the bottom outer layer will occur (Figure 5.12(d)). Subsequently, the spacer monofilament middle section will contact the loop head of the top outer layer (Figure 5.12(e)).

There are two approaches to take these interactions into account in the FE simulations. One straightforward but cost-prohibitive approach is to include all the geometric features of the multifilament and monofilament stitches. Alternatively, not deforming significantly under compression, the outer layers can be simplified as wavy homogeneous plates as schematically illustrated in Figure 5.12. To reduce the computational cost, instead of modelling the wavy shape geometrically, a cost-effective strategy to include the wavy effect on the contact behaviour physically is employed, by selectively using contact elements, while the outer layers are modelled with two flat plates of constant thickness. This strategy is also depicted in Figure 5.12, in which the dashed parts of the spacer monofilament are able to penetrate the inner surfaces of the plates (thin dotted line), whereas the solid part is unable to penetrate the plates. In this way, the wavy contact surfaces can be simulated physically rather than geometrically. The thickness of the flat plates should equal the thickness at the loop heads of the outer layers. However, as illustrated in Figure

5.11(b), in the zone of loop heads, the thickness varies from 0.4 mm (at the peak of a loop head) to 0.2 mm (for a side limb). It is hard to determine the point of the monofilament needle loop head that will be in contact with the spacer monofilament during compression. Therefore, the thickness of the two flat plates should be adjusted in modelling to find out an appropriate value.

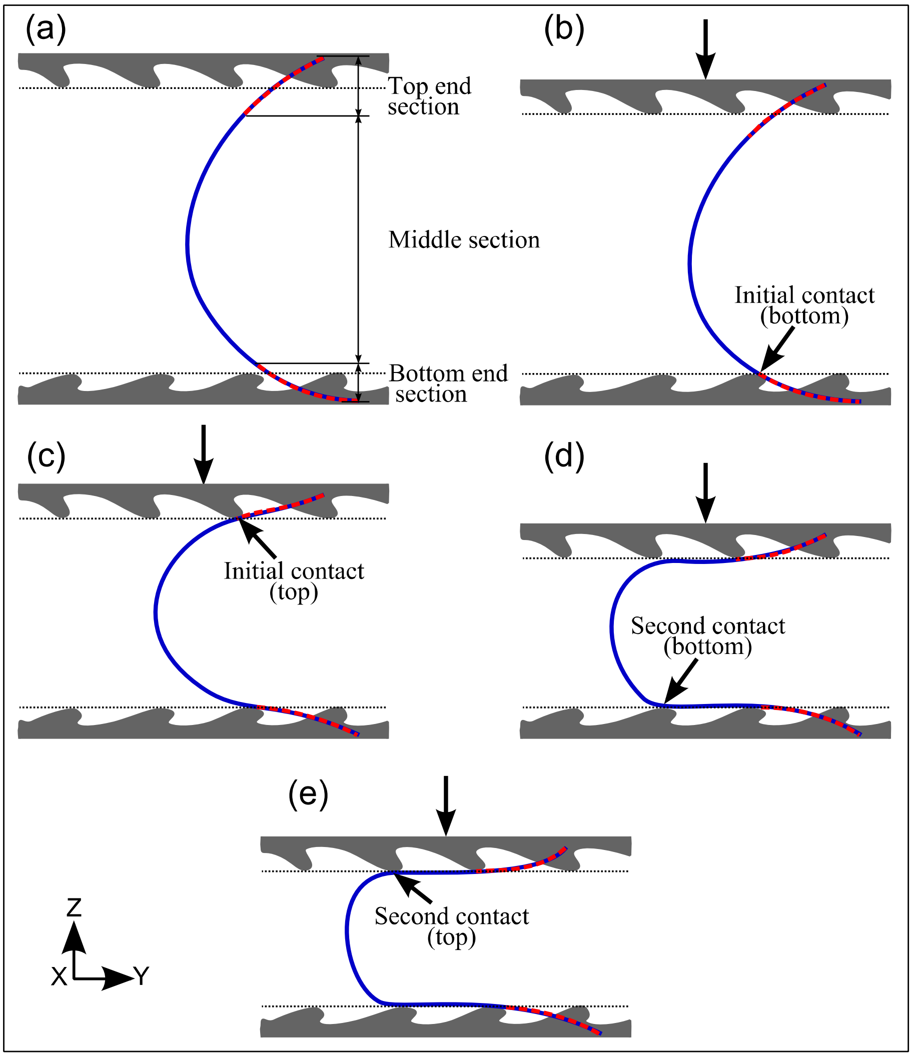

Figure 5.12 Speculative mechanism of the contact between the pillar spacer monofilament and the internal surfaces of outer layers.

In summary, this section provides the detailed information on the entanglements between the spacer monofilaments and multifilament stitches, and the analyses of the effect of the wavy outer layer internal surfaces on the contact behaviour. Unlike the unit cell's spacer layer being easy to determine, the precise unit cell's outer layer is hard to obtain. The analyses suggest that numerical methods should be used to determine the DOFs of the respective spacer monofilaments, and the wavy outer layers can be simulated with flat plates by selectively using contact elements, whereas the flat plate thickness should be numerically determined. These approaches will be implemented in Section 5.3.

5.3 FE implementation

5.3.1 Material model

The unit cell should be assigned with specific materials for FE implementation. Thus, the material properties, including Young's modulus, stress–strain relationship and friction coefficient (μ), for each part of the unit cell should be measured.

The spacer fabric S1 comprises the polyester multifilament (300D/96F) and monofilament (0.2 mm in diameter). The Young's modulus of the multifilament is much lower than that of the monofilament, which means that the contacts between the spacer monofilaments and the fluffy multifilament stitches do not affect the fabric compression properties significantly. By contrast, the indirect contact between the spacer monofilaments and monofilament stitches through the deformed multifilament stitches plays the key role in affecting the fabric compression behaviour. Besides, the in-plane deformation of the outer layers is small; hence, they can be considered to be linearly elastic, and the material properties of the polyester monofilament can be used to represent those of the outer layers. In this connection, only the material properties of the polyester monofilament should be measured.

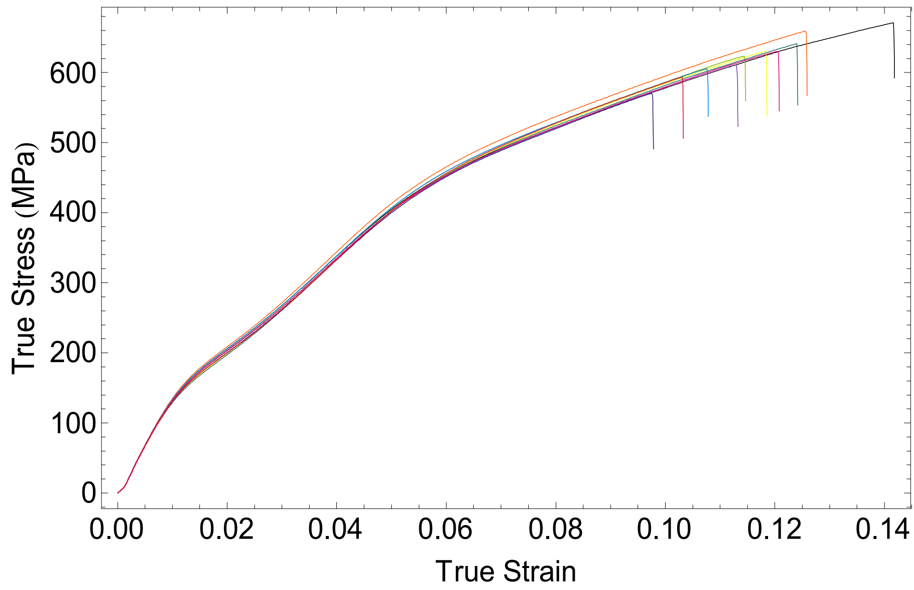

Figure 5.13 Tensile stress–strain curves of the polyester monofilament (ten samples).

Figure 5.13 shows the tensile stress–strain curves of the polyester monofilament measured on an Instron 5566 Universal Testing Machine with yarn grips, according to ASTM D2256-02 standard test method. The test speed was 300 mm/min, and the gage length was 250 mm. Nonlinear mechanical behaviour was observed. The spacer monofilaments will undertake large deflection in compression, and therefore a large strain will be reached. Thus, the complete nonlinear material properties of the polyester monofilament were introduced for the spacer monofilaments in the FE models. In contrast, the outer layers only undertake small deformation; the linearly elastic property, i.e., the initial modulus of the tensile stress–strain curves 12833 MPa, was assumed to reduce the computational cost. The polyester monofilament friction coefficient μ is 0.28 measured with a portable mechanical yarn friction tester with a drive unit (SDL Atlas Y096A/B).

5.3.2 FE models

This section implements the FE simulations by means of the commercial finite element code ANSYS®[2], using the unit cell's spacer layer identified in Section 5.2.2 and the strategies for modelling the unit cell's outer layers discussed in Section 5.2.3.

The unit cell for the FE models, using the precise geometric model of the spacer layer and modelling the two outer layers with two flat plates, is shown in Figure 5.14. The spacer monofilaments were meshed using the beam element BEAM188, and a circular section of 0.1 mm in radius was assigned. The nonlinear properties of the polyester monofilament were used for the beam elements, and a Poisson's ratio 0.3 was selected from the literature [135, 136]. By way of contrast, the outer layers were meshed with the shell element SHELL181. Linearly elastic properties, i.e., a Young's modulus of 12833 MPa and a Poisson's ratio of 0.3, were defined for the shell elements.

The spacer monofilaments were connected to the outer layers by using internal multipoint constraint (MPC) approach. MPC is an algorithm built in ANSYS to connect two separate bodies through generating internally coupling equations. Using MPC, the spacer yarns and outer layers meshed with different elements can be connected physically although their meshes are not matched. The two endpoints of each spacer monofilament were set as pilot nodes (i.e., sixteen in total). The nodes in the outer layers (on the middle surface of the shells) within an area corresponding to the monofilament needle loop for the respective spacer monofilaments were selected as contact nodes. By using the force-distributed constraint type of MPC, the pilot node (TARGE170) for each endpoint of the eight spacer monofilaments was connected to the corresponding contact nodes (CONTA175). Accordingly, sixteen

[2] ANSYS Release 13.0SP2 UP20110309, ANSYS Academic Teaching Introductory

MPC contact pairs were created to connect the sixteen endpoints of the eight spacer monofilaments to the two outer layers. In this way, the forces or displacements applied to the pilot nodes are distributed to the contact nodes, in an average sense, through shape functions. Hence, this method is effective in simulating the force and displacement transmission between a spacer monofilament and the related monofilament needle loop. In addition, both translational and rotational DOFs can be constrained using MPC. For the FE models, the translational DOFs (UX, UY, and UZ) at the endpoints of the eight spacer monofilaments were constrained, which means that no translational deformation takes place between each spacer monofilament endpoint and the outer layer where the endpoint located. By contrast, the rotational DOFs (ROTX, ROTY and ROTZ) of the sixteen endpoints have to be determined according to the binding structures of the outer layers later.

The contacts, friction and slide between the spacer monofilaments and outer layers as well as those among the spacer monofilaments will occur under compression. Contact problems are highly nonlinear with significant difficulties. The regions of contact are unknown until a simulation starts, depending on the loads, materials, boundary conditions, and other factors; surfaces can come into and go out of contact with each other in a largely unpredictable and abrupt manner, making solution convergence difficult. ANSYS utilizes a contact pair, i.e., contact elements in conjunction with target elements, to simulate how two bodies react when they come into contact with each other. There are five types of contact pairs available, including node-to-node, node-to-surface, surface-to-surface, line-to-line, and line-to-surface. A contact pair can either be rigid-to-flexible or flexible-to-flexible; whereas rigid means non-deformable, flexible means deformable. Each type of contact pair uses different set of contact elements and is appropriate for specific types of problems. To take account of those interactions in simulating the fabric compression, various contact pairs were created, and the details are presented as follows.

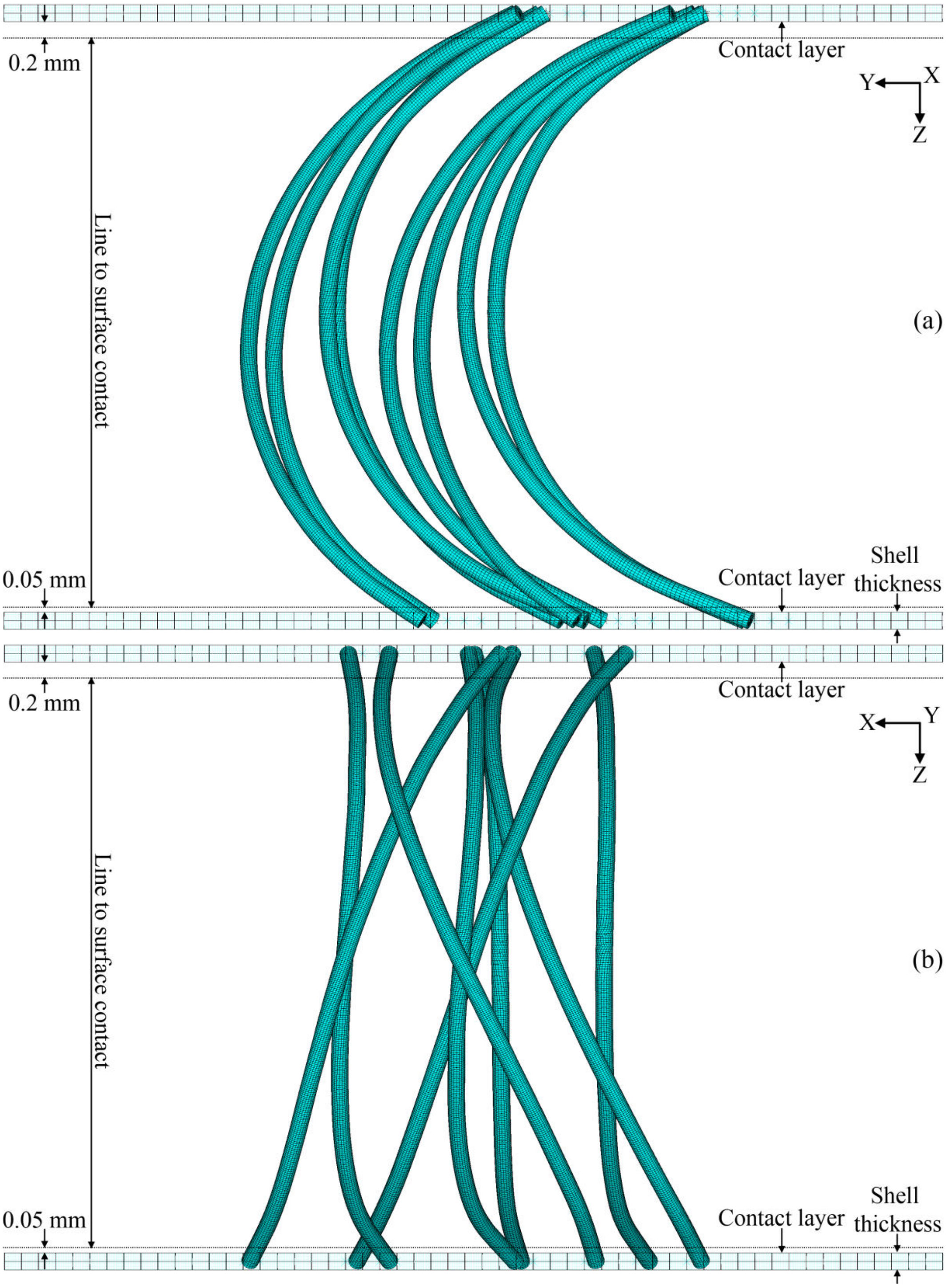

Figure 5.14 FE model for the unit cell observed from: (a) coursewise; (b) walewise.

Firstly, the interactions between the spacer monofilaments and outer layers are considered by creating flexible-to-flexible line-to-surface contact pairs. Two contact layers (TARGE170) were placed on the two outer layer internal surfaces, which the spacer monofilaments will contact during the compression of the fabric. As discussed previously, to include the effect of the wavy internal surfaces on the contacts, the contact elements should be selectively placed on the spacer monofilaments. For this purpose, the spacer monofilaments are divided into three sections along the thickness direction by using two boundary lines (Figure 5.14). According to the μCT reconstruction, the distance between the boundary line for the top end section and its nearby outer layer internal surface is 0.2 mm, while that for the bottom end section is 0.05 mm. To pair with the two contact layers placed on the outer layer internal surfaces, contact elements (CONTA177) were placed on the surfaces of the eight spacer monofilaments in the range of the middle sections to form two line-to-surface contact pairs. While the top and bottom end sections of the spacer monofilaments can penetrate the shell elements (i.e., the outer fabric layers), the middle sections of them are constrained by the contacting points between them and the two contact layers. For the line-to-surface contact pairs, the shell thickness and beam radius were taken into account. They were based on "Standard" flexible contact, and the friction was defined with 0.28. Both the eight beams representing the spacer monofilaments and the two shells representing the outer layers are deformable.

Secondly, the contacts, friction and slide among spacer monofilaments can affect the fabric compression behaviour; therefore, such interactions cannot be neglected as the previous investigations [118, 120, 121, 125]. To include the interactions, a self-contact pair was created. Both contact elements (CONTA176) and target elements

(TARGE170) were placed onto the surfaces of the eight spacer monofilaments to form a flexible-to-flexible line-to-line contact pair. It was also based on “Standard” flexible contact, and its friction was defined with 0.28. With this contact pair, all interactions among the spacer monofilaments can be detected and simulated.

Finally, in the compression tests, a specimen either was simply placed on the fixed platen or its two surfaces were glued to the platens. The two compression platens were created using rigid elements (TARGE170) just in contact with the outer surfaces of the two shells (the outer layers). The top rigid platen was set to transparent for better presentation (Figure 5.15). Two layers of surface contact elements (CONTA174) were placed on the two shell outer surfaces, representing the two outer layers, to pair the rigid elements, representing the two compression platens, to form two rigid-to-flexible surface-to-surface contact pairs. According to the test conditions, two contact types were set for the two contact pairs, i.e., “Bonded” corresponding to the glued case and “No Separation (always)” corresponding to the not glued case. In the former case, the compression platen and the outer layer are bonded with no relative motion. In the latter case, the compression platen and the outer layer are keeping in contact during compression, but they can slide frictionally within the contact plane. It is noteworthy that the two compression platens as rigid bodies are non-deformable, whereas the two outer fabric layers are deformable.

A pilot node was created for each rigid platen, and the boundary conditions can be just applied to the two pilot nodes because the two platens are rigid bodies. The forces and displacements applied to the pilot nodes are transmitted in an average sense to the respective outer layers. The boundary conditions for the developed FE models were defined according to the real-life compression tests. As illustrated in Figure 5.15, the bottom platen is fixed by constraining all the DOFs, while a displacement of 5.6 mm in a Z direction is applied to the pilot node of the top platen to simulate the static compression test.

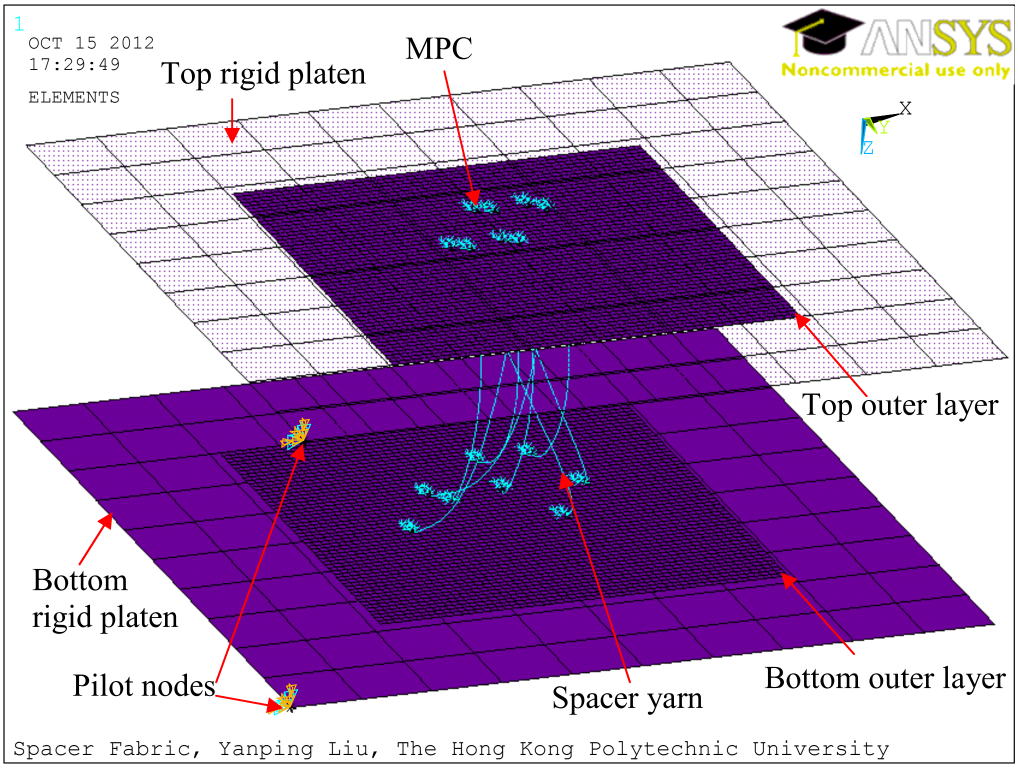

Figure 5.15 Simulation set-up for the spacer fabric unit cell compression.

Recall that the constraints on the eight spacer monofilaments and the thickness of the flat plates (or shells), representing the outer layers, are needed to be determined by adjusting numerical models as discussed in Section 5.2.3. The spacer monofilament endpoints have the rotational DOF about X-axis, but the rotational DOFs about Y- and Z-axes are not easy to define. To estimate the proper rotational DOFs at the sixteen spacer monofilament endpoints, four different models (FE-0.2, FE-0.2-p, FE-0.2-t and FE-0.2-pt) with different rotational DOFs applied to the endpoints were developed. In these models, the shell thickness was selected as 0.2 mm, equal to the outer layer thickness in the zone of loop side limbs (see Figure 5.11). This implies that the spacer monofilaments will contact the side limbs rather than the heads of the monofilament needle loops in the outer layers. FE-0.2 has free rotational DOFs at all the spacer monofilament endpoints. In FE-0.2-p, “ROTY and ROTZ” constraint was applied to the pillar spacer monofilament endpoints (p1, p2, p5 and p6), which means that their endpoints have no rotational DOFs about Y- and Z-axes. FE-0.2-t has “ROTY and ROTZ” constraints applied at the tricot spacer monofilament endpoints (t3, t4, t7 and t8). The ‘‘ROTY and ROTZ’’ constraint was applied to all the spacer monofilament endpoints in FE-0.1-pt. Another unknown parameter is the flat plate thickness (shell thickness). As indicated in Section 5.2.3, the thickness of the outer layers in the zone of loop heads varies from 0.4 mm at the peak of a loop head to 0.2 mm for a side limb along the coursewise direction. To introduce a reasonable value for the thickness, two additional FE models, i.e., FE-0.3-p and FE-0.4-p, were developed with the same constraints on the spacer monofilaments as those applied in FE-0.2-p but with two different shell thicknesses 0.3 mm and 0.4 mm, respectively. The contact types between the outer fabric layers and rigid platens for above six FE models were all defined as bonded. Besides, to simulate the two test conditions in the experiments, two extra FE models (FE-0.2-p-0.28 and FE-0.2-p-0.1) which have “No Separation (always)” contact type between the top outer layer and moveable rigid platen with friction coefficients of 0.28 and 0.1, respectively, were developed. The contact type for the contact pairs between the bottom outer layer and fixed platen for the two FE models was set as “Bonded” for convergence purpose. That is, the model FE-0.2-p corresponds to the glued case, while the model FE-0.2-p-0.28 and FE-0.2-p-0.1 correspond to the not glued case. The detailed descriptions of all the developed FE models are given in Table 5.1.

Table 5.1 Descriptions of finite element model codes

Model code	Constraints at the spacer monofilament endpoints		Shell thickness	Contact type between	
	pillar	tricot		top outer layer, moveable platen	bottom outer layer, fixed platen
FE-0.2	No	No	0.2 mm	Bonded	Bonded
FE-0.2-p	ROTY, ROTZ	No	0.2 mm	Bonded	Bonded
FE-0.2-t	No	ROTY, ROTZ	0.2 mm	Bonded	Bonded
FE-0.2-pt	ROTY, ROTZ	ROTY, ROTZ	0.2 mm	Bonded	Bonded
FE-0.3-p	ROTY, ROTZ	No	0.3 mm	Bonded	Bonded
FE-0.4-p	ROTY, ROTZ	No	0.4 mm	Bonded	Bonded
FE-0.2-p-0.28	ROTY, ROTZ	No	0.2 mm	No Separation (always)	Bonded
FE-0.2-p-0.1	ROTY, ROTZ	No	0.2 mm	No Separation (always)	Bonded

To compare the obtained simulated results with the experimental data, the force–displacement relationship of the representative unit has to be converted to the one for a specimen of 100 mm × 100 mm in size used in the experiment. According to the stitch density of the fabric 41.15 stitches/cm^2, a specimen with an area of 100 mm × 100 mm includes 1028.75 representative units.

5.4 Modelling of spacer fabric compression

This section concerns the identification of proper constraints applied to the spacer monofilament endpoints, the outer layer thickness, and the effect of the test boundary conditions on the fabric compression behaviour.

5.4.1 Constraints at the spacer monofilament endpoints

The FE models, i.e., FE-0.2-pt, FE-0.2-t, FE-0.2-p and FE-0.2, were solved using large displacement static method. Figure 5.16 presents the load–displacement relationships addressed with the four FE models. The load–displacement curve of Sample 2 in glued case in Figure 3.3(b) is also included in the figure for comparison purpose. It shows that when all the endpoints are constrained using ''ROTY and ROTZ'' option (FE-0.2-pt), the mechanical response is the stiffest behaviour among the four FE models. With the increase in displacement, the reaction force grows rapidly in the first stage of deformation. In the second stage, although the increase in reaction force slows down, there is no plateau in the curve as observed in the experiments. In FE-0.2-t, the ROTY and ROTZ of the tricot spacer monofilament endpoints are constrained showing a similar load–displacement relationship to that of FE-0.2-pt until the displacement achieves 2.6 mm when instabilities occur. The load declines steadily as the fabric loaded further. When the constraint is only applied to the pillar spacer monofilament endpoints (FE-0.2-p), the simulated result is in satisfactory agreement with the experimental data until the displacement is 4 mm. If no rotational constraints are applied to all the spacer monofilament endpoints (FE-0.2), instabilities happen when the fabric is compressed by 3 mm. In addition, before the instabilities, this FE model exhibits the lowest compression resistance among the four FE models.

The different mechanical responses of the four FE models are attributed to their different spacer monofilament deformation modes. Figures 5.17, 5.18, 5.19 and 5.20 show the Von Mises stress (VMS) plots of FE-0.2-pt, FE-0.2-t, FE-0.2-p and FE-0.2, respectively, at the displacements of 2 mm and 4 mm.

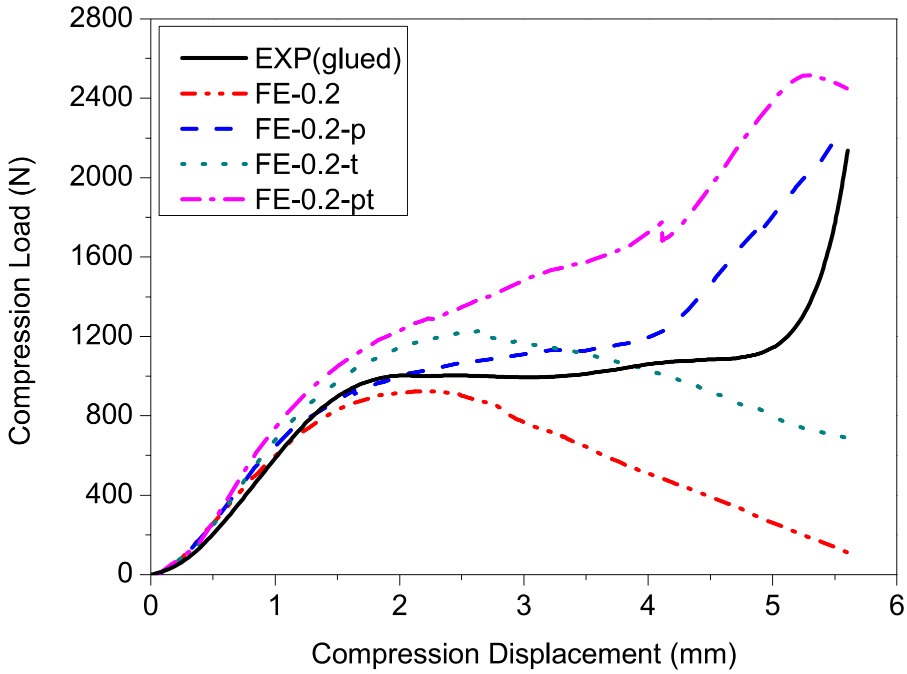

Figure 5.16 Load–displacement relationships of the FE models with different constraints at the spacer monofilament endpoints.

In FE-0.2-pt, the spacer monofilaments undertake postbuckling without obvious torsion and rotation at a displacement of 2 mm (Figure 5.17(a)). When the displacement reaches 4 mm, due to the contacts among the spacer monofilaments p1, t3 and t6, small torsion for the pillar spacer monofilament p1 can be observed (Figure 5.17(b)). Meanwhile, no obvious torsion can be observed from the others.

In FE-0.2-t, at a displacement of 2 mm, slight torsion can be observed for the pillar spacer monofilaments p2, p5 and p6, while relatively large rotation for p2 and p6 are also observed (Figure 5.18(a)). This is because no rotational constraints are applied to their endpoints; the contacts among the eight spacer monofilaments and their initial imperfections lead to the occurrence of torsion and rotation of the pillar spacer monofilaments. Meanwhile, the tricot spacer monofilaments do not show obvious torsion and rotation because the ROY and ROZ of their endpoints are constrained. This deformation mode leads to a lower reaction force of FE-0.2-t than that of FE-0.2-pt at the same displacement of 2 mm. In addition, at a displacement of 4 mm, large torsion and rotation occur for all the pillar spacer monofilaments (Figure 5.18(b)), and therefore FE-0.2-t gives an inclined reaction force.

In FE-0.2-p, no rotational constraints are applied to the tricot spacer monofilament endpoints. At a displacement of 2 mm, the contacts among the eight spacer monofilaments in the end sections and the initial geometric imperfections result in torsion of the tricot spacer monofilaments (Figure 5.19(a)). The pillar spacer monofilaments show nearly the same deformation mode as that in FE-0.2-pt (Figures 5.19(a) and 5.17(a)). Hence, the reaction force of FE-0.2-p is lower than that of FE-0.2-pt at the displacement of 2 mm. Figure 5.16 shows that the reaction force of FE-0.2-p is also lower than that of FE-0.2-t. This is because the reduction in the reaction force contributed by the large torsion of the tricot spacer monofilaments in FE-0.2-p is larger than that by the slight torsion of the pillar spacer monofilaments in FE-0.2-t. When the displacement is 4 mm, the pillar spacer monofilaments still behave the same as that in FE-0.2-pt, while the tricot spacer monofilaments undertake large torsion (Figure 5.19(b)). Since the pillar spacer monofilaments contribute more to the reaction force than the tricot ones, FE-0.2-p shows a plateau stage rather than instabilities with an inclined force.

In FE-0.2, the rotational DOFs at all the spacer monofilament endpoints are free. The spacer monofilaments undertake large rotation and torsion, and they are in contact with one another (Figure 5.20), resulting in a low reaction force at the displacement of 2 mm and instabilities with an inclined force at the displacement of 4 mm.

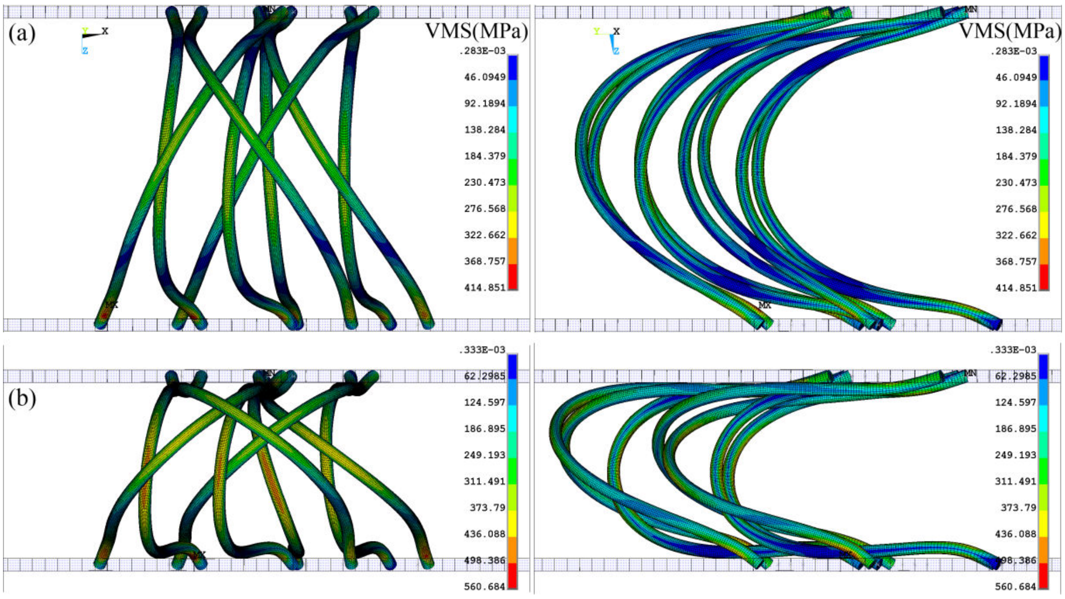

Figure 5.17 Von Mises stress plots of the deformed FE models for FE-0.2-pt at displacements: (a) 2 mm; (b) 4 mm.

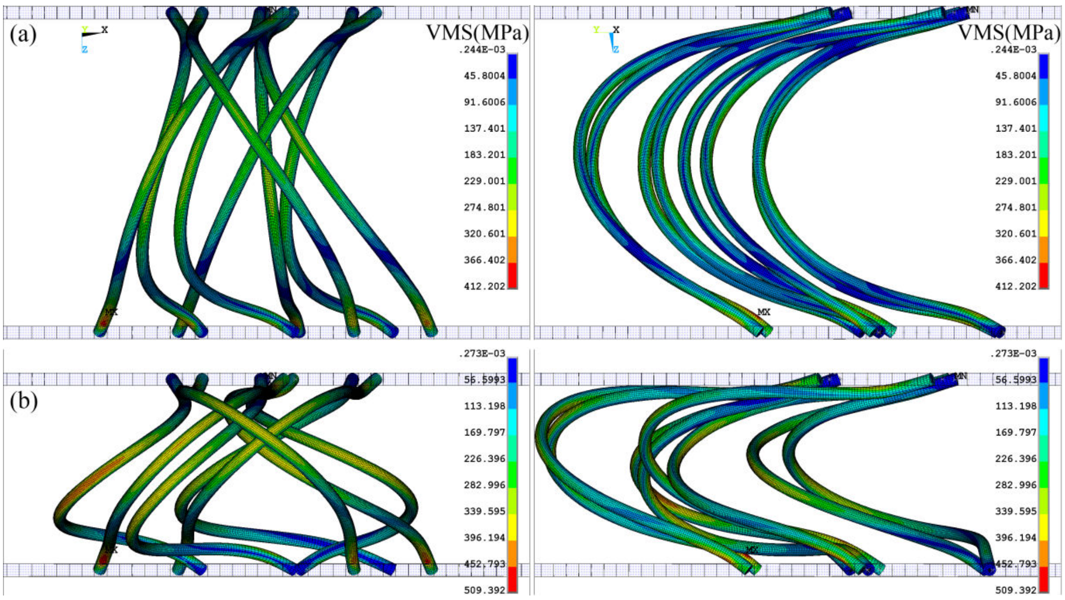

Figure 5.18 Von Mises stress plots of the deformed FE models for FE-0.2-t at displacements: (a) 2 mm; (b) 4 mm.

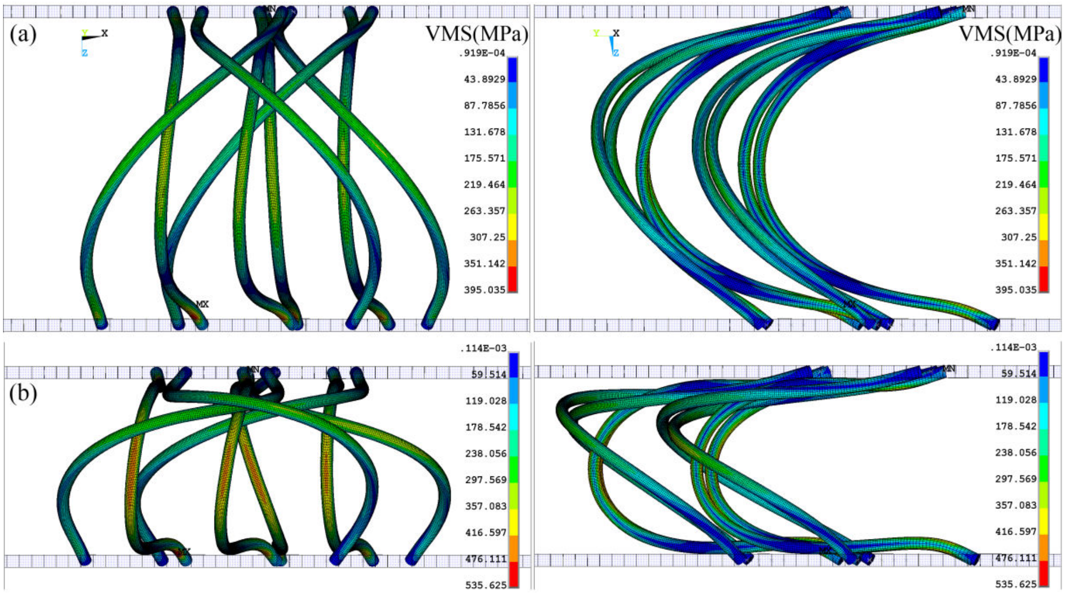

Figure 5.19 Von Mises stress plots of the deformed FE models for FE-0.2-p at displacements: (a) 2 mm; (b) 4 mm.

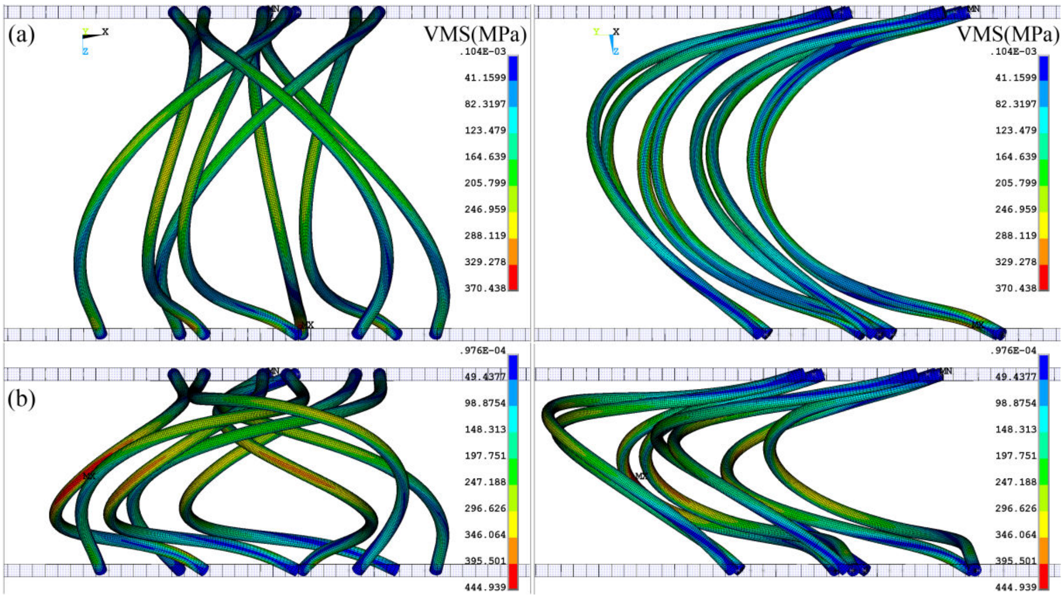

Figure 5.20 Von Mises stress plots of the deformed FE models for FE-0.2 at displacements: (a) 2 mm; (b) 4 mm.

In summary, how the multifilament stitches bind the spacer monofilaments determines the constraint type, thereby affecting the load–displacement relationship of the fabric. In other words, the load–displacement relationships of spacer fabrics can be manipulated by adjusting the outer layer knitting structure to achieve different constraints on the spacer monofilaments. For this particular spacer fabric, the load–displacement relationship of FE-0.2-p agrees well with the experimental result, indicating a reasonable estimate of the constraints imposed on the spacer monofilaments in the real fabric. Indeed, as discussed in Section 5.2.3, the observation suggests that the pillar spacer monofilaments have lower rotational DOFs about Y- and Z-axes than the tricot ones, which is consistent with the constraints applied in FE-0.2-p. Therefore, the result of FE-0.2-p is reasonable to represent the complicated deformation mechanism of this type of warp-knitted spacer fabric that has the key feature of behaving as cushioning materials, providing three distinct stages under compression, described as linear elasticity, plateau and densification.

5.4.2 Outer layer thickness

The outer layer internal surface morphologies can affect the contacts between the spacer monofilaments and the outer layers, thereby affecting the fabric compression behaviour. The analysis of the outer layer internal surface in Section 5.2.3 suggests that the wavy outer layers can be simulated with flat plates by selectively using contact elements, whereas the flat plate thickness should be numerically determined. In this section, the effect of the shell thickness in the FE models, representing the outer layer thickness, on the fabric compression behaviour is discussed.

Three FE models with different shell thicknesses (FE-0.2-p, FE-0.3-p and FE-0.4-p) are used to assess the wavy internal surface effect and also to determine a suitable value for the outer layer thickness of this particular spacer fabric.

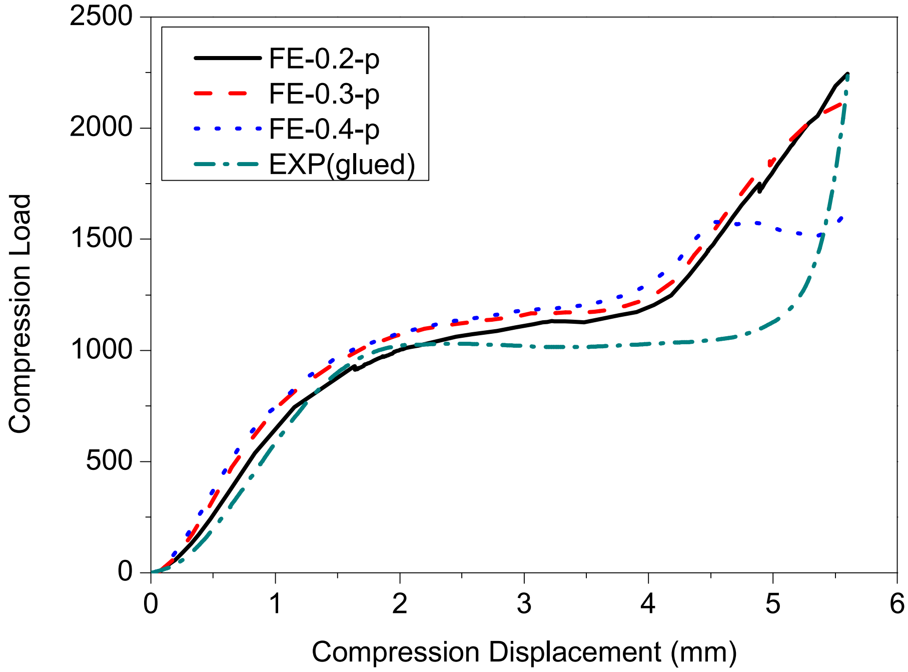

Figure 5.21 Load–displacement relationships of the FE models with different outer layer thicknesses.

Figure 5.21 presents the load–displacement curves for the FE models, showing similar shapes until the displacement achieves 4.5 mm. A stiffer mechanical response is obtained in a model with a higher shell thickness. This implies that the change of the outer layer thickness does not affect the deformation modes of the spacer monofilaments when the applied displacement is below 4.5 mm. Figure 5.22 presents the VMS plots of the three deformed FE models at a displacement of 4.5 mm. It confirms that the deformation modes for the three FE models are nearly the same when the displacement is below 4.5 mm. The end sections of the pillar spacer monofilaments contact the outer layers, and their middle sections undertake postbuckling with shorter effective lengths than those of the tricot spacer monofilaments. Consequently, large curvature can be observed from the middle sections of the pillar spacer monofilaments, which contribute more to the fabric compression resistance than the tricot ones. As can be seen in the deformed models observed from the coursewise direction, the outer layer thickness affects the effective lengths of the pillar spacer monofilaments undertaking postbuckling. The higher the outer layer thickness, the shorter the effective lengths of the pillar spacer monofilament middle sections. Therefore, a FE model with a higher shell thickness gives a stiffer mechanical response.

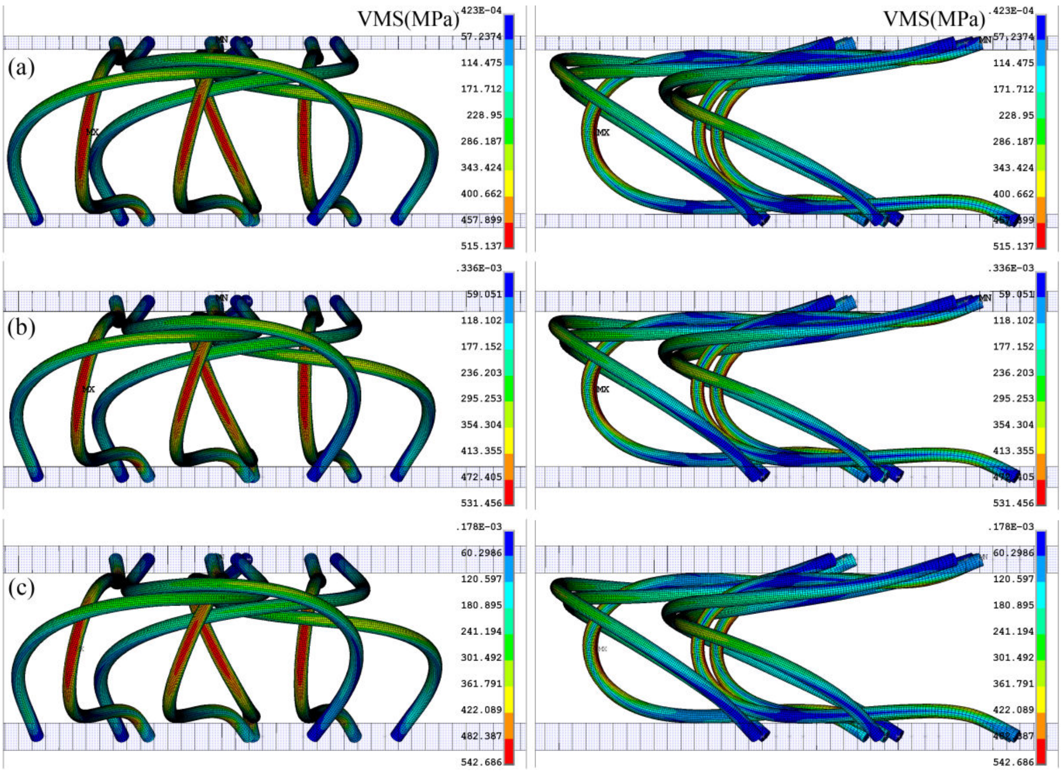

Figure 5.22 Von Mises stress plots of the deformed FE models at a displacement of 4.5 mm with different shell thicknesses: (a) 0.2 mm; (b) 0.3 mm; (c) 0.4 mm.

When the displacement rises up to 4.5 mm, the reaction force for FE-0.4-p decreases steadily with the further increase in displacement. Likewise, the reaction force for FE-0.3-p also starts to decrease from the displacement of 5.5 mm. Only FE-0.2-p gives a monotonic increasing response in reaction force in the densification stage.

That is, the difference in the outer layer thickness changes the deformation mode with displacements above 4.5 mm. Figure 5.23 gives the VMS plots of the deformed FE models at a displacement of 5.5 mm; for both FE-0.3-p and FE-0.4-p, their instabilities occur. The pillar spacer monofilament p2 behaves differently in the three FE models. Besides, a larger inclination of the pillar spacer monofilament middle sections can be observed in the model with a higher shell thickness. This is why FE-0.4-p gives the lowest reaction force response in this displacement range.

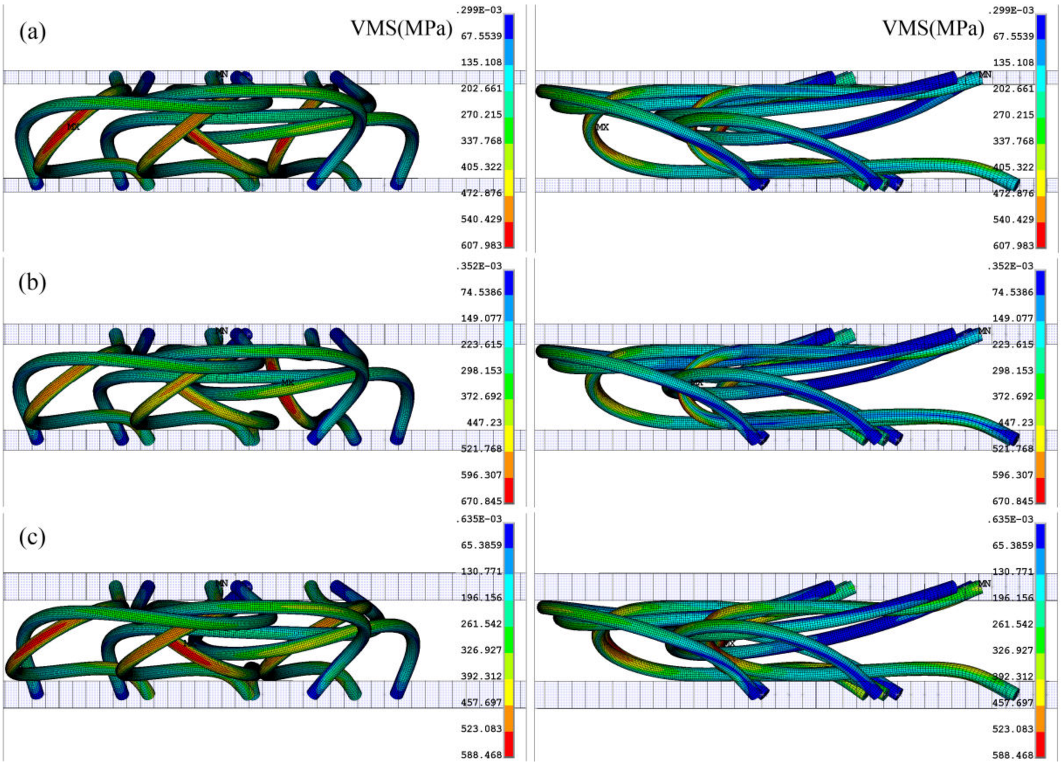

Figure 5.23 Von Mises stress plots of the deformed FE models at a displacement of 5.5 mm with different shell thicknesses: (a) 0.2 mm; (b) 0.3 mm; (c) 0.4 mm.

Comparing the experimental result, FE-0.2-p gives the best prediction among the three FE models. Therefore, the suitable value for the outer layer thickness of this particular spacer fabric is 0.2 mm. This means that the spacer monofilaments contact the side limbs of the monofilament needle loops rather than contact the monofilament needle loop heads in the outer layers. By referring to Figure 5.9, it is obvious that the contacts between the spacer monofilaments and the peaks of the needle loop heads will lead to the occurrence of instabilities. In contrast, if the contacting point is in between two side limbs of two neighbouring needle loops, the end sections of the spacer monofilaments that contact the outer layers are not easy to slide to cause instabilities, and therefore a monotonic increasing reaction force in the densification stage is obtained.

As has been noted, the constraints at the respective spacer monofilament endpoints and the outer layer thickness have been determined. In the next section, the effect of different test boundary conditions, including not glued and glued that employed in Chapter 3, on the fabric compression behaviour will be investigated by extending the FE model FE-0.2-p, the result of which fits well the experimental data.

5.4.3 Compression test boundary condition

As studied in Chapter 3, the experimental results for the spacer fabric S1 have shown that the mechanical responses under the not glued and glued conditions are similar, besides the slight effect on the plateau stage of deformation. Fluctuations exist in the compression load–displacement curves under the not glued test condition in the plateau stage, whereas the curves under the glued test condition are smooth and consistent. This implies that the test boundary conditions can affect the deformation behaviour of the spacer fabric to some extent. It is hard to identify the difference in the deformation processes under the two test boundary conditions from experimental observations, but it can be numerically simulated, thereby helping in understanding the compression mechanism of spacer fabrics under various circumstances in applications.

In the experiments, the spacer fabric was compressed with two circular platens. It is hard to determine the exact friction coefficient between the outer layers and the compression platens. To simulate the frictional contacts, “No Separation (always)” and two friction coefficients, i.e., 0.28 and 0.1, were chosen for the rigid-to-flexible surface-to-surface contact pairs between the top outer fabric layer and the moveable compression platen in FE-0.2-p-0.28 and FE-0.2-p-0.1, respectively. The contact type for the contact pairs between the bottom outer layer and fixed platen for the two FE models was set as “Bonded” as mentioned previously for convergence purpose. The bonded condition can be considered as that the friction coefficient is infinite.

Figure 5.24 presents the load–displacement relationships of the FE models with different contact types between the outer layers and their nearby rigid platens, having similar mechanical responses consisting of initial, linear elasticity, plateau and densification stages. In the initial stage, a higher friction gives a stiffer mechanical response, whereas the responses of the three FE models in the linear elasticity stage are nearly the same. In the plateau stage, a higher plateau force can be observed for the FE model with a lower friction coefficient. The FE model with bonded contact type FE-0.2-p has the lowest reaction force in the densification stage. These differences indicate different deformation processes of the FE models with different rigid-to-flexible contact pairs, namely, different test boundary conditions.

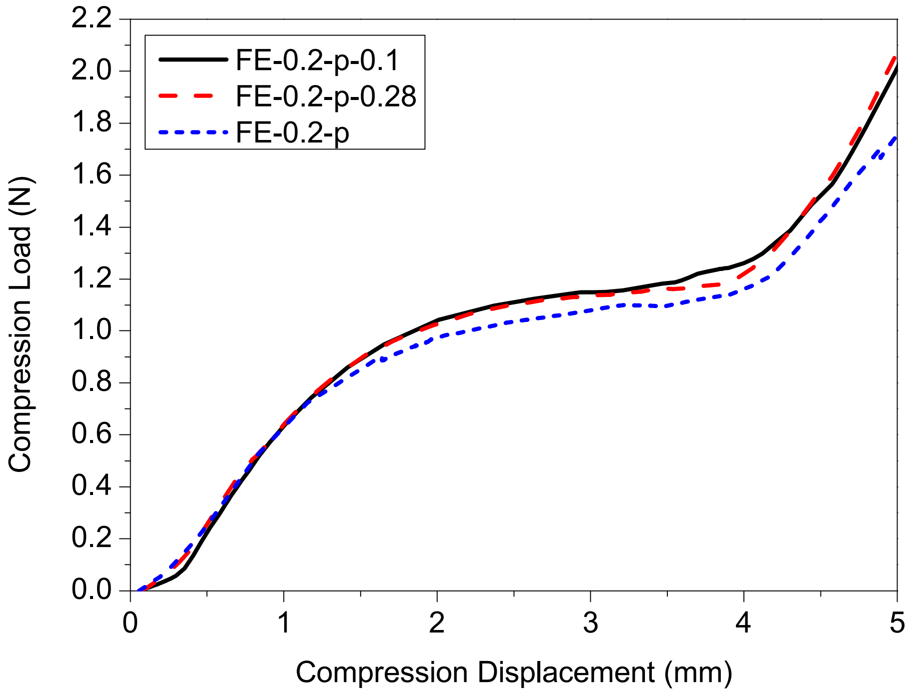

Figure 5.24 Load–displacement relationships of the FE models with different contact types between the outer fabric layers and their nearby rigid platens.

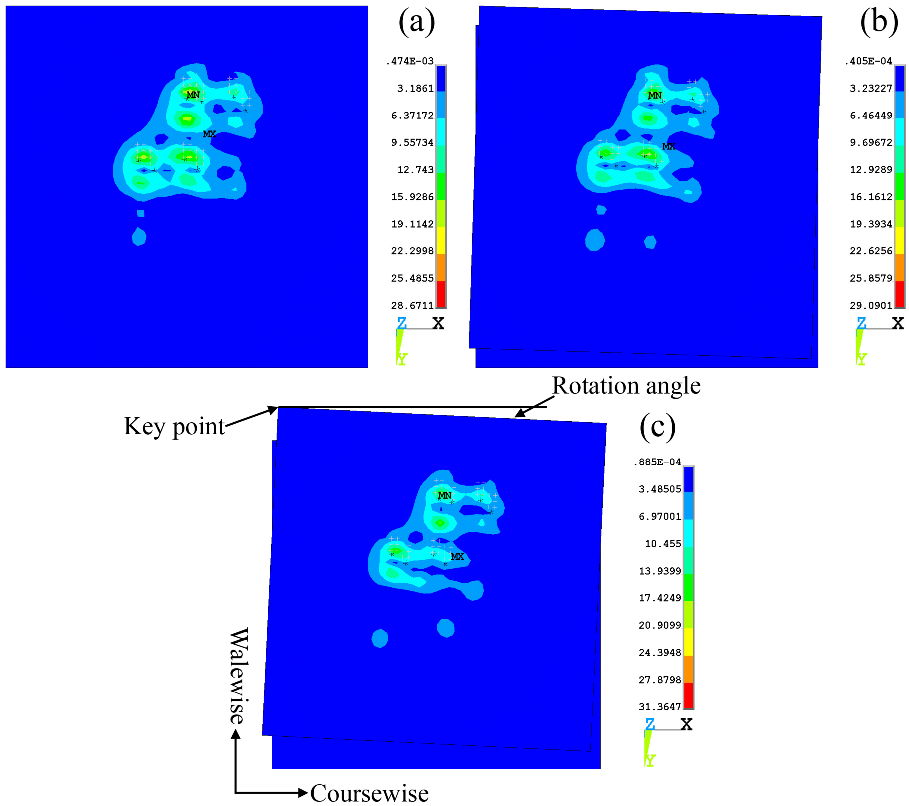

Figure 5.25 Top view of the deformed FE models with different rigid contact types at a displacement of 5 mm: (a) bonded; (b) μ=0.28; (c) μ=0.1.

Figure 5.25 presents the top view of VMS plots of the deformed FE models (the top outer layers) at a displacement of 5 mm. Shear and rotation of the top outer fabric layers can be clearly observed in both FE-0.2-p-0.28 and FE-0.2-p-0.1. Obviously, FE-0.2-p-0.1 has a larger shear displacement and rotation degree than FE-0.2-p-0.28. To track the shear and rotation movements of the top outer layers of the two FE models during the compression process, a key point and a rotation angle are selected and defined, respectively, as illustrated in Figure 5.25. The displacements along X- and Y-axes of the key point are plotted in Figure 5.26, showing the occurrences of shear along X- and Y-axes for the two FE models both in the initial stages. Afterwards, the movement of this key point is not obvious. It can also be found that FE-0.2-p-0.1 has larger shear displacements than FE-0.2-p-0.28 both along X- and Y-axes. Figure 5.27 shows the curves of the rotation angle against the compression displacement. The rotation results are similar to those of the shear movements. Larger rotation for the two FE models is both in the initial stages; after that, only small rotation can be observed. FE-0.2-p-0.1 with the lower friction coefficient also shows larger rotation during the compression.

It is clear that, during the compression process, shear and rotation of the outer fabric layers occur if they are not constrained. In the initial stage, the shear and rotation are caused by the unsymmetrical shapes of the spacer monofilaments (Figure 5.7). In this stage, the vertical reaction pressure between the outer fabric layer and the platen is low, leading to a low friction force. In this case, the torsion and rotation of the spacer monofilaments can easily cause the top outer layer to slide and rotate in-plane. With the increase in displacement, the compression pressure increases, bringing about an increase in the friction force, which blocks the in-plane movements of the top outer layer. That is the reason why the shear and rotation movements are mainly located in the initial stages.

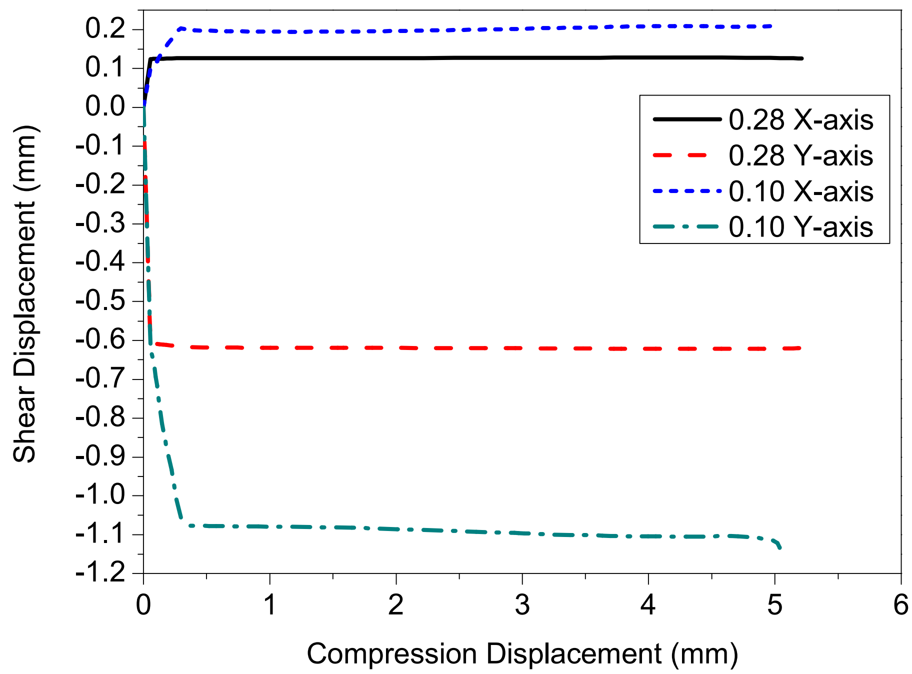

Figure 5.26 Effect of friction coefficient on shear behaviour of outer fabric layers.

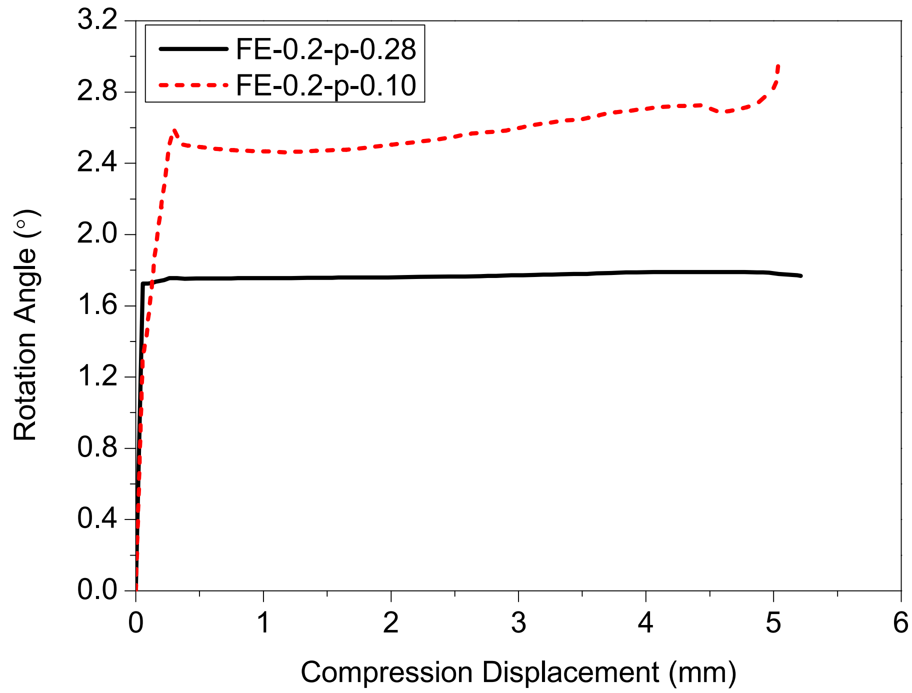

Figure 5.27 Effect of friction coefficient on rotation behaviour of outer fabric layers.

The shear and rotation movements of the outer layers are an interactive process. The deformation of the spacer monofilaments leads to the in-plane movements of the outer layers; meanwhile, the in-plane movements of the outer layers change the constraints at the spacer monofilament endpoints, thereby affecting the deformation modes of the spacer monofilaments. Figure 5.28 presents the side view of VMS plots of the deformed FE models with different rigid-to-flexible contact pairs, at a displacement of 5 mm. It shows that the inclinations of the pillar spacer monofilaments, the contacts among them, and the contacts between the spacer monofilaments and the outer layers are different among the three models. The endpoints in the top outer layer also move in the rigid contact plane, causing shear and rotation of the spacer monofilaments. In this connection, the reaction forces of the FE models are different. Furthermore, the different contact modes between the spacer monofilaments and the outer layers give rise to different contact stress distributions in the outer layers as shown in Figure 5.25.

Briefly, the in-plane movements of the outer layers create the moving boundary conditions for the spacer monofilament endpoints. This implies that the compression behaviour is not only dependent on fabric structures but also affected by the boundary conditions in applications. In other words, the compression mechanism of a spacer fabric is complicated and can be different by changing the test boundary conditions.

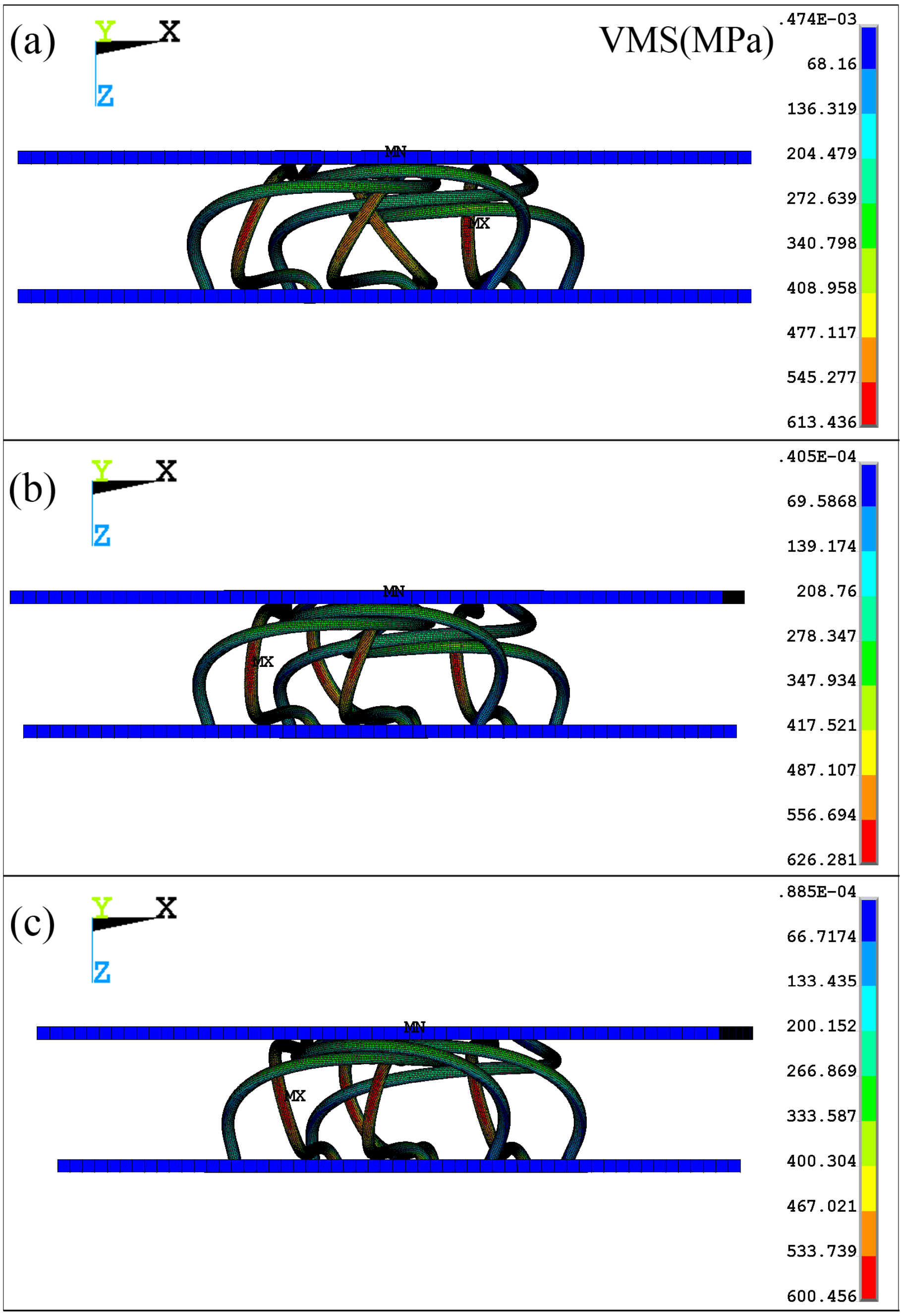

Figure 5.28 Side view of Von Mises stress plots of the deformed FE models with different rigid-to-flexible contact pairs at a displacement of 5 mm: (a) bonded; (b) μ=0.28; (c) μ=0.1.

5.4.4 Compression mechanism

In this section, the FE model FE-0.2-p, with bonded type for the contacts between the outer layers and compression platens, is selected to summarise a general compression mechanism for the spacer fabric. The structure of this section follows closely that of Section 3.4. The deformed FE models in different stages are analysed separately coupled with the corresponding load–displacement relationships.

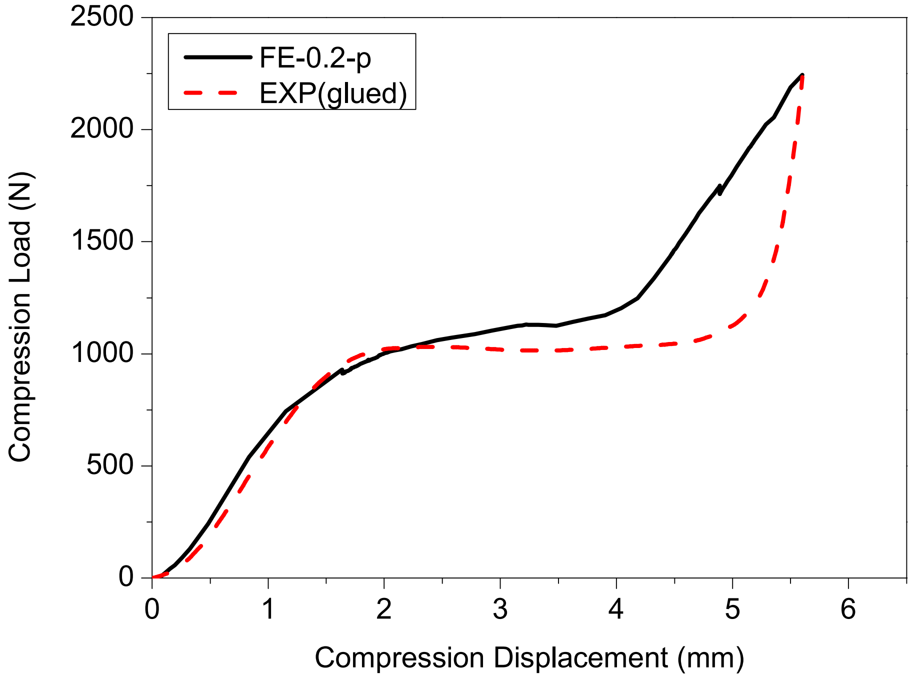

Figure 5.29 Comparison of load–displacement curves of spacer fabric between experiment and simulation.

Figure 5.29 presents a comparison between the simulated and experimental load–displacement curves of the spacer fabric S1. The cross sections of the deformed FE model, observed both from the walewise and coursewise directions, in the initial and linearly elastic, plateau, and densification stage are shown in Figures 5.30, 5.31 and 5.32, respectively.

In the initial stage, lower slopes are observed from both the experimental and simulated load–displacement curves. This is because the spacer monofilaments are not fully constrained due to the voids within the outer fabric layers and loose multifilament stitches, which leads to free postbuckling of the spacer monofilaments in this stage. From Figure 5.30, at the displacement of 0.05 mm, while the contacts between the pillar spacer monofilament bottom end sections and the bottom outer layer can be observed, the penetration of all the spacer monofilament top end sections into the top outer layer can also be observed. Because of the penetration, the VMS in the top end sections of all the spacer monofilaments is low, whereas the VMS in the bottom end sections of the pillar spacer monofilaments is high due to the initial contacts. This simulation demonstrates that while the tricot spacer monofilaments undertake free postbuckling in the initial stage, the pillar spacer monofilaments do not undertake completely free postbuckling as speculated in Chapter 3 and Chapter 4 because their bottom end sections contact the bottom outer layer. Such contacts bring about additional constraints on the pillar spacer monofilaments; meanwhile, there are no rotational constraints at the tricot spacer monofilament endpoints. This explains that the tricot spacer monofilaments are nearly stress-free. Hence, their reaction forces are lower than those of the pillar spacer yarns. The incompletely free postbuckling of the pillar spacer monofilaments and the completely free postbuckling of the tricot spacer monofilaments lead to the lower slope of the simulated load–displacement curve in the initial stage.

At the displacement of 0.5 mm, the tricot spacer monofilament end sections start to contact the outer layer internal surfaces; the contacting points provide additional constraints on the tricot spacer monofilaments, thereby increasing their VMS. This means that the tricot spacer monofilaments start to resist the applied external displacement and contribute to the increase in the reaction force of the FE model. In the linearly elastic stage, from the displacement of 0.5 mm to 1.6 mm, the postbuckling of the spacer monofilaments with additional constraints provided by the contacts leads to a sharper force increase. Especially, with the displacements from 1.1 mm to1.6 mm, the contacts between the top end sections of the pillar spacer monofilaments and the top outer layer can be observed. These contacts further increase the reaction force in this stage. This simulation clarifies the explanation presented in Chapter 3 for the linearly elastic stage that the spacer monofilaments buckle at a larger scale with the additional constraints at the contacting points.

When the FE model is compressed to the displacements in the range of 2 mm to 4.5 mm, the simulated result shows a nearly constant force with the magnitude at the level similar to the experimental one. Within this plateau stage, all the spacer monofilament end sections are in contact with the outer layers. From Figure 5.31, large torsion can be found for the tricot spacer monofilaments, causing the decreases in their reaction forces. Furthermore, at the displacements of 4 mm and 4.5 mm, it can be found that the pillar spacer monofilament middle sections start to contact the bottom and top outer layers, respectively. The contacts among the spacer monofilaments lead to shear and rotation of the pillar spacer monofilament middle sections. The torsion of the tricot spacer monofilaments, and the shear and rotation of the pillar spacer monofilaments jointly lead to a nearly constant reaction force in this stage. The FE simulation confirms the speculation on the deformation mechanism for the plateau stage presented in Chapter 3.

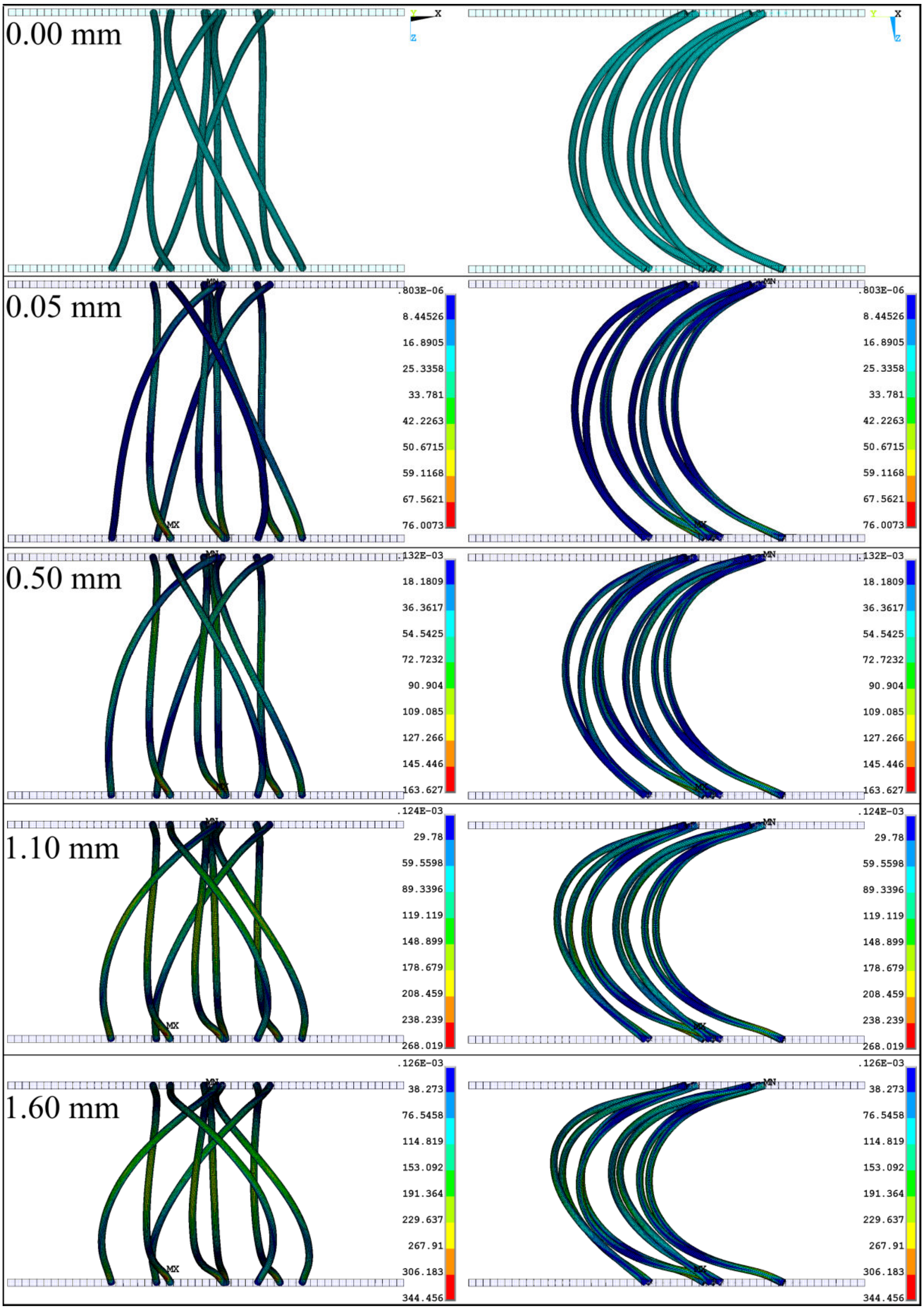

Figure 5.30 Cross sections of the FE-0.2-p at initial and elastic stages (displacements: 0–1.6 mm).

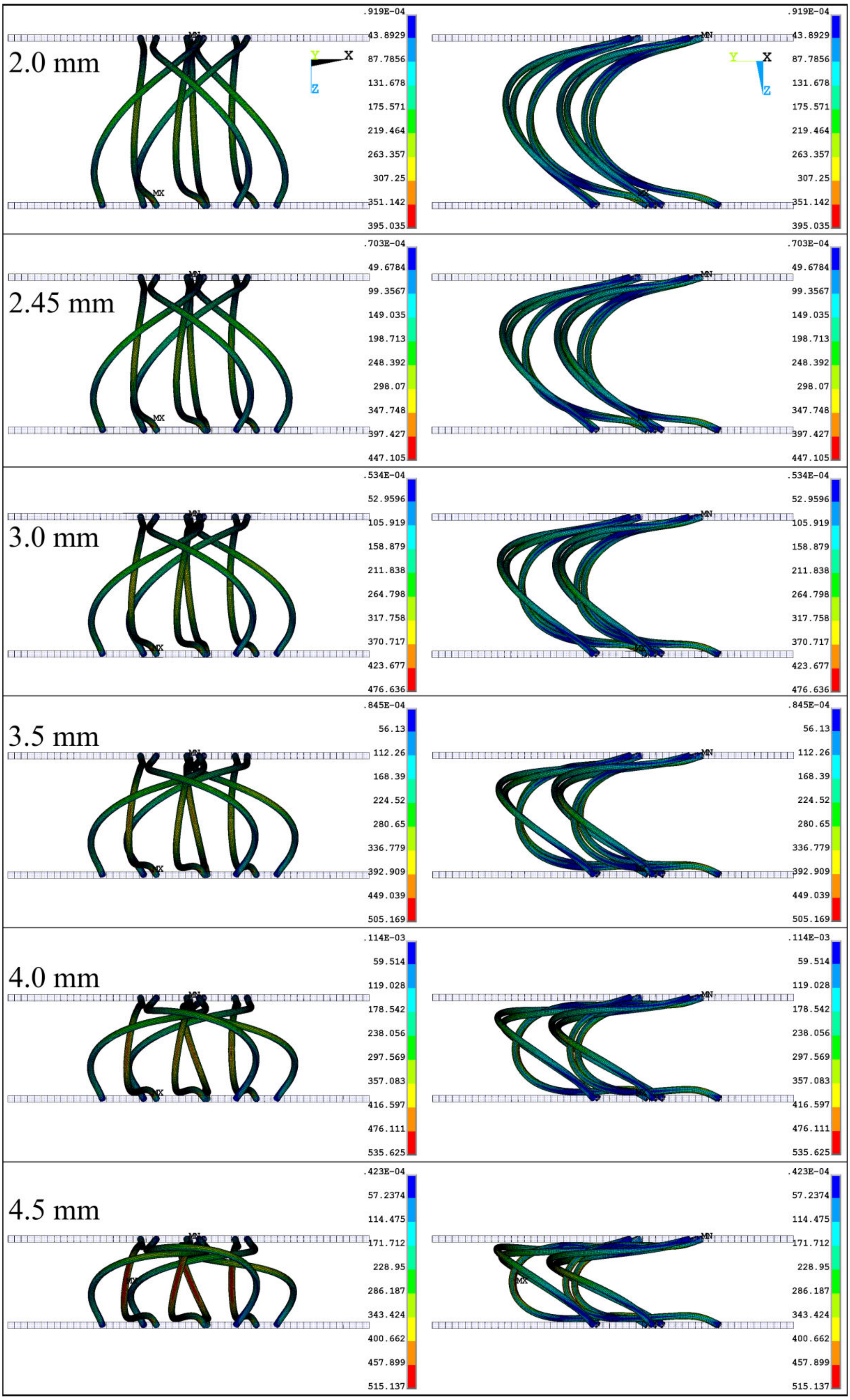

Figure 5.31 Cross sections of FE-0.2-p at plateau stage (displacements: 2–4.5mm).

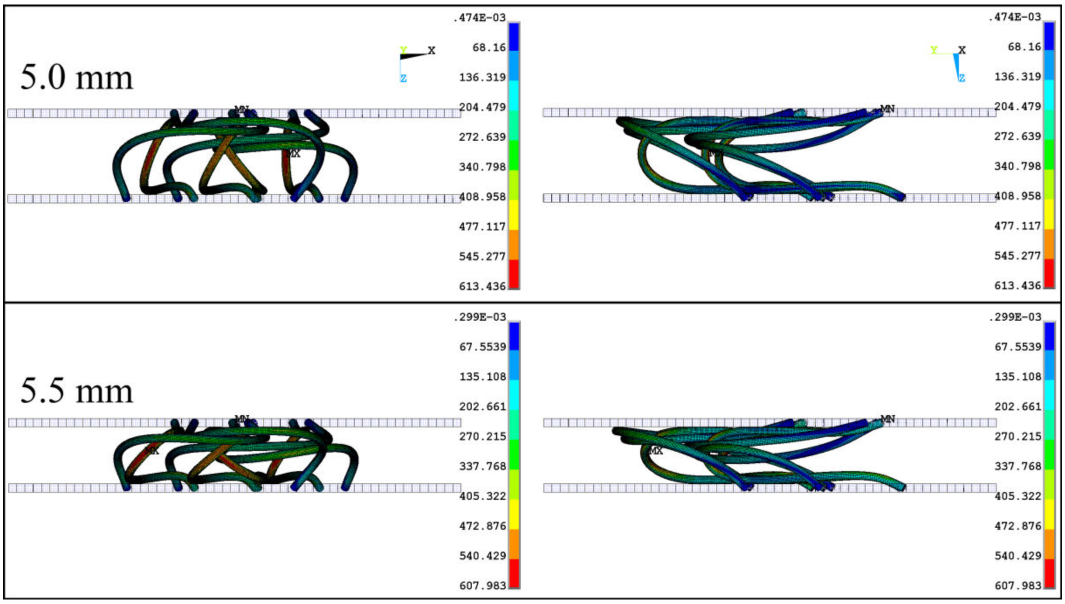

Figure 5.32 Cross sections of FE-0.2-p at densification stage (displacements: 5 and 5.5mm).

In the densification stage, a rapid growth of the overall reaction force is obtained. As mentioned above, the middle sections of the pillar spacer monofilaments are in contact with both the top and bottom outer layers from the displacement of 4.5 mm. In this case, the effective lengths of the pillar spacer monofilaments in postbuckling are the lengths of their middle sections between two contacting points, which shorten as the displacement increases. This leads to a sharp rise of the overall reaction force. It can be found from Figure 5.32 that, at the displacement of 5.5 mm, the spacer monofilaments are highly twisted, inclined, and also in contact with one another. Therefore, a densification of the entire fabric can be expected with further displacement increment. This simulation also confirms the speculation in Chapter 3.

In conclusion, the compression mechanism of the spacer fabric can be summarised as follows:

- In the initial stage, the pillar spacer monofilaments contact the bottom outer layer and contribute more to the total reaction force, while the tricot spacer monofilaments undertake free postbuckling and contribute less to the total reaction force.

- In the linearly elastic stage, the tricot spacer monofilaments start to contact the top and bottom outer layers. The postbuckling of the pillar and tricot spacer monofilaments with additional constraints provided by the contacting points leads to a rapid rise of the total reaction force.
- In the plateau stage, all the spacer monofilament end sections are in contact with the outer layers. While the tricot spacer monofilaments undertake large torsion, the contacts among the spacer monofilaments lead to shear and rotation of the pillar spacer monofilament middle sections, showing a nearly constant reaction force in this stage.
- In the densification stage, the pillar spacer monofilament middle sections contact the two outer layers. The length between the two contacting points for each pillar spacer monofilament decreases as the displacement increases, showing a dramatically rising total reaction force.

It is evident that the pillar spacer monofilaments are the main load-carrier of the spacer fabric in compression. Their deformations during the compression process are highly nonlinear. The contacts between the pillar spacer monofilaments and outer layers create the moving boundary conditions for the pillar spacer monofilaments and are the key factor in determining the nonlinear compression behaviour of the spacer fabric. Figure 5.33 gives the four critical contact states for the four pillar spacer monofilaments. The simulated result of the FE model agrees well with the speculation presented in Figure 5.12, showing high effectiveness in revealing the compression mechanism of the spacer fabric.

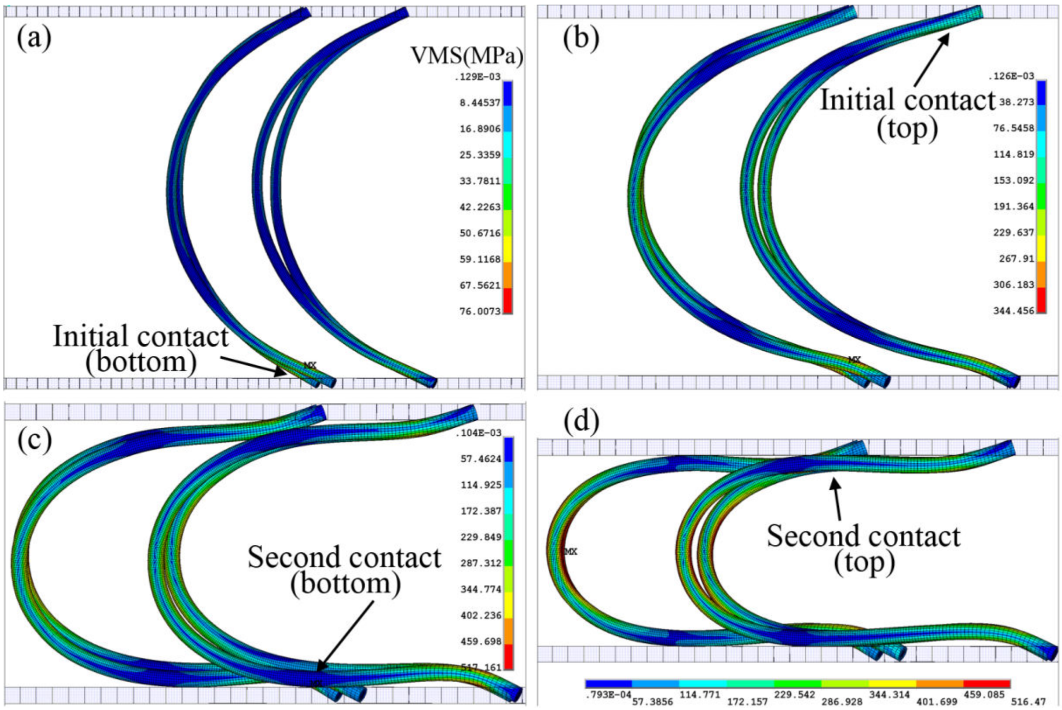

Figure 5.33 Contacts between the pillar spacer monofilaments and the outer fabric layers at different displacements: (a) 0.05 mm; (b) 1.6 mm; (c) 4 mm; (d) 4.5 mm.

It should be noted that the simulated and experimental load–displacement curves are not completely identical. In the experiment, the fabric reaches the final stage at the displacement of about 5 mm; however, in the simulation, it is about at the displacement of 4.5 mm. The reasons for the difference are the assumptions, not precisely describing the nonlinear interactions between the spacer monofilaments and the outer layers in the real fabric, made in the FE model, including:

- The constraints applied on the spacer monofilaments in the FE model are not completely identical to the real constraints provided by the outer layers to the spacer monofilaments.
- In the FE model, the outer fabric layers are assumed to be continuous and have smooth surfaces. In fact, the outer layers are complex, discontinuous,

uneven, and wavy both along coursewise and walewise directions. The nonlinear mechanical properties of the outer layers are assumed to be linear elastic, thereby affecting the predictive accuracy.

- Only eight spacer monofilaments are included in the FE model. The spacer monofilaments are of initial imperfections, and their initial shapes are not identical in a spacer fabric due to the complicated manufacturing process. The imperfections can affect the simulated results. Besides, the contacts among spacer monofilaments also affect the simulated results, and the eight spacer monofilaments are not enough to fully include this effect.
- The compression between the spacer monofilaments and the multifilament stitches are neglected in the model.

5.5 Parametric study

This section presents a parametric study to numerically investigate effects of structural parameters on spacer fabric compression behaviour based on the FE model FE-0.2-p. The structural parameters to be investigated include spacer monofilament inclination angle, fabric thickness and spacer monofilament fineness.

5.5.1 Effect of spacer yarn inclination angle

The FE model FE-0.2-p for the spacer fabric S1 has four pillar and four tricot spacer monofilaments. To investigate the effect of the spacer monofilament inclination angle on the compression behaviour, on the basis of FE-0.2-p (Figure 5.34(b)), the X coordinates of the nodes of the four tricot spacer monofilaments were adjusted, while their Y and Z coordinates are kept unchanged. In this way, the number of needles space underlapped can be adjusted, thereby changing the tricot spacer yarn inclination angle. The adjustment procedure can be briefly summarised as follows:

1. The X coordinates of the tricot spacer monofilament endpoints in the top outer layer remain unchanged.
2. From top to bottom, except for the endpoints in the top layer, each node in each tricot spacer monofilament was moved along X-axis to adjust the distance between the present and previous nodes. For the FE model with one-needle space underlapped, the original distances were multiplied 0.5 (Figure 5.34(a)). For the FE model with three-needle space underlapped, the original distances were multiplied 1.5 (Figure 5.34(c)).

Except for these geometric adjustments, other settings of the FE models are exactly the same as those of FE-0.2-p.

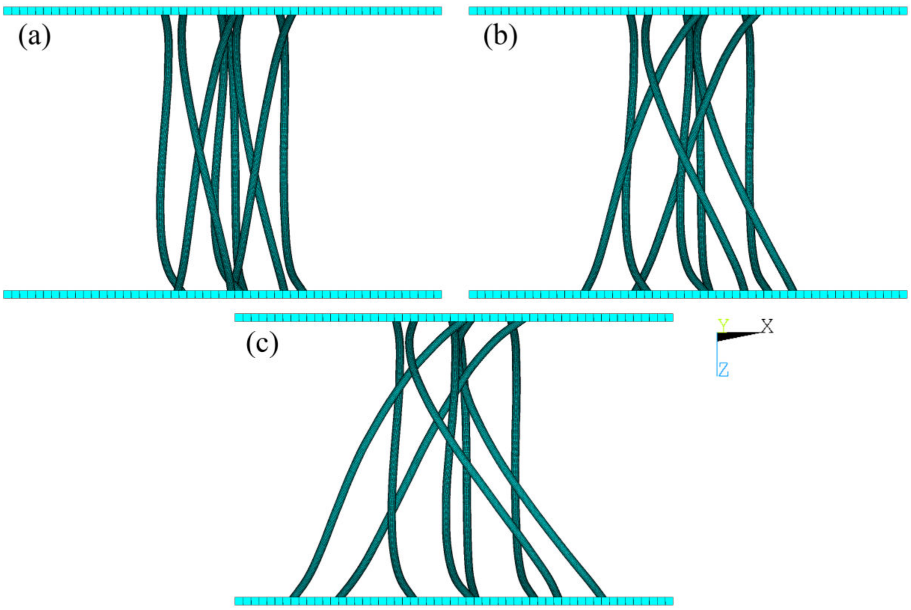

Figure 5.34 FE models with different numbers of needles space underlapped: (a) one-needle; (b) two-needle, FE-0.2-p; (c) three-needle.

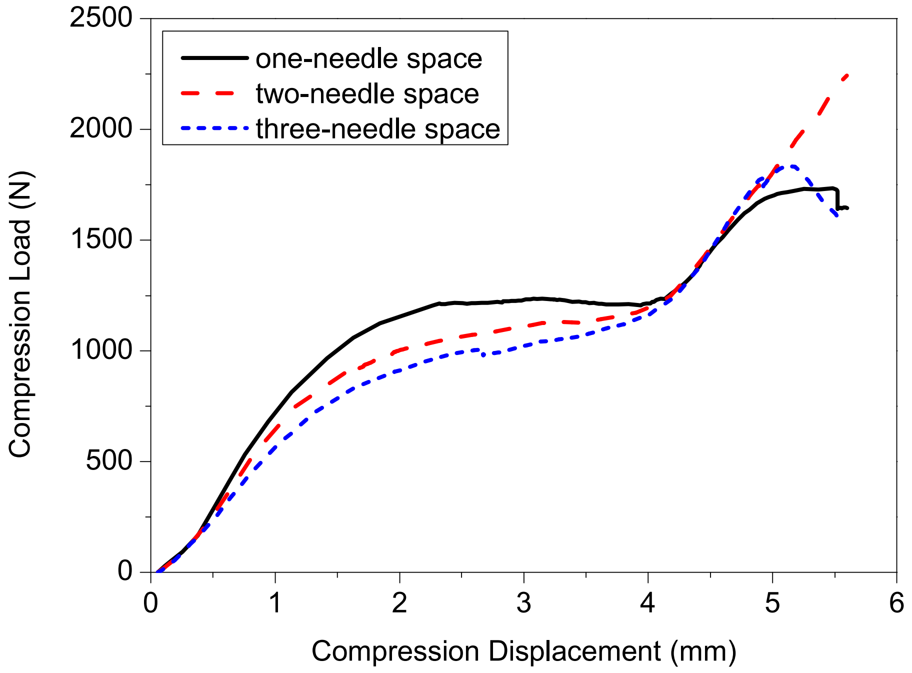

Figure 5.35 Load–displacement relationships of the FE models with different numbers of needles space underlapped.

The simulated results shown in Figure 5.35 indicate that the compression resistance increases as the spacer monofilament inclination decreases. However, in the densification stage, both the FE models with the lowest and highest numbers of needles space underlapped undertake instabilities. Hence, the more the spacer monofilaments orient to the outer fabric layers, the higher the compression resistance of the spacer fabric possesses.

5.5.2 Effect of spacer yarn fineness

In FE-0.2-p, the spacer monofilaments were meshed using beam elements with a circular beam section of 0.1 mm in radius. To evaluate the influence of the spacer monofilament fineness on the compression behaviour, two extra FE models were created by varying the spacer monofilament radius. For the FE models (Figure 5.36), two radii, i.e., 0.05 mm and 0.08 mm, are used, and other parameters are kept constant.

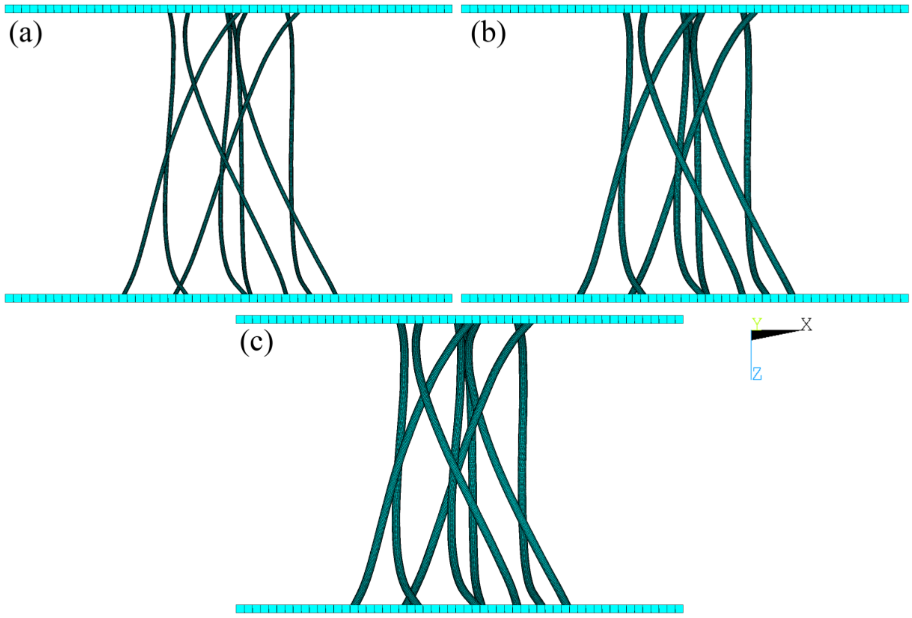

Figure 5.36 FE models with different radii of the spacer monofilaments: (a) 0.05 mm; (b) 0.08 mm; (c) 0.1 mm, FE-0.2-p.

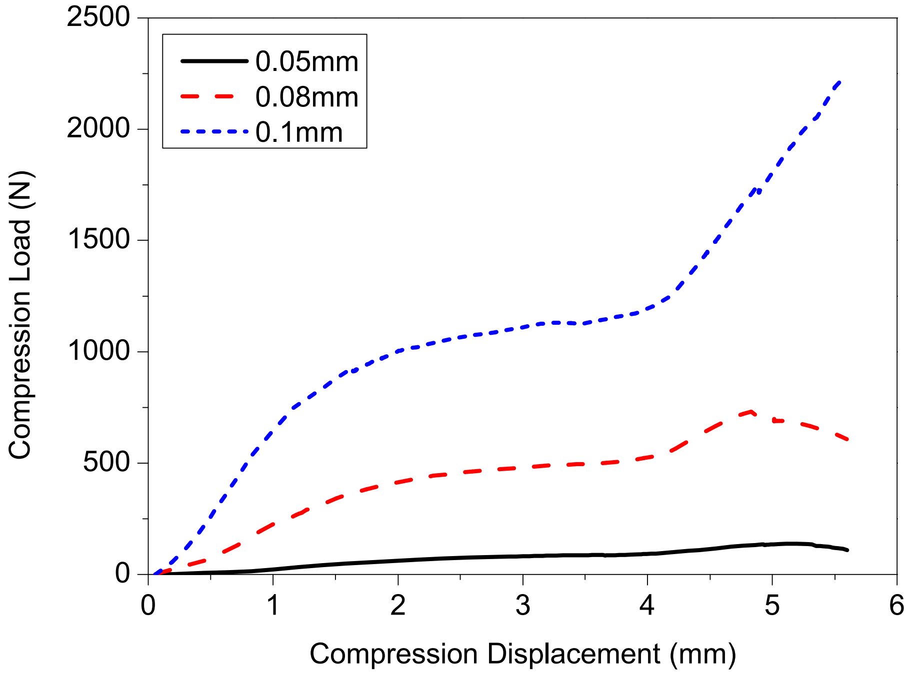

Figure 5.37 Load–displacement relationships of the FE models with different radii of the spacer monofilaments.

As shown in Figure 5.37, the FE model with coarser spacer monofilaments gives a stiffer mechanical response. The physical basis for this result is that the spacer monofilament fineness directly influences its bending rigidity. By virtue of Equation (4.19), the bending rigidity is proportional to the fourth power of the radius. Consequently, the fabric compression resistance can be increased dramatically when the spacer monofilament radius is increased. This FE simulated result is consistent with the analytical result presented in Section 4.5.2.

5.5.3 Effect of fabric thickness

To investigate the effect of the fabric thickness on the compression behaviour of spacer fabrics, two extra FE models were created as shown in Figure 5.38. In the μCT scanning, one slice of the scanning image represents 0.021 mm through the specimen thickness. It is easy to adjust the fabric thickness by assigning different values to the thickness of one slice. Herein, two values, 0.015 mm and 0.03 mm, are selected with the resultant fabric thicknesses 5.08 mm and 10.17 mm, respectively.

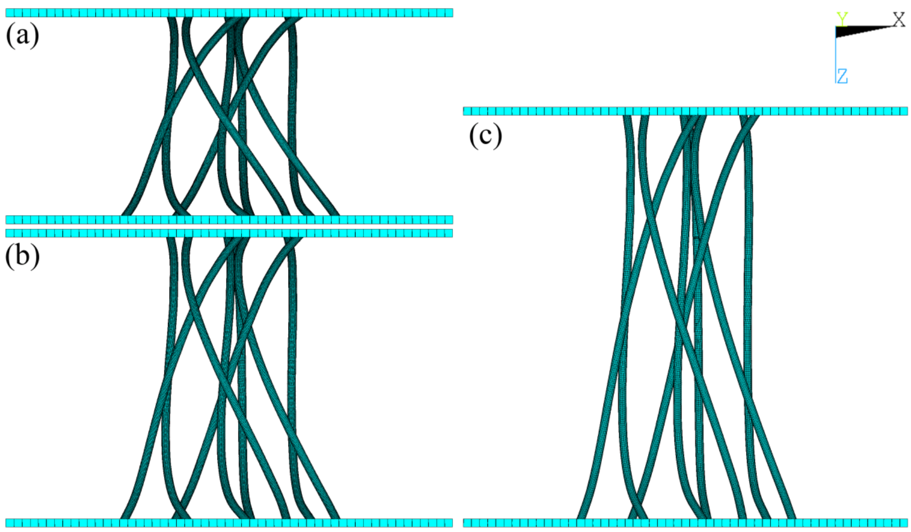

Figure 5.38 FE models with different fabric thicknesses: (a) 5.08 mm; (b) 7.52 mm, FE-0.2-p; (c) 10.17 mm.

The simulated results in Figure 5.39 show that the compression resistance increases with decreasing the fabric thickness. The higher the fabric thickness, the longer the plateau stage of the fabric, which agrees with the analytical result presented in Section 4.5.4.

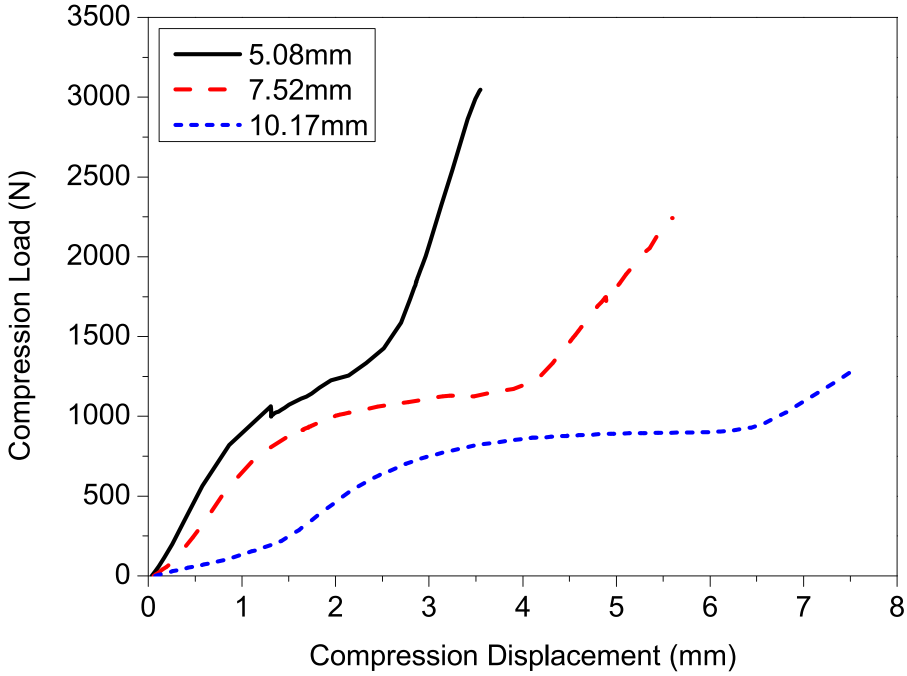

Figure 5.39 Load–displacement relationships of the FE models with different fabric thicknesses.

To summarise, the parametric study proves that the developed FE model is effective in assessing the effects of the structural parameters on the compression behaviour of spacer fabrics. It should be emphasized that, except for FE-0.2-p, the geometric models for the FE models employed in this parametric study are not based on real spacer fabrics. The parametric simulation only provides a general view on the relationship between the structural parameters and the compression behaviour rather than simulates real spacer fabrics.

5.6 Conclusions

In this chapter, finite element modelling of the spacer fabric S1 with a typical structure in compression has been carried out. The precise geometric model from μCT scanning has been used to establish the FE models. The constraints on the spacer monofilaments and the outer fabric layer thickness have been determined by adjusting numerical models. With the developed FE models, the test boundary condition effect and the compression mechanism of the spacer fabric have been investigated. In addition, a parametric study has also been conducted to assess the effects of the structural parameters on the compression properties of spacer fabrics. According to the analyses, the following conclusions can be drawn.

- The rotational DOFs at the tricot and pillar spacer monofilament endpoints are not identical under compression.
- The position that the spacer monofilaments contact the outer layers is in between two side limbs of two neighbouring needle loops.
- If the friction coefficients of employed compression platens are different, the postbuckling modes of the spacer monofilaments, the contacts among the spacer monofilaments, and the contacts between the spacer monofilaments and the outer layers can be different due to the in-plane shear and rotation of the outer fabric layers.
- In the initial stage, the pillar spacer monofilaments contact the bottom outer layer, while the tricot spacer monofilaments undertake free postbuckling. In the linearly elastic stage, the tricot spacer monofilaments start to contact the two outer layers. The additional constraints provided by the contacts lead to a rapid rise of total reaction force. In the plateau stage, all the spacer monofilament end sections are in contact with the outer layers. While the

tricot spacer monofilaments undertake large torsion, the contacts among the spacer monofilaments lead to the shear and rotation of the pillar spacer monofilament middle sections; therefore, a nearly constant reaction force is obtained in this stage. In the densification stage, the pillar spacer monofilament middle sections contact the two outer layers. The length between the two contacting points for each pillar spacer monofilament decreases with the increase of displacement. As a consequence, the total reaction load rises dramatically.

- The spacer fabric with a smaller spacer yarn inclination, coarser spacer yarn and lower fabric thickness has higher compression resistance.

From the experimental study presented in Chapter 3, and the theoretical modelling in Chapter 4 and Chapter 5, the compression mechanism of the typical spacer fabric is clear. The studies have also identified the structural parameters affecting the compression properties of spacer fabrics. The succeeding two chapters focus on the effects of the identified structural parameters on both the flatwise static and impact compression behaviour of spacer fabrics.

CHAPTER 6 EFFECTS OF STRUCTURAL PARAMETERS ON COMPRESSION AND CUSHIONING PROPERTIES OF WARP-KNITTED SPACER FABRICS

6.1 Introduction

In Chapter 4, the analytical model for predicting the compression properties of warp-knitted spacer fabrics was established. The structural parameters affecting the compression properties of warp-knitted spacer fabrics, including spacer yarn inclination, spacer yarn diameter, course density and fabric thickness, have been identified with the analytical model. Chapter 5 presented the further theoretical work by FE modelling with the precise geometric model. It has been shown that the FE simulated result agrees well with the experimental result. In addition, the structural parameters, including spacer monofilament inclination and fineness as well as fabric thickness, were used to conduct a parametric study for assessing their effects on the compression behaviour of spacer fabrics.

This chapter aims to validate the FE parametric study on structure–property relationships with experimental results from flatwise compression tests. In addition, this chapter also aims at developing warp-knitted spacer fabrics as cushioning materials for human body protection, with an attempt to enlarge the plateau zone and reasonably control the load level in the plateau stage. For this purpose, a series of warp-knitted spacer fabrics were produced by varying the identified influencing structural parameters, i.e., spacer yarn inclination angle and fineness, fabric thickness, and outer layer structure. In addition to the compression properties, the attention is also paid to the cushioning performance of those spacer fabrics. The compression tests for the typical spacer fabric S1 under two test conditions (not glued and glued) and in different sizes were described in Chapter 3, in which an appropriate compression test method was selected. The selected test method was also used in the compression tests described in this Chapter.

This chapter is organized as follows. Firstly, the cushioning behaviour of a typical spacer fabric is analysed based on its compression stress–strain relationship. Secondly, an energy–absorption diagram is defined to better understand the cushioning property of the spacer fabric. Thirdly, the effects of the structural parameters, including spacer yarn inclination angle and fineness, fabric thickness, and outer layer structure, on the compression behaviour and the cushioning properties are discussed, respectively. Their experimental results are interpreted through stress–strain curves to validate the FE parametric study results presented in Chapter 5. Meanwhile, the experimental results are also discussed by means of energy–absorption diagrams to analyse the cushioning performance. It is expected that a clear picture for tailoring a warp-knitted spacer fabric with promising cushioning properties could be established from the study presented in this chapter.

6.2. Experimental

6.2.1 Samples

Twelve warp-knitted spacer fabrics were produced on the same GE296 high speed double-needle bar Raschel machine of gauge E18 as that used for the spacer fabric S1 studied in Chapter 3. Similarly, whereas 300D/96F polyester multifilament was used to create the binding structure in the knitting process through GB1, GB2 for the top outer layer and GB5, GB6 for the bottom outer layer, the polyester monofilament of 0.2 mm in diameter was used as spacer yarns to connect the two outer layers together through GB3 and GB4. Four different structures, i.e., locknit, chain plus inlay, small-size rhombic mesh, and large-size hexagonal mesh, were used for knitting the outer layers. The chain notation for each of these structures is shown in Table 6.1. Three different yarn guide bar lapping movements were used for the spacer yarns to connect two outer layers with different inclination angles. The chain notation for each movement is shown in Table 6.2. By considering different outer layer structures, different lapping movements of the spacer yarn guide bars, and different fabric thicknesses, eleven spacer fabric samples were produced. With one extra sample made with finer spacer yarn (0.16 mm in diameter), a total of twelve spacer fabric samples were tested. After the knitting process, the fabrics were subjected to a heat setting treatment at a temperature of 180 ºC for 3 minutes. The details of all the fabric samples after heat setting are listed in Table 6.3.

Table 6.1 Chain notation of yarn guide bars for outer layers

Structure	GB1/GB6	GB2/GB5	Threading
Locknit (L)	1-0 0-0/3-2 3-3//	2-1 1-1/ 1-0 0-0//	full
Chain+ Inlay (CI)	0-0 0-0/ 5-5 5-5//	1-0 0-0/ 1-0 0-0//	full
Rhombic Mesh (RM)	1-0 0-0/1-2 2-2/2-3 3-3/2-1 1-1//	2-3 3-3/2-1 1-1/1-0 0-0/ 1-2 2-2//	1 full 1 empty
Hexagonal Mesh (HM)	(1-1 1-0/ 3-3 3-2)×3/(4-4 5-4 /3-3 3-2)×3//	(4-4 5-4/3-3 3-2)×3/(1-1 1-0/3-3 3-2)×3//	2 full 2 empty

Table 6.2 Chain notation of yarn guide bars for spacer yarns

Lapping	GB3	GB4	Threading
I	1-0 2-1/2-1 1-0//	2-1 1-0/1-0 2-1//	1 full 1 empty
II	1-0 3-2/3-2 1-0//	3-2 1-0/1-0 3-2//	1 full 1 empty
III	1-0 4-3/4-3 1-0//	4-3 1-0/1-0 4-3//	1 full 1 empty

Table 6.3 Details of the spacer fabrics

Fabrics	Top outer layer	Spacer layer	Bottom outer layer	Thickness (mm)	Areal density (g/m^2)	Bulk density (kg/m^3)	Stitches / cm^2
S1	L	II	L	7.52 ±0.06	1008.29 ±10.68	134.08 ±1.42	41.15
S2	CI	I	CI	7.57 ±0.08	900.11 ±9.01	118.87 ±1.19	37.95
S3	CI	II	CI	7.59 ±0.10	901.75 ±14.58	118.84 ±1.92	37.26
S4	CI	III	CI	7.40 ±0.06	923.20 ±8.44	124.76 ±1.14	37.95
S5	CI	II	CI	5.64 ±0.03	790.63 ±14.51	140.08 ±2.57	34.98
S6	CI	II	CI	8.45 ±0.09	1022.08 ±13.38	120.96 ±1.58	43.50
S7	CI	II	CI	10.62 ±0.10	1010.42 ±8.83	95.14 ±0.83	37.95
S8	RM	II	CI	7.20 ±0.05	830.05 ±11.53	115.22 ±1.60	39.33
S9	RM	II	RM	7.76 ±0.06	907.24 ±17.07	116.91 ±2.20	51.10
S10	HM	II	CI	7.56 ±0.08	812.70 ±6.61	107.50 ±0.87	37.95
S11	HM	II	HM	7.62 ±0.06	724.82 ±8.34	95.17 ±1.10	38.86
S12	CI	III	CI	7.06 ±0.09	746.53 ±6.81	105.68 ±0.96	39.44

6.2.2 Compression tests

The specimens of the spacer fabrics were tested on the same Instron 5566 Universal Testing Machine as used in Chapter 3. The size of all the specimens was 10 cm × 10 cm. The compression tests were conducted at a speed of 12 mm/min up to a deformation 80% of the initial thickness of each fabric in an environment of 20 °C and 65% relative humidity. Each specimen was tested under two test conditions as defined in Chapter 3, i.e., either the specimen was simply placed on the fixed platen (not glued case) or two surfaces of the specimen were glued to the platens using double-side adhesives (glued case) to avoid possible outer layer movements. Five tests were carried out for each sample under each test condition. Unless otherwise specified, each compression stress–strain curve presented is the curve close to an average of the five test results. It was found that, except for sample S2, the overall stress–strain curves of one sample under the above two test conditions are similar for the other samples. Only slight difference in plateau stage can be observed for samples S3–S12 as the results of sample S1 presented in Chapter 3. However, there is a significant deviation in the results of sample S2 under the two test conditions. Therefore, the results of sample S2 under the above two test conditions are presented, while for the other samples only the test results without gluing specimens to the platen surfaces are presented throughout this chapter.

6.3 Cushioning properties

6.3.1 Typical cushioning behaviour

Figure 6.1 shows a typical compression stress–strain curve of a spacer fabric sample (S1) under the not glued test condition. As treated in Chapter 3, the compression process is divided into four different stages, i.e., initial stage (stage I), elastic stage (stage II), plateau stage (stage III), and densification stage (stage IV), according to the changes in the slope of the curve. It can be found that the spacer fabric possesses good cushioning effect because a nearly constant compression stress in stage III is obtained with a displacement range of about 3.6 mm, which is nearly half of the initial thickness (7.52 mm) of the fabric and corresponds to a strain of almost 50%. This behaviour is just the requirement for cushioning applications. From the initial stage I to the end of stage III, the area under the curve represents the energy absorbed by the fabric within the fairly constant stress. It should be noted that the compression test was conducted at a low strain rate (12 mm/min). Although the fabric will not have exactly the same behaviour at higher strain rates under impact, the absorbed energy calculated at the low strain rate can still be used as a good reference to evaluate the cushioning performance of a warp-knitted spacer fabric because it is relatively equivalent to the absorbed kinetic energy of a mass that might impact on the fabric.

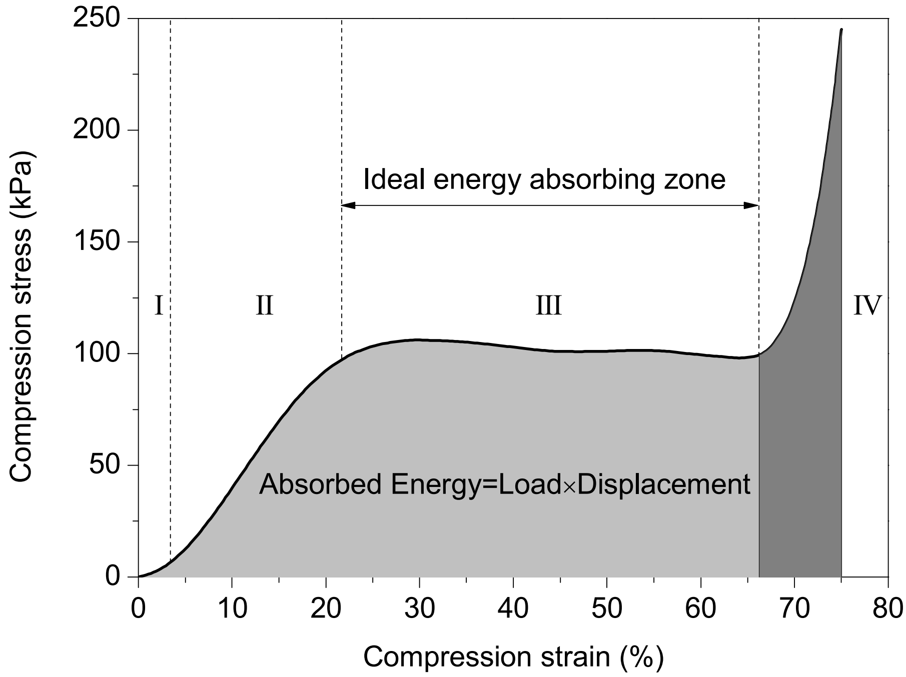

Figure 6.1 A typical compression stress–strain curve of the spacer fabric S1.

It is necessary to point out that an optimum energy-absorbing material should dissipate the impact energy while keeping the load below the allowable limit. Thus, two criteria should be considered. One is the amount of the energy needed to be absorbed by the impacted object, and the other is the stress with specific impact area to be allowed. As shown in Figure 6.1, the energy absorbed by the fabric is low in the densification stage, but the stress steeply increases. In this circumstance, for a specific application, the fabric preferably dissipates all the energy before reaching the densification stage in order to prevent the unpredictably increased reacting stresses in this insecure stage. In addition, it is necessary to ensure that the stress in the plateau zone of the fabric is lower than the maximal stress allowed to the protected object. Thus, the amount of the energy absorbed before the densification stage and the stress level in the plateau stage should be two key parameters needed to be optimized for a warp-knitted spacer fabric to meet the requirements of a specific end-use.

6.3.2 Energy–absorption diagram

The above analysis shows that the determination of the energy absorbed by a spacer fabric under compression is important. Although the stress–strain curve can directly show the energy–absorption behaviour of a spacer fabric, it would be more useful to use the energy–absorption diagram to get a better understanding on the cushioning behaviour of the spacer fabric. An energy–absorption diagram is obtained by plotting the absorbed energy per unit volume W_c as a function of the stress σ [20]. The absorbed energy per unit volume is the area under the stress (σ)-strain (ε) curve calculated according to Equation (6.1)

$$W_c = \int_0^{\varepsilon} \sigma(\varepsilon)\, d\varepsilon. \qquad (6.1)$$

As the function required for a cushioning material is to absorb as much as possible of the energy generated during impact and to transmit a force lower than the allowable value, an ideal cushioning material can be defined as one that transmits an allowable constant force to the protected object over a given range of compression strains. However, it is difficult to produce such an ideal cushioning material, and real materials generally have the stress–strain curve as shown in Figure 6.1. In order to better understand the energy–absorption capacity of a cushioning material, the energy–absorption efficiency E_c can be used to analyse its energy–absorption process. The efficiency E_c is defined as the ratio of the energy absorbed by a real cushioning material compressed to a given strain and energy absorbed by an ideal cushioning material that transmits a constant stress of the same value at the same given strain. It is useful to plot the efficiency as a function of the stress to obtain the indication for optimum usage. The efficiency E_c is expressed by Equation (6.2)

$$E_c = \frac{A_c h_c \int_0^{\varepsilon} \sigma(\varepsilon) d\varepsilon}{A_c h_c \sigma} = \frac{\int_0^{\varepsilon} \sigma(\varepsilon) d\varepsilon}{\sigma}, \tag{6.2}$$

where A_c and h_c are the area and the thickness of the cushioning material, respectively; σ is the stress at the strain ε. Both absorbed energy-stress and efficiency–stress curves of sample S1 are shown in Figure 6.2 as an example. It can be found that the absorbed energy steadily increases with the stress from the beginning of compression. However, when the stress approaches the plateau stress, a dramatic increase of the absorbed energy is observed, although the stress is maintained almost unchanged in this zone. After that, the absorbed energy slowly increases with a rapid rising of the stress. From the absorbed energy-stress curve, it is easy to determine the associated stress of a fabric for a given amount of energy to be absorbed; therefore, it is convenient to select an appropriate fabric or to optimize the fabric performance for a specific application for which the amount of energy to be absorbed and the allowable stress level are specified.

For the efficiency–stress curve, the same tendency is observed until the densification stage starts. The maximum energy–absorption efficiency is obtained at the end of the plateau stage. After this point, the efficiency starts to decrease because the fabric density rapidly increases due to the densification of the entire structure. The point at the maximum energy–absorption efficiency can also be considered as a critical point between the plateau zone and the densification zone. In this study, this point is used to define the plateau stress, which is calculated by dividing the plateau load to the area of the specimen. In order to better understand the relationship between the energy–absorption efficiency and the stress, the contours of the energy absorbed per unit volume (iso-energetic curves), calculated by multiplying E_c and σ, i.e., $E_c\sigma$, are also drawn in Figure 6.2. For example, point A on the contour of 20 kJ/m^3 is a multiplication of stress 50 kPa and efficiency 0.4. From these contours, it can be seen that for a given stress the higher the efficiency–stress curve, the higher the energy is absorbed. While the efficiency–stress curve can intuitively show the maximum efficiency point, the contours of the energy absorbed per unit volume can clearly demonstrate the amount of the energy at this point. In addition, both efficiency–stress curves and contours of the energy absorbed can be useful for the determination of the preferable working range of the fabric. Therefore, for a prescribed amount of energy to be absorbed, the better cushioning performance for a spacer fabric should function at a lower stress level but with a higher efficiency. As the efficiency diagram including efficiency–stress curves and the contours of the energy absorbed is easy to use and has a sound fundamental basis, they will be used throughout this chapter to investigate the effects of different structural parameters, including the spacer yarn inclination and fineness, fabric thickness and outer layer structure, on the compression behaviour of the warp-knitted spacer fabrics for cushioning applications.

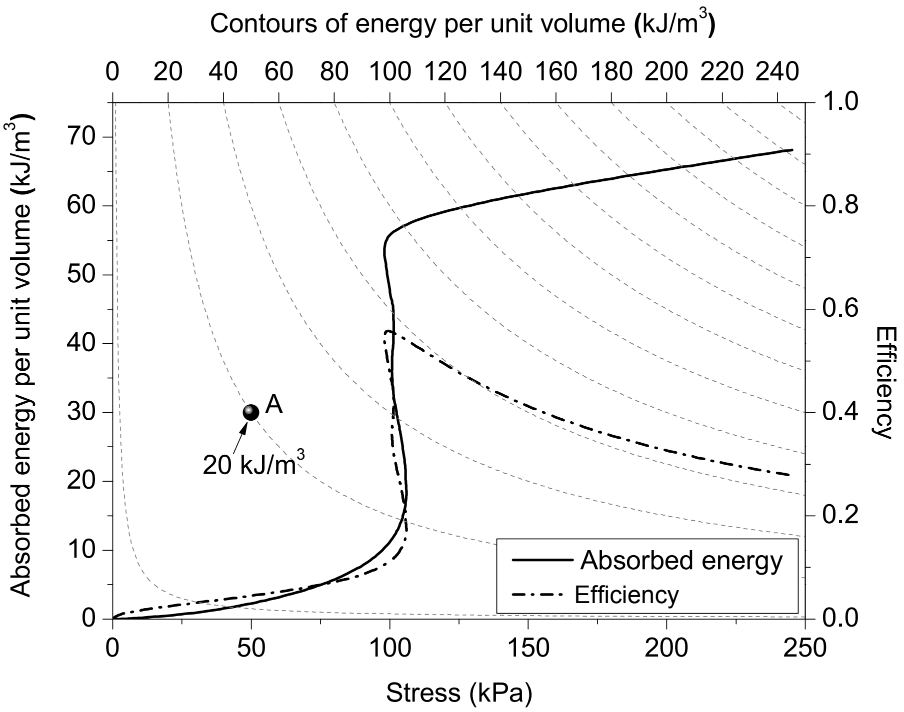

Figure 6.2 Typical energy-stress and efficiency–stress curves of the spacer fabric S1.

6.4 Effects of structural parameters

6.4.1 Effect of spacer yarn inclination angle

Spacer yarns are used to connect two outer layers, and their inclination angle and length depend on the number of needles underlapped between the front- and back-needle bars. In order to investigate the effect of spacer yarn inclination on the compression behaviour of warp-knitted spacer fabrics, three fabric samples (S2, S3 and S4) with three different numbers of needles underlapped, i.e., 1-0/2-1, 1-0/3-2, and 1-0/4-3, are used for the comparison study. These fabrics have the same outer layer structure (type CI). At the same time, their other parameters are nearly the same (Table 6.3).

The cross-sectional microscopic pictures of these three fabrics observed from the walewise direction are shown in Figure 6.3. There are two types of spacer yarns in each of the three fabrics, i.e., pillar spacer yarn and tricot spacer yarn as defined in Chapter 4. Since the pillar spacer yarns are nearly vertical observed from walewise, only the effect of the different inclinations of the tricot spacer yarns of the three fabrics on their compression properties is analysed. While the inclination angles of the selected left oblique tricot spacer yarns for S2, S3 and S4 are 5.86º, 22.15º and 37.42º, respectively, those of the right oblique tricot spacer yarns are 13.66º, 23.13º and 33.55º, respectively, for the same fabrics. These differences in inclination angle between the left and right oblique tricot spacer yarns originate from the difficulty of producing the fabrics with exactly symmetrical tricot spacer yarns in a complicated manufacturing and finishing process. Obviously, the spacer yarn inclination angle increases as the number of needles underlapped increases. The biggest difference of the spacer yarn inclination angles between the left and right oblique tricot spacer yarns was observed in sample S2, which is 7.8º. This big difference in spacer yarn inclination angles makes sample S2 asymmetric and unstable in the fabric structure, which leads to the occurrence of shear between two outer layers along the coursewise direction under compression. As a result, the compression stress–strain curve of S2 has a sharp drop in the plateau zone, as clearly shown in Figure 6.4(a). In order to avoid the influence of shear, the outer layer surfaces of the fabric were glued to the compression platens before testing. The test result under this condition is also shown in Figure 6.4(a). As expected, the sharp drop disappears. The curves for samples S3 and S4 are also shown in Figure 6.4(a) for the comparison. It is found that the compression resistance of the spacer fabrics in the initial and elastic stages increases as the spacer yarn inclination angle decreases. This result is consistent with the FE simulation in Section 5.5.1. However, after the strain reaches about 47.5%, the situation is getting opposite. From this point to the end of the plateau zone, the plateau stress of sample S2 has an obvious drop, but that of sample S4 has a slight increase. The plateau stress of sample S3 remains nearly constant.

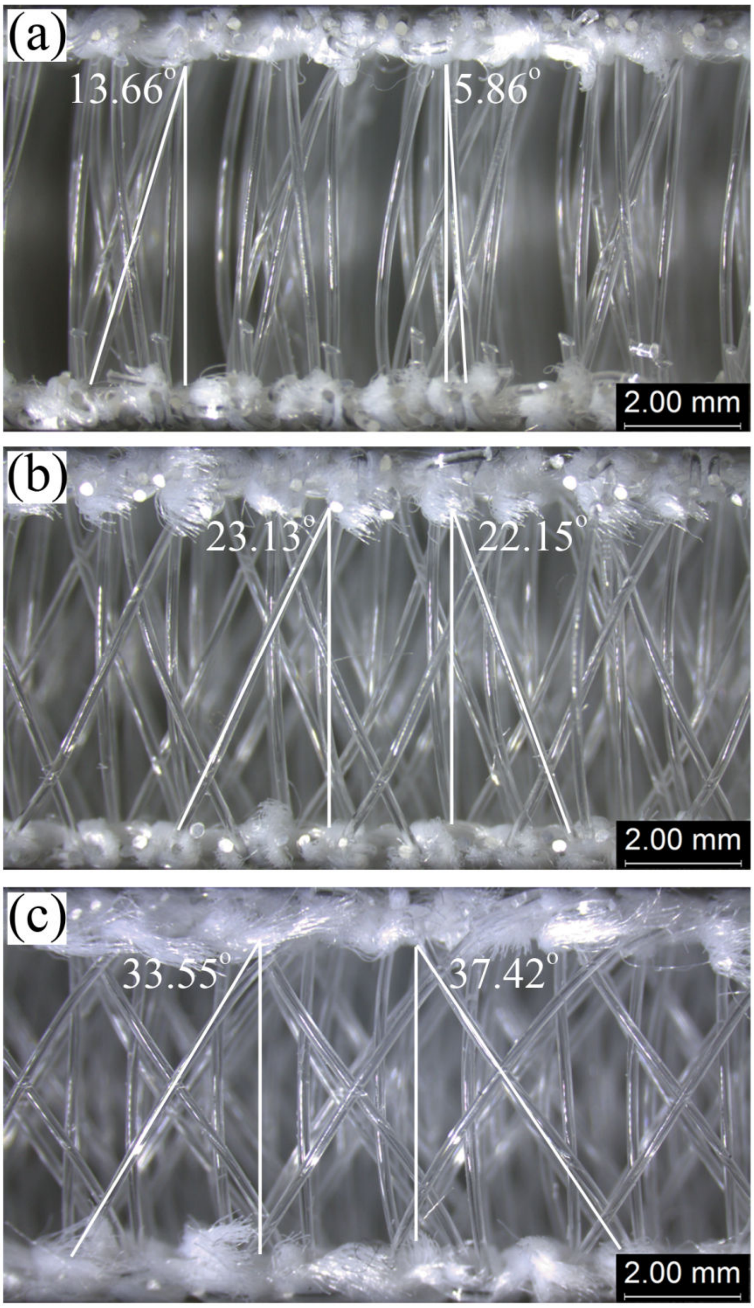

Figure 6.3 The cross-sectional microscopic pictures of the warp-knitted spacer fabrics observed from the walewise direction: (a) Sample S2; (b) Sample S3; (c) Sample S4.

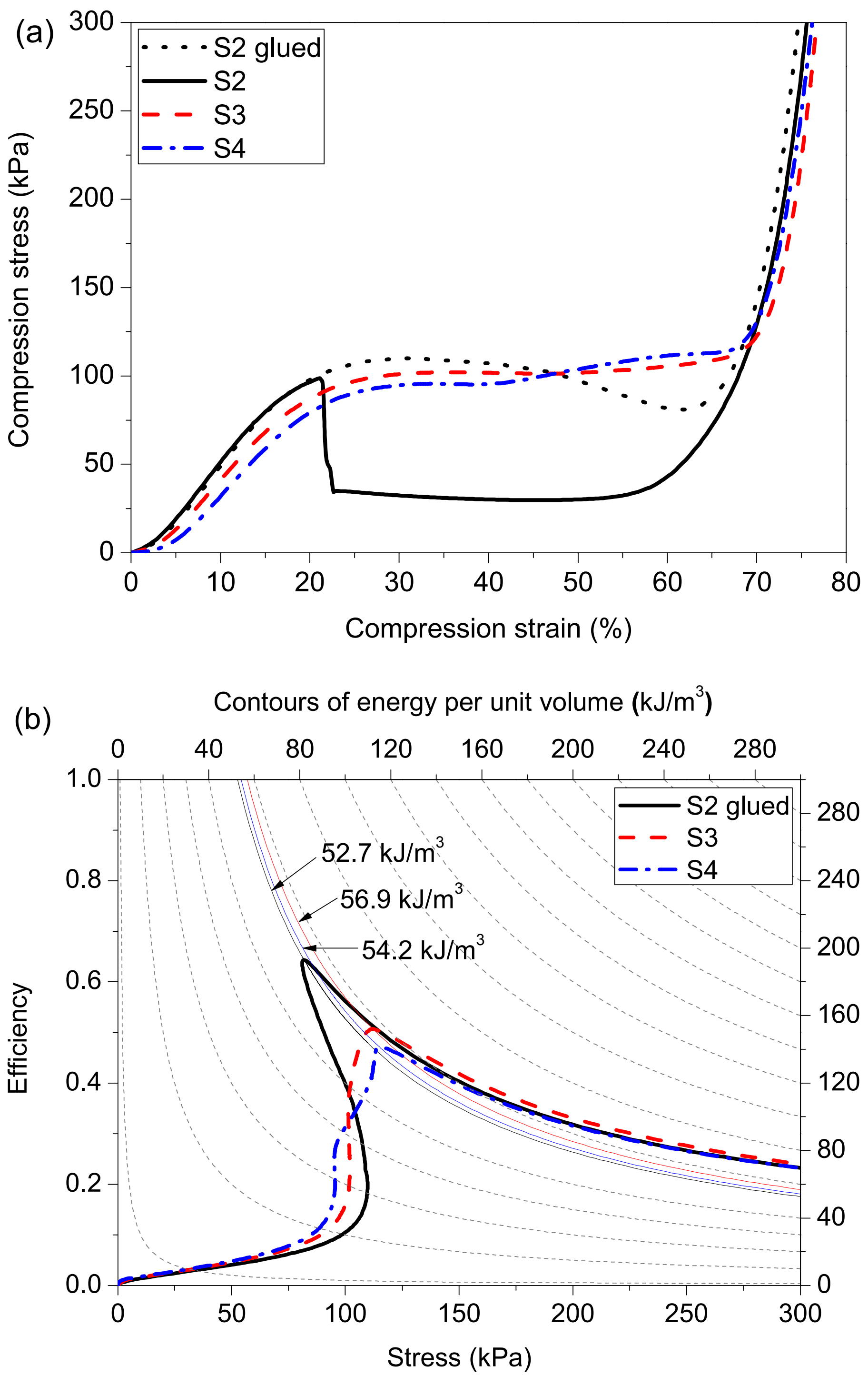

Figure 6.4 Effect of the spacer yarn inclination angle on the compression behaviour of the spacer fabrics: (a) Stress–strain curves; (b) Efficiency diagram.

The efficiency diagram, i.e., efficiency–stress curves and contours of the energy absorbed per unit volume is shown in Figure 6.4(b). It is found that the maximum efficiencies of all these three fabrics are less than 0.7, which decrease with increasing the spacer yarn inclination angle. It can also be observed that the stress at the maximum efficiency point increases as the spacer yarn inclination angle increases. At lower energy levels less than about 35 kJ/m^3, sample S4 has the highest efficiency and therefore has the lowest stress for a given energy. However, after this energy level, its efficiency reverses. The behaviour of sample S2 is just the opposite of S4. Sample S3 exhibits the moderate performance on all occasions. In Figure 6.4(b), the contour of energy passing by the maximum efficiency point is also demonstrated for each fabric. It can be seen that sample S3 can absorb more energy than the others over a wide level of energy, so it has better cushioning performance.

In summary, the fabric with larger spacer yarn inclination angle has better cushioning performance at lower energy level, and the fabric with smaller spacer yarn inclination angle exhibits preferable cushioning property at higher energy level.

6.4.2 Effect of spacer yarn fineness

Two fabrics (S4 and S12) with the same number of needles underlapped for the spacer yarns (type III) and the same outer layer structure (type CI) but with two different diameters of spacer yarns (0.2 and 0.16 mm) are chosen to analyse the effect of spacer yarn fineness on the compression behaviour of warp-knitted spacer fabrics. These two fabrics have almost the same thickness, and their outer layer stitch densities are also very close (Table 6.3).

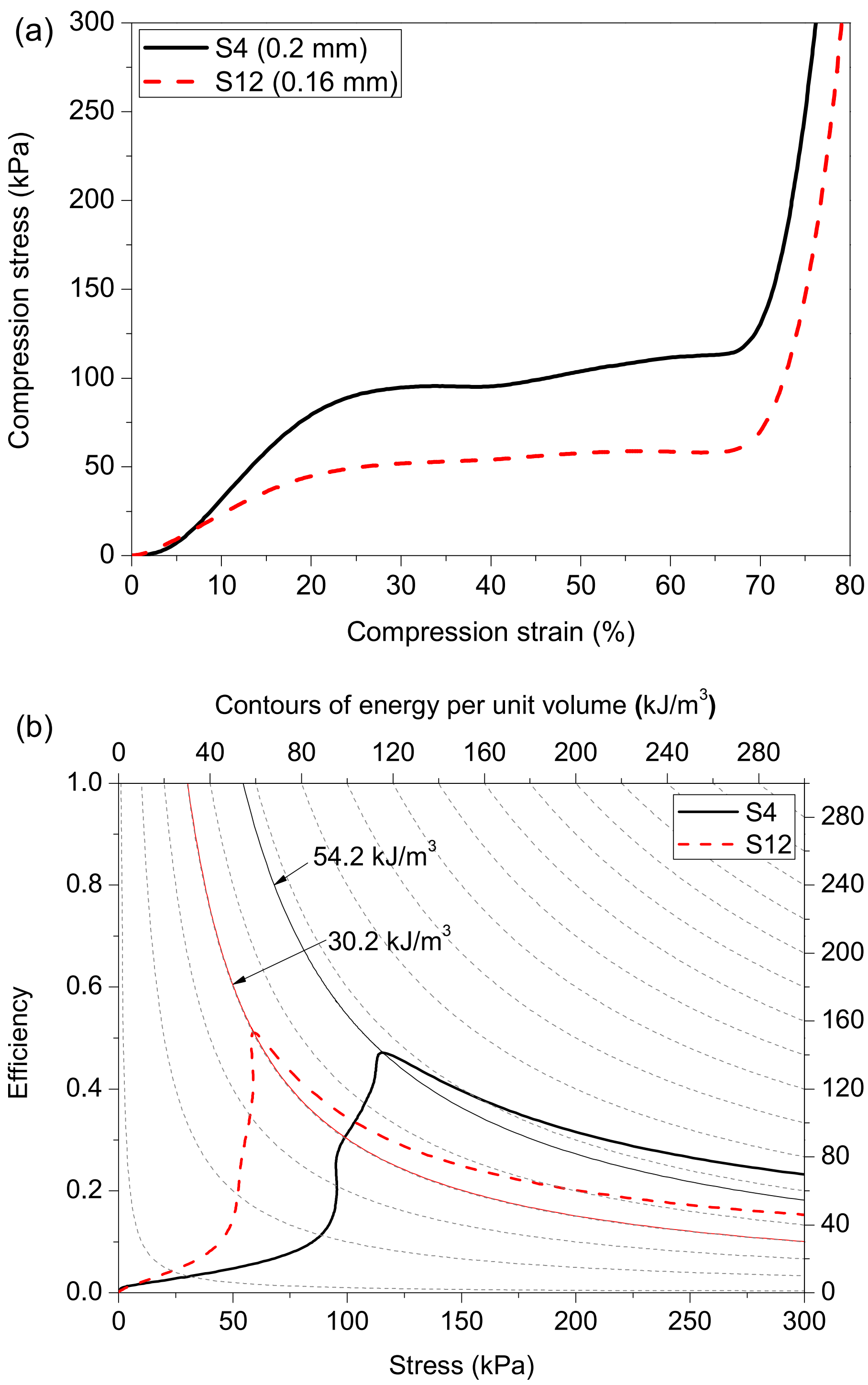

Figure 6.5 Effect of the spacer yarn fineness on the compression behaviour of the spacer fabrics: (a) Stress–strain curves; (b) Efficiency diagram.

The compression stress–strain curves of these two fabrics are shown in Figure 6.5(a). It can be seen that the fabric of a coarser spacer yarn has higher compression resistance and a higher value plateau. By referring to Figure 5.37, the FE simulated result agrees well with the experimental result. From the efficiency diagram shown in Figure 6.5(b), it is found that the maximum efficiency can be achieved at lower stress and energy for the fabric of a finer spacer yarn due to its lower plateau level. However, the energy at the maximum efficiency is much higher for the fabric of a coarser spacer yarn than that of the fabric of a finer spacer yarn, which indicates that the fabric of a coarser spacer yarn can absorb more energy but at a higher stress level. It should be stressed that the fabric of the spacer yarn of 0.16 mm in diameter has a high efficiency in a range of stresses lower than 100 kPa. Thus, for a given energy to be absorbed, the associated stress of the spacer fabric can be varied by simply adjusting the diameter of the spacer yarn according to the maximum stress allowed for a protected object to achieve a high efficiency of energy absorption. In a word, fabrics of a finer spacer yarn are suitable for lower energy absorption and lower stress levels, and fabrics of a coarser spacer yarn are suitable for higher energy absorption and higher stress levels.

6.4.3 Effect of fabric thickness

Four fabric samples (S5, S3, S6, and S7) produced with the same number of needles underlapped for the spacer yarns (type II) and the same outer layer structure (type CI) but with different thicknesses (5.64, 7.59, 8.45 and 10.62 mm) are used in this section to analyse the effect of fabric thickness on the compression behaviour of warp-knitted spacer fabrics.

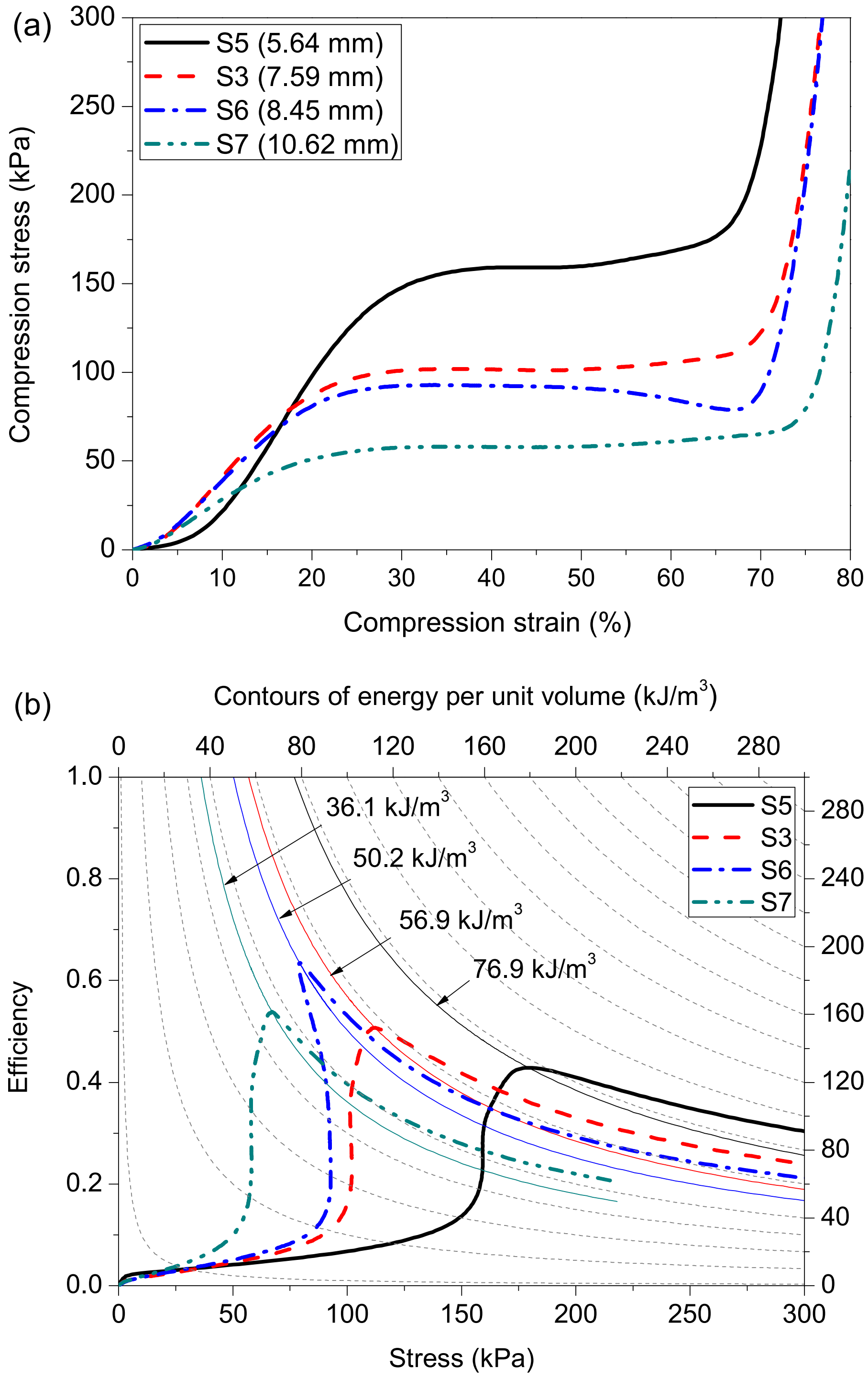

Figure 6.6 Effect of the fabric thickness on the compression behaviour of the spacer fabrics: (a) Stress–strain curves; (b) Efficiency diagram.

The stress–strain curves of the samples are shown in Figure 6.6(a). It is found that the compression resistance decreases as the fabric thickness increases. The thicker a fabric, the longer and lower plateau zone observed. With reference to Figure 5.39 presented in Chapter 5, the FE simulations agree well with the experimental results. The efficiency diagram is shown in Figure 6.6(b). It can be seen that the thicker fabric is able to absorb a specified amount of energy in a larger deformation but at a lower stress level due to its low-value plateau. In contrast, the thinner fabric does absorb the same amount of energy in a lower deformation but at a higher stress level. Furthermore, the thicker fabric reaches its maximum efficiency point at a lower stress and energy level, whereas the thinner fabric reaches its maximum efficiency point at a much higher stress and energy level. In these circumstances, the fabrics of different thicknesses have different ranges of applications and do not lend themselves to direct comparison. The fabric thickness should be selected according to the amount of the energy to be absorbed and the allowable stress level. Thus, by employing the efficiency diagram, the efficiency of a fabric can be optimized for a specific application.

6.4.4 Effect of outer layer structure

As the monofilaments in a spacer layer are bound by the multifilament stitches in the outer layer, the distribution, binding condition, and inclination angle of the spacer yarns can be affected by the outer layer knitted structure. In this regard, six fabrics (S1, S3, S8, S9, S10 and S11) with the same number of underlapped needles for spacer yarns (Type II) and nearly the same thickness but with different outer layer structures (Table 6.3) are chosen to investigate the effect of outer layer structure on the compression behaviour of warp-knitted spacer fabrics. The outer layer structures can be divided into three categories, i.e., both outer layers with close structure (S1 and S3), the top layer with open structure and the bottom layer with close structure

(S8 and S10), both outer layers with open structure (S9 and S11). As listed in Table 6.3, the close structures include locknit and chain plus inlay, and the open structures include small-size rhombic mesh and large-size hexagonal mesh. The outer layers of these structures are shown in Figure 6.7, from which the distribution, shape and size of the stitches in the outer layers can be clearly observed. It has been found that the outer layer structures can slightly affect the stitch density of the outer layers and the spacer yarn inclination angle, though these parameters are maintained the same during the knitting process.

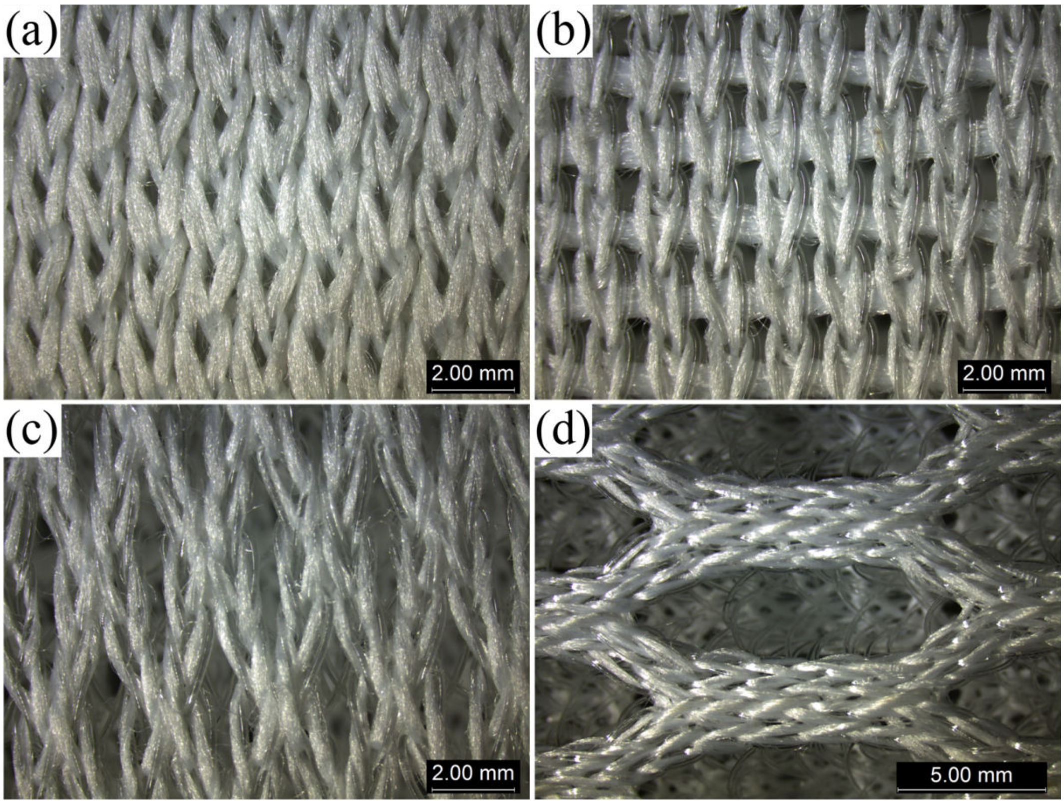

Figure 6.7 Pictures of outer layers: (a) locknit; (b) chain+inlay; (c) rhombic mesh; (d) hexagonal mesh.

The compression stress–strain curves are shown in Figure 6.8(a). It is found that in the initial and elastic stages, both samples S10 (HM+CI) and S11 (HM+HM) exhibit the lowest compression resistance compared with the other fabrics. In the plateau stage, sample S11 has the lowest value, but sample S10 has close value to that of S1 and S3 with close outer layer structures. These differences in compression behaviour come from the uneven distribution of the stitches, the changes in stitch density of the outer layers and the spacer yarn inclination angle due to changing outer layer structure. It is necessary to point out that samples S9 (RM+RM) and S8 (RM+CI) have higher value plateau than the others. This implies that small-size rhombic mesh structure has better stability and is more suitable for absorbing higher energy. The results also show that the fabrics with close outer layer structures (S1 and S3) have moderate compression resistance and plateau values.

The efficiency diagram is shown in Figure 6.8(b). It can be seen that while the fabrics with open structures in both outer layers (S11 and S9) have the lowest and highest values, respectively, of the energy absorbed at their maximum efficiency point, the fabrics with close structures in one or two outer layers (S1, S3, S8 and S10) have intermediate values between the lowest and highest values. These results show that a large range of the variations in the energy absorbed for different applications can be obtained with the open structures. While the fabric with the large-size hexagonal mesh structure in both outer layers can be used to absorb the energy at a lower stress level, the fabric with the small-size rhombic mesh structure can be used to absorb the energy at a higher stress level. Thus, the variation of the outer layer structure can be another approach to select the fabrics, which can absorb the same quantity of the energy, but with different stress levels for different applications.

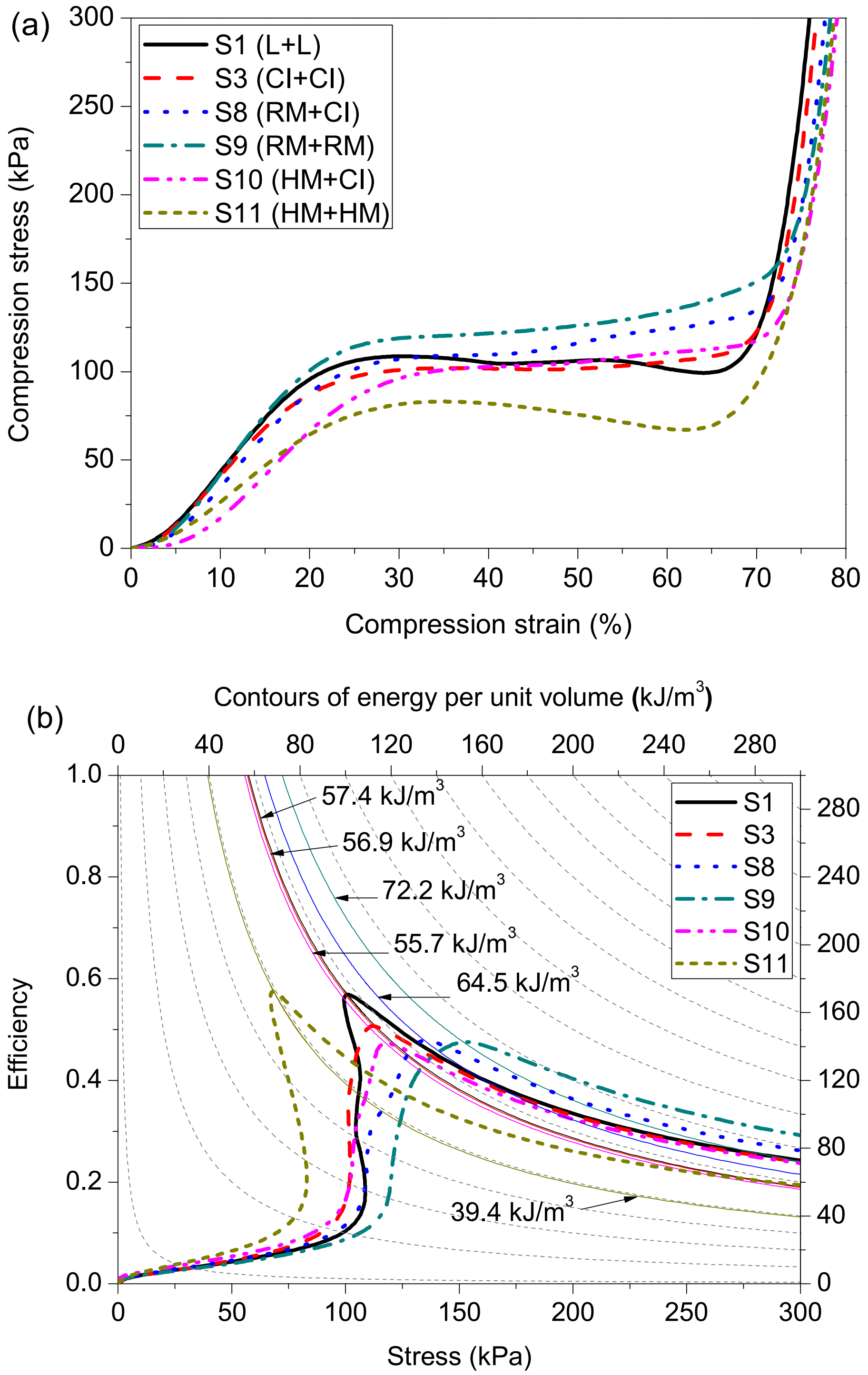

Figure 6.8 Effect of the outer layer structure on the compression behaviour of the spacer fabrics: (a) Stress–strain curves; (b) Efficiency diagram.

6.5 Conclusions

Both compression stress–strain curves and efficiency diagrams have been employed in investigating the compression behaviour of the warp-knitted spacer fabrics for cushioning applications. The effects of different structural parameters, including the spacer yarn inclination angle and fineness, fabric thickness and outer layer structure, have been examined. According to the experimental results and analyses, the following conclusions can be drawn.

- The good agreement between the FE simulations and experiments allow concluding that the FE models yield satisfactory results. The FE models thus can be used to optimize the cushioning performance of warp-knitted spacer fabrics to meet specific requirements.
- Warp-knitted spacer fabrics can be used as energy absorbers for cushioning applications. Their energy–absorption capacity can easily be tailored to meet specific end-use requirements by simply varying their structural parameters.
- Efficiency diagram is a good tool for analysing the cushioning performance of these fabrics. For a given energy to be absorbed, it is convenient to use the efficiency diagram for selecting appropriate fabrics working at the stress levels allowed.
- All the structural parameters have obvious effects on compression behaviour and cushioning performance of spacer fabrics. The fabrics with larger spacer yarn inclination angle, higher fabric thickness, finer spacer yarns and larger size mesh of the outer layers, which have lower compression resistance, can be used to absorb lower energy with a higher efficiency. In contrast, the fabrics with smaller spacer yarn inclination angle, lower fabric thickness, coarser spacer yarns and smaller size mesh of the outer layers can be used to absorb higher energy with a higher efficiency. Thus, to design a spacer fabric

with required compression behaviour, selecting the suitable structural parameters is important.

In the remaining chapters, the compression and cushioning properties of the developed warp-knitted spacer fabrics are evaluated and analysed under impact conditions. Chapter 7 presents the experimental characterisation of the warp-knitted spacer fabrics using flatwise impact tests, in terms of impact process, contact force and transmitted force. In Chapter 8, the impact protective properties of the warp-knitted spacer fabrics of the curvatures for human body protection are described.

CHAPTER 7 EFFECTS OF STRUCTURAL PARAMETERS ON IMPACT COMPRESSION PROPERTIES OF WARP-KNITTED SPACER FABRICS

7.1 Introduction

The use of warp-knitted spacer fabrics as cushioning materials in personnel protective clothing and equipment against impact requires them to be capable of adequate capacity in energy absorption and impact force attenuation [11, 137, 138]. In the previous chapter, the study on the compression and cushioning properties has confirmed that the developed warp-knitted spacer fabrics can be used as cushioning materials for such a type of application. However, the results were only obtained from the static compression test condition.

It has been confirmed that the compression behaviour of a cushioning material under static and dynamic conditions can be different [20]. During an impact process, the impact object will undergo a period of deceleration, which is determined by the specified impact energy and the impact compression behaviour of the impacted material [21, 22]. A peak contact force will be generated on the impacted side of the cushioning material, and this force will partially be transmitted to the other side of the material during the impact process [139, 140]. For human body protection, the peak force transmitted to a particular part of the body during the impact process should not exceed the tolerance that tissue or bones can bear. This implies that the cushioning material should dissipate the kinetic energy of the impacting mass and keep the peak force transmitted below the limit of the particular part of the human body. There is no doubt that under the impact condition, the contact force and transmitted force are not identical. This is quite different from the static compression, during which the acceleration is zero. Under a static compression test, the compression forces applied to both sides of the tested material are the same. However, under an impact compression test, the contact force applied to the impacted side of the material by the striker is different from the force transmitted to the other side. In this regard, the analysis of the contact force and transmitted force, as well as their relationship, can help us better understand the impact compression behaviour of a protective material and its performance.

This chapter thus aims to investigate the compression behaviour of the developed warp-knitted spacer fabrics under an impact test condition. The layout of the chapter follows closely that of Chapter 6. A drop-weight impact tester was used to test these fabrics with a specified impact kinetic energy. A typical spacer fabric is first used to analyse the impact process based on the impact contact force–displacement curve, energy absorbed–contact force curve, and transmitted force–time curve. The effects of the structural parameters, including spacer yarn inclination and fineness, fabric thickness, and outer layer structure, on the impact compression behaviour and protective performance of the fabrics are also discussed. It is expected that the study presented in this chapter could provide a deeper understanding of the impact compression behaviour of warp-knitted spacer fabrics and could help us optimize their structural design for human body protection.

7.2 Experimental

7.2.1 Impact compression tests

The impact compression tests were conducted on a drop-weight impact tester manufactured by King Design Company in Taiwan according to ASTM D 1596-97 (Standard Test Method for Dynamic Shock Cushioning Characteristics of Packaging Material). The impact tester is capable of measuring the changes in acceleration of the drop striker and the force transmitted from the top side to the bottom side of the specimen [139]. As shown in Figure 7.1, the striker is released and drops along a vertically guided path onto the sample placed on the anvil during the impact. The mass centre of the falling block just lies over the centre of the anvil. The striker weight was 6.5 kg, and it was made of polished steel with a circular face of 150 mm in diameter. The impact energy is controlled by changing the height of the striker. The anvil was also made of polished steel with the same circular face. The anvil was mounted on a massive base (1000 kg) of the tester through a load cell (1210AF–50KN from Interface Inc. Scottsdale, Arizona, USA, with a sensitivity of 4.171 mV/V) in line with its sensitive axis. While the transmitted force was measured by this load cell, the acceleration of the drop striker was measured through an Isotron® accelerometer (2250 AM 1–10 from Endevco, San Juan Capistrano, California, USA, with a sensitivity of 9.929 mV/g and a measuring range of ±500 g) glued to the striker. Two identical charge amplifiers (Interface Inc. Scottsdale, Arizona, USA) were used to detect and amplify the impact signals in voltage. Signals from the charge amplifiers were recorded through two channels at 10^5 Hz, Channel 1 as the triggered channel for the transmitted force, and Channel 2 for the acceleration. A high-speed data capture card NI6040E (PCI Bus) was employed to record both the transmitted force and the acceleration. The distance from the striker to the anvil was controlled by a CPJ strain gage conditioner (SCAIME S.A.S., Technosite Altéa, 74105 Annemasse cedex, France).

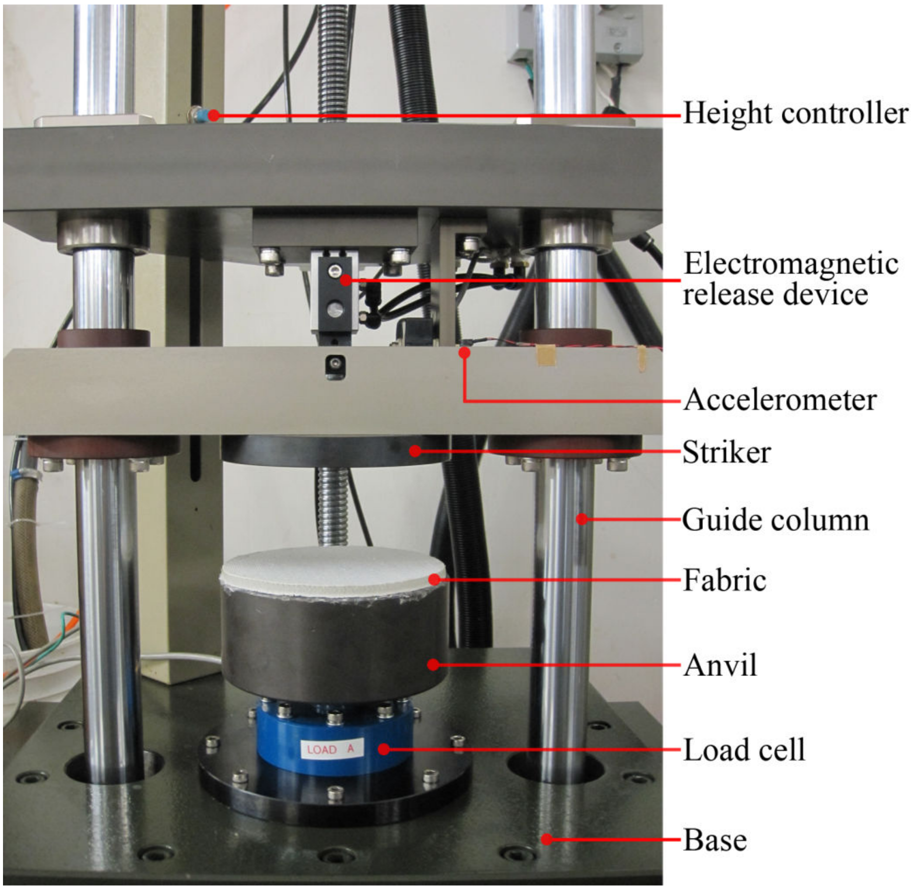

Figure 7.1 Drop-weight impact tester according to ASTM D 1596-97.

The specimens in a circular form of 145 mm in diameter were cut by GFK Marcatex FLEXI–150, a commercial pulsed CO_2 laser machine manufactured by Eurotrend Group (Spain). The generated wavelength of laser beam was set at 10.6 µm, and the power was set at 280 W. Each specimen was cut seven times. All the tests were carried out with the same impact energy (12.74 J) and impact speed (1.98 m/s), which corresponded to a striker drop height of 200 mm, at 20 °C and 65% relative humidity. In order to avoid the possible movement of the specimen during testing, its bottom surface was secured to the anvil. Three specimens were tested for each fabric and all the curves presented are the most representative curve close to the average of three test results.

7.2.2 ANOVA analysis

The peak contact forces and peak transmitted forces of the samples were evaluated by using one-way analysis of variance (ANOVA, SPSS 17.0) for each dependent variable. Any differences for each dependent variable were considered to be significant if the p-value was equal to or less than 0.05. The ANOVA analysis results are shown in the parentheses in case they are needed to confirm the comparison.

7.3 Impact process analysis

7.3.1 Treatment of the acceleration and transmitted force signals

Taking sample S1 as an example, its acceleration and transmitted force signals, as a function of time from one test in both the original form and the form after filtering using a low-pass filter through Fast Fourier Transform at a set cutoff frequency of 5000 Hz, are shown in Figure 7.2. The cutoff frequency was determined according to MIL-STD-883F Method 2002.4, which indicated that a cutoff frequency of a half-sine waveform should be at least five times of the fundamental frequency of the shock pulse. The method also indicated that the pulse duration should be measured between the point at 10% of the peak acceleration during the rising time and the point at 10% of the peak acceleration during the decaying time. Because the obtained signal was not an exact half-sine waveform, only the peak wave was considered here, and its duration was about 1.2 ms. In this case, the cutoff frequency should be higher than 4166 Hz. To meet this requirement and to obtain a good presentation, 5000 Hz was employed throughout this study. It can be seen that the low-pass filter with this cutoff frequency is effective to eliminate the noise with high accuracy.

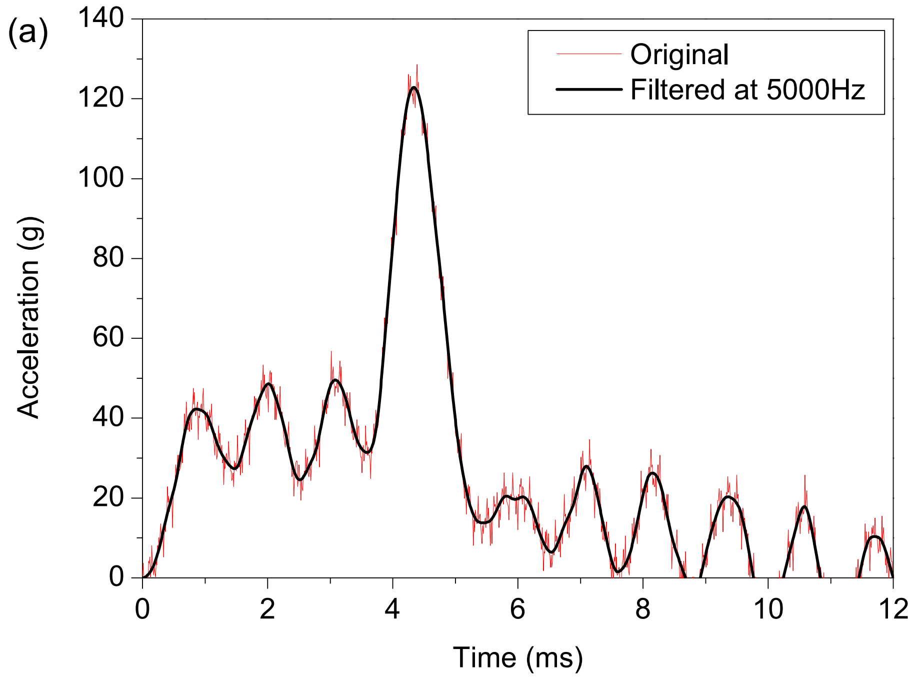

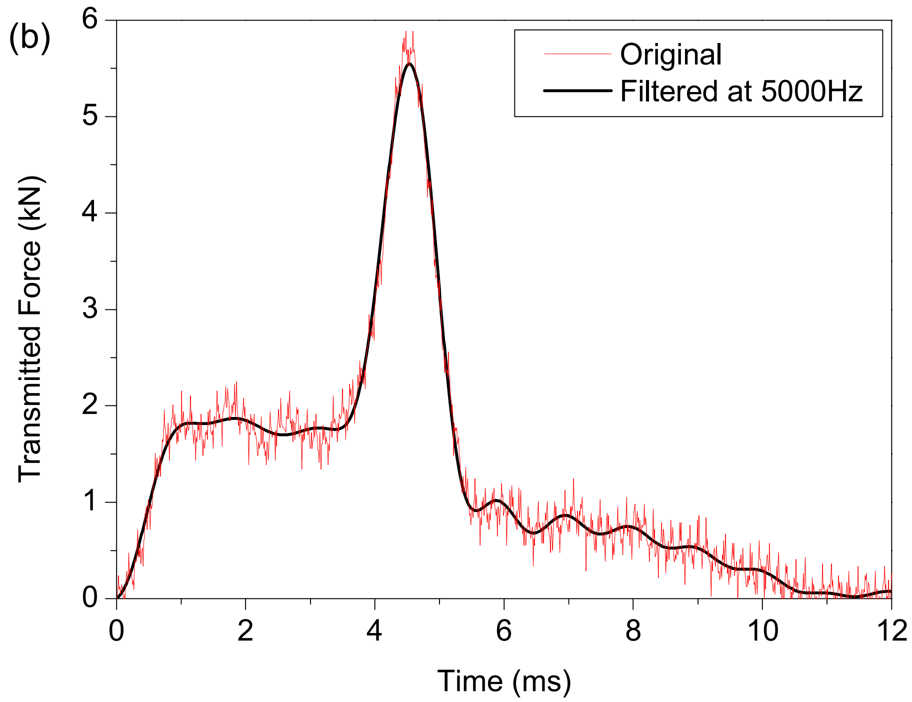

Figure 7.2 Original and filtered signals for sample S1: (a) acceleration; (b) transmitted force.

7.3.2 Comparison of the contact force and transmitted force

The contact force is proportional to the acceleration and can be calculated according to the Newton's second law:

$$F = ma, \tag{7.1}$$

where m is the mass of the striker (6.5 kg) and a is the acceleration. To better understand the impact process, both the contact force and transmitted force for sample S1 are plotted together against the time, as shown in Figure 7.3. It can be found that the contact force reaches its peak point after about 4.3 ms of the impact, and the impact process completes within about 12 ms. According to the theorem of momentum, a longer duration of the impact will lead to a lower acceleration and a lower dynamic reaction force. In the absence of the fabric the motion of the dropping striker is instantaneously stopped by the anvil, producing a very high acceleration and dynamic contact force. However, with the fabric located on the anvil surface the striker experiences deceleration as it strikes the fabric. During the deceleration the fabric first stores and dissipates the kinetic energy of the impact and then releases the stored energy over a longer duration, thereby leading to a reduction in the acceleration of the striker and generating a smaller contact force between the striker face and the upper surface of the fabric. In addition, the inherent damping of the fabric can dissipate the kinetic energy and consequently causes a further reduction in the contact force or acceleration. The contact force is transmitted to the anvil through the specimen in the form of shock wave propagation.

As has been identified in Chapter 5, the highly complicated impacting process might include postbuckling, torsion, shear, rotation and contacts of the spacer monofilaments, as well as their contacts with the outer layers. These deformations contribute to the overall nonlinear deformation of the warp-knitted spacer fabric, which can store and dissipate the kinetic energy of the impact at the same time. It can be observed from Figure 7.3 that the contact force and the transmitted force do not reach their peak points simultaneously. The transmitted force reaches its peak point with a time delay of 0.2 ms due to the shock wave propagation. In addition, the peak transmitted force is much lower than the peak contact force. It should be pointed out that the shock wave propagation through the discrete fabric is complicated, and the energy loss during the wave propagation contributes to the lower transmitted force.

From Figure 7.3, it can also be found that the fluctuations exist in the contact force curve. It is believed that these fluctuations originate from the shear and rotation deformations of the spacer monofilament yarns. It can be seen that these fluctuations are mitigated after transmission to the anvil.

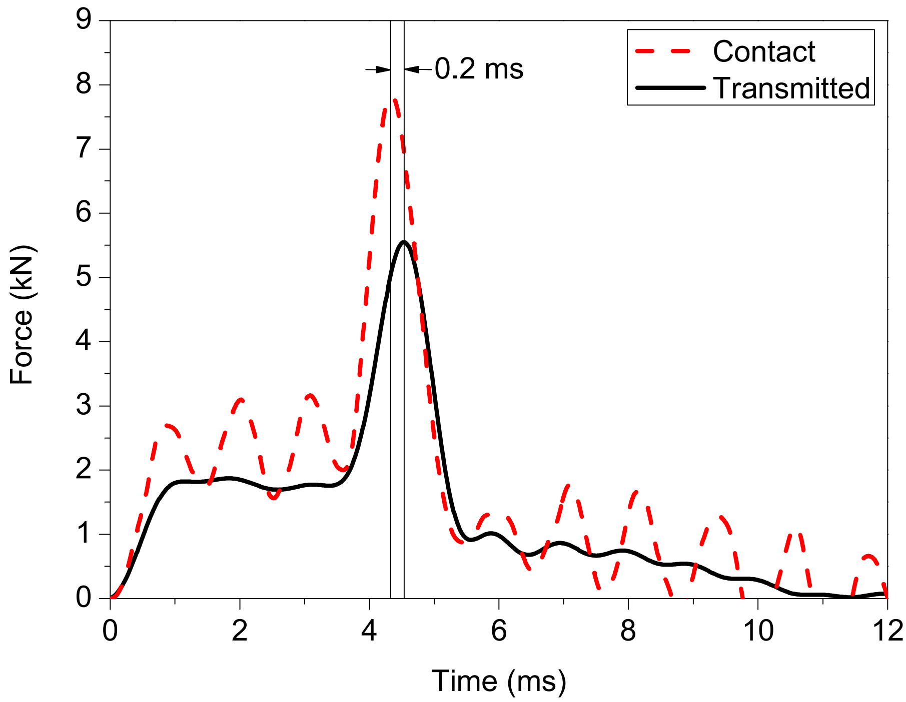

Figure 7.3 Comparison between contact force and transmitted force for sample S1.

7.3.3 Calculation of velocity and displacement of the striker

The velocity and displacement of the striker can be calculated by integrating the acceleration-time curve according to the following equations:

$$v = \sqrt{2gH_s} - \int a dt, \tag{7.2}$$

$$s_s = \sqrt{2gH_s}t - \int \left(\int a dt \right) dt, \tag{7.3}$$

where v is the velocity, s_s is the displacement, a and t are acceleration and time, respectively, and H_s is the initial height of the striker.

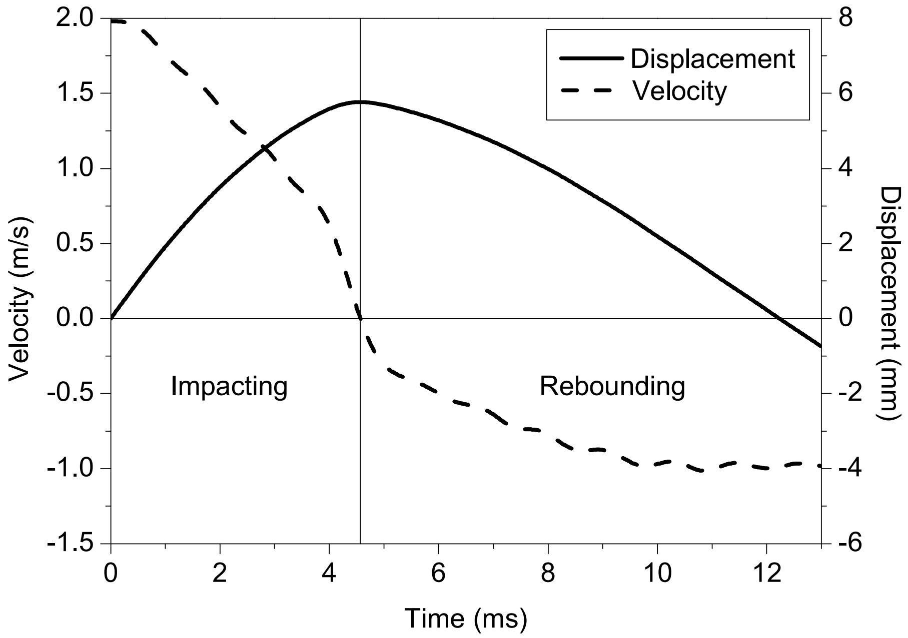

Figure 7.4 Velocity and displacement as a function of time for sample S1.

The curves of the velocity and the displacement for sample S1 as a function of time are shown in Figure 7.4. It can be seen that the impact process can be split into two phases: impacting and rebounding. The impacting phase corresponds to a deceleration process from the start point when the striker starts to contact the fabric at the highest impact velocity (1.98 m/s) to the rebounding point when the velocity reaches 0 m/s. At the rebounding point, both the acceleration and the displacement reach their maximum values. While the impacting phase is related to the compression process of the fabric, the rebounding phase is related to the recovery process of the fabric. It is evident that the rebounding intensity largely depends on the recovery capacity of the spacer monofilament yarns, which function like springs in the compressed fabric.

7.3.4 Impact compression behaviour analysis

In order to analyse the impact compression behaviour of the fabric, the contact force is plotted against the displacement, as shown in Figure 7.5. For comparison, the compression force–displacement curve of the same fabric obtained under the static compression condition (i.e., compression speed 12 mm/min, compressed to 80% of its initial thickness) is also shown in Figure 7.5. It is found that the general trends of the two curves are similar. However, some differences can be found. In the static curve, an obvious plateau stage can be observed. However, in the impact curve, the fluctuations dominate in this stage. This phenomenon has not yet been clearly explained. It may result from the shear and rotation deformations of the spacer monofilament yarns, as explained before. In addition, the impact contact force is higher than the static force during almost the entire compression process. For the impact test, the fabric was compressed to the largest displacement of 5.74 mm with a peak contact force 7.83 kN. The static force at this displacement with a value of 5.25 kN is much lower than the contact force under impact. It is evident that the spacer fabric inherently exhibits strain rate sensitivity, which is similar to the polyester filaments used as spacer yarns. The monofilament spacer yarn inertia to rotation and deformation especially at high strain rates can also play a significant role. The rate dependency of the spacer fabric leads to a higher energy absorption capacity in impact than that in static compression. This is confirmed by the energy absorbed-displacement curves also shown in Figure 7.5. At the point of peak contact force or the largest displacement in impact, the energy absorbed is 12.74 J. At the same displacement under static compression, the energy absorbed is much lower, with a value of 9.2 J.

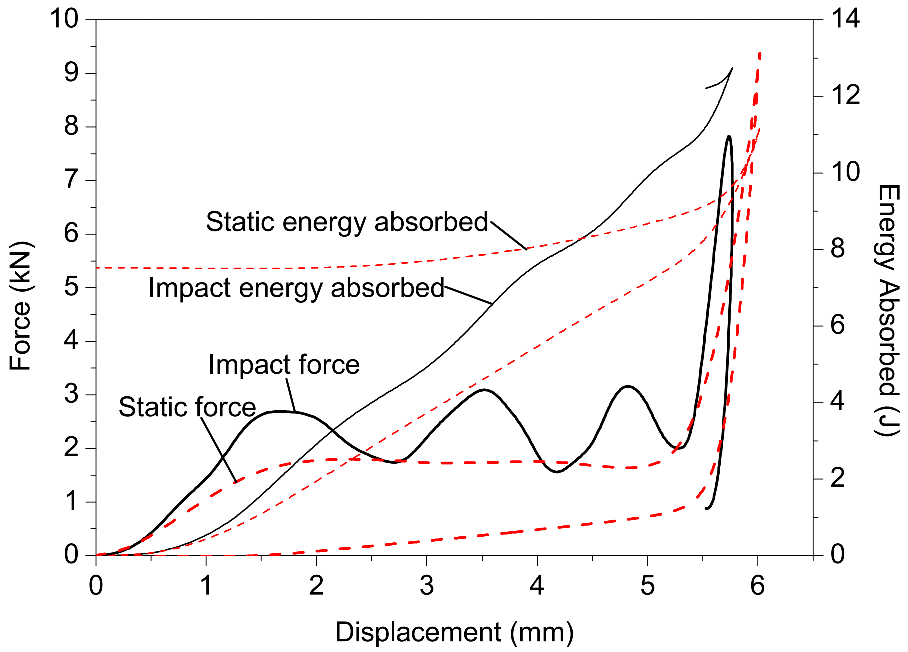

Figure 7.5 Force and energy absorbed versus displacement curves under impact and static compression for sample S1.

As discussed in Chapter 6, the energy absorbed within the plateau stage and the relevant plateau force are two key parameters to select and optimize a warp-knitted spacer fabric for impact protection. To better understand the protective performance of the spacer fabric under impact, the energy absorbed by the spacer fabric is plotted against the contact force, as shown in Figure 7.6. It is found that the spacer fabric can absorb the majority of the impact energy before reaching the peak contact force. This can be confirmed by comparing the energy absorbed at point A, from which the contact force starts rising to its peak point B, to the total energy absorbed. At point A, the energy absorbed is about 10.5 J, which represents about 82.5% of the total energy absorbed (12.74 J). For comparison, the energy absorbed-force curve under static compression is also included in Figure 7.6. It is observed that the force under static compression is lower than the contact force under impact for the same level of energy absorbed from the beginning to the point at about 7.5 J. After this point, the static force becomes much higher than the contact force. At the end of the static compression with a displacement 6.02 mm, the energy absorbed is 11.18 J, which is lower than the energy absorbed in the impact test (12.74 J) at its maximum displacement of 5.74 mm. This result shows that the warp-knitted spacer fabric is an effective material for absorbing impact energy for protective application. Moreover, the energy-absorbing performance in terms of energy-absorbing capacity and contact force is rate dependency.

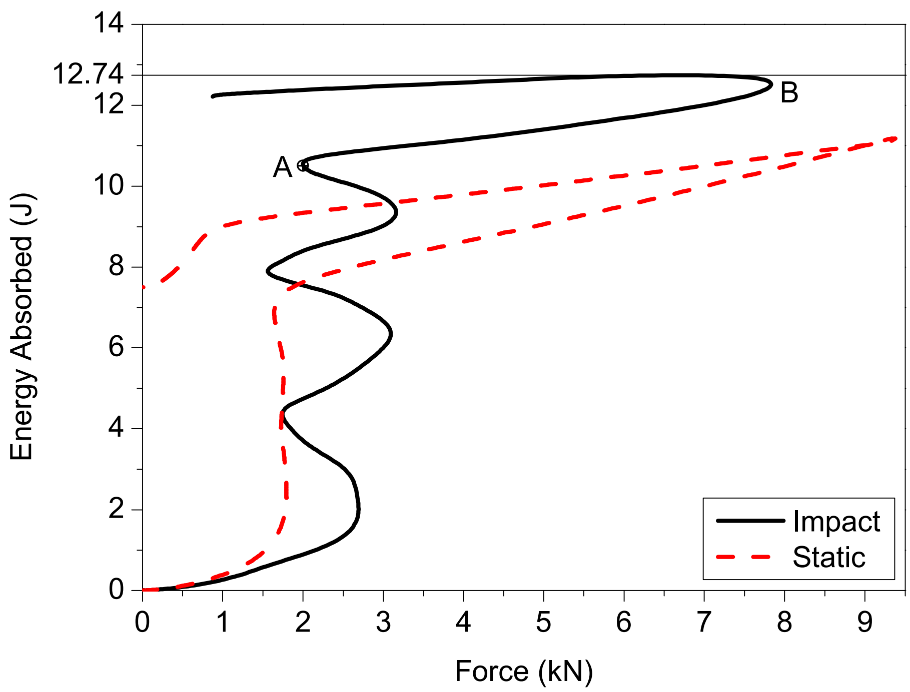

Figure 7.6 Energy absorbed versus force curves under impact and static compression for sample S1.

The above analysis shows that the compression behaviour of the warp-knitted spacer fabric under impact is different from the behaviour under the static situation.

7.4 Effects of structural parameters

In this section, the discussions focus on the effects of the structural parameters on the impact compression behaviour of the warp-knitted fabrics based on their impact contact force–displacement curves, energy absorbed–contact force curves, and transmitted force–time curves. Following a similar pattern as presented in Section 6.4, different groups of spacer fabrics are used for comparing and analysing.

7.4.1 Effect of spacer yarn inclination angle

A group of three fabrics (S2, S3 and S4) with different spacer yarn inclination angles (shogging one-needle, two-needle and three-needle space between the front and back needles) is used to analyse the effect of spacer yarn inclination on the impact compression behaviour of warp-knitted spacer fabrics. As explained in Chapter 6, both the spacer yarn inclination and length depend on the needle space shogged between the front and back needles, and they increase with increasing the number of the needle space shogged. The contact force–displacement curves, energy absorbed–contact force curves, and transmitted force–time curves of these fabrics are shown in Figure 7.7(a)–(c), respectively. Their peak contact forces and peak transmitted forces are also shown in Figure 7.8. From Figures 7.7 and 7.8, the following phenomena can be observed.

- The average level of the contact force in the plateau stage until 3.5 mm of displacement increases with decreasing the spacer yarn inclination (Figure 7.7(a)). This is consistent with the FE simulation and static compression results. However, an obvious drop of the contact force at the end of the plateau stage is observed for the spacer fabric (S2) with only shogging one-needle space of spacer yarns. There is a difference in the sharp drop of reaction force in the plateau stage for this fabric between the static compression and flatwise impact. With reference to Figure 6.4(a), the drop for the simply placed case under static compression is at the beginning of the plateau stage. By contrast, Figure 7.7(a) shows that the drop is at the middle of its plateau stage under flatwise impact. This is more close to that for the glued case under static compression.

- The same trend is also found from the transmitted force-time curves (Figure 7.7(c)), where the average level of the transmitted force increases with decreasing the spacer yarn inclination within 2 ms of the impact. A sharp drop of the transmitted force is also observed for the spacer fabric with only shogging one-needle space of spacer yarns.
- Both the peak contact forces and peak transmitted forces of the fabrics with shogging one- and three-needle space of spacer yarns are much higher than those of the fabric with shogging two-needle space of spacer yarns. The one-way ANOVA test results indicate that the effects of spacer yarn inclination on both the peak contact force ($F_{(2, 6)} = 46.071$, $p < 0.001$) and peak transmitted force ($F_{(2, 6)} = 46.374$, $p < 0.001$) are highly significant. However, when the peak contact forces of the fabrics with shogging one- and three-needle space of spacer yarns have almost the same value (no significant difference according to the ANOVA analysis result: $F_{(1, 4)} = 2.331$, $p = 0.202$), the peak transmitted force of the fabric with shogging one-needle space of spacer yarns is higher than that of the fabric with shogging three-needle space of spacer yarns (the difference exists according to the ANOVA analysis result: $F_{(1, 4)} = 9.354$, $p = 0.038$).

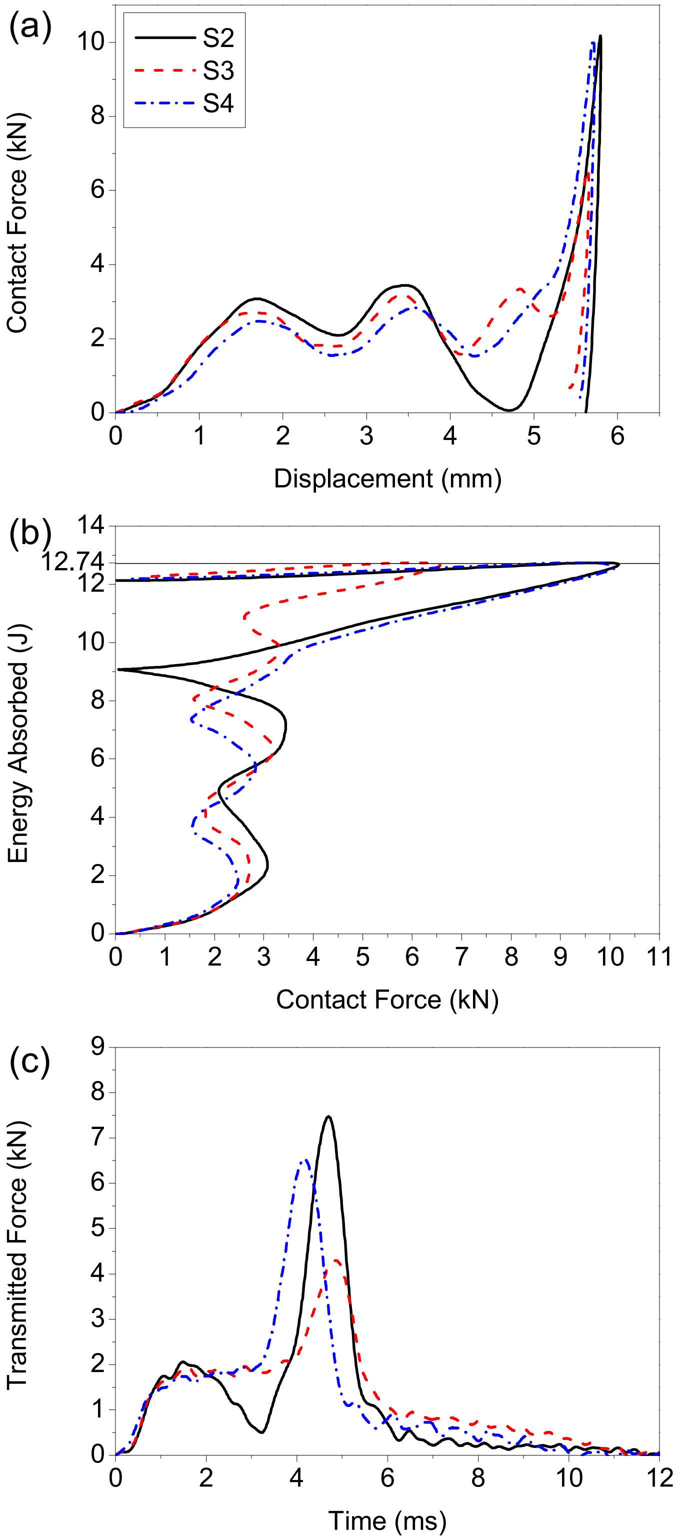

Figure 7.7 Effect of the spacer yarn inclination on impact compression behaviour: (a) contact force–displacement curves; (b) energy absorbed–contact force curves; (c) transmitted force–time curves.

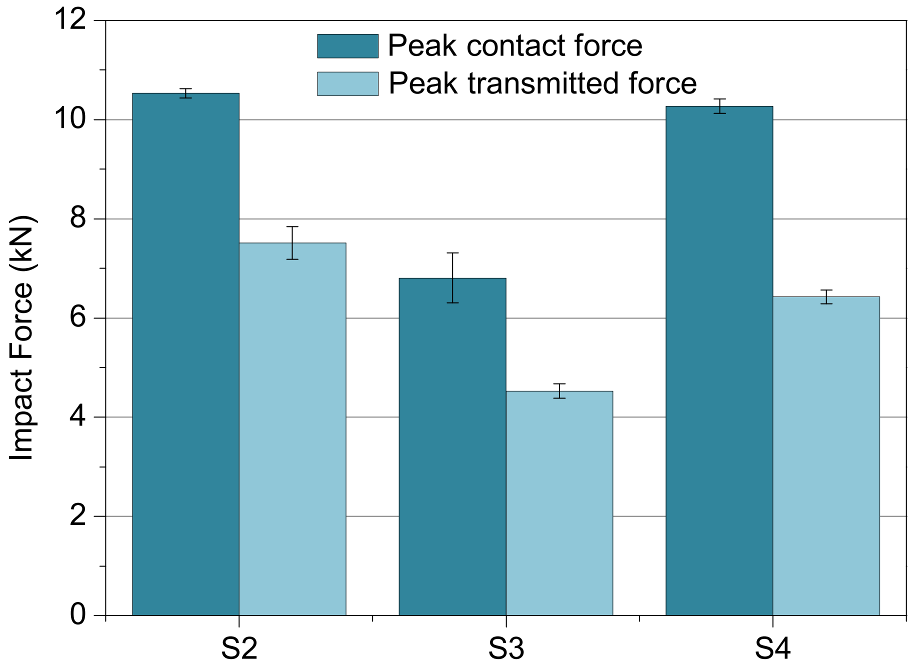

Figure 7.8 Effect of the spacer yarn inclination on the peak contact force and peak transmitted force.

These phenomena can be explained by analysing how the spacer yarns withstand the contact force during the impact process. It is necessary to point out that the compression resistance of spacer fabrics increases with decreasing the inclination of the spacer yarns because the spacer yarns with lower inclination are more oriented to the direction of the impact. According to the parametric study with the analytical model in Section 4.5.1 or the parametric study with the FE models in Section 5.5.1, a spacer fabric with a smaller number of needles underlapped has higher compression resistance. This theoretical prediction was confirmed by the experimental static compression results presented in Section 6.4.1. Therefore, the fabric with smaller inclination will also have higher compression resistance during impact compression. However, if the spacer yarns become too vertical to the outer layers (shogging one-needle space), as discussed in Section 6.4.1, the fabric structure will become less stable and shear can easily take place between the two outer layers because the spacer yarns tend to tilt along the coursewise direction under the impact loads. This explains why an obvious drop of the contact force at the end of the plateau stage is found for sample S2 with one-needle space shogging of spacer yarns. The only difference in the force–displacement relationship between the static compression and flatwise impact is that the drops for the two conditions are located at different positions of the plateau stages: at the beginning for static compression and at the end for flatwise impact. A possible explanation for this phenomenon is presented as follows. In Section 5.4.3, the FE simulation for different test boundary conditions has indicated that the shear movements of the outer fabric layers are affected by the friction coefficient and the applied pressure. The higher the coefficient of friction and the applied pressure, the higher the friction force is produced. It was shown in Section 7.3.4 that the contact force under impact is higher than the reaction force in static compression due to the strain rate effect. This results in an increasing friction force between the striker and the top outer fabric layer, thereby blocking the in-plane movements between them. That is why the sharp drop of the contact force for the impact test occurs at a larger displacement compared to that for the static compression test.

On the other hand, if the spacer yarns are too inclined (e.g., shogging three-needle space), they can easily be crushed under the contact force. As a result, the fabric will absorb less energy in the plateau stage. At the same time, the fabric with more inclined spacer yarns can be easier to densify under the impact. The lower energy absorption capacity in the plateau stage and the higher densification of the fabric with more inclined spacer yarns can result in a higher peak contact force. However, as there are more spacer yarns within the fabric knitted with shogging three-needle space, it may be more difficult for the shock wave to go through its thickness. In this connection, its peak transmitted force is lower than that of the fabric knitted with shogging one-needle space.

The above analysis shows that the spacer yarn inclination can significantly affect the impact behaviour of warp-knitted spacer fabrics. Both the fabrics with smaller inclination of spacer yarns (shogging one-needle space) and larger inclination of spacer yarns (shogging three-needle space) have higher peak contact and transmitted forces.

7.4.2 Effect of spacer yarn fineness

Two fabrics (S4 and S12) with two different spacer monofilament diameters (0.2 and 0.16 mm) are chosen to study the effect of spacer yarn fineness on the impact compression behaviour of warp-knitted spacer fabrics. While their contact force–displacement curves, energy absorbed–contact force curves, and transmitted force–time curves are respectively shown in Figure 7.9(a)–(c), their peak contact forces and peak transmitted forces are shown in Figure 7.10. From Figures 7.9 and 7.10, the following phenomena can be observed and explained.

- The average level of the contact force in the elastic and plateau stages increases with increasing spacer monofilament diameter. This is due to the different moments of inertia of the spacer monofilaments with different radii. According to the analytical model and the FE simulation, it is clear that the radius has a significant effect on the postbuckling load under compression. The static and impact results make the similar responses to the change of the spacer monofilament fineness.

- While the fabric with the coarser spacer monofilament can absorb more energy in the elastic and plateau stages than the fabric with the finer spacer monofilament because of the higher force level in these stages, the fabric with the finer spacer monofilament should absorb more energy in the densification stage (Figure 7.9(a)). Therefore, the contact force of the fabric with the finer spacer monofilament is much higher than that of the fabric with the coarser spacer monofilament in the densification stage. The different level of densification is also a reason for the peak contact force and peak transmitted force increasing with decreasing the spacer monofilament diameter. The ANOVA test results indicate that the effects of the spacer yarn fineness on the peak contact force ($F_{(1,\ 4)} = 158.861$, $p < 0.001$) and peak transmitted force ($F_{(1,\ 4)} = 996.446$, $p < 0.001$) are both highly significant.
- The contact and transmitted forces of the fabrics with different spacer monofilament diameters do not reach their peak points simultaneously. The spacer fabric with the finer spacer monofilament yarns first reaches its peak contact force point and peak transmitted force point during the impact process. This is because the higher acceleration in the densification stage of the fabric with finer spacer monofilament yarns can stop the striker in a shorter period of time. It is necessary to emphasize that the period of deceleration is essential to the impact protection since the impact process should be as long as possible to minimize peak acceleration, which is directly related to the peak contact force and peak transmitted force.

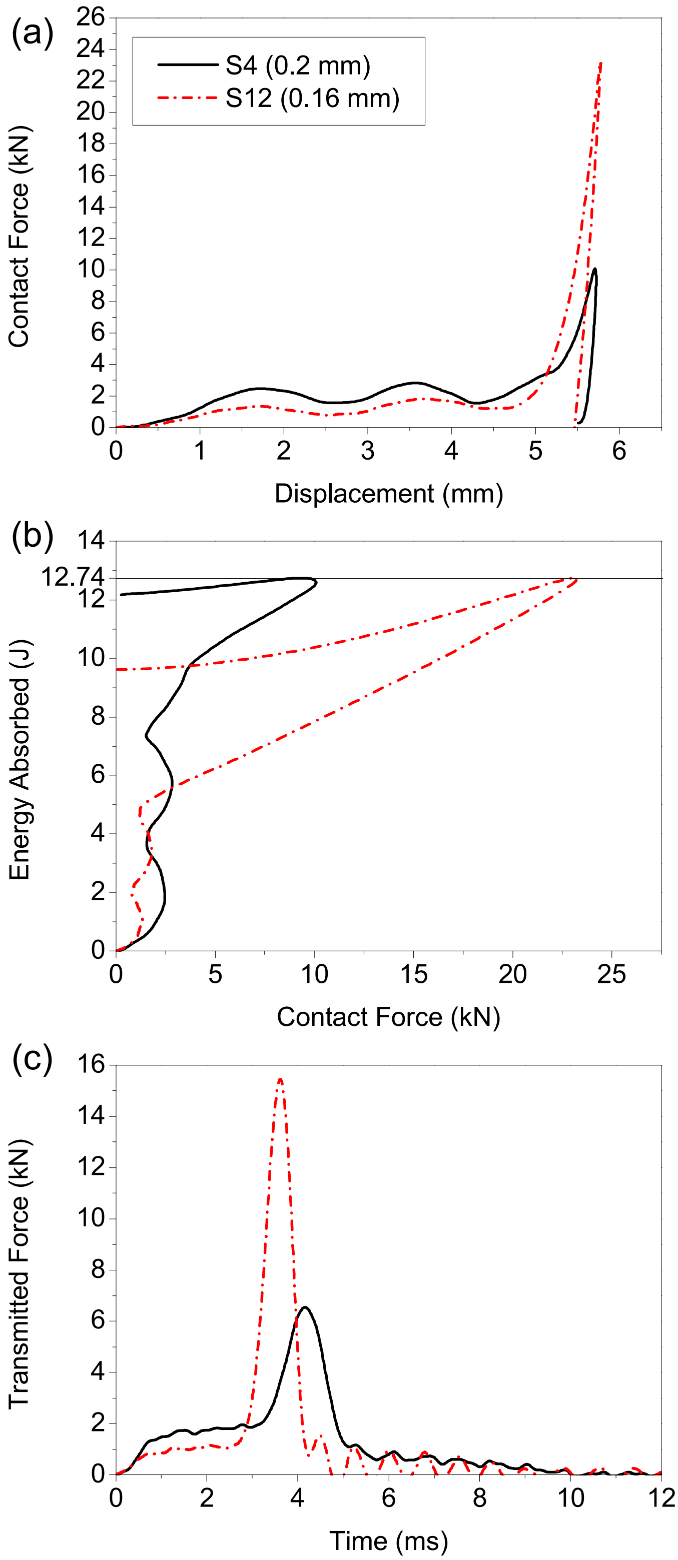

Figure 7.9 Effect of the spacer yarn fineness on the impact compression behaviour: (a) contact force–displacement curves; (b) energy absorbed–contact force curves; (c) transmitted force–time curves.

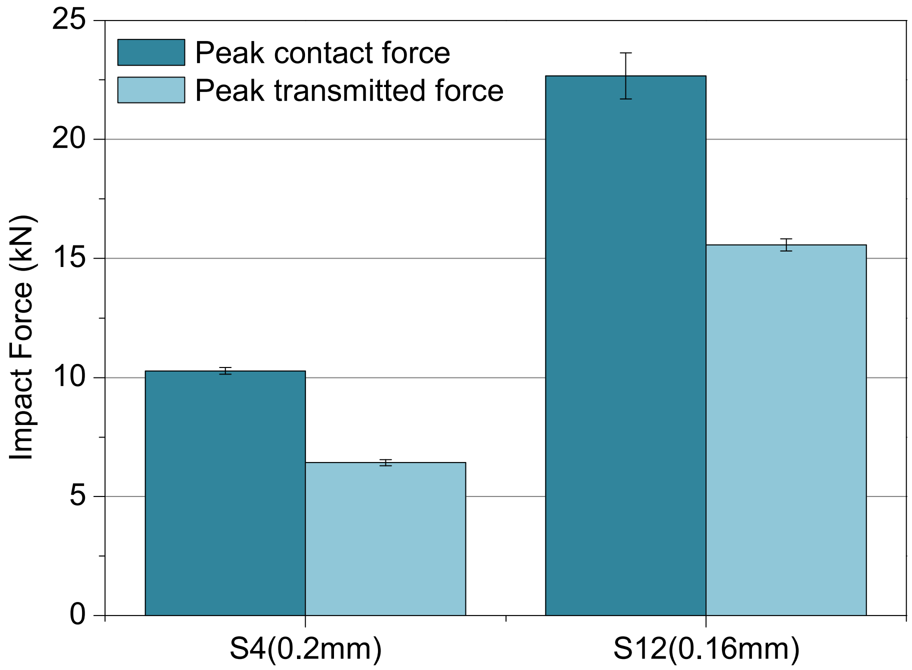

Figure 7.10 Effect of the spacer monofilament fineness on the peak contact force and peak transmitted force.

From the above analysis, it can be found that the reduction of spacer monofilament diameter can considerably decrease the energy absorption capacity of warp-knitted spacer fabrics and their protective performance. However, increasing the spacer monofilament diameter will increase the fabric stiffness and thus decrease the comfort property of a spacer fabric. In this regard, the balance between the comfort and protective performance should be taken into consideration by selecting suitable spacer monofilament fineness for a specific protective application.

7.4.3 Effect of fabric thickness

A group of four fabric samples (S5, S3, S6, and S7) with different thicknesses (5.64, 7.59, 8.45 and 10.62 mm) is used to analyse the effect of fabric thickness on the impact compression behaviour of warp-knitted spacer fabrics. The contact force–

displacement curves, energy absorbed–contact force curves, and transmitted force–time curves of these fabrics are shown in Figure 7.11(a)–(c), respectively. Their peak contact forces and peak transmitted forces are shown in Figure 7.12. The following phenomena can be observed from Figures 7.11 and 7.12:

- The fluctuations of the contact force–displacement curves before rising to the peak forces decrease with increasing the fabric thickness. The obvious plateau stage is obtained for the thicker spacer fabrics (Figure 7.11(a)).
- The average level of the contact force in the elastic and plateau stages decreases with increasing the fabric thickness, but the displacement in the plateau stage increases with the thickness (Figure 7.11(a)).
- The thinner fabrics can absorb more energy before starting to rise to the peak forces than the thicker fabrics but at a higher contact force level (Figure 7.11(b)).
- The same trend was found from the transmitted force-time curves (Figure 7.11(c)), where the average level of the transmitted force decreases with increasing the fabric thickness in the elastic and plateau stages.
- The peak contact forces and peak transmitted forces firstly decrease and then increase with increasing the fabric thickness. The ANOVA test results indicate that the effects of the fabric thickness on the peak contact force ($F_{(3, 8)} = 18.999$, $p = 0.001$) and peak transmitted force ($F_{(3, 8)} = 56.243$, $p < 0.001$) are both highly significant.

All the above phenomena could be explained by the following reasons:

- In agreement with the theoretical prediction and the static compression result, the thicker fabrics will become softer due to the longer spacer yarns, and their compression force levels in the plateau stage will become lower than those of the thinner fabrics. At the same time, the softer fabrics can be easier to densify under impact, which can lead to a slow increase of the peak contact force in the densification stage with increasing the fabric thickness. On the other hand, the reduction of the spacer yarn length in a thinner spacer fabric makes it stiffer. If the fabric thickness is reduced to a certain level, the fabric can become very stiff. In this case, the reaction force between the fabric and the drop striker can considerably increase, which can result in an increase of the peak contact force. Thus, an optimized fabric thickness exists for obtaining a lower peak contact force.

- It is normal that the displacement increases with increasing the fabric thickness since there is more space between the outer layers in a thicker spacer fabric than in a thinner spacer fabric. With the increase of fabric thickness, the compression process of the fabric under impact becomes smoother, and thus slight fluctuations in the plateau stage for a thicker spacer fabric can be observed. Conversely, more vibrations during the impact process will be produced in a thinner fabric, which can result in sharp fluctuations in its contact force–displacement curve.
- The energy absorbed from the starting impact point to the end point of the plateau depends on both the displacement and the contact force level in the plateau stage. For the thicker fabrics, although their displacements are larger, the lower contact force level reduces the amount of the energy that they absorb from the starting impact point to the end point of the plateau. However, too low a thickness can considerably decrease the displacement, which can result in reducing the total energy absorbed at the end of the

plateau. Thus, an optimized fabric thickness exists for obtaining higher energy absorption with a lower force.

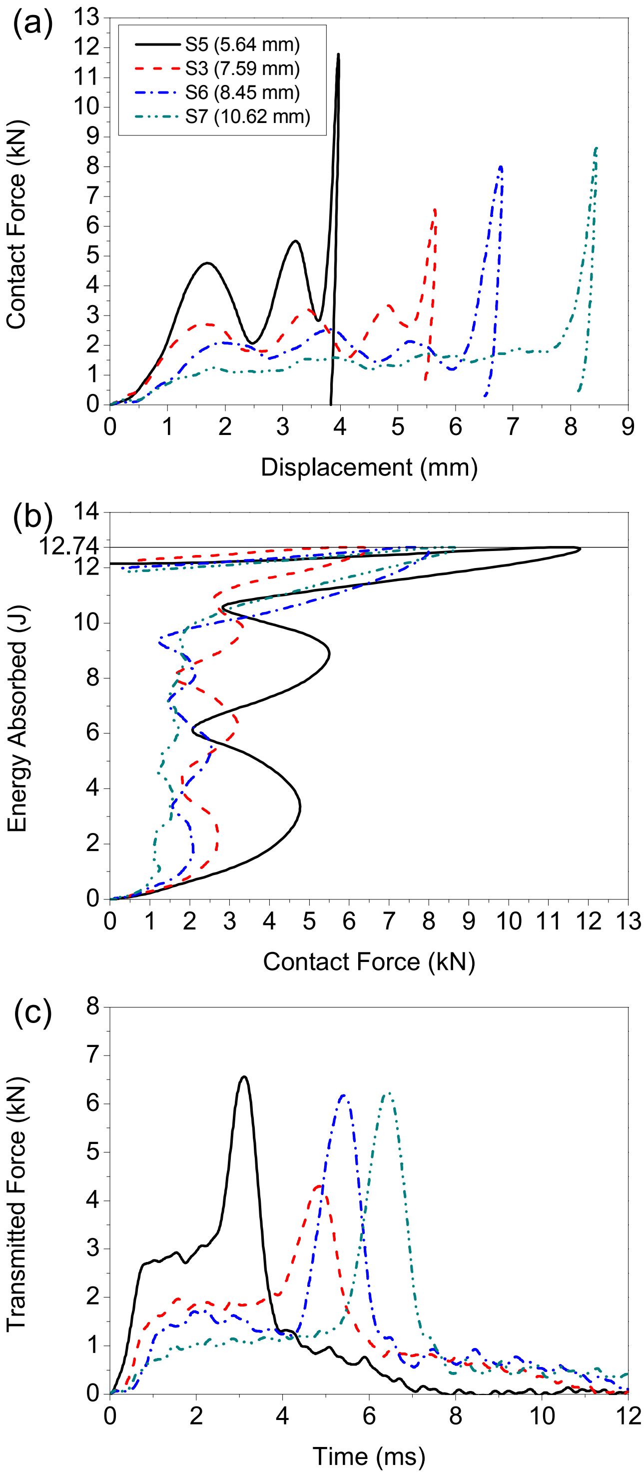

Figure 7.11 Effect of the fabric thickness on the impact compression behaviour: (a) contact force–displacement curves; (b) energy absorbed–contact force curves; (c) transmitted force–time curves.

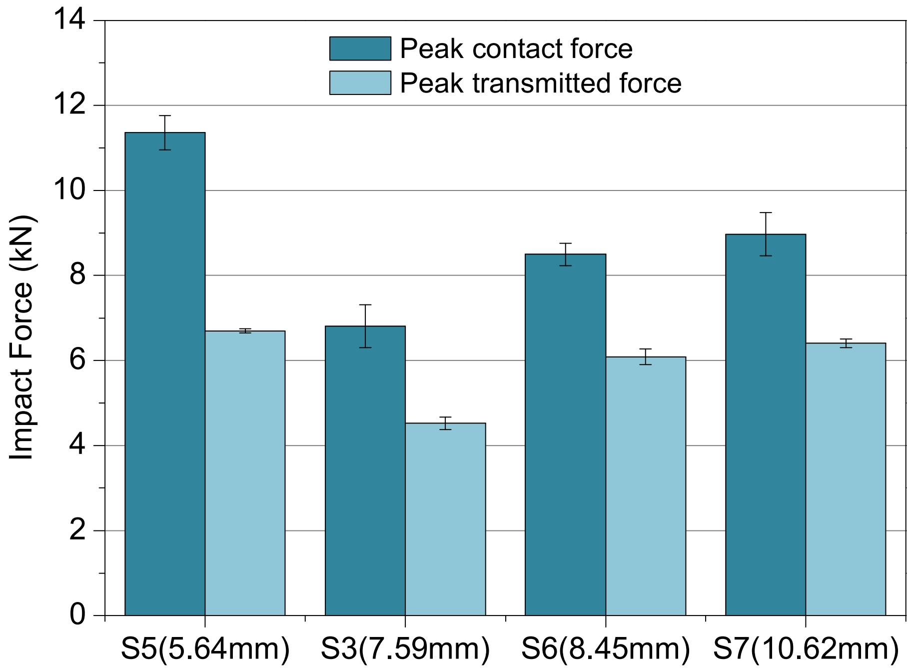

Figure 7.12 Effect of the fabric thickness on the peak contact force and peak transmitted force.

The above analysis shows that the fabric thickness significantly affects the impact compression behaviour of warp-knitted spacer fabrics. The protective performance of a spacer fabric can be optimized by selecting a suitable fabric thickness when other structural parameters are kept unchanged.

7.4.4 Effect of outer layer structure

Following the way used in Section 6.4.4, a group of six fabrics (S1, S3, S8, S9, S10 and S11) with different outer layer structures is chosen to investigate the effect of outer layer structure on the impact compression behaviour of warp-knitted spacer fabrics. The contact force–displacement curves, energy absorbed–contact force curves, and transmitted force–time curves of these fabrics are shown in Figure 7.13(a)–(c), respectively. Their peak contact forces and peak transmitted forces are shown in Figure 7.14. It is found that the outer layer structures have an obvious effect on the peak contact force ($F_{(5, 12)} = 82.920$, $p < 0.001$), the energy absorbed, and the peak transmitted force ($F_{(5, 12)} = 320.512$, $p < 0.001$). While the fabric knitted with large-size hexagonal mesh for both outer layers has the highest peak contact force ($F_{(1, 16)} = 33.636$, $p < 0.001$) and the highest peak transmitted force ($F_{(1, 16)} = 38.770$, $p < 0.001$), as well as the lowest energy absorption capacity at the end of the plateau stage, the fabric knitted with small-size rhombic mesh for both outer layers has the lowest peak contact force ($F_{(1, 16)} = 10.264$, $p = 0.006$) and the lowest peak transmitted force ($F_{(1, 16)} = 10.782$, $p = 0.005$), as well as the highest energy absorption capacity at the end of the plateau stage. It is also found that the fabric knitted with large-size hexagonal mesh for the top outer layer has a higher peak contact force ($F_{(1, 4)} = 3.617$, $p = 0.130$) and a higher peak transmitted force ($F_{(1, 4)} = 24.54$, $p = 0.008$) than those of the fabric knitted with small-size rhombic mesh for the top outer layer, although their bottom outer layers are knitted with the same chain plus inlay structure. In addition, the fabrics knitted with the close structures for both the top and bottom outer layers have moderate peak contact force and peak transmitted force. In the close structures, the fabric knitted with chain plus inlay has a lower peak contact force ($F_{(1, 4)} = 8.516$, $p = 0.043$) and a lower peak transmitted force ($F_{(1, 4)} = 29.571$, $p = 0.006$) than those of the fabric knitted with locknit.

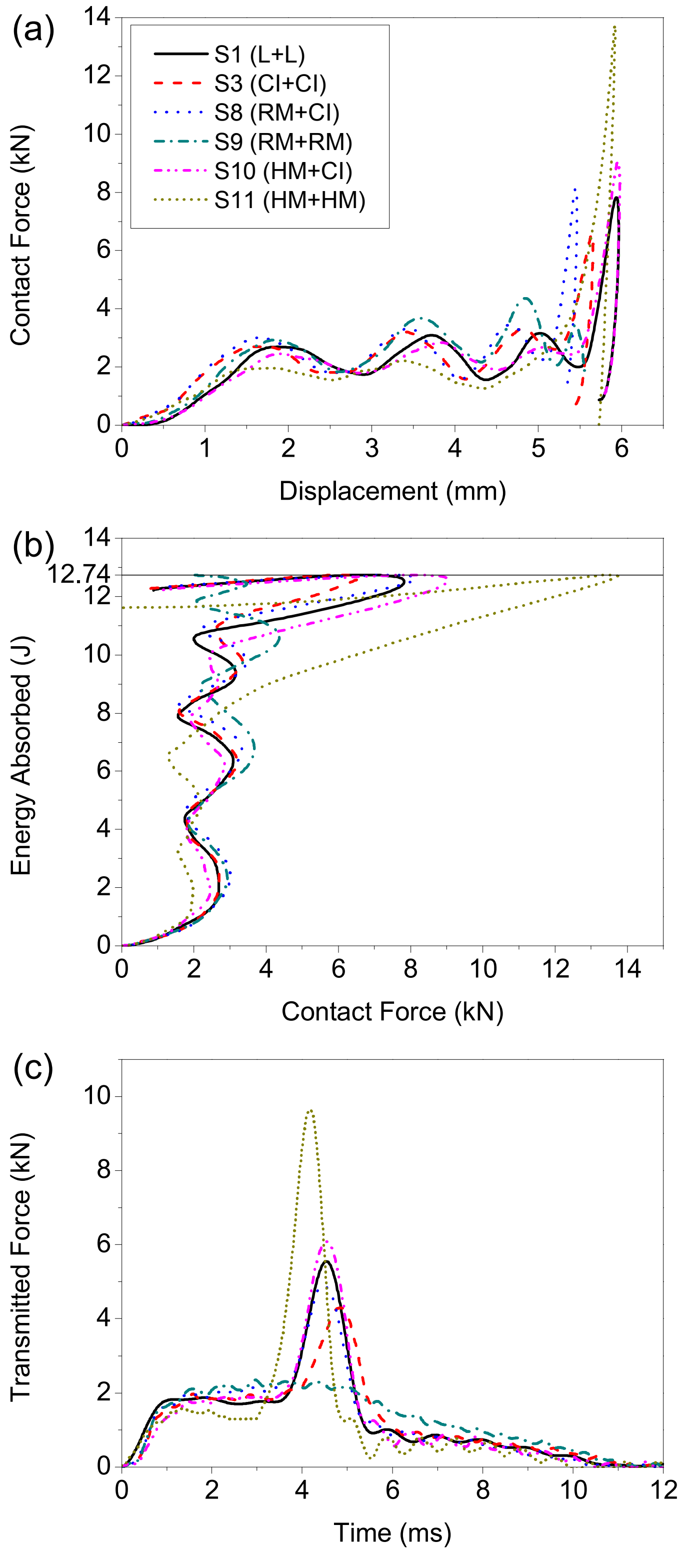

Figure 7.13 Effect of the outer layer structure on the impact compression behaviour: (a) contact force–displacement curves; (b) energy absorbed–contact force curves; (c) transmitted force–time curves.

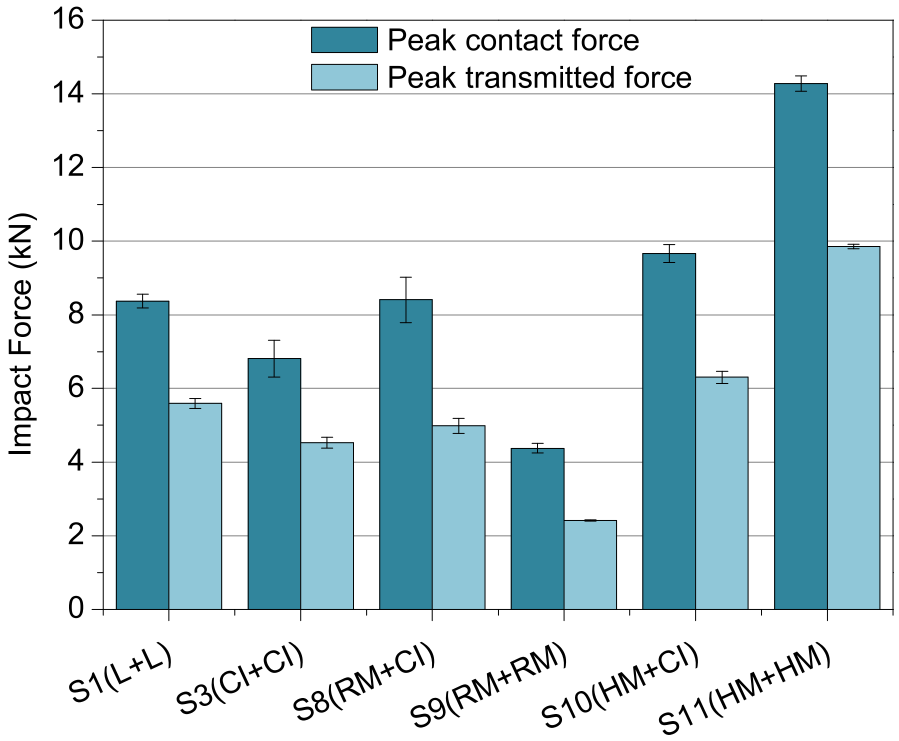

Figure 7.14 Effect of the outer layer structure on the peak contact force and peak transmitted force.

These phenomena can be understood by analysing the distribution, binding condition, and inclination of spacer monofilaments. It is well known that the buckling load of an elastic rod is determined by its boundary condition and initial geometric shape. Observing the microscopic pictures of outer layers shown in Figure 6.7, it can be found that the fabrics knitted with the close structures have larger and looser stitches in the outer layers than those of the fabrics knitted with the mesh structures. In addition, the needle loops in the outer layers of the fabric knitted with chain plus inlay are smaller than those of the fabric knitted with a locknit structure. This implies that the ends of the monofilament yarns are more tightly bound by the multifilament stitches in the fabrics knitted with mesh outer layer structures than in close outer layer structures. In the close structures, the monofilament yarns are more tightly bound by chain plus inlay than locknit. The other factor that determines the buckling load is the initial shape of the spacer monofilament yarns. Observing the cross-sectional microscopic pictures of the fabrics shown in Figure 7.15, it can be found that the large-size hexagonal mesh outer layer makes the spacer monofilament yarns highly inclined and buckled (Figure 7.15(d) and (f)), which leads to the decrease of the compression resistance. In contrast, there are no significant differences for the initial shapes of spacer monofilament yarns among the fabrics knitted with close and small-size mesh outer layer structures (Figure 7.15(a)–(c) and (e)). By considering the boundary conditions and initial geometric shapes of spacer monofilament yarns, it is easy to understand that the fabrics knitted with large-size mesh structures exhibit the poorest impact protection performance due to the highly buckled and inclined spacer monofilament yarns, and the fabrics knitted with small-size mesh demonstrate the best impact protection ability due to the tight binding structures. The fabrics knitted with a close structure have moderate impact protection performance because of the combination effects of loose binding structures and lowly buckled and inclined spacer monofilament yarns.

Another aspect that should be considered for human body protection is the formability of warp-knitted spacer fabrics. The close outer layer structures make the fabrics stiffer and more difficult to fit the body shape with higher fabric thicknesses. However, the fabric knitted with the small-size mesh outer layer structure is good both in shapability and protective performance. The shape and size of the mesh structures in the outer layers of warp-knitted spacer fabrics can be adjusted to meet different requirements of protection. The balance between the shapability and protective performance should be taken into consideration by selecting a suitable outer layer structure for a specific protective application.

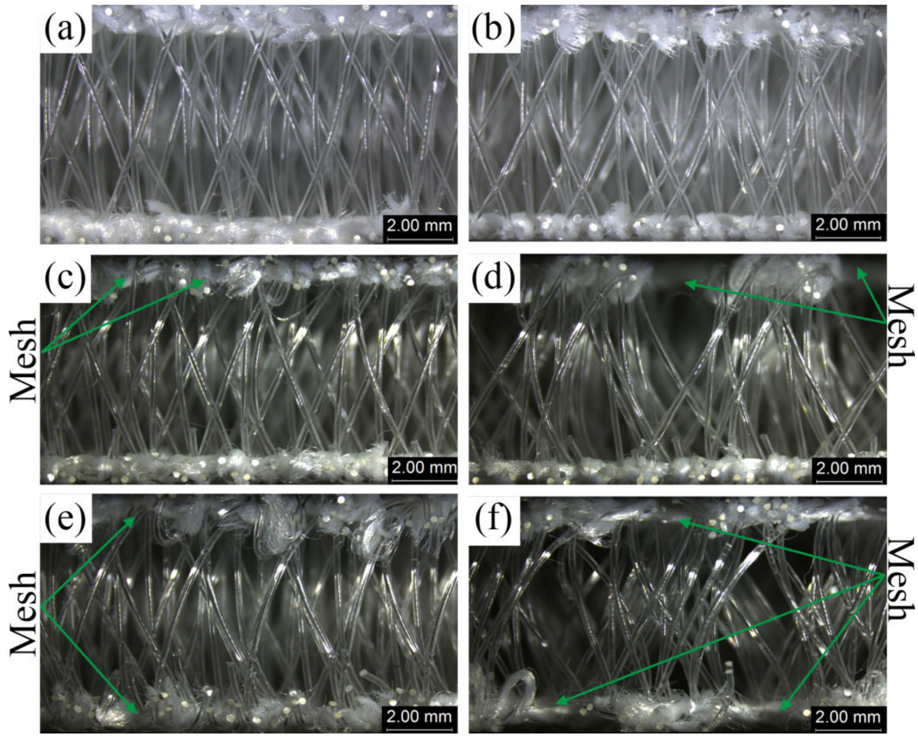

Figure 7.15 Cross-sectional microscopic pictures of the warp-knitted spacer fabrics observed from the walewise direction: (a) sample S1; (b) sample S3; (c) sample S8; (d) sample S10; (e) sample S9; (f) sample S11.

7.5 Relationship between peak contact force and peak transmitted force

The peak transmitted force is an important parameter to determine the protective performance of a spacer fabric. As explained previously, the peak force transmitted to a particular part of the body during the impact process should not exceed the tolerance that tissue or bones can bear. Thus, it is important to know how much peak contact force can be transmitted from the impacted side to the other side of a fabric. The peak transmitted force against the peak contact force for all the spacer fabric samples is shown in Figure 7.16. It can be seen that the peak transmitted force has an obviously linear relationship with the peak contact force. The linear regression calculation has given F_t = 0.6684 F_c, R^2=0.994, where F_t and F_c are the peak transmitted force and peak contact force, respectively. This means that about 66.84% of the peak contact force is transmitted from the impacted side to the other side of the fabric, and this transmitting rate is nearly the same for all the warp-knitted spacer fabrics regardless of their structural parameters. It is normal that the lower the peak contact force, the lower the force transmitted. For this reason, the optimized design of a spacer fabric should be focused on decreasing the peak contact force by selecting suitable structural parameters for a specified impact energy.

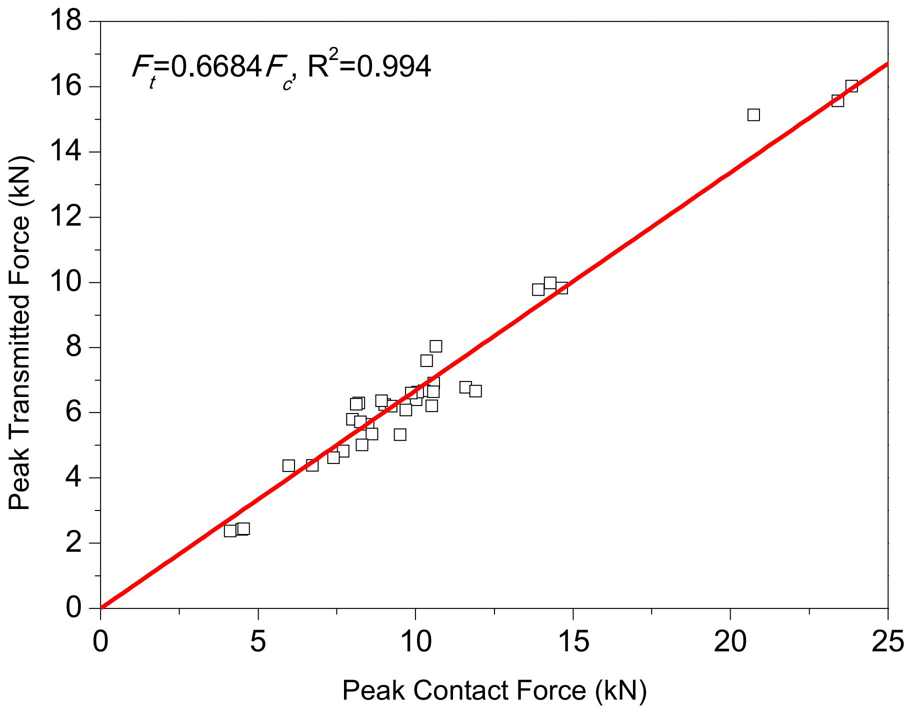

Figure 7.16 The relationship between peak transmitted forces and peak contact forces.

7.6 Conclusions

The warp-knitted spacer fabrics were tested on a drop-weight impact tester with a predefined impact energy. Both the acceleration and transmitted force signals were measured and treated with a low-pass filter. The peak contact force and transmitted force as a function of time were compared, and the velocity and displacement of the striker were calculated. The impact compression behaviour of a typical fabric was analysed based on both the contact force–displacement curve and energy absorbed–contact force curve. The effects of different structural parameters, including the spacer monofilament yarn inclination and fineness, fabric thickness and outer layer knitted structures, on the impact compression behaviour of the warp-knitted spacer fabrics were analysed based on the contact force–displacement curves, energy absorbed–contact force curves and transmitted force–time curves. The relationship between the peak transmitted force and peak contact force was established.

According to the experimental results and analyses, the following conclusions can be drawn.

- The compression behaviour of the warp-knitted spacer fabrics under impact is different from the behaviour under static compression. The impact contact force is higher than the static force during almost the entire compression process. The rate dependency of the spacer fabrics leads to a higher energy absorption capacity in impact than that in static compression.
- The peak contact force and peak transmitted force are different at their peak time and peak value. The peak transmitted force reaches its peak point with a time delay due to shock wave propagation. The peak transmitted force is much lower than peak contact force.
- An optimized spacer yarn inclination and fabric thickness exists for obtaining better protective performance with a lower peak contact force and peak transmitted force. The peak contact force and peak transmitted force increase

with decreasing the spacer monofilament diameter due to the lower energy absorption capacity at the end of the plateau stage. The spacer fabrics knitted with the large-size mesh structure for both the top and bottom outer layers have higher peak contact forces and higher peak transmitted forces than the spacer fabrics knitted with the small-size mesh and close structures.

- A linear relationship exists between the peak contact force and peak transmitted force. The transmitting rate is about 66.84% and is nearly the same for all the warp-knitted spacer fabrics studied, regardless of their structural parameters.

The next chapter will describe the assessment of the protective properties of the developed warp-knitted spacer fabrics of hemispherical shape obtained from impact tests conducted strictly in accordance with the European Standard BS EN 1621-1:1998.

CHAPTER 8 PROTECTIVE PROPERTIES OF WARP-KNITTED SPACER FABRICS FOR HUMAN BODY PROTECTION

8.1 Introduction

The experimental investigations into the static and impact compression behaviour of the developed warp-knitted spacer fabrics of planar shape have been described in Chapter 6 and Chapter 7, respectively. The energy absorption and force attenuation capability of these fabrics under flatwise static and impact compression has been analysed in detail. These studies indicated that the developed fabrics have the key feature of behaving as cushioning materials, providing three distinct stages in static and dynamic compression, described as linear elasticity, plateau and densification. However, in order to offer an adequate combination of protection and comfort, the protective material must conform to the shape and curvature of the body part being protected. There is no doubt that the impact properties of a protective material of curved shape are different from those of a planar shape due to the change in boundary conditions during loading. Hence, to obtain a deeper understanding of the protective properties of warp-knitted spacer fabrics for human body protection, their energy absorption mechanism and force attenuation properties in curved shapes should be studied.

As noted in the literature review, a series of standard tests have been developed for evaluating the protective performance of commercial impact protectors for a variety of sporting applications. In those standards impact protection is generally measured by the force transmitted during impact; a striker of specified shape, size and weight drops freely onto the protector placed on a hemispherical anvil with the required velocity and impact energy. The hemispherical anvils have different curvatures to simulate the areas of the body to be protected. The radius of the anvils ranges from 12.5 to 150 mm, and the impact energies for the various types of protectors lie between 1 and 60 J. For safe protection, resultant transmitted forces should not exceed specific values. Among those standards the two European Standards for motorcyclists' impact protectors are those most commonly quoted for evaluating protective performance, one for limbs and shoulders (BS EN 1621-1:1998) and the other for back protection (BS EN 1621-2:2003). Under the European directive on personal protective equipment any clothing claiming to provide protection from injury must be tested and labelled that it complies with the relevant standard.

This chapter describes the assessment of the protective properties of the developed warp-knitted spacer fabrics obtained from impact tests conducted strictly in accordance with the European Standard BS EN 1621-1:1998 in hemispherical form, in order to simulate the realistic requirements of human body protection. This chapter is organized as follows. Section 8.3 focuses on the analysis of the impact behaviour of a typical spacer fabric in order to understand the impact process, energy absorption and force attenuation mechanism of the spacer fabric. Section 8.4 discusses the effect of structural parameters and lamination on the impact protective performance of the fabrics.

8.2 Impact tests

The impact tests were conducted on the same drop-weight impact tester used in

Chapter 7 but with different striker and anvil. The equipment was specially designed in strict accordance with the European Standard BS EN 1621-1:1998. As shown in Figure 8.1, the striker was constructed of polished steel, with a weight of 5 kg and a face size 40 mm × 80 mm with 5 mm radius edges. The impact energy can be controlled by changing the dropping height of the striker. The anvil was also made of polished steel, with a total height of 170 mm and a hemispherical surface of radius 50 mm, to simulate the curvature of human shoulder, elbow, knee, forearm, tibia or hip. Similar to the flatwise impact tests, the hemispherical anvil was mounted on the massive base through the load cell (1210AF–50KN) in line with its sensitive axis, to measure the transmitted force. In addition, in order to obtain more information during the impact process, the acceleration of the striker was measured by means of accelerometers glued or screwed to it. Since the measured accelerations will be higher than those from the flatwise impacts, in addition to the Isotron® accelerometer used in the flatwise impacts (Model 2250AM1–10), two additional accelerometers were used, corresponding to the degree of the resultant acceleration of the striker. The one was Isotron® accelerometer from Endevco Company (USA), Model 25B (sensitivity 4.550 mV/g and measuring range ±1000 g). It was glued to the striker for the impact tests. The other one screwed to the striker for the impact tests was a Model 8704B5000 K–SHEAR® accelerometer (sensitivity 0.976 mV/g and measuring range ±5000 g) from Kistler Instrumente, Winterthur, Switzerland.

The specimens were conformed onto the anvil using a ring fixture as shown in Figure 8.2. Elastic straps were angled downwards around the anvil to pull the sample down to the anvil without significant additional compression of the sample. The straps were connected to a flat elastic ring surrounding the impact area without covering it. Since areas of the human body may in practice be subjected to different levels of energy impact in different sports or other activities, impact energies ranging from 1 to 60 J are required for testing impact protectors according to the standards reviewed in Chapter 2. In order to obtain a full picture of the impact behaviour of a typical warp-knitted spacer fabric under different levels of impact energy 5, 10, 20, 30, and 40 J were selected for the impact tests in the study, in addition to the 50 J specified in BS EN 1621-1:1998. All the tests were conducted at 20 °C and 65% relative humidity. For each impact energy level, a total of 10 repeat tests were carried out to ensure consistency.

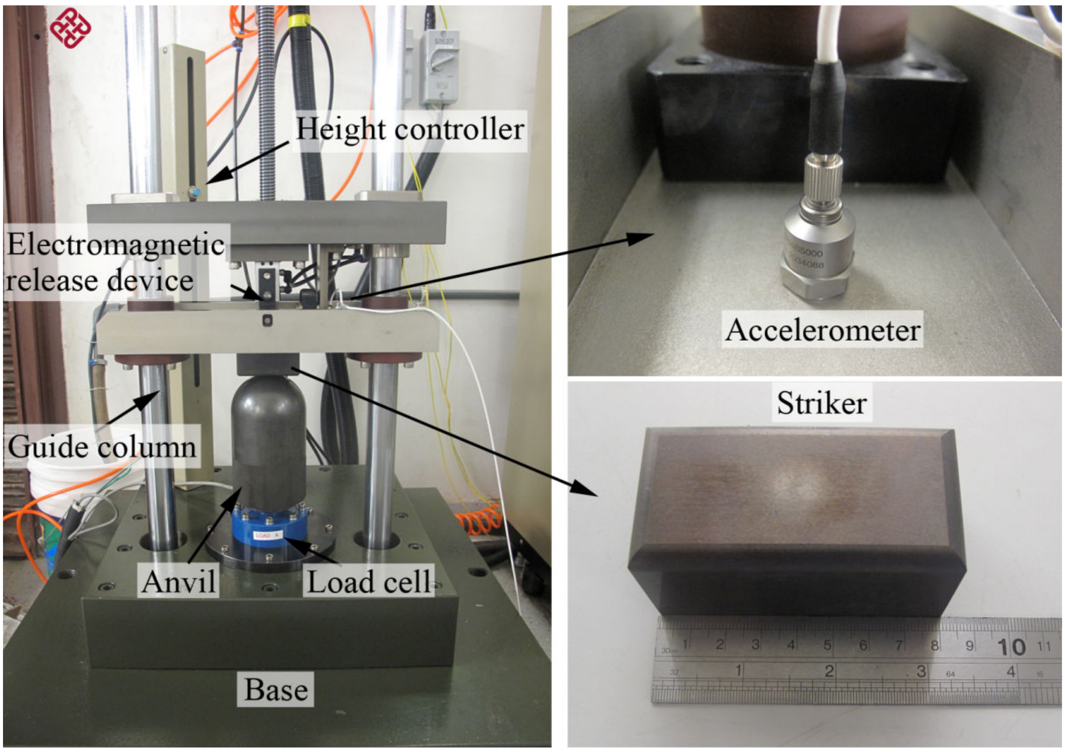

Figure 8.1 Drop-weight impact tester according to European Standard BS EN 1621-1:1998.

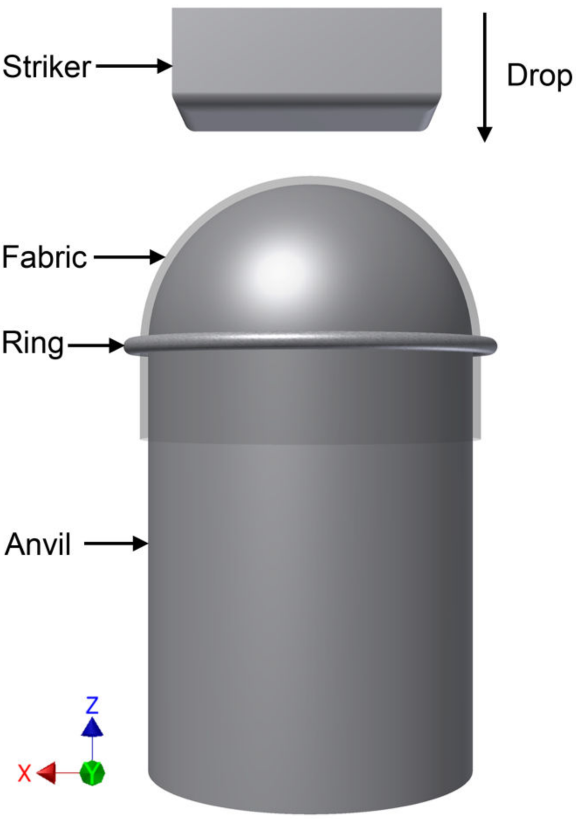

Figure 8.2 Schematic presentation of the impact test.

8.3 Impact behaviour of spacer fabric in hemispherical shape

This section focuses on the analysis of the impact behaviour of a typical spacer fabric (S1) of hemispherical shape impacted with different levels of kinetic energy in order to understand the impact process, energy absorption and force attenuation properties of the spacer fabric.

8.3.1 Impact process analysis

Typical acceleration and transmitted force signals for different levels of impact energy are shown in Figure 8.3(a) and (b), respectively. Figure 8.3(a) shows that in the initial stage the acceleration gives a lower value over a relatively longer time, and then rapidly rises to a peak in the second stage. Under higher energy impact a greater peak in acceleration response is obtained over a shorter time. According to the theorem of momentum, a shorter duration of impact will lead to a higher acceleration and a higher reaction force. In the absence of fabric the dropping striker is instantaneously stopped by the anvil, producing a very high acceleration and dynamic contact force. However, with the fabric located on the anvil surface the striker experiences deceleration as it strikes the fabric. During the deceleration the fabric first stores and dissipates the kinetic energy of the impact and then releases the stored energy over a longer duration, thereby leading to a reduction in the acceleration of the striker and generating a lower contact force between the striker face and the upper surface of the fabric. It should be noted that the increase in impact energy will lead to an increase in the velocity of the striker at the beginning of its contact with the fabric. Due to the increase in the initial contact velocity, the time taken by the striker to compress the fabric to its denser state is shortened. Since the fabric has higher compression resistance in its densified state, it is able to stop the striker more quickly, and at the peak point the increase in impact energy will therefore result in a reduction in impact time and an increase in acceleration. During the impact process, the force is transmitted to the anvil through the deformed fabric, and the transmitted force curves therefore have a similar form to the acceleration curves shown in Figure 8.3(b). For a similar reason a higher level of impact energy will result in a greater transmitted peak force over a shorter duration.

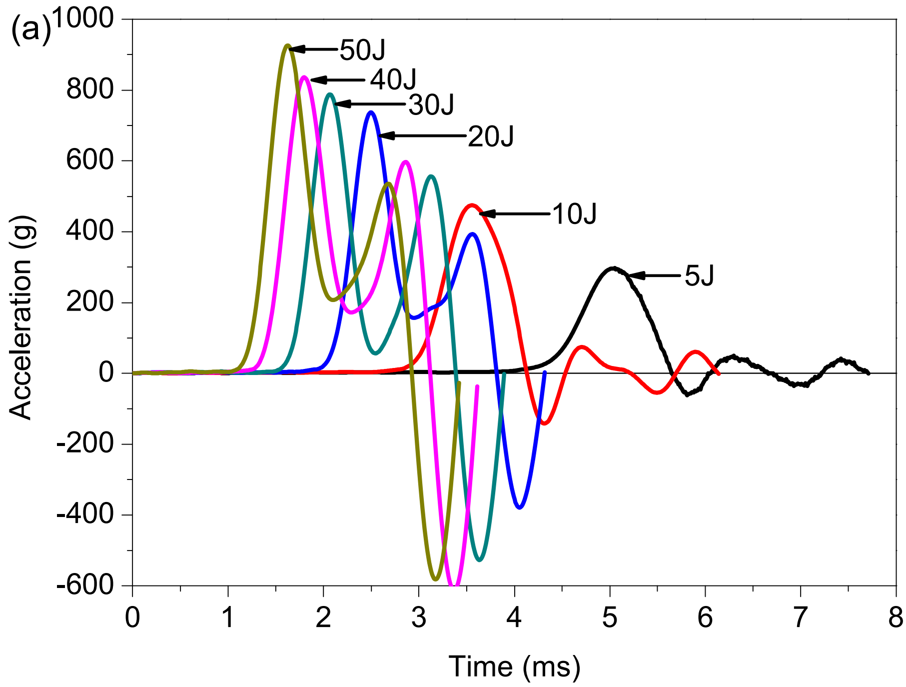

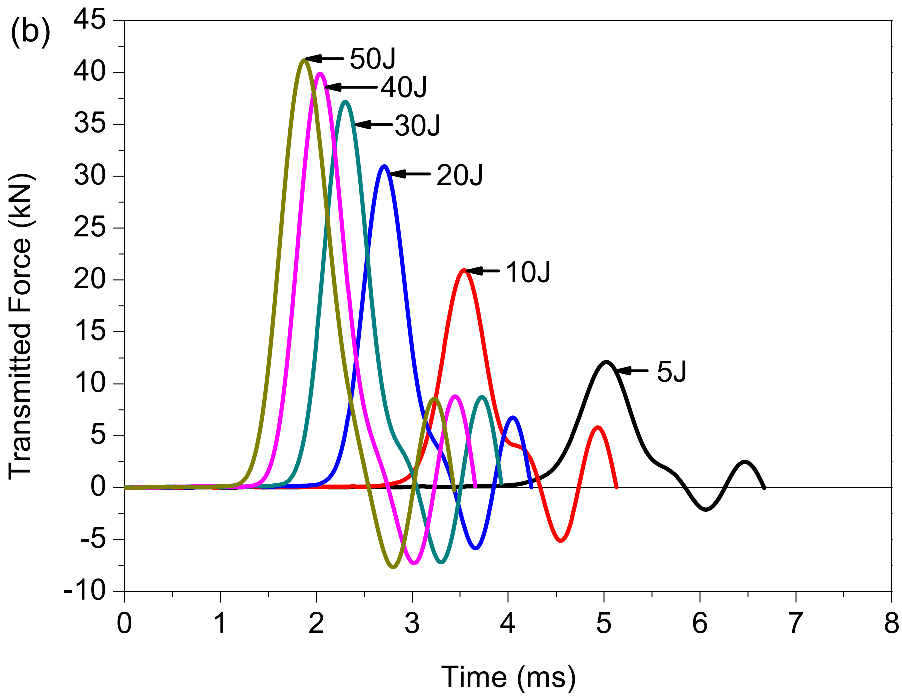

Figure 8.3 Impact signals at different energy levels: (a) acceleration; and (b) transmitted force.

The contact force–displacement curves are obtained by integrating the respective acceleration curves, as shown in Figure 8.4. Inset is a magnified view of the curves. Similar to the acceleration and transmitted force signals, two clear stages in the contact force can be observed, the first very slowly increasing and the second increasing rapidly. The slowly increasing stage of the curves is generally located in the displacement range below 5.5 mm, corresponding to a compression strain of 73%. Subsequently, as the displacement increases, the contact force increases rapidly. Figure 8.4 also shows that the curves are sensitive to strain rate. As the impact energy is controlled by the dropping height of the striker, the change in impact energy implies a change in initial contact velocity or strain rate. The spacer fabric is made up of polyester fibres with strain rate sensitivity, and its impact properties are therefore also sensitive to strain rate. Figure 8.4 indicates that a striker of higher kinetic energy can more quickly compress the fabric into its densification stage and with a larger final displacement. This is one of the reasons why the fabric has a higher peak contact force when it is impacted at higher kinetic energy.

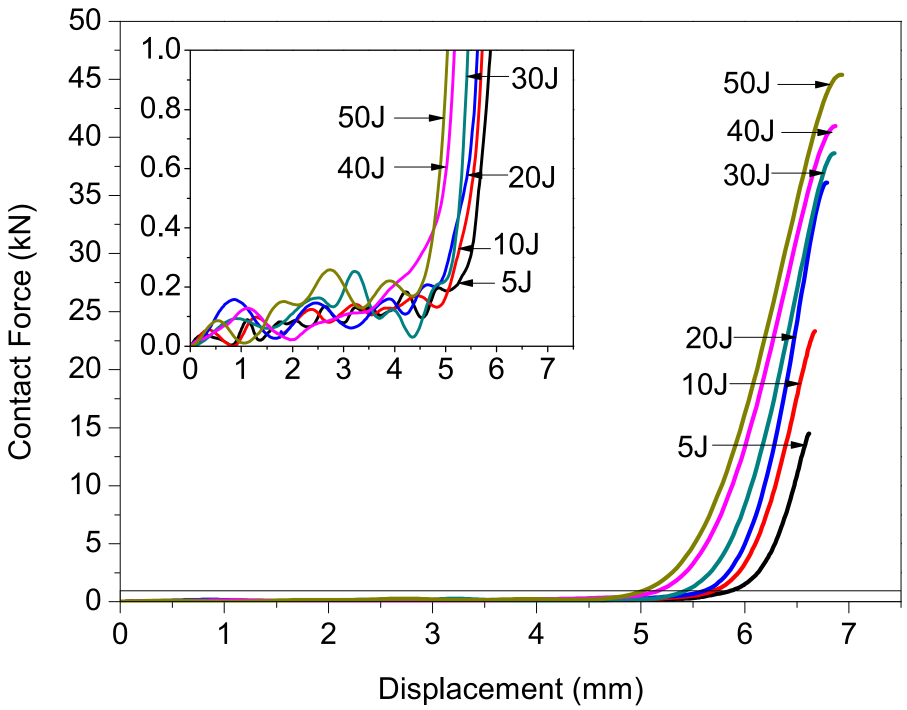

Figure 8.4 Contact force–displacement curves at different energy levels.

It is interesting to compare the impact behaviour of the same fabric impacted in different shapes. Chapter 7 has shown that the force–displacement curve of the fabric S1 under flatwise impact includes three main stages, linear elasticity, plateau and densification. However, the impact contact force–displacement curves of the spacer fabric in the hemispherical form show only two stages, as mentioned above, and no plateau stage is observed under hemispherical impact. This difference originates from the different boundary conditions of the spacer fabric in planar and hemispherical shapes. One reason is that, under flatwise impact, the contact area between the striker face and the fabric surface remains constant throughout the entire impact process. By contrast, the contact area for the fabric in the hemispherical form is changed during the impact process and increases with the displacement of the striker. This can be confirmed by the following geometric analysis.

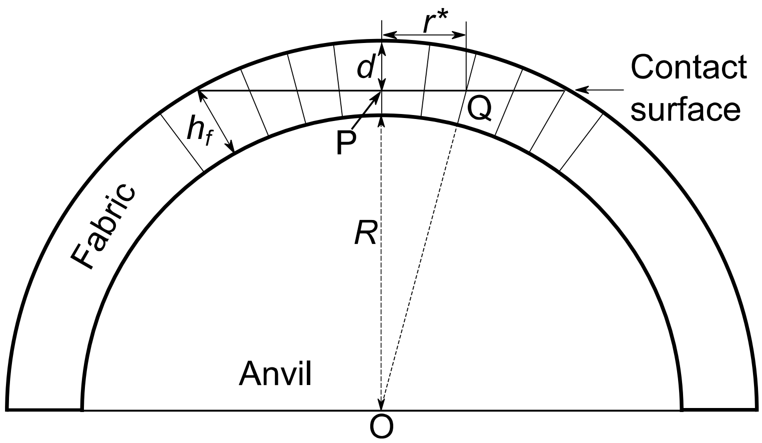

Figure 8.5 Cross-section of the fabric on the anvil.

As shown in Figure 8.5, a cross-section of the fabric through the central axis of the anvil is used to derive the contact area between the striker face and the fabric surface during the impact, based on the axis-symmetrical property of the fabric shape and the anvil. Geometric analysis of Figure 8.5 gives the following relationship:

$$A_c = \pi\left[\left(R + h_f\right)^2 - \left(R + h_f - d\right)^2\right], \tag{8.1}$$

where A_c is the contact area, h_f is the fabric thickness, R is the anvil radius, and d is the displacement of the striker. In this study, R and h_f are equal to 50 mm and 7.52 mm, respectively. Using these values, the variation in contact area with the displacement of the striker is plotted in Figure 8.6. It can be seen that the contact area of the fabric with the striker rapidly increases as the displacement of the striker increases. As the contact area increases, the contact force cannot remain constant. Therefore, the plateau stage of the contact force–displacement curves obtained under the flatwise impact condition is not possible under a hemispherical-shaped impact.

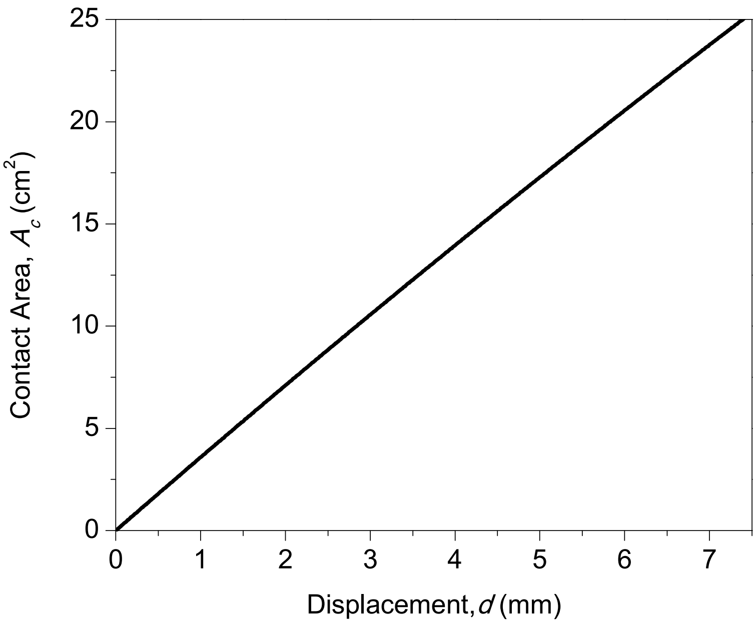

Figure 8.6 Variation in contact area with displacement of the striker.

Another reason for no plateau stage being observed under hemispherical impact is that the spacer monofilaments within the fabric deform in different ways under flatwise impact and under impact of the fabric in the hemispherical form. Under flatwise impact all the spacer monofilaments simultaneously withdraw the impact load and are subjected to the same deformation. On the other hand, in the hemispherical form the spacer monofilaments at different positions experience different deformations. As shown in Figure 8.7, when the displacement of the striker is larger than the densification displacement of the fabric obtained under flatwise impact, the linear elasticity, plateau and densification of the spacer monofilaments within the fabric can all be observed at the same time under the impact of the fabric in the hemispherical form. It can be seen that the closer the position of a spacer monofilament to the central axis of the anvil, the greater the deformation it experiences.

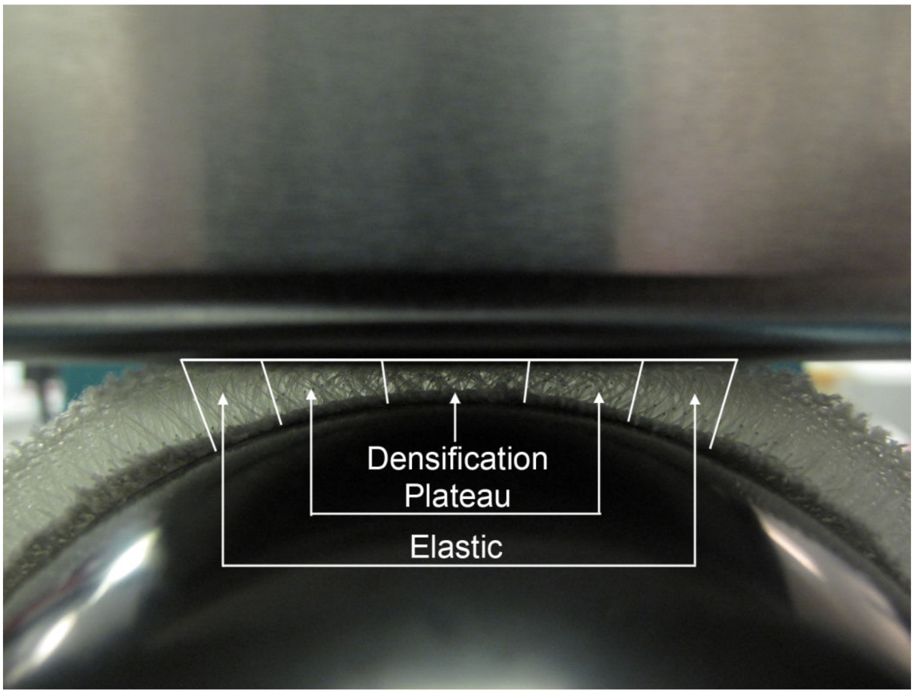

Figure 8.7 Different deformations of the spacer monofilaments within the fabric in the hemispherical form under impact.

With reference to Figure 8.5, the strain of a spacer monofilament ε at an arbitrary point Q on the contact surface for a given displacement of the striker d is determined by:

$$\varepsilon = \left(R + h_f - \sqrt{\left(R + h_f - d\right)^2 + r^{*2}}\right) \Big/ h_f, \tag{8.2}$$

where r^* is the distance between points Q and P on the central axis of the striker. The distribution of strain ε with r^* for a given displacement of the striker d (d = 5mm) is shown in Figure 8.8(a). It can be seen that ε changes with r^* in a parabolic manner. The maximal deformation is located at the central point of the contact surface. The distribution of strain ε with r^* for various values of d in a cross-section of the fabric through the central axis of the anvil is shown in Figure 8.8(b). It is clearly seen that all the deformations on the contact surface increase with increase in d. Since the spacer monofilaments within the fabric can deform differently, the plateau stage cannot be observed in the contact force–displacement curves of the fabric under impact in the hemispherical form.

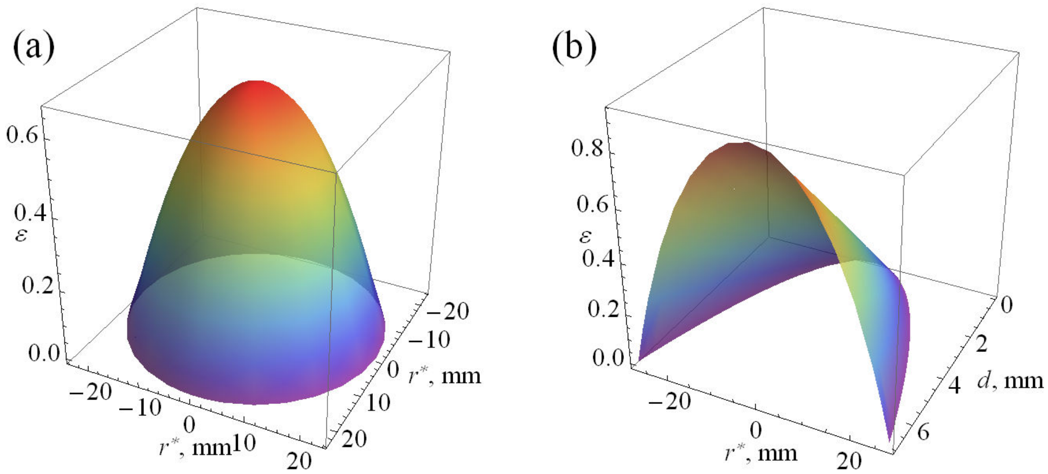

Figure 8.8 Distribution of strain ε with r^*: (a) for a given displacement of the striker d = 5 mm; (b) for varied values of d in the cross-section of the fabric.

8.3.2 Energy absorption and force attenuation properties

The impact process of the spacer fabric in the hemispherical shape is complicated. During the impact, the kinetic energy of the striker is transformed into different energy forms, including the energy absorbed by the deformation and damage to the fabric, the energy absorbed by the deformation of the testing system (striker, anvil and supporting mechanism), and the energy lost due to the propagation of stress wave. At the point of maximal deflection and acceleration the total kinetic energy of the striker is completely transformed into deformation energy and the dissipated energy, which include the energy stored by the elastic deformation of the fabric and the testing system, the energy dissipated by the plastic and damage to the fabric and the testing system, and the energy dissipated by the propagation of the stress wave. After this point, the stored energy will transfer to the kinetic energy of the striker, causing the striker to rebound. By neglecting the energy dissipated by the plastic deformation and damage to the testing system, and the energy lost due to the propagation of stress wave, the following energy expressions can be obtained:

$$U_{\text{kinetic}} = U_{\text{elastic}} + U_{\text{elastoplastic}} + U_{\text{damage}} + U_{\text{machine}}, \tag{8.3}$$

$$U_{\text{mechanical}} = U_{\text{elastic}} + U_{\text{elastoplastic}}, \tag{8.4}$$

$$U_{\text{residual}} = U_{\text{damage}} + U_{\text{machine}}, \tag{8.5}$$

where U_{kinetic} is the kinetic energy of the striker, U_{elastic} is the energy stored by elastic deformation of the fabric, $U_{\text{elastoplastic}}$ is the energy absorbed by elastoplastic deformation of the fabric, U_{damage} is the energy dissipated by damage to the filaments, $U_{\text{mechanical}}$ is the energy absorbed by the elastic and elastoplastic deformation of the fabric (the area under the contact force–displacement curve, shown in Figure 8.9), U_{machine} is the energy stored by elastic deformation of the testing system, and U_{residual} is the residual kinetic energy of the striker after being absorbed by the elastic and elastoplastic deformations of the fabric, which need to be dissipated by damage to the fabric (U_{damage}), or transferred to the testing machine (U_{machine}).

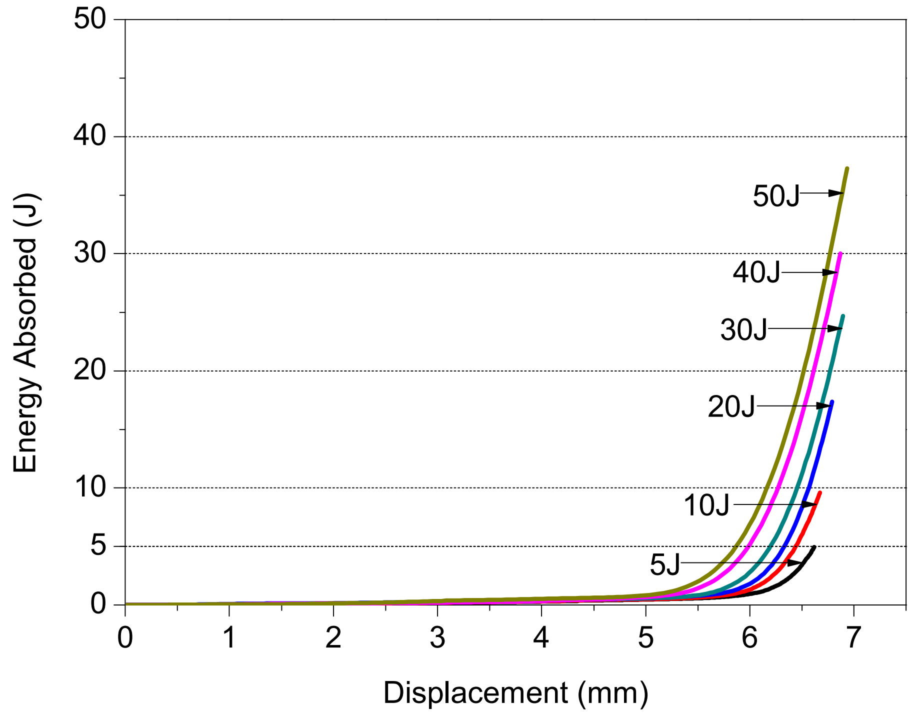

Figure 8.9 Energy absorbed by the elastic and elastoplastic deformations of the fabric against the displacement of the striker under different impact energies.

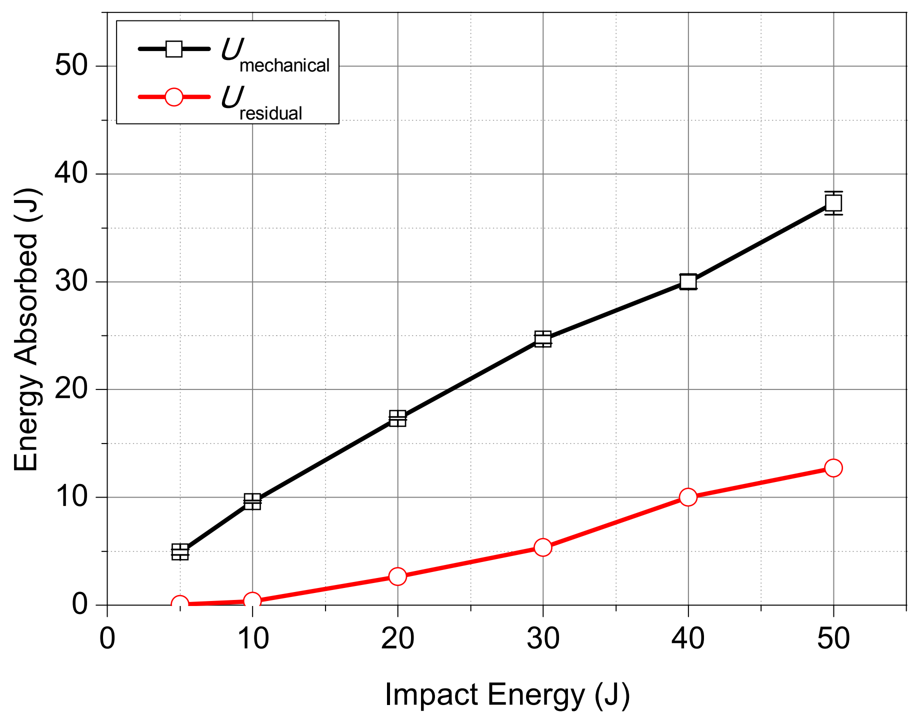

Figure 8.10 Energy absorbed by the elastic and elastoplastic deformations of the fabric and residual energy for different levels of impact energy.

Figure 8.9 shows the energy absorbed by the elastic and elastoplastic deformations of the fabric ($U_{\text{mechanical}}$) against the displacement of the striker at different levels of impact energy. It can be seen that the absorbed energy increases with increase in impact energy. Since impact by the striker at a higher level of kinetic energy can result in a higher final displacement of the fabric, more energy is absorbed by the fabric due to its greater deformation. Figure 8.10 shows the energy absorbed by the elastic and elastoplastic deformations of the fabric and the residual energy of the striker. It can be seen that when the impact energy is below 10 J the kinetic energy of the striker is almost completely absorbed by the elastic and elastoplastic deformations of the fabric without heat generation. However, when the impact energy is greater than 10 J, the kinetic energy of the striker cannot be totally absorbed by the elastic and elastoplastic deformations of the fabric, although the energy absorbed by such deformations of the fabric increases as the impact energy increases. In this case, the kinetic energy of the striker not absorbed by the elastic and elastoplastic deformations of the fabric is transferred to the residual energy. As shown in Figure 8.10, the residual energy of the striker also increases as the impact energy increases. When the purely elastic and elastoplastic deformations of the fabric cannot totally absorb the higher kinetic energy of the striker, damage to the filaments takes place. It should be noted that while one part of the residual energy is transformed into heat, the other part together with U_{elastic} and the elastic deformation energy of $U_{\text{elastoplastic}}$ makes the striker rebound.

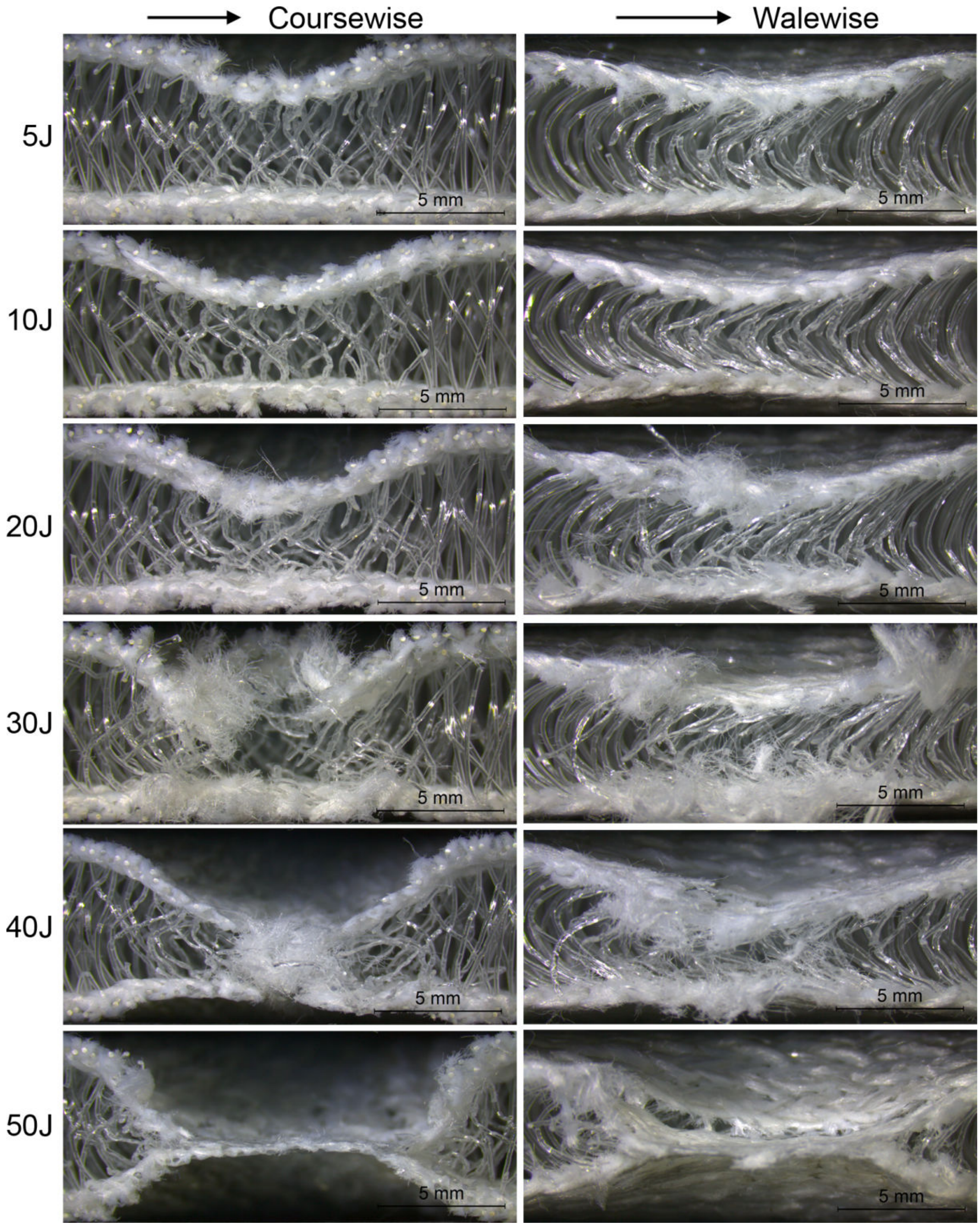

Figure 8.11 Deformation and damage to the fabric after impact at different levels of impact energy.

Figure 8.11 shows the deformation and damage of the fabric after impact at different levels of impact energy. Severe plastic deformation of the monofilaments in the spacer layer can be observed under lower impact energies (5 J and 10 J). In this case, the monofilaments become kinked, distorted or squashed. Some breakage of the monofilaments is also observed at 10J impact energy. However, no obvious deformation of the multifilaments is observed in the outer fabric layers. When the impact energy is increased to 20 J, in addition to plastic deformation and breakage of the monofilaments, some breakage of the multifilaments in the outer layers is also observed. When the impact energy reaches 30 J, a hole in the outer upper layer of the fabric is produced by the impact, and at the same time a number of mono- and multifilaments are broken. When the impact energy is 40 J, both mono- and multifilaments are broken and become fused together by the heat generated. When the impact energy reaches 50 J, mono- and multifilaments are broken and become a rigid plastic through a thermoplastic process. It can be speculated that a large amount of heat is generated during the impact, thereby thermosoftening the filaments.

The above analysis shows that the fabric is deformed and damaged in different modes when subject to different impact energies. When the energy absorption capacity of the fabric due to elastic and elastoplastic deformations is higher than the kinetic energy of the striker, the impact energy is totally absorbed by the fabric. In this case, the contact law is determined by the stress–strain nature of the spacer fabric. On the other hand, when the impact energy is higher than the energy absorption capacity due to the elastic and elastoplastic deformations, damage is caused to the fabric as it absorbs the remainder of the kinetic energy of the striker. In this case, the contact law between the striker face and the fabric may change significantly and a very large contact force could be produced, as the striker may collide directly with the anvil. In this study no direct collisions occurred between the striker and the anvil, as there were no perforated holes present in the fabrics after impact, as shown in Figure 8.11. The peak contact force is therefore determined by the contact stiffness of the compressed fabric at the rebounding point. There is no doubt that a highly densified fabric has a high modulus and therefore high contact stiffness. Hence, the kinetic energy of the striker is preferably absorbed before the fabric is compressed to its high densification stage. As mentioned previously, there is a longer plateau stage for the contact force under flatwise impact. This response allows the fabric to absorb a large amount of kinetic energy at a lower constant contact force by elastoplastic deformation. As a result, the spacer fabric possesses superior force attenuation performance under flatwise impact. However, as shown in Figure 8.4, under impact in the hemispherical form, the contact force curves have a monotonically increasing trend with the displacement, since the spacer monofilaments within the spacer fabric in the hemispherical shape cannot effectively resist the impact load.

To understand the relationship between the force attenuation and the energy absorption behaviour of the spacer fabric under impact in the hemispherical form, the energy absorbed by the spacer fabric may be plotted against the contact force, as shown in Figure 8.12, which indicates that the energy absorbed increases nonlinearly with the contact force. Obviously, to absorb more kinetic energy, the spacer fabric must be compressed with a larger displacement into a highly densified stage. This leads to greater contact stiffness, a larger contact area, and a higher peak contact force between the striker face and the fabric surface. Compared with the impact in the planar shape, the lower efficiency of force attenuation of the spacer fabric in the hemispherical shape is because not all of the spacer monofilaments are able to contribute to the resistance to impact loading.

During the impact, the contact force is transmitted to the anvil through the deformed specimen in the form of stress waves. The transmitting process is complicated and its mechanism is not relevant to this study. Figure 8.13 shows the variation in both the peak contact force and the peak transmitted force with impact energy. The results show that both the forces increase nonlinearly as the impact energy increases. In addition, the peak transmitted force remains below the peak contact force for all impacts. However, the ratio between them is not constant when the impact energy changes. This difference may arise from their different modes of deformation and damage, which can affect the stress wave propagation and damping behaviour of the fabric. For instance, for the impact with a kinetic energy of 30 J, the transmitting ratio is higher than those for the other impacts. This is the result of a hole created in the top outer fabric layer when many mono- and multifilaments are broken, as can be observed in Figure 8.11.

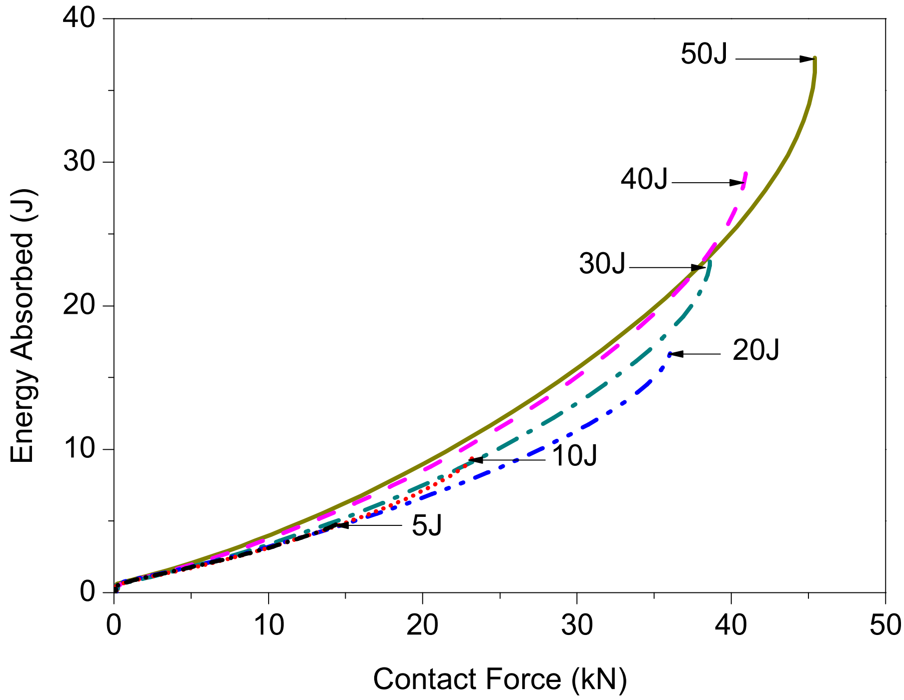

Figure 8.12 Energy absorbed versus contact force at different impact energies.

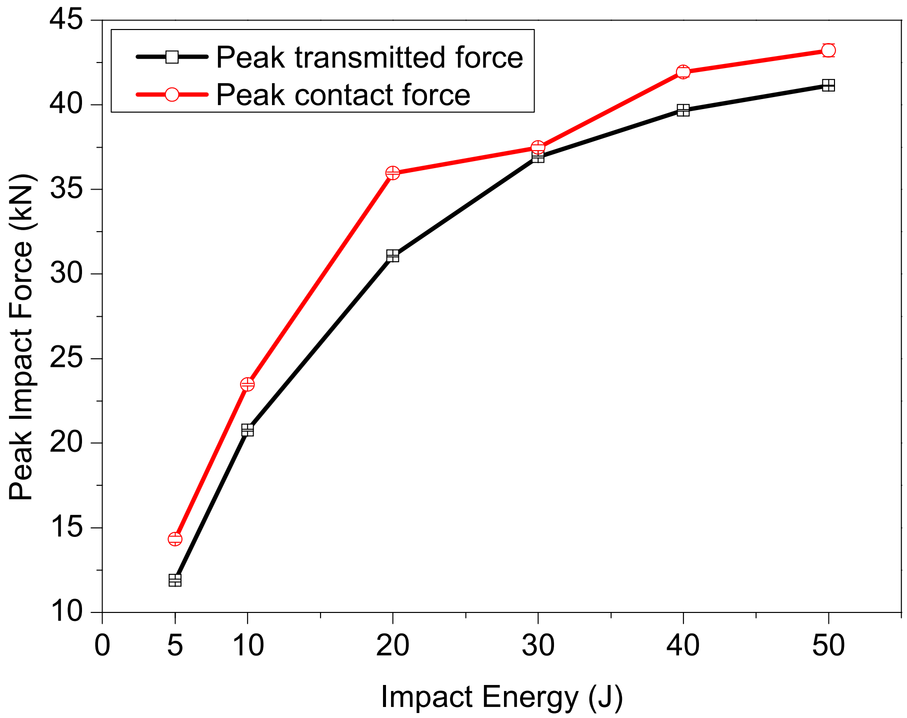

Figure 8.13 Variations of the peak contact force and the peak transmitted force with impact energy.

According to the European Standard BS EN 1621-1:1998, for motorcyclists' limb impact protectors the mean value of the transmitted forces must not exceed 35 kN and no single value shall exceed 50 kN at an impact energy of 50 J. The test results obtained show that when the impact energy is below 30 J a single layer of the fabric can meet the force transmission requirement. However, when the impact energy is 50 J, as specified in the standard, the transmitted force is 41.14±0.024 kN, which exceeds the value allowed. Due to the severity of motorcycle impacts, a single layer of this particular fabric is thus insufficient to offer adequate protection. In this case, the structure of the fabric should be optimized and lamination employed to enable the protective performance of spacer fabrics to give the required protection. The effects of structural parameters and lamination on protective properties will be discussed in the next section.

8.4 Effects of structural parameters and lamination on the protective performance

Following a similar pattern to the investigation into the effects of the structural parameters on the flatwise impact behaviour of the spacer fabrics presented in Chapter 7, in this section, a further study that focused on the effects of the structural parameters and lamination of the spacer fabrics on the force attenuation properties in the hemispherical shape for impact protectors is presented in this section.

All the samples employed in Chapters 6 and 7 were utilized. The spacer fabrics laminated in single layer, double layers and triple layers were tested with kinetic energies of 5, 10, 20, 30, 40 and 50 J, respectively, following the method indicated by the European Standard BS EN 1621-1:1998. Ten specimens were tested for each kind of spacer fabric sample and lamination method to obtain accurate results. As the transmitted force is required by the standard to assess the impact force attenuation properties of an impact protector, only the results of transmitted forces are adopted for the discussion. All the transmitted force-time curves presented are the most representative curves, and all the peak transmitted forces presented are the mean values of ten test results with standard error.

8.4.1 Effect of spacer yarn inclination angle

A group of three fabrics (S2, S3 and S4) with different spacer monofilament inclinations (shogging one-needle, two-needle and three-needle space between the front- and back-needle bars) is used to analyse the effect of spacer yarn inclination on the impact force attenuation properties of warp-knitted spacer fabrics. The shogging space determines the spacer monofilament inclination and length. The higher the number of the needles underlapped, the longer and more inclined the spacer monofilaments.

As shown in Figure 8.14, the transmitted force-time curves of these fabrics in single layer under impact at a kinetic energy of 5 J are used as an example for discussing the effect of the spacer monofilament inclination with the same impact energy. It can be seen that while the duration from the beginning point where the striker contacts the fabric upper surface to the peak point where the transmitted force reaches the maximal value increases as the spacer monofilament inclination increases, the peak transmitted force decreases as the spacer yarn inclination increases. This means that the spacer fabric with a larger spacer monofilament inclination and a longer spacer monofilament length more effectively resists the impact due to a lower peak transmitted force.

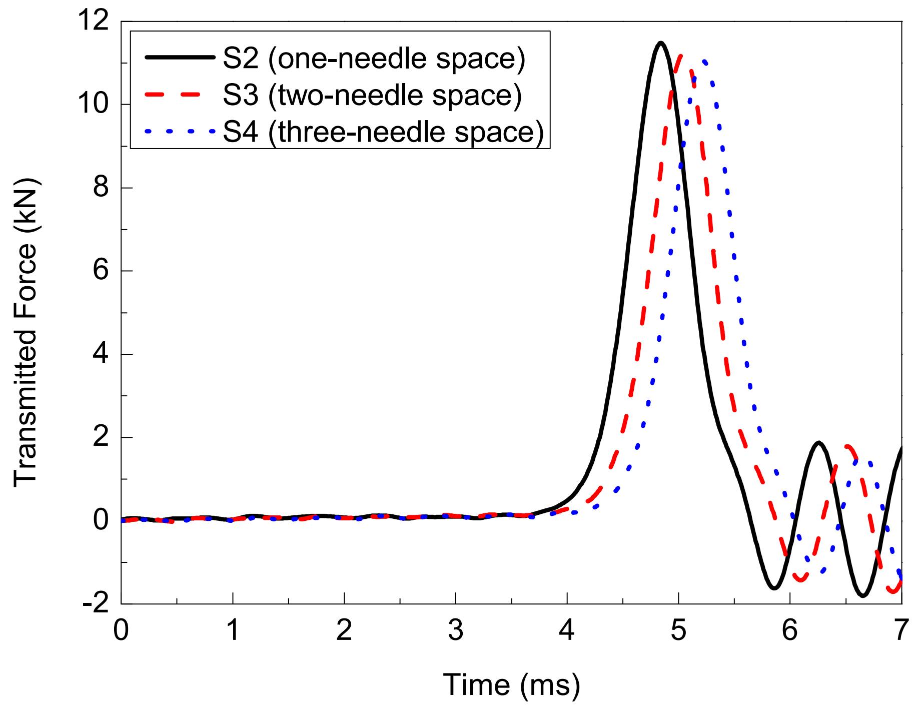

Figure 8.14 Effect of the spacer yarn inclinations on transmitted force-time curves (fabric layer: 1; impact energy: 5 J).

This result is quite different from the flatwise impact test result presented in Chapter 7, which has demonstrated that the fabric with moderate inclination spacer monofilaments (two-needle space underlapped) has the lowest peak transmitted force. Under the flatwise impact, the fabric with too vertical spacer yarns (one-needle space underlapped) becomes less stable and shear can easily occur between the two outer layers. On the other hand, too inclined spacer monofilaments (three-needle space underlapped) in a fabric have longer length and are less oriented to the impact compression direction. According to the theory of elastic stability, a longer elastic rod which is less oriented to the direction of the compression has a lower critical load. Therefore, the fabric with moderate inclination spacer monofilaments (two-needle space underlapped) has the best compression resistance to the flatwise impact, which makes it absorb more impact energy in the plateau stage. As a result, the peak transmitted force is the lowest. However, under impact in the hemispherical shape, the situation becomes complicated. When a planar spacer fabric is placed on the hemispherical surface of the anvil, its upper outer layer will be extended, and the bottom layer will be contracted. This special boundary condition makes the spacer monofilaments easier to shear rather than to buckle under impact. In this case, the stability of the spacer monofilaments becomes a critical point for the spacer fabric to resist the impact because the shear movements will decrease the compression resistance of the spacer yarns to the impact load, which leads to a high peak transmitted force. Since the fabric with larger inclination spacer monofilaments has higher shear resistance, it will have a lower peak transmitted force. Therefore, among these three fabrics, the force attenuation performance of the spacer fabrics increases as the length and inclination of spacer yarns increase under impact in the hemispherical shape.

The peak transmitted forces of fabric samples S2, S3 and S4 under impact with different kinetic energies and laminated layers are listed in Table 8.1. The similar trend, in which the peak transmitted force decreases as the spacer monofilament inclination increases, is obtained for the other levels of impact energies and laminated layers. However, the peak transmitted forces are dramatically reduced as the number of fabric layers increases.

Table 8.1 Effect of spacer monofilament inclination on peak transmitted force

Lamination	Sample	Peak transmitted force (kN)					
		5 J	10 J	20 J	30 J	40 J	50 J
Single layer	S2	11.38 ±0.051	20.61 ±0.046	31.66 ±0.064	37.10 ±0.000	39.66 ±0.060	41.18 ±0.049
	S3	11.35 ±0.048	20.53 ±0.065	31.27 ±0.037	37.08 ±0.037	39.6 ±0.032	41.14 ±0.051
	S4	11.06 ±0.027	20.22 ±0.051	31.68 ±0.063	36.94 ±0.024	39.46 ±0.040	40.9 ±0.063
Double layers	S2	4.98 ±0.128	12.98 ±0.162	25.18 ±0.086	35.45 ±0.052	38.52 ±0.037	39.74 ±0.051
	S3	4.36 ±0.040	11.74 ±0.060	24.66 ±0.075	34.82 ±0.057	38.42 ±0.049	39.30 ±0.045
	S4	3.90 ±0.032	11.70 ±0.071	23.30 ±0.032	34.46 ±0.083	38.38 ±0.037	39.60 ±0.032
Triple layers	S2	2.52 ±0.124	7.76 ±0.051	18.68 ±0.080	28.12 ±0.136	35.46 ±0.201	38.28 ±0.058
	S3	1.22 ±0.037	5.70 ±0.055	16.58 ±0.116	25.90 ±0.192	34.30 ±0.055	37.86 ±0.112
	S4	1.06 ±0.040	5.50 ±0.055	15.56 ±0.040	25.00 ±0.152	33.24 ±0.098	37.08 ±0.049

In a single layer, although the peak transmitted force decreases with the increase of the spacer monofilament inclination, the effect is not evident. However, by increasing the fabric layers, the effect of the spacer monofilament inclination becomes significant. This is because a single layer of the spacer fabrics is not strong enough to resist the impact with a high kinetic energy and is easier to be compressed into a high densification stage. In a single layer, all the three fabrics were compressed into their high densification stages. In these cases, the striker compressed the monofilament material rather than making the spacer monofilaments buckle. The transmitted force depends on the contact stiffness of the compressed yarn material as explained previously. Since all the fabrics were made of polyester monofilaments, the difference in peak transmitted force among fabric samples S2, S3 and S4 is not significant. However, as the fabric layers increase, the energy absorption of the laminated fabrics increases, and therefore they will not be compressed into a high densification stage. In this case, the postbuckling of spacer monofilaments plays the key role in resisting the impact loading, and the spacer monofilament inclination effect works. Therefore, a big difference in the value of the peak transmitted force can be observed for the specimens with more layers. Another point that needs to be noted is that by increasing the fabric layers, better impact force attenuation of spacer fabrics can be obtained when the impact energy is at a lower level. For instance, under impacts with the kinetic energies of 5 J and 10 J, adding one layer of the fabrics can nearly reduce the peak transmitted forces by half.

8.4.2 Effect of spacer yarn fineness

Two fabrics (S4 and S12) with the same spacer yarn inclination (underlapping three-needle space) and the same outer layer structure (chain plus inlay) but with two different spacer monofilament diameters (0.2 and 0.16 mm) are chosen to study the effect of spacer yarn fineness on the impact force attenuation properties of warp-knitted spacer fabrics. The thickness and outer layer stitch density of the two fabrics are also kept nearly the same.

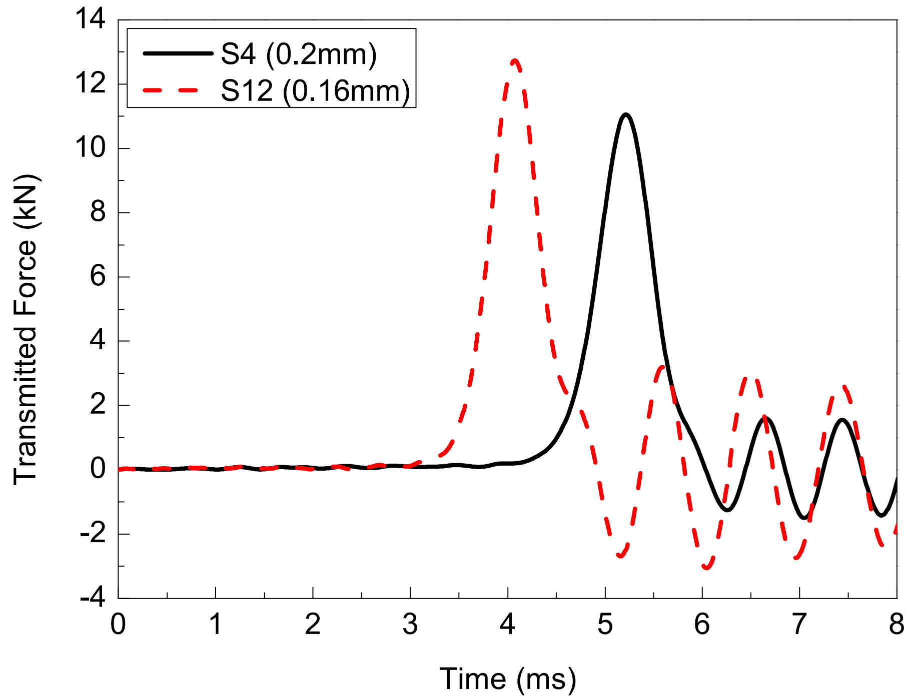

Figure 8.15 Effect of spacer monofilament diameter on transmitted force-time curves (fabric layer: 1; impact energy: 5 J).

As shown in Figure 8.15, the transmitted force-time curves of these two fabrics in a single layer under impact at a kinetic energy of 5 J are used as an example to analyse the effect of the spacer monofilament fineness with the same impact energy. It can be seen that the spacer fabric with the coarser spacer monofilament has a lower peak transmitted force and a longer time to the peak point and, therefore, has a better impact force attenuation property. This result is consistent with that obtained from the flatwise impact test, although the boundary condition is changed to the hemispherical form. This is normal because the fabric with coarser spacer monofilaments has higher compression resistance which can decelerate the striker more quickly and make the striker experience a longer time to reach the peak transmitted force point than the fabric with finer spacer monofilaments. Since the duration of deceleration is essential to the impact protection, the impact process should be as long as possible to absorb more energy in order to reduce the peak transmitted force. As shown in Table 8.2, this result is also valid for the other impact energy levels and fabric laminated layers. Similar to the flatwise impact, by increasing the spacer monofilament diameter, the force attenuation properties of spacer fabrics in the hemispherical shape can be improved considerably.

Table 8.2 Effect of spacer monofilament fineness on peak transmitted force

Lamination	Sample	Peak transmitted force (kN)					
		5 J	10 J	20 J	30 J	40 J	50 J
Single layer	S4	11.06 ±0.027	20.22 ±0.051	31.68 ±0.063	36.94 ±0.024	39.46 ±0.040	40.9 ±0.063
	S12	12.72 ±0.057	21.77 ±0.063	33.16 ±0.058	37.08 ±0.020	40.23 ±0.033	42.27 ±0.088
Double layers	S4	3.90 ±0.032	11.70 ±0.071	23.30 ±0.032	34.46 ±0.083	38.38 ±0.037	39.60 ±0.032
	S12	6.12 ±0.049	15.92 ±0.086	27.48 ±0.066	36.12 ±0.044	38.86 ±0.040	39.82 ±0.049
Triple layers	S4	1.06 ±0.040	5.50 ±0.055	15.56 ±0.040	25.00 ±0.152	33.24 ±0.098	37.08 ±0.049
	S12	2.84 ±0.040	8.38 ±0.049	20.08 ±0.136	30.32 ±0.139	37.30 ±0.071	38.88 ±0.058

It should be noted that although increasing the spacer monofilament diameter can considerably improve the force attenuation capacity of a spacer fabric in the hemispherical shape, increasing the spacer monofilament diameter can increase the fabric stiffness and, thus, decrease the comfort property of the fabric. In this regard, the balance between the comfort and protective performance should be taken into consideration by selecting suitable spacer monofilament fineness for a specific protective application.

8.4.3 Effect of fabric thickness

A group of four fabric samples (S5, S3, S6, and S7) produced with the same spacer monofilament diameter (0.20 mm), the same spacer monofilament inclination (underlapping two-needle space), and the same outer layer structure (chain plus inlay) but with different thicknesses (5.64, 7.59, 8.45 and 10.62 mm) is used to analyse the effect of fabric thickness on the impact force attenuation properties of warp-knitted spacer fabrics in the hemispherical form.

As shown in Figure 8.16, the transmitted force-time curves of these fabrics in a single layer under impact at a kinetic energy of 5 J are selected as an example to analyse the effect of the fabric thickness with the same impact energy. It can be found that the peak transmitted force decreases and the duration from the starting point to the peak transmitted force point increases as the fabric thickness increases. This phenomenon can be explained as follows. On the one hand, more time is required to compress a thicker fabric to its densification stage at a larger displacement. Since the increase of the compression time and displacement allows a thicker fabric to absorb more impact energy, a lower peak transmitted force can be obtained for a thicker fabric. On the other hand, as mentioned before, the contact area of a fabric with the striker rapidly increases as the displacement of the striker increases. A thicker fabric can be compressed into a larger displacement, and therefore more spacer monofilaments are involved in resisting impact loading. Therefore, the thicker fabric has a lower peak transmitted force under impact in the hemispherical shape.

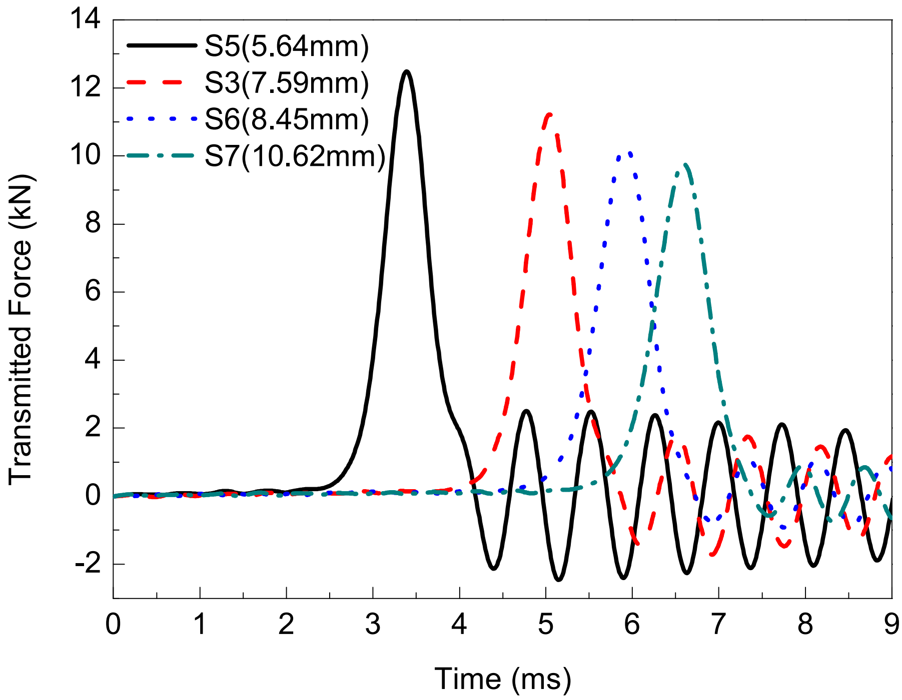

Figure 8.16 Effect of the fabric thickness on transmitted force-time curves (fabric layer: 1; impact energy: 5 J).

The peak transmitted forces for different impact energies and laminated layers are listed in Table 8.3. The similar trend, in which the peak transmitted force decreases as the fabric thickness increases, is also obtained for the other impact energy levels and laminated layers when all the fabric samples have the same destruction modes under impact. However, two exceptions are found for a single layer of the fabrics under impact with 20 J and double layers of the fabrics under impact with 50 J. In these two special cases, the thickest fabrics do not have the lowest peak transmitted forces due to its different destruction modes compared with the other fabric samples. Under impact at a kinetic energy of 20 J, obvious damage to multifilaments in the top outer layers of fabric samples S5, S3 and S6 in a single layer can be observed, but no obvious damage can be observed in S7 which is the thickest. The same phenomenon is obtained in double layers of the fabrics under impact with 50 J. Since fabric sample S7 cannot absorb additional impact energy because of damage to the fabric structure in these two cases, its peak transmitted force can be higher than that of a thinner fabric. The above analysis demonstrates that the fabric thickness should be carefully selected according to the destruction modes when a spacer fabric will be subjected to impact with higher levels of kinetic energies during use.

Table 8.3 Effect of the fabric thickness on peak transmitted force

Lamination	Sample	Peak transmitted force (kN)					
		5 J	10 J	20 J	30 J	40 J	50 J
Single layer	S5	12.27 ±0.075	21.11 ±0.043	33.12 ±0.039	36.86 ±0.081	40.30 ±0.100	41.45 ±0.050
	S3	11.35 ±0.048	20.53 ±0.065	31.27 ±0.037	37.08 ±0.037	39.6 ±0.032	41.14 ±0.051
	S6	10.18 ±0.061	19.42 ±0.036	30.89 ±0.046	36.88 ±0.037	39.58 ±0.020	40.84 ±0.040
	S7	9.74 ±0.069	19.10 ±0.026	32.06 ±0.033	36.54 ±0.040	39.30 ±0.000	40.50 ±0.000
Double layers	S5	5.68 ±0.020	14.60 ±0.126	27.78 ±0.037	35.83 ±0.047	39.00 ±0.032	40.38 ±0.020
	S3	4.36 ±0.040	11.74 ±0.060	24.66 ±0.075	34.82 ±0.057	38.42 ±0.049	39.30 ±0.045
	S6	3.34 ±0.068	10.08 ±0.139	22.78 ±0.146	32.95 ±0.086	37.88 ±0.058	39.00 ±0.045
	S7	2.86 ±0.075	8.72 ±0.066	21.46 ±0.144	31.45 ±0.192	37.94 ±0.051	39.74 ±0.051
Triple layers	S5	1.98 ±0.020	7.74 ±0.068	18.50 ±0.109	29.24 ±0.136	36.84 ±0.081	38.90 ±0.063
	S3	1.22 ±0.037	5.70 ±0.055	16.58 ±0.116	25.90 ±0.192	34.30 ±0.055	37.86 ±0.112
	S6	0.96 ±0.040	4.78 ±0.080	14.54 ±0.108	24.08 ±0.198	31.86 ±0.216	35.02 ±0.066
	S7	1.00 ±0.063	4.42 ±0.102	13.42 ±0.166	22.04 ±0.144	29.08 ±0.132	33.44 ±0.098

8.4.4 Effect of outer layer structure

A group of six fabrics (S1, S3, S8, S9, S10 and S11) with the same underlapped needles for the spacer yarns (two-needle space) and nearly the same thickness but with different outer layer structures is chosen to investigate the effect of outer layer structure on the impact force attenuation properties of warp-knitted spacer fabrics. The details of these fabrics can be found in Table 6.3.

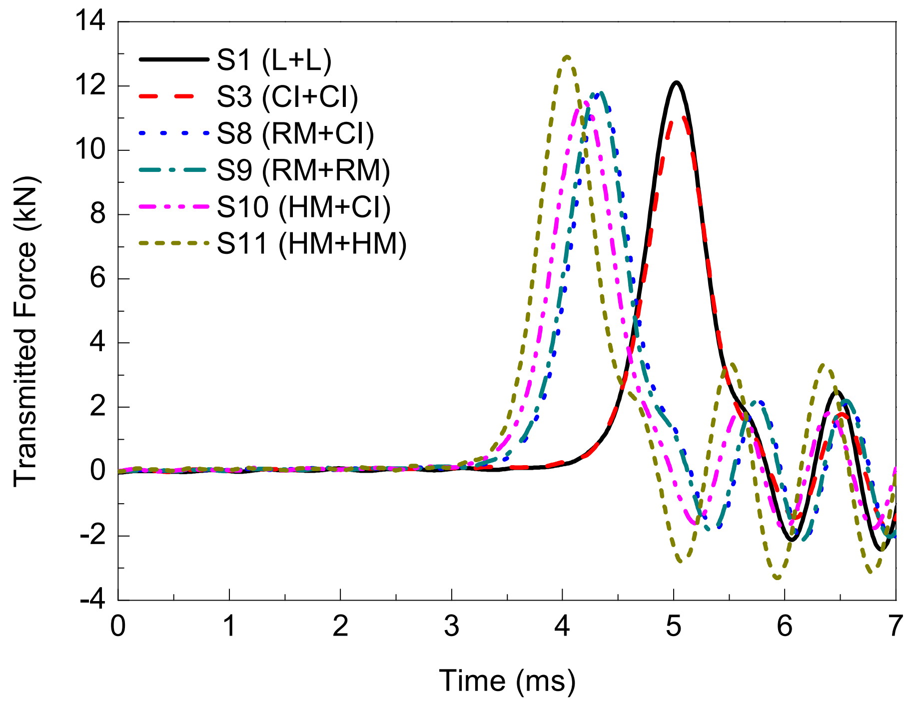

Figure 8.17 Effect of the outer layer structure on transmitted force-time curves (fabric layer: 1; impact energy: 5 J).

As shown in Figure 8.17, the transmitted force-time curves of these fabrics in a single layer under impact at a kinetic energy of 5 J are used as an example for analysing the effect of the outer layer structure on the impact force attenuation properties. It is found that the outer layer structures have an obvious effect. While fabric sample S11 knitted with large-size hexagonal meshes for both outer layers has the highest peak transmitted force and the shortest duration from the starting point to the peak transmitted force point, fabric sample S3 knitted with a chain plus inlay structure for both outer layers has the lowest peak transmitted force and the longest impact duration. The peak transmitted forces of the fabrics with the other outer layers structures (S1, S8, S9, and S10) are between the values for these two fabric samples.

Table 8.4 Effect of the outer layer structure on peak transmitted force

Lamination	Sample	Peak transmitted force (kN)					
		5 J	10 J	20 J	30 J	40 J	50 J
Single layer	S1	11.88 ±0.084	20.77 ±0.054	31.06 ±0.045	36.92 ±0.058	39.68 ±0.037	41.14 ±0.024
	S3	11.35 ±0.048	20.53 ±0.065	31.27 ±0.037	37.08 ±0.037	39.6 ±0.032	41.14 ±0.051
	S8	11.81 ±0.049	20.82 ±0.053	31.72 ±0.074	36.76 ±0.024	39.28 ±0.049	40.96 ±0.068
	S9	11.87 ±0.062	20.57 ±0.067	31.50 ±0.068	37.06 ±0.024	39.62 ±0.073	41.32 ±0.037
	S10	11.45 ±0.040	19.80 ±0.071	31.03 ±0.042	36.92 ±0.037	39.56 ±0.040	41.16 ±0.051
	S11	12.98 ±0.077	21.50 ±0.056	31.29 ±0.144	37.28 ±0.073	40.27 ±0.133	41.65 ±0.050
Double layers	S1	4.44 ±0.075	12.04 ±0.133	26.18 ±0.080	35.12 0.039±	38.52 ±0.037	39.48 ±0.020
	S3	4.36 ±0.040	11.74 ±0.060	24.66 ±0.075	34.82 ±0.057	38.42 ±0.049	39.30 ±0.045
	S8	4.54 ±0.040	12.72 ±0.124	26.34 ±0.060	35.53 ±0.058	38.74 ±0.024	39.74 ±0.051
	S9	5.38 ±0.080	12.84 ±0.068	26.68 ±0.097	35.63 ±0.030	38.72 ±0.037	39.64 ±0.051
	S10	5.08 ±0.097	13.46 ±0.223	25.34 ±0.198	35.17 ±0.184	38.88 ±0.037	39.98 ±0.049
	S11	6.22 ±0.020	15.44 ±0.098	28.18 ±0.171	36.10 ±0.122	39.30 ±0.000	40.92 ±0.049
Triple layers	S1	1.66 ±0.060	6.28 ±0.116	17.02 ±0.132	27.23 ±0.085	35.24 ±0.196	38.12 ±0.066
	S3	1.22 ±0.037	5.70 ±0.055	16.58 ±0.116	25.90 ±0.192	34.30 ±0.055	37.86 ±0.112
	S8	1.48 ±0.020	6.20 ±0.000	17.46 ±0.051	27.84 ±0.060	35.40 ±0.105	37.80 ±0.089
	S9	1.44 ±0.024	6.42 ±0.058	17.46 ±0.117	28.10 ±0.114	35.98 ±0.080	38.10 ±0.077
	S10	1.62 ±0.020	6.54 ±0.075	18.08 ±0.162	27.50 ±0.147	34.48 ±0.213	37.74 ±0.246
	S11	2.02 ±0.080	7.68 ±0.080	21.34 ±0.196	31.60 ±0.192	37.36 ±0.150	38.88 ±0.058

As listed in Table 8.4, similar results are also obtained for the other levels of impact energies and laminated layers. These differences mainly come from different geometric features of outer layer structures which lead to different geometric arrangements of multifilaments and different inclinations and binding conditions of spacer monofilaments. As indicated in Chapter 7, the fabric knitted with large-size meshes exhibits the poorest impact protective performance due to highly buckled and inclined spacer monofilaments, and the fabric knitted with small-size meshes demonstrates the best impact protection ability due to tight binding conditions. The fabrics knitted with a close structure have moderate impact protection performance due to the combined effects of loose binding structures and lowly buckled and inclined spacer monofilaments. Under impact in the hemispherical shape, apart from the above stated factors, the deformation of the outer layer structures to fit the shape of the anvil also plays a significant role in affecting the impact force attenuation properties of the fabrics.

There is no doubt that a close structure is more stable and stiffer than an open or mesh structure. For the close structures, the chain plus inlay structure is more stable out-of-plane than the locknit structure because the chain loops and the inlay yarns are crossed in a perpendicular manner, which are more difficult to extend and shear than the locknit stitches. When placed onto the hemispherical surface of the anvil, a fabric with a more stable outer layer structure can be less extended and sheared than a fabric with a less stable outer layer structure. Therefore, the number of spacer monofilaments which can resist the impact cannot be significantly reduced due to a lower deformation of the stable outer layer structure. On the other hand, the stable outer layers make the fabric stiffer, which is helpful to disperse the stress wave to a larger area and absorb more energy. As a result, the fabric knitted with the most stable outer layer structure (chain plus inlay) has the best force attenuation performance. The combined effects of low stable outer layer structure and highly buckled and inclined spacer monofilaments make the fabric knitted with large-size hexagonal meshes have the poorest impact force attenuation.

The above analysis shows that the effects of outer layer structure on the force attenuation properties under impact in the planar and hemispherical forms are different. The comfort and formability of fabrics stand in contradiction to the impact force attenuation properties. The fabric knitted with a stable and stiff outer layer structure has better force attenuation ability than the fabric with a flexible structure. However, the stiff outer layer structure makes the fabric uncomfortable and difficult to fit a curved shape. Therefore, the balance between the comfort and protective performance requires further investigations to select a suitable outer layer structure for a specific protective application.

8.4.5 Discussion

The influences of the structural parameters, including spacer monofilament inclination and fineness, fabric thickness, and outer layer structure as well as fabric lamination, on the impact force attenuation properties of the warp-knitted spacer fabrics have been analysed. The results have shown that these structural parameters have significant effects on the resultant peak transmitted force. Hence, a warp-knitted spacer fabric can be designable by maximizing its force attenuation capacity and meanwhile minimizing its density and thickness for wearing comfort. The results have also shown that the structural parameters do not determine the peak transmitted force independently. The peak transmitted force is also affected by the predefined impact kinetic energy. Therefore, no best spacer fabric exists for all impact kinetic energy levels. To optimize the structure of spacer fabrics, the specific application with an impact kinetic energy level should be identified first. Then suitable spacer fabrics can be tailored by varying their structural parameters quantitatively to achieve a specific peak transmitted force under a particular impact kinetic energy.

As reviewed in Chapter 2, human body could be subjected to different levels of energy impacts in different circumstances or sports, and various types of impact protectors have been available on the market for human body protection. To date, the use of the European Standard BS EN 1621-1:1998 to assess motorcycle protective clothing has been widely accepted. In order to evaluate the feasibility of replacing commonly used polymeric foams with the developed spacer fabrics, the protective performance of these fabrics are compared with the requirement of the standard. According to the standard, the peak transmitted force of the limb protectors for motorcyclists shall not exceed 35 kN, and no single value shall exceed 50 kN under impact at a kinetic energy of 50 J. Figure 8.18 shows the peak transmitted forces of all the developed spacer fabrics laminated with three layers. It can be found that only fabric samples S6 and S7 comply with the standard. These two spacer fabrics are knitted with the same outer layer structure (chain plus inlay), but with different thicknesses and different stitch densities. Although sample S6 has a lower thickness than sample S7, three layers of S6 still have a total thickness of 25.35 mm, which is too thick for use in protective clothing. Since a fabric knitted with coarser and more inclined spacer monofilaments has a better force attenuation capacity, the thickness can be decreased by increasing the diameter or inclination of the spacer monofilaments. However, increasing spacer monofilament diameter will make the fabric stiffer, resulting in a reduction in comfort. Further design and optimization of spacer fabrics by manipulating the structural parameters is required to achieve a good balance between the force attenuation capacity and comfort.

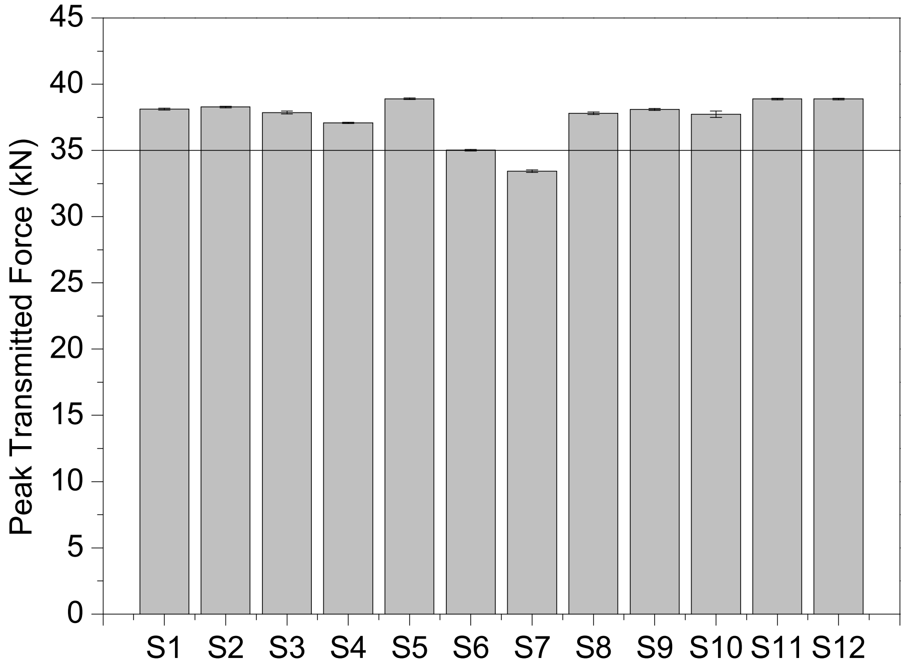

Figure 8.18 Peak transmitted forces for spacer fabrics laminated with three layers.

8.5 Conclusions

The warp-knitted spacer fabrics developed for human body protection against impact were tested in the hemispherical form at various levels of impact energy and laminated layers. The impact process, energy absorption and force attenuation properties were investigated in the light of the experimental results of the spacer fabric S1 with a typical structure. Then the effects of the structural parameters including spacer yarn inclination and fineness, fabric thickness, and outer layer structure as well as fabric lamination on the peak transmitted forces have been analysed to investigate the structure–property relationship. According to the experimental results and analyses, the following conclusions can be drawn.

- The boundary condition determines the impact response of the spacer fabric. The plateau stage of the spacer fabric under impact in the hemispherical form is not clearly observed due to the change of the contact area of the fabric during the impact process and different deformation stages of spacer yarns under similar displacement of the striker.
- The energy absorbed by the fabric depends on its energy absorption capacity and the applied impact kinetic energy level. When the impact energy is lower than the energy absorption capacity of the fabric, the impact energy can be totally absorbed by the elastic and elastoplastic deformations of the fabric. Otherwise, damage to the fabric cannot be avoided. The severity of the damage to the fabric increases as the impact energy increases. Under impact in the hemispherical form the energy absorption capacity of the fabric is decreased. High curvature of the spacer fabric reduces its energy absorption capability and therefore also its force attenuation properties.
- The peak contact force of a spacer fabric is determined by its energy absorption capacity and the applied impact kinetic energy. These determine the densified level of the spacer fabric under impact. High densification leads to high contact stiffness and, therefore, a high peak contact force. High densification also causes the stress wave to transmit easily and produce a high peak in the transmitted force. A certain level of destruction is helpful to dissipate energy, by decreasing the densification and hence reducing the peak transmitted force.

- The structural parameters of a spacer fabric significantly affect its protective performance. Among a group of spacer fabrics, the spacer fabric knitted with coarser spacer monofilaments, a higher fabric thickness, and a more stable outer layer structure will have a better force attenuation capacity, if its destruction modes under different levels of impact energies are not different from the others. The fabric of spacer yarns shogging three-needle space with an inclination angle of around 35º has better protective performance.
- The boundary condition in the hemispherical shape can change the effects of spacer monofilament inclination and outer layer fabric structure on the force attenuation properties of the spacer fabrics.
- Lamination of spacer fabrics can improve the force attenuation properties. Three layers of the spacer fabric knitted with a chain plus inlay structure for both outer layers in a total thickness of about 2.5 cm can comply with the European Standard BS EN 1621-1:1998.

CHAPTER 9 CONCLUSIONS AND FUTURE WORK

9.1 Conclusions

In order to gain wider acceptance and encourage the use of impact protectors to reduce the risk of sports injuries, warp-knitted spacer fabrics with good comfort properties have been proposed to be used as cushioning materials in developing impact protectors. This study set out to establish a clear picture for engineering the cushioning properties of warp-knitted spacer fabrics for human body protection, by revealing the compression deformation mechanism, establishing the quantitative structure–property relationships, analysing the effects of structural parameters on the cushioning properties, and examining the effects of impact compression and curved shape of fabrics on the protective properties.

The comprehensively theoretical and experimental investigations on the compression properties of warp-knitted spacer fabrics under different loadings, boundary conditions and spatial shapes laid a solid foundation for the further development of the fabrics for human body protection. The major findings for the specific objectives are summarised as follows.

9.1.1 Compression deformation mechanism

The results from the experimental investigations, analytical and finite element modelling have clearly revealed the compression mechanism of a typical warp-knitted spacer fabric with the key feature of behaving as cushioning materials, providing three distinct stages under compression, described as linear elasticity, plateau and densification, with an additional short initial stage.

- In the initial stage, the pillar spacer monofilaments contact the bottom outer layer and contribute more to the total reaction load, while the tricot spacer monofilaments undertake free postbuckling and contribute less to the total reaction load.
- In the linearly elastic stage, the tricot spacer monofilaments start to contact the top and bottom outer layers. The postbuckling of the pillar and tricot spacer monofilaments with additional constraints provided by the contacts leads to a rapid rise of the total reaction load.
- In the plateau stage, all the spacer monofilament end sections are in contact with the outer layers. While the tricot spacer monofilaments undertake larger torsion, the contacts among the spacer monofilaments lead to shear and rotation of the pillar spacer monofilament middle sections. As a result, a nearly constant reaction load is obtained in this stage.
- In the densification stage, the pillar spacer monofilament middle sections contact the two outer layers. The length between the two contacting points for each pillar spacer monofilament decreases as the displacement increases. As a consequence, the total reaction load rises dramatically.

The developed FE models are able to simulate the detailed deformation process of the spacer fabric in compression and therefore are helpful in revealing the compression mechanism, while the analytical model can provide insights into the underlying compression mechanism.

9.1.2 Influencing structural parameters

The analysis with the analytical model has indicated that the structural parameters that affect the compression properties of warp-knitted spacer fabrics include spacer yarn inclination and diameter, course density and fabric thickness. In addition, FE modelling has demonstrated that, the profile of the internal surface of the outer fabric layers, the geometric imperfections and entanglements of spacer monofilaments also affect the compression behaviour.

9.1.3 Quantitative structure–property relationship

The analytical and FE models made attempts to establish the quantitative structure–property relationships of warp-knitted spacer fabrics in static compression.

The analytical model has established a direct relationship between the reaction force and the fabric structural parameters based on the manufacturing parameters, without considering spacer monofilament diameter, outer fabric layer thickness, contacts among spacer monofilaments and yarn material's nonlinearity. The analytical model is able to give a clear view on how the structural parameters affect the compression resistance in physical sense, although the prediction is not accurate due to the assumptions. The developed FE models have successfully bridged the fabric structural parameters with the compression load–displacement relationships with satisfactory agreement, providing an effective approach to predict the compression behaviour of a spacer fabric with a specified structure quantitatively. With the FE models, the required properties of warp-knitted spacer fabrics can be achieved by numerical simulations rather than empirical trails. They are effective to reduce cost and carry out exact design of warp-knitted spacer fabrics to meet specific requirements.

9.1.4 Effects of structural parameters on static compression and cushioning properties

The results from the static experimental investigations have shown that spacer fabrics with larger spacer yarn inclination angles, higher fabric thicknesses, finer spacer yarns and larger size mesh of the outer layers, having lower compression resistance, can be used to absorb lower energy with higher efficiency. On the contrary, the fabrics with smaller spacer yarn inclination angles, lower fabric thicknesses, coarser spacer yarns and smaller size mesh of the outer layers, having higher compression resistance, can be used to absorb higher energy with higher efficiency.

9.1.5 Effects of structural parameters on impact compression properties

Warp-knitted spacer fabrics are strain rate dependent that leads to higher impact contact forces and energy absorption capacity of them under impact than those under static compression. The effects of structural parameters on impact compression properties of warp-knitted spacer fabrics are different from those on static compression properties. These effects can be summarised as follows.

- An optimized spacer yarn inclination and fabric thickness exist for getting better protective performance with lower peak contact force and peak transmitted force.
- The peak contact force and peak transmitted force increase as the spacer yarn diameter decreases.

- The spacer fabrics knitted with large-size mesh structures for outer layers have higher peak contact force and higher peak transmitted force than the spacer fabrics knitted with small-size mesh and close structures.

A linear relationship exists between the peak contact force and peak transmitted force. The transmitting rate is about 66.84% and is nearly the same for all the warp-knitted spacer fabrics studied regardless of their structural parameters.

9.1.6 Protective properties for human body protection

The energy absorption capacity of a warp-knitted spacer fabric in hemispherical form is decreased compared with that in planar form. The energy absorbed by a spacer fabric depends on its energy absorption capacity and the applied impact kinetic energy. When the impact energy is lower than or equal to the energy absorption capacity of the fabric, the impact energy can be totally absorbed by the elastic and elastoplastic deformations of the fabric. Otherwise, damage to the fabric will occur. The severity of damage to the fabric increases as the impact energy increases. High curvature of a spacer fabric will reduce the energy absorption and therefore reduce the force attenuation properties. A spacer fabric with a coarser spacer monofilament, higher thickness and stable outer layer structure has a higher force attenuation capacity, if it has the same destruction modes as the counterparts. Increasing the inclination of spacer monofilaments to around 35° is helpful to enhance their shear resistance and therefore increases the force attenuation of the spacer fabric under impact in hemispherical shape. Lamination of spacer fabrics can improve the force attenuation effectively. Three layers of the spacer fabric knitted with chain plus inlay structure for both outer layers with a thickness about 2.5 cm in total can comply with the European Standard BS EN 1621-1:1998.

9.2 Contributions

A deeper understanding of the deformation mechanism and quantitative structure–property relationships of warp-knitted spacer fabrics in compression has been achieved with this study. This study also presents one of the most comprehensive investigations to date on the structure–property relationships of warp-knitted spacer fabrics under different loadings and boundary conditions as well as in different spatial shapes. A principle for engineering the cushioning properties of warp-knitted spacer fabrics for human body protection has been established. By using the knowledge gained from this study, it is now possible to conduct virtual prototyping of warp-knitted spacer fabrics to ensure that their cushioning properties meet the desired requirements of human body protection. This dramatically reduced the time and costs in both design and manufacturing as physical prototyping and testing. Hence, the present research has made a contribution to the use of warp-knitted spacer fabrics as cushioning materials in developing impact protectors for human body protection. Another long term significance of this study is to provide a solid theoretical and experimental foundation and a deeper understanding on the improvement of the quality of warp-knitted spacer fabrics to explore their further applications in multifunctional clothing and other technical fields.

9.3 Limitations

There were limitations to this study due to the constraints in time and resources, including:

- The analytical model was failed to accurately predict the compression load–displacement relationship of the spacer fabric due to the assumptions made in the model.
- Only one of the developed warp-knitted spacer fabrics was scanned by using μCT technique. The parametric FE study was conducted by adjusting the geometric model of the scanned fabric. This does not lend the simulated results to directly compare with the experimental results with different structural parameters.
- The present study has focused on the identification of the deformation mechanism and the establishment of quantitative structure–property relationships as well as the investigation of the effects of structural parameters on the cushioning properties of warp-knitted spacer fabrics in different loading and boundary conditions. However, fabric parameters were not optimized for a specific application.

9.4 Recommendations for future work

Based on the work described in this thesis, the research on cushioning properties of warp-knitted spacer fabrics can be further enhanced and extended by the following:

- The analytical model needs to be revised, to improve the accuracy of force–displacement relationship prediction, by taking into account precise spacer yarn shapes, spacer yarn diameter, outer fabric layer profile and yarn material's nonlinearity.
- The developed FE models can be extended to other types of spacer fabrics. Further study can be conducted by adjusting the material's property, outer layer structure, spacer yarn configurations, to enhance the understanding of

the structure–property relationships of spacer fabrics in compression. Explicit FE models are recommended to be created to simulate the impact compression properties of spacer fabrics, by taking account of the effect of rate-dependant material properties of yarns. Furthermore, building FE models for simulating the impact properties of warp-knitted spacer fabrics in hemispherical shape is also recommended. By doing that, the protective properties of spacer fabrics for human body protection can be assessed numerically.

- Geometric models are prerequisite for conducting the numerical design of spacer fabrics for specific applications with the FE models. The analytical model can be used to calculate the initial shape of spacer yarns based on manufacturing parameters. This explores a way to perform a virtual design of spacer fabrics. Future work should be carried out in this way to optimize the fabric structure for a specific impact protector.
- There is a need to systematically study the out-of-plane behaviour of warp-knitted spacer fabrics and how the out-of-plane behaviour affects their impact protective performance in hemispherical shape. Quantitative investigations into the effects of the curvatures of spacer fabrics on their protective properties are required in order to engineer warp-knitted spacer fabrics to protect different parts of the human body.

REFERENCES

[1] J. Conn, J. Annest and J. Gilchrist, "Sports and recreation related injury episodes in the US population, 1997–99," *Inj. Prev.*, vol. 9, pp. 117–123, 2003.

[2] S. Schneider, et al., "Sports injuries: population based representative data on incidence, diagnosis, sequelae, and high risk groups," *Br. J. Sports Med.*, vol. 40, pp. 334–339, 2006.

[3] M. Avalle, G. Belingardi and R. Montanini, "Characterization of polymeric structural foams under compressive impact loading by means of energy-absorption diagram," *Int. J. Impact Eng.*, vol. 25, pp. 455–472, 2001.

[4] P. I. Bellfy, "Attachment of protective pads for protection of joint surfaces," U.S. Patent 7 487 557, Feb. 10, 2009.

[5] E. Maklewska, I. Krucinka and G. E. Mayers, "Estimating the shock-absorbing ability of protector materials by use of pressure films," *Fibres Text. East. Eur.*, vol. 13, pp. 52–55, 2005.

[6] E. Maklewska, et al., "New measuring stand for estimating a material's ability to damp the energy of impact strokes," *Fibres Text. East. Eur.*, vol. 12, pp. 48–52, 2004.

[7] S. L. Wiener, et al., "Force reduction by an external hip protector on the human hip after falls," *Clin. Orthop.*, vol. 398, pp. 157–168, 2002.

[8] A. C. Laing and S. N. Robinovitch, "The force attenuation provided by hip protectors depends on impact velocity, pelvic size, and soft tissue stiffness," *J. Biomech. Eng.*, vol. 130, pp. 061005, 2008.

[9] N. J. Mills, et al., "Polymer foams for personal protection: cushions, shoes and helmets," *Composites Sci. Technol.*, vol. 63, pp. 2389–2400, 2003.

[10] S. Dlugosch, H. Hu and C. Chan, "Impact protective clothing in sport: areas of application and level of utilization," *Research Journal of Textile and Apparel*, vol. 16, pp. 18–28, 2012.

[11] E. L. Goodwin, "Protective device using a spacer fabric," U.S. Patent 8 070 705, Dec. 6, 2011.

[12] X. H. Miao and M. Q. Ge, "The Compression behavior of warp knitted spacer fabric," *Fibres Text. East. Eur.*, vol. 16, pp. 90–92, 2008.

[13] Y. Liu and H. Hu, "Compression property and air permeability of weft-knitted spacer fabrics," *J. Text. I.*, vol. 102, pp. 366–372, 2011.

[14] A. Mouritz, et al., "Review of applications for advanced three-dimensional fibre textile composites," *Compos. Part A*, vol. 30, pp. 1445–1461, 1999.

[15] R. Kamiya, et al., "Some recent advances in the fabrication and design of three-dimensional textile preforms: a review," *Composites Sci. Technol.*, vol. 60, pp. 33–47, 2000.

[16] X. Chen, L. W. Taylor and L. J. Tsai, "An overview on fabrication of three-dimensional woven textile preforms for composites," *Text. Res. J.*, vol. 81, pp. 932–944, 2011.

[17] X. Ye, et al., "Application of warp-knitted spacer fabrics in car seats," *J. Text. I.*, vol. 98, pp. 337–344, 2007.

[18] D. M. Armakan and A. Roye, "A study on the compression behavior of spacer fabrics designed for concrete applications," *Fiber Polym.*, vol. 10, pp. 116–123, 2009.

[19] D. Mecit and A. Roye, "Investigation of a testing method for compression behavior of spacer fabrics designed for concrete applications," *Text. Res. J.*, vol. 79, pp. 867–875, 2009.

[20] J. Miltz and G. Gruenbaum, "Evaluation of cushioning properties of plastic foams from compressive measurements," *Polym. Eng. Sci.*, vol. 21, pp. 1010–1014, 1981.

[21] G. Gruenbaum and J. Miltz, "Static versus dynamic evaluation of cushioning properties of plastic foams," *J. Appl. Polym. Sci.*, vol. 28, pp. 135–143, 1983.

[22] O. Ramon, S. Mizrahi and J. Miltz, "Merits and limitations of the drop and shock tests in evaluating the dynamic properties of plastic foams," *Polym. Eng. Sci.*, vol. 34, pp. 1406–1410, 1994.

[23] G. Lyn and N. J. Mills, "Design of foam crash mats for head impact protection," *Sports Eng.*, vol. 4, pp. 153–163, 2001.

[24] C. M. Harris and A. G. Piersol, *Harris' Shock and Vibration Handbook*. New York: McGraw-Hill, 2002.

[25] R. Subramanian, "Motor vehicle traffic crashes as a leading cause of death in the United States, 2001," *Young*, vol. 1, pp. 3, 2003.

[26] E. R. Braver, "Race, Hispanic origin, and socioeconomic status in relation to

motor vehicle occupant death rates and risk factors among adults," *Accid. Anal. Prev.*, vol. 35, pp. 295–309, 2003.

[27] A. S. McIntosh, "Impact injury in sport," in *IUTAM Symposium on Impact Biomechanics: From Fundamental Insights to Applications*, 2005, pp. 231–245.

[28] A. McIntosh and P. McCrory, "Preventing head and neck injury," *Br. J. Sports Med.*, vol. 39, pp. 314–318, 2005.

[29] D. C. Viano, et al., "Prevention of commotio cordis in baseball: an evaluation of chest protectors," *J. Trauma Acute Care Surg.*, vol. 49, pp. 1023–1028, 2000.

[30] R. Rønning, et al., "The efficacy of wrist protectors in preventing snowboarding injuries," *Am. J. Sports Med.*, vol. 29, pp. 581–585, 2001.

[31] M. J. Parker, W. J. Gillespie and L. D. Gillespie, "Effectiveness of hip protectors for preventing hip fractures in elderly people: systematic review," *BMJ*, vol. 332, pp. 571–574, 2006.

[32] M. Lemair and D. Pearsall, "Evaluation of impact attenuation of facial protectors in ice hockey helmets," *Sports Eng.*, vol. 10, pp. 65–74, 2007.

[33] D. T. Bernhardt, "Protective Sports Equipment," in *The Young Athlete*, H. Hebestreit and O. Bar-Or, Eds. New York: Wiley, 2008, pp. 164–168.

[34] F. B. D. Vecchio, et al., "Energy absorbed by electronic body protectors from kicks in a taekwondo competition," *Biol. Sport*, vol. 28, pp. 75–78, 2011.

[35] J. Parkkari, U. M. Kujala and P. Kannus, "Is it possible to prevent sports injuries? Review of controlled clinical trials and recommendations for future work," *Sports Med.*, vol. 31, pp. 985–995, 2001.

[36] D. Q. Sun, "Computer aided design system of cushioning materials," in *Computer-Aided Industrial Design and Conceptual Design (CAIDC), 2006 7th International Conference*, 2006, pp. 1–7.

[37] J. Parkkari, et al., "Force attenuation properties of various trochanteric padding materials under typical falling conditions of the elderly," *J. Bone Miner. Res.*, vol. 9, pp. 1391–1396, 1994.

[38] J. Miltz and O. Ramon, "Energy absorption characteristics of polymeric foams used as cushioning materials," *Polym. Eng. Sci.*, vol. 30, pp. 129–133, 1990.

[39] D. M. Wang, Z. W. Wang and Q. H. Liao, "Energy absorption diagrams of paper honeycomb sandwich structures," *Packag. Technol. Sci.*, vol. 22, pp. 63–67, 2009.

[40] M. A. Sek, et al., "A new method for the determination of cushion curves," *Packag. Technol. Sci.*, vol. 13, pp. 249–255, 2000.

[41] G. Burgess, "Generation of cushion curves from one shock pulse," *Packag. Technol. Sci.*, vol. 7, pp. 169–173, 1994.

[42] R. R. Janssen, "A method for the paper selection of a package cushion material and its dimensions," North American Aviation, Rep. NA-51-1004, 1952.

[43] J. Zhang and M. F. Ashby, "Mechanical selection of foams and honeycombs used for packaging and energy absorption," *J. Mater. Sci.*, vol. 29, pp. 157–163, 1994.

[44] K. C. Rusch, "Load-compression behavior of brittle foams," *J. Appl. Polym. Sci.*, vol. 14, pp. 1263–1276, 1970.

[45] C. C. Lin, et al., "Elucidating the design and impact properties of composite nonwoven fabrics with various filaments in bulletproof vest cushion layer," *Text. Res. J.*, vol. 79, pp. 268–274, 2009.

[46] K. Fukaya and M. Uchida, "Protection against impact with the ground using wearable airbags," *Ind. Health*, vol. 46, pp. 59–65, 2008.

[47] D. M. Wang, "Cushioning properties of multi-layer corrugated sandwich structures," *J. Sandw. Struct. Mater.*, vol. 11, pp. 57–66, 2009.

[48] D. M. Wang, "Energy absorption diagrams of multi-layer corrugated boards," *J. Wuhan Univ. Technol. Mater. Sci. Ed.*, vol. 25, pp. 58–61, 2010.

[49] D. M. Wang, "Impact behavior and energy absorption of paper honeycomb sandwich panels," *Int. J. Impact Eng.*, vol. 36, pp. 110–114, 2009.

[50] D. M. Wang and Z. W. Wang, "Experimental investigation into the cushioning properties of honeycomb paperboard," *Packag. Technol. Sci.*, vol. 21, pp. 309–316, 2008.

[51] A. Maji, et al., "Mechanical properties of polyurethane-foam impact limiters," *J. Eng. Mech.*, vol. 121, pp. 528–540, 1995.

[52] M. Bianchi, F. L. Scarpa and C. W. Smith, "Stiffness and energy dissipation in polyurethane auxetic foams," *J. Mater. Sci.*, vol. 43, pp. 5851–5860, 2008.

[53] J. Zhang, et al., "Constitutive modeling of polymeric foam material subjected to dynamic crash loading," *Int. J. Impact Eng.*, vol. 21, pp. 369–386, 1998.

[54] S. W. Lye, S. G. Lee and S. B. Tor, "A parametric study of the shock characteristics of expandable polystyrene foam protective packaging," *Polym. Eng. Sci.*, vol. 38, pp. 558–565, 1998.

[55] L. Di Landro, G. Sala and D. Olivieri, "Deformation mechanisms and energy absorption of polystyrene foams for protective helmets," *Polym. Test.*, vol. 21, pp. 217–228, 2002.

[56] J. Miltz, O. Ramon and S. Mizrahi, "Mechanical behavior of closed cell plastic foams used as cushioning materials," *J. Appl. Polym. Sci.*, vol. 38, pp. 281–290, 1989.

[57] P. Kannus, J. Parkkari and J. Poutala, "Comparison of force attenuation properties of four different hip protectors under simulated falling conditions in the elderly: an in vitro biomechanical study." *Bone*, vol. 25, pp. 229–235, 1999.

[58] R. Bouix, P. Viot and J. L. Lataillade, "Polypropylene foam behaviour under dynamic loadings: Strain rate, density and microstructure effects," *Int. J. Impact Eng.*, vol. 36, pp. 329–342, 2009.

[59] P. Viot, "Hydrostatic compression on polypropylene foam," *Int. J. Impact Eng.*, vol. 36, pp. 975–989, 2009.

[60] Y. S. Lee, N. H. Park and H. S. Yoon, "Dynamic mechanical characteristics of expanded polypropylene foams," *J. Cell. Plast.*, vol. 46, pp. 43–55, 2010.

[61] C. Gontier, A. Bouchou and C. Vinot, "A mechanical model for the computation of phenolic foams in compression," *Int. J. Mech. Sci.*, vol. 43, pp. 2371–2384, 2001.

[62] N. S. Ramesh and N. Malwitz, "Bubble growth dynamics in olefinic foams," in *ACS SYMPOSIUM SERIES*, 1997, pp. 206–213.

[63] L. J. Gibson and M. F. Ashby, *Solids, Structure and Properties: Structure and Properties*. New York: Cambridge University Press, 1997.

[64] H. Zhu, N. Mills and J. Knott, "Analysis of the high strain compression of open-cell foams," *J. Mech. Phys. Solids*, vol. 45, pp. 1875–1904, 1997.

[65] F. Scarpa, L. Ciffo and J. Yates, "Dynamic properties of high structural integrity auxetic open cell foam," *Smart Mater. Struct.*, vol. 13, pp. 49–56,

2003.

[66] J. Elliott, et al., "In-situ deformation of an open-cell flexible polyurethane foam characterised by 3D computed microtomography," *J. Mater. Sci.*, vol. 37, pp. 1547–1555, 2002.

[67] N. Mills and H. Zhu, "The high strain compression of closed-cell polymer foams," *J. Mech. Phys. Solids*, vol. 47, pp. 669–695, 1999.

[68] N. Daphalapurkar, et al., "Tomography and simulation of microstructure evolution of a closed-cell polymer foam in compression," *Mech. Adv. Mater. Struct.*, vol. 15, pp. 594–611, 2008.

[69] G. Lu and T. Yu, *Energy Absorption of Structures and Materials*. Cambridge: Woodhead Publishing Limited, 2003.

[70] L. J. Gibson, "Biomechanics of cellular solids," *J. Biomech.*, vol. 38, pp. 377–399, 2005.

[71] N. Mao and S. J. Russell, "The thermal insulation properties of spacer fabrics with a mechanically integrated wool fiber surface," *Text. Res. J.*, vol. 77, pp. 914–922, 2007.

[72] S. M. Bruer, N. Powell and G. Smith, "Three-dimensionally knit spacer fabrics: a review of production techniques and applications," *Journal of Textile and Apparel, Technology and Management*, vol. 4, pp. 1–29, 2005.

[73] M. Abounaim, et al., "Development of flat knitted spacer fabrics for composites using hybrid yarns and investigation of two-dimensional mechanical properties," *Text. Res. J.*, vol. 79, pp. 596–610, 2009.

[74] M. Abounaim, et al., "Thermoplastic composite from innovative flat knitted 3D multi-layer spacer fabric using hybrid yarn and the study of 2D mechanical properties," *Composites Sci. Technol.*, vol. 70, pp. 363–370, 2010.

[75] M. Abounaim, et al., "Thermoplastic composites from curvilinear 3D multi-layer spacer fabrics," *J. Reinf. Plast. Compos.*, vol. 29, pp. 3554–3565, 2010.

[76] M. Abounaim, O. Diestel and C. Cherif, "High performance thermoplastic composite from flat knitted multi-layer textile preform using hybrid yarn," *Composites Sci. Technol.*, vol. 71, pp. 511–519, 2011.

[77] M. Bannister, R. Braemar and P. Crothers, "The mechanical performance of 3D woven sandwich composites," *Compos. Struct.*, vol. 47, pp. 687–690, 1999.

[78] A. Van Vuure, J. Ivens and I. Verpoest, "Mechanical properties of composite panels based on woven sandwich-fabric preforms," *Compos. Part A*, vol. 31, pp. 671–680, 2000.

[79] A. Van Vuure, et al., "Modelling the core properties of composite panels based on woven sandwich-fabric preforms," *Composites Sci. Technol.*, vol. 60, pp. 1263–1276, 2000.

[80] A. Van Vuure, I. Verpoest and F. Ko, "Sandwich-fabric panels as spacers in a constrained layer structural damping application," *Compos. Part B*, vol. 32, pp. 11–19, 2001.

[81] M. Li, et al., "Effect of structure on the mechanical behaviors of three-dimensional spacer fabric composites," *Appl. Compos. Mater.*, vol. 16, pp. 1–14, 2009.

[82] H. Fan, et al., "An experiment study on the failure mechanisms of woven textile sandwich panels under quasi-static loading," *Compos. Part B*, vol. 41, pp. 686–692, 2010.

[83] H. Fan, W. Yang and Q. Zhou, "Experimental research of compressive responses of multi-layered woven textile sandwich panels under quasi-static loading," *Compos. Part B*, vol. 42, pp. 1151–1156, 2011.

[84] H. Fan, et al., "Ductile deformation mechanisms and designing instructions for integrated woven textile sandwich composites," *Composites Sci. Technol.*, vol. 72, pp. 1338–1343, 2012.

[85] S. S. Badawi. "Development of the weaving machine and 3D woven spacer fabric structures for lightweight composites materials," Ph.D dissertation, Technischen Universität Dresden, Dresden, Germany, 2008.

[86] A. W. Van Vuure, "Composite panels based on woven sandwich-fabric preforms," Ph.D dissertation, Katholieke Universiteit Leuven, Leuven, Belgium, 1997.

[87] S. Vasile, L. Van Langenhove and S. De Meulemeester, "Effect of production process parameters on different properties of a nonwoven spacer produced on a 3D web linker®," *Fibres Text. East. Eur.*, vol. 14, pp. 68–74, 2006.

[88] B. Schimanz, "Modellierung und experimenteller Nachweis von Zusammenhängen zwischen Parametern des Vernadelns, der Faseroberfläche und des Porenvolumens von dreidimensionalen Vliesstoffen," 2005.

[89] G. Le Roy, C. Binetruy and P. Krawczak, "Continuous manufacturing and performance of 3D reinforced sandwich structures," in *Sandwich Structures 7: Advancing with Sandwich Structures and Materials*, O.T. Thomsen, E.Bozhevolnaya, A. Lyckegaard, Eds. Berlin: Springer-Verlag, 2005, pp. 693–702.

[90] N. Njeugna, et al., "Development of a new 3D nonwoven for automotive trim applications," in *New Trends and Developments in Automotive Industry*, M. Chiaberge, Ed. InTech, 2011, pp. 323–346.

[91] G. Le Roy, "Method and device for producing composite laps and composites thereby obtained," U.S. Patent 5 475 904, December 19, 1995.

[92] K. Kunde, "Spacer fabrics-their application and future opportunities," *Melliand International*, vol. 10, pp. 283–286, 2004.

[93] W. Fung and M. Hardcastle, *Textiles in Automotive Engineering*. Cambridge: Woodhead Publishing Limited, 2001.

[94] X. Ye, H. Hu and X. Feng, "Development of the warp knitted spacer fabrics for cushion applications," *J. Ind. Text.*, vol. 37, pp. 213–223, 2008.

[95] A. Roye and T. Gries, "3-D textiles for advanced cement based matrix reinforcement," *J. Ind. Text.*, vol. 37, pp. 163–173, 2007.

[96] J. Meyer, et al., "Design and modeling of a textile pressure sensor for sitting posture classification," *IEEE Sensors J.*, vol. 10, pp. 1391–1398, 2010.

[97] J. Meyer, P. Lukowicz and G. Troster, "Textile pressure sensor for muscle activity and motion detection," in *2006 10th IEEE International Symposium on Wearable Computers*, 2006, pp. 69–72.

[98] J. Meyer, "Textile pressure sensor: design, error modeling and evaluation," Ph.D dissertation, ETH, Zurich, Switzerland, 2008.

[99] S. Pereira, et al., "A study of the structure and properties of novel fabrics for knee braces," *J. Ind. Text.*, vol. 36, pp. 279–300, 2007.

[100] G. Lee, S. Rajendran and S. Anand, "New single-layer compression bandage system for chronic venous leg ulcers," *Br. J. Nurs.*, vol. 18, pp. S4–S18, 2009.

[101] U. Wollina, M. Heide and M. Swerev, "Spacer fabrics–a potential tool in the prevention of chronic wounds," *Exogenous Dermatology*, vol. 1, pp. 276–278, 2000.

[102] U. Wollina, et al., "Spacer fabrics and related textile solutions," *Aktuelle*

Dermatologie, vol. 30, pp. 8–10, 2004.

[103] U. Wollina, et al., "Functional textiles in prevention of chronic wounds, wound healing and tissue engineering," *Textiles and the Skin*, vol. 31, pp. 82–97, 2003.

[104] J. Yip and S. P. Ng, "Study of three-dimensional spacer fabrics: Physical and mechanical properties," *J. Mater. Process. Technol.*, vol. 206, pp. 359–364, 2008.

[105] J. Yip and S. P. Ng, "Study of three-dimensional spacer fabrics: Molding properties for intimate apparel application," *J. Mater. Process. Technol.*, vol. 209, pp. 58–62, 2009.

[106] V. T. Bartels, "Thermal comfort of aeroplane seats: influence of different seat materials and the use of laboratory test methods," *Appl. Ergon.*, vol. 34, pp. 393–399, 2003.

[107] S. Borhani, et al., "Computational and experimental investigation of moisture transport of spacer fabrics," *J. Eng. Fiber Fabr.*, vol. 5, pp. 42–48, 2010.

[108] T. Dias, R. Monaragala and E. Lay, "Analysis of thick spacer fabrics to reduce automobile interior noise," *Meas. Sci. Technol.*, vol. 18, pp. 1979–1991, 2007.

[109] T. Dias, et al., "Analysis of sound absorption of tuck spacer fabrics to reduce automotive noise," *Meas. Sci. Technol.*, vol. 18, pp. 2657–2666, 2007.

[110] Y. Liu and H. Hu, "Sound absorption behavior of knitted spacer fabrics," *Text. Res. J.*, vol. 80, pp. 1949–1957, 2010.

[111] W. Doyen, et al., "Spacer fabric supported flat-sheet membranes: A new era of flat-sheet membrane technology," *Desalination*, vol. 250, pp. 1078–1082, 2010.

[112] C. Hertleer, et al., "Design of textile antennas for smart clothing," in *The 7th UGent PhD symposium*, Ghent, Belgium, 2006.

[113] C. Hertleer, et al., "Aperture-coupled patch antenna for integration into wearable textile systems," *IEEE Antennas Wireless Propag. Lett.*, vol. 6, pp. 392–395, 2007.

[114] M. Klemm, I. Locher and G. Troster, "A novel circularly polarized textile antenna for wearable applications," in *Wireless Technology, 2004. 7th European Conference*, 2004, pp. 285–288.

[115] I. Locher, et al., "Design and characterization of purely textile patch antennas," *IEEE Adv. Packag.*, vol. 29, pp. 777–788, 2006.

[116] T. Stegmaier, M. Linke and H. Planck, "Bionics in textiles: flexible and translucent thermal insulations for solar thermal applications," *Philos. T. Roy. Soc. A.*, vol. 367, pp. 1749–1758, 2009.

[117] W. Renkens and Y. Kyosev, "Geometry modelling of warp knitted fabrics with 3D form," *Text. Res. J.*, vol. 81, pp. 437–443, 2011.

[118] B. Supeł and Z. Mikołajczyk, "Model of the connector for 3D distance knitted fabric fastened by articulated joints," *Fibres Text. East. Eur.*, vol. 16, pp. 77–82, 2008.

[119] M. Konopasek, "Improved procedures for calculating the mechanical properties of textile structures," Ph.D dissertation, University of Manchester Institute of Science and Technology, Manchester, UK, 1970.

[120] B. Supeł and Z. Mikołajczyk, "Model of the compressing process of a one- and two-side fastened connector of a 3D distance knitted fabric," *Fibres Text. East. Eur.*, vol. 16, pp. 44–48, 2008.

[121] B. Supeł and Z. Mikołajczyk, "Modelling the process of the compression of distance knitted fabrics in the aspect of 'elastica curves'," *Fibres Text. East. Eur.*, vol. 18, pp. 52–55, 2010.

[122] F. Mokhtari, et al., "Compressibility behaviour of warp knitted spacer fabrics based on elastic curved bar theory," *J. Eng. Fiber Fabr.*, vol. 6, pp. 23–33, 2011.

[123] M. Sheikhzadeh, et al., "A modeling study on the lateral compressive behavior of spacer fabrics," *J. Text. I.*, vol. 101, pp. 795–800, 2010.

[124] C. M. Van Wyk, "Note on the compressibility of wool," *J. Text. I.*, vol. 37, pp. 285–292, 1946.

[125] N. Psilla, C. Provatidis and D. Mecit, "Numerical modelling of the compressional behaviour of warp-knitted spacer fabrics," *Fibres Text. East. Eur.*, vol. 17, pp. 56–61, 2009.

[126] C. Wang, "Post-buckling of a clamped-simply supported elastica," *Int. J. Non-Linear Mech.*, vol. 32, pp. 1115–1122, 1997.

[127] R. H. Plaut, et al., "Deflections and buckling of a bent elastica in contact with a flat surface," *Int. J. Solids Structures*, vol. 36, pp. 1209–1229, 1999.

[128] M. Vaz and D. Silva, "Post-buckling analysis of slender elastic rods subjected to terminal forces," *Int. J. Non-Linear Mech.*, vol. 38, pp. 483–492, 2003.

[129] R. H. Plaut, R. P. Taylor and D. A. Dillard, "Postbuckling and vibration of a flexible strip clamped at its ends to a hinged substrate," *Int. J. Solids Structures*, vol. 41, pp. 859–870, 2004.

[130] S. P. Timoshenko and J. M. Gere, *Theory of Elastic Stability*. New York: McGraw-Hill, 1961.

[131] T. E. Shoup, "An analytical investigation of the large deflections of flexible beam springs," Ph.D dissertation, The Ohio State University, Columbus, Ohio, USA, 1969.

[132] P. F. Byrd and M. D. Friedman, *Handbook of elliptic integrals for engineers and physicists*. Berlin: Springer-Verlag, 1954.

[133] U. Sonmez, "Compliant mechanism design and synthesis using buckling and snap-through buckling of flexible members," Ph.D dissertation, The Pennsylvania State University, Pennsylvania, USA, 2000.

[134] Y. S. Koo, "Bending behavior of coated yarns," *Fiber Polym.,* vol. 2, pp. 148–152, 2001.

[135] P. Mott and C. Roland, "Limits to Poisson's ratio in isotropic materials," *Phys. Rev. B*, vol. 80, pp. 132104, 2009.

[136] S. Zhang and J. Li, "Anisotropic elastic moduli and Poisson's ratios of a poly (ethylene terephthalate) film," *J. Polym. Sci., Part B: Polym. Phys.*, vol. 42, pp. 260–266, 2004.

[137] M. Rock and K. Lohmueller, "Three-dimensional knit spacer fabric for footwear and backpacks," U.S. Patent 5 896 758, April 27, 1999.

[138] B. B. Sorensen, "A device for protection of the hips," EP 1 684 604, May 2, 2007.

[139] X. Chen, Y. Sun and X. Gong, "Design, manufacture, and experimental analysis of 3D honeycomb textile composites, part II: experimental analysis," *Text. Res. J.*, vol. 78, pp. 1011–1021, 2008.

[140] X. Gong, "Investigation of different geometric structure parameter for honeycomb textile composites on their mechanical performance," Ph.D dissertation, The Manchester University, Manchester, UK, 2011.